

**A Regional Model Study of High Latitude Tropospheric Ozone  
and its Precursors.**

Thomas Munro Thorp

Submitted in accordance with the requirements for the degree of  
Doctor of Philosophy

The University of Leeds  
School of Earth and Environment

June, 2021



## **Declaration of Authorship**

The candidate confirms that the work submitted is his own, except where work which has formed part of jointly-authored publications has been included. The contribution of the candidate and the other authors to this work has been explicitly indicated below. The candidate confirms that appropriate credit has been given within the thesis where reference has been made to the work of others.

The work in Chapter 4 and Chapter 5 has appeared in the “Pan-Eurasian Experiment (PEEX) – Part 2” special edition of Atmospheric Chemistry and Physics as follows:

Thorp, T., Arnold, S. R., Pope, R. J., Spracklen, D. V., Conibear, L., Knote, C., Arshinov, M., Belan, B., Asmi, E., Laurila, T., Skorokhod, A. I., Nieminen, T., and Petäjä, T.: Late-spring and summertime tropospheric ozone and NO<sub>2</sub> in western Siberia and the Russian Arctic: regional model evaluation and sensitivities, *Atmos. Chem. Phys.*, 21, 4677–4697, <https://doi.org/10.5194/acp-21-4677-2021>, 2021.

Conceptualisation of research was done by T. Thorp and S.R. Arnold, with support from D. V. Spracklen. T. Thorp performed model simulations, model evaluation and data analysis. C. Knote provided WRFotron modelling scripts. M. Arshinov, B. Belan, E. Asmi, T. Laurila, A. I. Skorokhod, T. Nieminen and T. Petäjä provided ground observation data used in model evaluation. T. Thorp wrote the manuscript. All authors provided comments on the manuscript.

This copy has been supplied on the understanding that it is copyright material and that no quotation from the thesis may be published without proper acknowledgement.

The right of Thomas Thorp to be identified as Author of this work has been asserted by him in accordance with the Copyright, Designs and Patents Act 1988.

© 2021 The University of Leeds and Thomas Thorp

## **Acknowledgements**

Firstly, I would like to thank my primary supervisor Steve Arnold, who provided expertise, guidance and support throughout my PhD, especially during the challenging circumstances a nationwide lockdown presents. I would also like to thank my secondary supervisor Dom Spracklen, for his valuable feedback and thoughts on my work. I am extremely grateful to both Luke Conibear and Richard Pope, who provided technical support throughout my PhD, and answered any question I ever had.

I would like to thank all co-authors who provided me with help and feedback, in particular Christoph Knote, who provided the WRFotron scripts to automate the WRF-Chem model. I would like to thank both past and present members of the Biosphere-Atmosphere Group (BAG) research group for providing a supportive and enjoyable atmosphere throughout. Thanks to everyone in office 10.126, in particular Chris, Sarah and Laura, who I especially enjoyed sharing the ups and downs of a PhD with. A special mention to all those at ICAS coffee, especially Nigel Richards, who often provided entertaining distractions.

A special thanks to my parents for all their support throughout the years, I would not be where I am today without you. Finally, my biggest thanks goes to Charlotte, who's continued belief in me has kept me positive throughout my PhD from start to finish.

I acknowledge the NERC SPHERES DTP studentship (grant no. NE/L002574/1) for funding this project.

## Abstract

The Arctic has warmed disproportionately relative to mid-latitudes over recent decades. This warming is predominantly controlled by radiative forcing from well-mixed greenhouse gases, amplified by efficient Arctic climate feedbacks. However, warming from changes in short-lived climate pollutants (SLCPs), such as tropospheric ozone, have been shown to contribute substantially to Arctic warming, whilst also degrading air quality. Arctic SLCP abundances are controlled by long-range transport from mid-latitudes, and by local sources within the Arctic. At present, high latitude emissions of SLCPs and ozone precursors (e.g nitrogen dioxide [NO<sub>2</sub>]) are poorly quantified, with a paucity of in-situ observations. Using a regional chemistry transport model, this thesis aims to improve the understanding of processes controlling tropospheric ozone abundances and distributions in areas of limited in-situ observations at high latitudes.

In western Siberia there is widespread negative bias in modelled tropospheric column NO<sub>2</sub> when compared to satellite observations from May–August. Despite the large negative bias, the spatial correlations between model and observed NO<sub>2</sub> columns suggest that the spatial pattern of NO<sub>x</sub> sources in the region is well represented. Scaling the two largest anthropogenic sectors (energy & transport) by a factor of 2 reduces column NO<sub>2</sub> bias (fractional mean bias = -0.66 to -0.35). The findings in this thesis suggest that western Siberian ozone is more sensitive to anthropogenic emissions, particularly from the transport sector, and the contribution from fire emissions maximises in June and is largely confined to latitudes south of 60°N. Ozone dry deposition fluxes from the model simulations show that the dominant ozone dry deposition sink in the region is to forest vegetation, averaging 8.0 Tg of ozone per month.

In Fairbanks, Alaska, modelled surface ozone is overestimated during springtime, with an interplay between ozone being vertically mixed down from ozone-rich air above and subsequent ozone loss to NO ( $O_3 + NO = NO_2$ ) dominating ozone abundances, suppressing surface ozone. This also leads to

significant overestimations in surface NO<sub>2</sub>. Sensitivity studies tested modelled ozone sensitivity to Fairbanks NO<sub>x</sub> emissions and model upper boundary conditions. Results suggest that upper troposphere ozone is sensitive to a 20% reduction in initial boundary condition ozone, which brings the values in-line with observations. Whilst a doubling of NO<sub>x</sub> emissions from within Fairbanks improves the model ozone bias at the surface, but still leads to model overestimation above the boundary layer.

## Table of Contents

<b>Declaration of Authorship .....</b>	<b>iii</b>
<b>Acknowledgements .....</b>	<b>v</b>
<b>Abstract .....</b>	<b>vi</b>
<b>Table of Contents .....</b>	<b>viii</b>
<b>List of Figures .....</b>	<b>xi</b>
<b>List of Tables .....</b>	<b>xxii</b>
<b>Abbreviations.....</b>	<b>xxiii</b>
<b>1. Introduction.....</b>	<b>1</b>
1.1 Motivation .....	1
1.3 Thesis Aims .....	2
1.4 Thesis Layout .....	3
<b>2. Background.....</b>	<b>5</b>
2.1 Introduction.....	5
2.2 Earth's Atmosphere .....	5
2.3 Tropospheric Chemistry .....	6
2.3.1. Tropospheric Ozone.....	9
2.3.1.1 Ozone Formation.....	10
2.3.1.1 Ozone Production in the Troposphere .....	11
2.3.1.2 Hydroxyl Radical .....	13
2.3.1.3 Oxidation of methane and carbon monoxide.....	14
2.3.1.4 Photochemical sinks of tropospheric ozone, NO <sub>x</sub> and HO <sub>x</sub> .....	16
2.3.1.5 Ozone production dependencies.....	18
2.4 Air Pollutants at High Latitudes .....	20
2.4.1 Arctic Haze .....	20
2.4.2 Long Range Transport .....	22
2.4.2 Local Emission Sources .....	25
2.4.2.1 Anthropogenic Sources .....	26
2.4.2.2 Natural Sources.....	30
2.5 Climate Impacts of Air Pollution at High Latitudes.....	31
2.6 Air Quality Impacts at High Latitudes .....	33
2.7 Summary .....	34

<b>3. Methodology</b> .....	<b>35</b>
3.1 Air Quality Modelling.....	35
3.2 Weather Research and Forecasting Model with Chemistry.....	37
3.2.1 Model Setup.....	38
3.2.2 Physics .....	41
3.2.3. Chemistry.....	42
3.2.4 Emissions .....	44
3.3 Statistical Testing for Air Quality Modelling .....	45
<b>4. Evaluating regional NO<sub>2</sub> emissions in Western Siberia</b> .....	<b>47</b>
4.1 Introduction .....	47
4.2 Emission Inventories for Western Siberia.....	47
4.2.1 EDGAR HTAP v2.....	48
4.2.2 ECLIPSE v5a.....	49
4.2.3 Anthropogenic Soil NO <sub>x</sub> Emissions.....	49
4.3 Ozone Monitoring Instrument Satellite Data .....	50
4.4 WRF-Chem Setups.....	53
4.5 Results .....	56
4.5.1 Anthropogenic Emission Inventory Comparisons .....	56
4.5.1 Evaluation of WRF-Chem Tropospheric Column NO <sub>2</sub> .....	59
4.5.2 Model NO <sub>2</sub> Sensitivity tests .....	65
4.5.3 Evaluation of WRF-Chem Tropospheric Column NO <sub>2</sub> Using Scaled Emissions .....	66
4.5.4 NO <sub>2</sub> Source Contributions.....	69
4.6 Summary .....	72
<b>5. Key drivers of tropospheric ozone in Western Siberia: A quantification of high latitude sources and sinks.</b> .....	<b>73</b>
5.1 Introduction .....	73
5.2 Surface Observation Data .....	73
5.3 WRF-Chem Setup .....	76
5.4 Results .....	77
5.4.1 Surface Ozone Evaluation .....	77
5.4.2 Ozone Source Contributions.....	83
5.4.4 Chemical and Dynamical Contributions to Simulated Ozone .....	84
5.4.4.1 Total Domain .....	84
5.4.4.2 Vertical Profiles.....	88

5.4.3 Ozone Dry Deposition .....	94
5.4.3.1 Total Domain .....	94
5.4.3.2 Land Surface Types .....	96
5.5 Summary .....	100
<b>6. Physical and chemical controls of near-surface ozone in Fairbanks, Alaska .....</b>	<b>102</b>
6.1 Introduction .....	102
6.2 Observational Datasets .....	103
6.2.1 Ground Observations .....	104
6.2.2 MACSSIMIZE Campaign .....	105
6.2.3 Radiosonde Data .....	106
6.3 WRF-Chem Setup .....	107
6.3.1 Anthropogenic Emissions .....	107
6.3.2 Socioeconomic Data and Application Center (SEDAC) Population Data .....	109
6.3.3 Planetary Boundary Layer Setups .....	110
6.4 Results .....	114
6.4.1 Model Air Temperature Evaluation .....	114
6.4.1.1 Ground Observation Comparisons .....	114
6.4.1.2 Radiosonde Comparisons .....	119
6.4.1.3 Aircraft Vertical Profile Comparisons .....	124
6.4.1.4 Overall Comparisons .....	127
6.4.2 Model Surface NO Evaluation .....	129
6.4.3 Model Surface NO <sub>2</sub> Evaluation .....	132
6.4.4 Model Surface NO <sub>x</sub> Evaluation .....	135
6.4.5 Model Surface Ozone Evaluation .....	138
6.4.6 Model Surface O <sub>x</sub> Evaluation .....	142
6.4.7 MACSSIMIZE Flight Profiles .....	145
6.5 Summary .....	154
<b>7. Conclusion .....</b>	<b>156</b>
7.1 Completion of Aims .....	156
7.2 Synthesis .....	161
7.3 Future Work .....	162
<b>List of References .....</b>	<b>164</b>

## List of Figures

- Figure 2.1** – *Generalised vertical distribution of temperature (solid line) throughout the atmosphere. Met Office (2017).* 6
- Figure 2.2** – *Bar chart showing radiative forcing (hatched) and effective radiative forcing (solid) between 1750 – 2011. Uncertainties are shown in dotted (radiative forcing) and solid lines (effective radiative forcing). IPCC AR5 estimates, taken from Myhre et al., (2013), Figure 8.15.* 8
- Figure 2.3** – *Average ozone profile in the atmosphere, peaking on average at 8 ppmv in the stratospheric ozone layer (NASA, 2018)* 10
- Figure 2.4** – *Isopleth map showing ozone concentrations (ppbv) simulated by a regional photochemical model as a function of NO<sub>x</sub> and hydrocarbon emissions. Adapted from Sillman, et al., (1990).* 19
- Figure 2.5** – *Long term trends (plot A) and seasonal variations (plot B) of 6-hourly equivalent BC concentrations at Alert. Adapted from Law and Stohl (2007).* 21
- Figure 2.6** – *Schematic showing 3 key pathways for the transport of air pollution into the Arctic as described in Stohl et al., (2006): 1) wintertime low-level transport of already cold air into polar dome mainly from northern Eurasia; 2) lifting of pollutants at lower latitudes followed by upper tropospheric transport and slow descent or mixing into polar dome; 3) low-level transport from midlatitude emission regions followed by uplift at the Arctic front (AMAP, 2015).* 22
- Figure 2.7** – *Projected oil and gas production in the Arctic region and associated emissions of selected air pollutants (Peters et al., 2011).* 27
- Figure 2.8** – *Arctic shipping routes and maximum and minimum sea-ice extent for 2015 (AMAP, 2015).* 28

- Figure 2.9** – Future emission scenarios shown for  $\text{NO}_x$  (a), black carbon (b) and  $\text{SO}_2$  (c) based on ECLIPSE v5a and the Representative Concentration Pathway (RCP) emission data sets for regions north of  $60^\circ\text{N}$ . The coloured lines show different future scenarios from the ECLIPSE emissions: Baseline, current legislation (CLE), maximum technologically feasible reduction (MTFR), no further control (NFC) and short-lived climate-forcing pollutant mitigation (SLCP). The dotted lines show the different RCP scenarios. Adapted from Schmale et al., (2018). 30
- Figure 4.1** - Schematic of OMI's measurement technique, highlighting key parameters. Adapted from McCormick et al. (2013). 52
- Figure 4.2** - Map of domain used for model simulations. Centred on Western Siberia region, major cities (squares) (population > 100,000) shown in bold. Observation sites (star symbols) are given in italics 54
- Figure 4.3** - Monthly mean plots of GEIA anthropogenic soil  $\text{NO}_x$  emissions across Western Siberia. 56
- Figure 4.4** –Spatial distribution of anthropogenic emissions according to EDGAR HTAP v2.2 (panel (a)) and ECLIPSE v5a (panel (b)) inventories. Difference between the 2 inventories is shown in panel (c) (ECLIPSE v5a – EDGAR HTAP v2.2). 57
- Figure 4.5** - Observed tropospheric column  $\text{NO}_2$ . Panels a-d show monthly mean OMI tropospheric column  $\text{NO}_2$  for May – August. 59
- Figure 4.6** - Observed and model-observed tropospheric column  $\text{NO}_2$ . Panels a-d show mean OMI tropospheric column  $\text{NO}_2$  for May-August. Panels e-h show WRF-Chem bias (model – satellite) using the EDGAR HTAP v2.2 anthropogenic emission inventory for May-August. Panels i-l show WRF-Chem bias using the ECLIPSE v5a anthropogenic emission inventory for May-August. 60
- Figure 4.7** - Observed tropospheric column  $\text{NO}_2$  and satellite/model significant differences. Panels a-d show mean OMI tropospheric column  $\text{NO}_2$  for April-August. Panels e-l show where modelled and satellite differences in tropospheric column  $\text{NO}_2$  are statistically different for May to August for EH2 (e-h) and ECL (i-l). 61

- Figure 4.8** - *WRF-Chem simulated versus OMI tropospheric column NO<sub>2</sub> using ECL (magenta) and EH2 (green), for May (a), June (b), July (c) and August (d). All plots show total domain south of 65°N. Slope, correlation coefficient (R) and fractional mean bias (FMB) are shown in each panel.* 62
- Figure 4.9** - *Fractional mean bias of monthly simulated tropospheric column NO<sub>2</sub> for major cities (population >100,000) within Western Siberia when compared with OMI values. Panel (a) shows results using the EH2 anthropogenic emission inventory. Panel (b) shows results using the ECL anthropogenic emission inventory.* 64
- Figure 4.10** - *Observed and model-observed tropospheric column NO<sub>2</sub>. Panels a-d show mean OMI tropospheric column NO<sub>2</sub> for May-August. Panels e-h show WRF-Chem bias (model – satellite) using ECL\_SCALED anthropogenic emission inventory for May-August.* 67
- Figure 4.11** - *WRF-Chem simulated versus OMI tropospheric column NO<sub>2</sub> using ECL (magenta), EH2 (green), and ECL\_SCALED (blue) for May (a), June (b), July (c) and August (d). All plots show total domain south of 65°N. Slope, correlation coefficient (R) and fractional mean bias (FMB) are shown in each panel.* 69
- Figure 4.13** - *Simulated control and sensitivity run changes in surface NO<sub>2</sub> concentrations. Panels (a)–(d) show monthly means of WRF-Chem surface NO<sub>2</sub> for May-August using ECL\_SCALED emissions. Panels (e)-(h) show monthly means of WRF-Chem Surface NO<sub>2</sub> with all fire emissions switched off in domain (fires\_off simulation) minus control simulation for May-August. Panels (i)-(l) show monthly means of WRF-Chem Surface NO<sub>2</sub> with all transport emissions switched off in domain (trans\_off) minus control simulation for May-August. Panels (m)-(p) show monthly means of WRF-Chem Surface NO<sub>2</sub> with all energy emissions switched off in domain (ene\_off) minus control simulation for May-August.* 71
- Figure 5.1** - *Map of domain used for model simulations. Centred on Western Siberia region, major cities (squares) (population > 100,000) shown in bold. Observation sites (star symbols) are given in italics* 74

**Figure 5.2** – Hourly time series of surface ozone comparisons for WRF-Chem (blue) and ground observations (red) for three sites within the study domain: (a) ZOTTO, (b) Tomsk and (c) Tiksi. WRF-Chem output is taken from the ECL\_SCALED simulation. 77

**Figure 5.3** - Daily mean surface ozone comparisons for three ground observation sites within the study domain: ZOTTO (magenta), Tomsk (blue) and Tiksi (green) for 01/05/11 – 31/08/11. Panel (a) shows WRF-Chem surface ozone using EH2 anthropogenic emissions; panel (b) shows WRF-Chem surface ozone using ECL anthropogenic emissions; panel (c) shows WRF-Chem surface ozone using ECL\_SCALED anthropogenic emissions. 79

**Figure 5.4** - Panels (a) – (d) show monthly means of WRF-Chem surface wind direction plotted on top of wind speed. 80

**Figure 5.5** - Simulated control and sensitivity run changes in surface ozone concentrations. Panels (a)–(d) show monthly means of WRF-Chem surface ozone for May-August using ECL\_SCALED emissions. Panels (e)–(h) show monthly means of WRF-Chem Surface ozone with all fire emissions switched off in domain (fires\_off simulation) minus control simulation for May-August. Panels (i)–(l) show monthly means of WRF-Chem Surface ozone with all transport emissions switched off in domain (trans\_off) minus control simulation for May-August. Panels (m)–(p) show monthly means of WRF-Chem Surface ozone with all energy emissions switched off in domain (ene\_off) minus control simulation for May-August. 81

**Figure 5.6** - Surface ozone change relative to control simulation for the section of the domain north of 60°N (left panel) and south of 60°N (right panel) for the 3 sensitivity simulations, fires\_off (red), ene\_off (blue) and trans\_off (green). 83

**Figure 5.7** – Change in ozone due to horizontal advection between the surface and 900 hPa for May (a), June (b), July (c) and August (d). 85

**Figure 5.8** – Change in ozone due to vertical advection between the surface and 900 hPa for May (a), June (b), July (c) and August (d). 86

**Figure 5.9** – *Change in ozone due to convection between the surface and 900 hPa for May (a), June (b), July (c) and August (d). Note axis -1 to 1 ppbv.* 86

**Figure 5.10** – *Change in ozone due to vertical mixing (and dry deposition) between the surface and 900 hPa for May (a), June (b), July (c) and August (d).* 87

**Figure 5.12** – *Monthly mean vertical profiles of hourly change in ozone due to chemical tendencies above Novosibirsk in May (a), June (b), July (c) and August (d). Horizontal advection (Advh) is shown in red, vertical advection (Advz) is shown in orange, chemistry (chem) is shown in purple, convection (conv) is shown in green, vertical mixing (vmix) is shown in blue and the sum of tendencies is shown in dashed line.* 90

**Figure 5.13** - *Monthly mean vertical profiles of hourly change in ozone due to chemical tendencies above Kazan in May (a), June (b), July (c) and August (d). Horizontal advection (Advh) is shown in red, vertical advection (Advz) is shown in orange, chemistry (chem) is shown in purple, convection (conv) is shown in green, vertical mixing (vmix) is shown in blue and the sum of tendencies is shown in dashed line.* 91

**Figure 5.14** - *Simulated control and sensitivity run changes in surface ozone dry deposition flux. Panels (a)–(d) show monthly means of WRF-Chem surface ozone dry deposition flux for May-August using ECL\_SCALED emissions. Panels (e)-(h) show monthly means of WRF-Chem Surface ozone dry deposition flux with all fire emissions switched off in domain (fires\_off simulation) minus control simulation for May-August. Panels (i)-(l) show monthly means of WRF-Chem Surface ozone dry deposition flux with all transport emissions switched off in domain (trans\_off) minus control simulation for May-August. Panels (m)-(p) show monthly means of WRF-Chem Surface ozone dry deposition flux with all energy emissions switched off in domain (ene\_off) minus control simulation for May-August.* 95

- Figure 5.15** – *Grouped land surface types based on the modified IGBP MODIS Noah land surface scheme across Western Siberia for: Tundra (14.2% coverage of model domain), Snow, Ice and Water (22.3%), Urban & Built Up (0.1%), Cropland (10.8%), Permanent Wetlands (0.2%), Savanna & Grassland (13.1%), Shrubland (10.3%) and Forest (29.0%).* 96
- Figure 5.16** - *Quantity of ozone deposited to modified IGBP MODIS NOAH land surface cover categories per month for total domain (solid bars) and for the section of the domain north of 60°N (pale bars).* 98
- Figure 6.1** - *Surface-based temperature inversion frequency based on historic radiosonde data from Fairbanks, Alaska. The long-term mean frequency of temperature inversions shows the percentage of days with an inversion in a month. Radiosonde launches occur at 0000 UTC (1500 AST) and 1200 UTC (0300 AST). From Bourne et al.,( 2010).* 103
- Figure 6.2** - *Example flight path for 23/03/18. Outbound flight shown in red, return flight shown in blue. Blue shaded area denotes nonattainment area.* 105
- Figure 6.3** – *Panel (a) shows model domain in the context of Alaska and the surrounding area. Panel (b) shows the location of Fairbanks where the flight campaign is based, and the largest city in Alaska by population, Anchorage.* 107
- Figure 6.4** – *The Fairbanks North Star Borough region designated as a PM<sub>2.5</sub> nonattainment zone in 2009 by the EPA, which includes the city of Fairbanks (Alaska DEC, 2020).* 110
- Figure 6.5** – *Time series plots showing model and observation air temperature comparisons at the NCore site in downtown Fairbanks for 10/03/18 – 31/03/18. Comparisons shown for model PBL setups described in Table 6.1.* 115

- Figure 6.6** – Scatter plot showing model and observation air temperature comparisons at the NCore site in downtown Fairbanks for 10/03/18 – 31/03/18. Comparisons shown for model PBL setups described in Table 6.1. Values shown for correlation coefficient ( $R$ ), mean bias ( $MB$ ) and slope. 115
- Figure 6.7** – Weekly plots of simulated and observed surface air temperature diurnal cycles at the NCore site in downtown Fairbanks for: 10/03/18 – 16/03/18 (Week 1), 17/03/18 – 22/03/18 (Week 2) and 23/03/18 (Week 3). 117
- Figure 6.10** – Vertical profile plot showing radiosonde vertical profiles from 10/03/18 – 29/03/18. Twice-daily sondes shown are at 0300 and 1500 local time. First sonde shown on plot for each respective day is at 0300. 119
- Figure 6.9** – Mean bias plots showing vertical profiles from 10/03/18 – 29/03/18 for each model setup. Vertical plot shows model – observations at the same time as the radiosonde observations. 120
- Figure 6.10** – Contour plot showing radiosonde vertical temperature change from 10/03/18 – 29/03/18. Twice-daily sondes shown are at 0300 and 1500 local time. First sonde shown on plot for each respective day is at 0300. Red indicates an increase in temperature with elevation (temperature inversion occurring). Dashed lines are days where temperature observations are available and solid lines are where temperature and ozone observations are available. 121
- Figure 6.11** – Mean bias plots showing vertical temperature change from 10/03/18 – 29/03/18 for each model setup. Contour plot shows model – observations at the same time as the radiosonde observations. Red indicates an increase in temperature with elevation. 121
- Figure 6.12** – Comparison of simulated and observed vertical profiles from within the Fairbanks nonattainment area on the 11/03/18. Plot (a) shows the outbound flight, plot (b) shows return flight. Flight time is 1200 – 1645 local time. 124
- Figure 6.13** – Comparison of simulated and observed vertical profiles from within the Fairbanks nonattainment area on the 13/03/18. Plot (a) shows the outbound flight, plot (b) shows return flight. Flight time is 1030 – 1530 local time. 124

- Figure 6.14** – Comparison of simulated and observed vertical profiles from within the Fairbanks nonattainment area on the 20/03/18. Plot (a) shows the outbound flight, plot (b) shows return flight. Flight time is 1000 – 1535 local time. 125
- Figure 6.15** – Comparison of simulated and observed vertical profiles from within the Fairbanks nonattainment area on the 22/03/18. Plot (a) shows the outbound flight, plot (b) shows return flight. Flight time is 1200 – 1730 local time. 125
- Figure 6.16** – Comparison of simulated and observed vertical profiles from within the Fairbanks nonattainment area on the 23/03/18. Plot (a) shows the outbound flight, plot (b) shows return flight. Flight time is 1100 – 1630 local time. 126
- Figure 6.17** - Time series plots showing model and observation NO comparisons at the NCore site in downtown Fairbanks for 10/03/18 – 31/03/18. 129
- Figure 6.18** - Scatter plot showing model and observation NO comparisons at the NCore site in downtown Fairbanks for 10/03/18 – 31/03/18. Values shown for correlation coefficient (R), mean bias (MB) and slope. 130
- Figure 6.19** - Weekly plots of simulated and observed surface NO diurnal cycles at the NCore site in downtown Fairbanks for: 10/03/18 – 16/03/18 (Week 1), 17/03/18 – 22/03/18 (Week 2) and 23/03/18 (Week 3). 131
- Figure 6.20** - Time series plots showing model and observation NO<sub>2</sub> comparisons at the NCore site in downtown Fairbanks for 10/03/18 – 31/03/18. 132
- Figure 6.21** - Scatter plot showing model and observation NO<sub>2</sub> comparisons at the NCore site in downtown Fairbanks for 10/03/18 – 31/03/18. Values shown for correlation coefficient (R), mean bias (MB) and slope. 133
- Figure 6.22** - Weekly plots of simulated and observed surface NO<sub>2</sub> diurnal cycles at the NCore site in downtown Fairbanks for: 10/03/18 – 16/03/18 (Week 1), 17/03/18 – 22/03/18 (Week 2) and 23/03/18 (Week 3). 134

- Figure 6.23** - *Time series plots showing model and observation NO<sub>x</sub> comparisons at the NCore site in downtown Fairbanks for 10/03/18 – 31/03/18.* 135
- Figure 6.24** - *Scatter plot showing model and observation NO<sub>x</sub> comparisons at the NCore site in downtown Fairbanks for 10/03/18 – 31/03/18. Values shown for correlation coefficient (R), mean bias (MB) and slope.* 136
- Figure 6.25** - *Weekly plots of simulated and observed surface NO<sub>x</sub> diurnal cycles at the NCore site in downtown Fairbanks for: 10/03/18 – 16/03/18 (Week 1), 17/03/18 – 22/03/18 (Week 2) and 23/03/18 (Week 3).* 137
- Figure 6.26** - *Time series plots showing model and observation ozone comparisons at the NCore site in downtown Fairbanks for 10/03/18 – 31/03/18.* 138
- Figure 6.27** - *Scatter plot showing model and observation ozone comparisons at the NCore site in downtown Fairbanks for 10/03/18 – 31/03/18. Values shown for correlation coefficient (R), mean bias (MB) and slope.* 139
- Figure 6.28** - *Weekly plots of simulated and observed surface ozone diurnal cycles at the NCore site in downtown Fairbanks for: 10/03/18 – 16/03/18 (Week 1), 17/03/18 – 22/03/18 (Week 2) and 23/03/18 (Week 3).* 140
- Figure 6.29** - *Time series plots showing model and observation O<sub>x</sub> comparisons at the NCore site in downtown Fairbanks for 10/03/18 – 31/03/18.* 142
- Figure 6.30** - *Scatter plot showing model and observation O<sub>x</sub> comparisons at the NCore site in downtown Fairbanks for 10/03/18 – 31/03/18. Values shown for correlation coefficient (R), mean bias (MB) and slope.* 143
- Figure 6.31** - *Weekly plots of simulated and observed surface O<sub>x</sub> diurnal cycles at the NCore site in downtown Fairbanks for: 10/03/18 – 16/03/18 (Week 1), 17/03/18 – 22/03/18 (Week 2) and 23/03/18 (Week 3).* 144

- Figure 6.33** – Accumulated tendencies on the 11/03/2018 for WRF-Chem (control) ozone for: vertical mixing (panel a), advection (panel b), chemistry (panel c) and the sum of all tendencies (panel d). Tendency rate is ppbv/hour. 146
- Figure 6.34** – Accumulated tendencies on the 11/03/2018 for WRF-Chem ( $\text{NO}_x \cdot 2$  edit) ozone for: vertical mixing (panel a), advection (panel b), chemistry (panel c) and the sum of all tendencies (panel d). Tendency rate is ppbv/hour. 147
- Figure 6.35** – Vertical profiles on the 20/03/2018 of observed (black line) and model ozone for control (yellow line),  $\text{NO}_x \cdot 2$  (red line) and  $\text{IBC} \cdot 0.8$  (purple line) simulations. These are shown for the outbound flight at 1000 (panel a), return flight at 1535 (panel b), and the difference (return – outbound) between the two flights (panel c). 148
- Figure 6.36** - Accumulated tendencies on the 20/03/2018 for WRF-Chem (control) ozone for: vertical mixing (panel a), advection (panel b), chemistry (panel c) and the sum of all tendencies (panel d). Tendency rate is ppbv/hour. 149
- Figure 6.37** – Accumulated tendencies on the 20/03/2018 for WRF-Chem ( $\text{NO}_x \cdot 2$  edit) ozone for: vertical mixing (panel a), advection (panel b), chemistry (panel c) and the sum of all tendencies (panel d). Tendency rate is ppbv/hour. 150
- Figure 6.38** – Vertical profiles on the 23/03/2018 of observed (black line) and model ozone for control (yellow line),  $\text{NO}_x \cdot 2$  (red line) and  $\text{IBC} \cdot 0.8$  (purple line) simulations. These are shown for the outbound flight at 1100 (panel a), return flight at 1630 (panel b), and the difference (return – outbound) between the two flights (panel c). 151
- Figure 6.39** - Accumulated tendencies on the 23/03/2018 for WRF-Chem (control) ozone for: vertical mixing (panel a), advection (panel b), chemistry (panel c) and the sum of all tendencies (panel d). Tendency rate is ppbv/hour. 153

**Figure 6.40** – *Accumulated tendencies on the 23/03/2018 for WRF-Chem (NO<sub>x</sub>\*2 edit) ozone for: vertical mixing (panel a), advection (panel b), chemistry (panel c) and the sum of all tendencies (panel d). Tendency rate is ppbv/hour.*

**Figure 7.1** – *Schematic illustration of key processes controlling tropospheric ozone over high-latitude regions. 1 - Upper tropospheric ozone is controlled by large scale advection. 2 – Mixing down of ozone-rich air to surface layer. 3 – Suppressed surface ozone through reaction with NO leads to NO<sub>2</sub> production. 4 – Major loss mechanism of ozone is via dry deposition to vegetation, in particular the Siberian forest.*

## List of Tables

<b>Table 3.1</b> – WRF-Chem base setup used in this thesis.	39
<b>Table 4.1</b> - <i>WRF-Chem model experimental descriptions</i>	54
<b>Table 4.2</b> - <i>Total NO<sub>x</sub> emissions (kilotons per month) for the study domain from EH2 and ECL anthropogenic emission inventories, and soil NO<sub>x</sub> contribution from GEIA. Contributions from energy and transport sectors shown for each inventory</i>	58
<b>Table 4.3</b> - <i>Root mean squared error (RMSE) values for monthly simulated tropospheric column NO<sub>2</sub> in urban and background regions within Western Siberia when compared with OMI values, for each of the model simulations using EH2 and ECL emissions.</i>	63
<b>Table 4.4</b> - <i>Root mean squared error (RMSE) values for monthly simulated tropospheric column NO<sub>2</sub> in urban and background regions within Western Siberia when compared with OMI values, for each of the model simulations using ECL_SCALED emissions.</i>	68
<b>Table 5.1</b> – WRF-Chem ozone deposition velocity to different model land surface types as shown in Figure 5.15.	97
<b>Table 6.2</b> - <i>WRF-Chem model setups describing 6 simulations using different PBL schemes and meteorological nudging options.</i>	112
<b>Table 6.2</b> – <i>RMSE values shown for all model setup comparisons with observations presented in Section 6.4.1. Boxes coloured by RMSE value.</i>	127

## Abbreviations

<b>AFWA</b>	Air Force Weather Agency
<b>AK</b>	Averaging Kernel
<b>AMAP</b>	Arctic Monitoring and Assessment Programme
<b>AMF</b>	Air Mass Factor
<b>AMSA</b>	Arctic Marine Shipping Assessment
<b>AR5</b>	Fifth Assessment Report
<b>AST</b>	Alaskan Standard Time
<b>CLE</b>	Current Global Legislation
<b>CMAQ</b>	Community Multiscale Air Quality model
<b>CTM</b>	Chemistry Transport Model
<b>DOAS</b>	Differential Optical Absorption Spectroscopy
<b>DOMINO</b>	Dutch OMI for tropospheric NO <sub>2</sub>
<b>ECLIPSE</b>	Evaluating the Climate and Air Quality Impacts of Short-Lived Pollutants)
<b>EDGAR</b>	Emissions Database for Global Atmospheric Research
<b>ENSO</b>	El Niño-Southern Oscillation
<b>EPA</b>	Environment Protection Agency
<b>FAAM</b>	Facility for Airborne Atmospheric Measure
<b>FDDA</b>	Four Dimensional Data Assimilation
<b>FINN</b>	Fire Inventory from NCAR
<b>FMB</b>	Fractional Mean Bias
<b>FMI</b>	Finnish Meteorological Institute
<b>FTUV</b>	Fast Tropospheric Ultraviolet-Visible
<b>GAINS</b>	Greenhouse gas-Air pollution Interactions and Synergies

<b>GCM</b>	General Circulation Model
<b>GEIA</b>	Global Emissions Initiative
<b>GFS</b>	Global Forecasting System
<b>GHG</b>	Greenhouse Gases
<b>GPW v4</b>	Gridded Population of the World, Version 4
<b>GOCART</b>	Georgia Institute of Technology-Goddard Global Ozone Chemistry Aerosol Radiation and Transport
<b>GWP</b>	Global Warming Potential
<b>HTAP</b>	Hemispheric Transport of Air Pollution
<b>IAO</b>	Institute of Atmospheric Optics
<b>IEA</b>	International Energy Agency
<b>IGBP</b>	International Geosphere-Biosphere Programme
<b>IGRA</b>	Integrated Global Radiosonde Archive
<b>IIASA</b>	International Institute for Applied Systems Analysis
<b>IPCC</b>	Intergovernmental Panel On Climate Change
<b>JPL</b>	Jet Propulsion Laboratory
<b>LAI</b>	Leaf Area Index
<b>LES</b>	Large-Eddy Simulation
<b>MACSSIMIZE</b>	Measurements of Arctic Clouds, Snow, and Sea Ice nearby the Marginal Ice Zone
<b>MEGAN</b>	Model of Emissions of Gases and Aerosols from Nature
<b>MODIS</b>	Moderate Resolution Imaging Spectroradiometer
<b>MOSAIC</b>	Model for Simulating Aerosol Interactions and Chemistry
<b>MOZART</b>	Model of Ozone and Related Chemical Tracers
<b>MY</b>	Mellor-Yamada
<b>MYNN2.5</b>	Mellor-Yamada Nakanishi and Niino Level 2.5

<b>NAAQS</b>	National Ambient Air Quality Standard
<b>NAO</b>	North Atlantic Oscillation
<b>NCAR</b>	National Center for Atmospheric Research
<b>NCEP</b>	National Centers for Environmental Prediction
<b>NCore</b>	National Core Network
<b>NEI</b>	National Emission Inventory
<b>NOAA</b>	National Oceanic and Atmospheric Administration
<b>NWP</b>	Numerical Weather Prediction
<b>ODI</b>	Ozone Depletion Event
<b>OMI</b>	Ozone Monitoring Instrument
<b>PAN</b>	Peroxyacetyl Nitrate
<b>PBL</b>	Planetary Boundary Layer
<b>PCPI</b>	Polar Climate Predictability Initiative
<b>POLARCAT</b>	Polar Study using Aircraft, Remote Sensing, Surface Measurements and Models, of Climate, Chemistry, Aerosols and Transport
<b>POLMIP</b>	POLARCAT Model Intercomparison Project
<b>PPP</b>	Polar Prediction Project
<b>RAINS</b>	Regional Air Pollution Information and Simulation
<b>RAS</b>	Russian Academy of Sciences
<b>RMSE</b>	Root mean square error
<b>RRTM-G</b>	Rapid Radiative Transfer Model for GCMS
<b>SEDAC</b>	Socioeconomic Data and Application Center
<b>SLCPs</b>	Short Lived Climate Pollutants
<b>TEMIS</b>	Tropospheric Emissions Monitoring Internet Service
<b>TF HTAP</b>	Task Force Hemispheric Transport of Air Pollution

<b>TKE</b>	turbulent kinetic energy
<b>TROICA</b>	Transcontinental observation into the chemistry of the atmosphere
<b>TUV</b>	Tropospheric Ultraviolet-Visible
<b>USGS</b>	United States Geological Survey
<b>VCD</b>	Vertical Column Density
<b>VOCs</b>	Volatile Organic Compounds
<b>WACCM</b>	Whole Atmosphere Community Climate Model
<b>WHO</b>	World Health Organisation
<b>WMO</b>	World Meteorological Organisation
<b>WRF</b>	Weather Research and Forecasting model
<b>WRF-Chem</b>	Weather Research and Forecasting with Chemistry model
<b>WPS</b>	WRF Pre-processing System
<b>YOPP</b>	Year of the Polar Prediction
<b>YSU</b>	Yonsei University
<b>ZOTTO</b>	Zotino Tall Tower Observatory

## **1. Introduction**

### **1.1 Motivation**

The Arctic is currently warming at twice the rate of the global average, a process known as Arctic amplification (Arctic Monitoring and Assessment Programme (AMAP), 2017; Cohen et al., 2020). This has accelerated rates of sea ice loss and snow melt in the region, with a potential summer free of sea ice in the Arctic Ocean occurring in the 2030s (Screen and Simmonds, 2010). A key driver of this disproportional warming is through increased emissions of well mixed greenhouse gases such as carbon dioxide (CO<sub>2</sub>), methane (CH<sub>4</sub>) and nitrous oxide (N<sub>2</sub>O), predominantly sourced from fossil fuel combustion. Greenhouse gases act to warm the atmosphere through absorbing outgoing longwave radiation. This trapped longwave radiation is re-emitted in all directions, with the downward directed component heating the lower layers of the atmosphere (Cubasch et al., 2013). The global atmospheric burdens of these greenhouse gases are still increasing relative to pre-industrial levels, with CO<sub>2</sub> levels increasing by 40% since 1750 (Hartmann et al., 2013). Feedback effects associated with an increase in Arctic temperatures are also shown to be a causal factor of Arctic amplification, in particular the surface albedo effect (Pithan and Mauritsen, 2014).

However, though this warming is predominantly driven by well mixed greenhouse gases, short-lived climate pollutants (SLCPs) with atmospheric lifetimes shorter than typical hemispheric mixing times (approximately days to 1 month), can lead to regional scale warming of the climate (P. K. Quinn et al., 2007; Sand et al., 2016). Due to their short lifetime, SLCP distribution is not homogenous like long life greenhouse gases, meaning that the highest concentrations are often close to the source (Baker et al., 2015). SLCPs are aerosols or trace gases which can have detrimental effects on climate, air quality

and human health, either directly or through the formation of secondary pollutants, such as tropospheric ozone (Kirtman et al., 2013; Myhre et al., 2013). SLCPs can have both natural (e.g. forest fires) and anthropogenic (e.g. fossil fuel combustion) sources, but due to seasonal trends of emissions, contributions from key source sectors can differ throughout the year. At present, SLCP emissions at high latitudes are poorly quantified, in part due to insufficient in-situ observations. This problem is likely to be exacerbated in the future as Arctic SLCP emissions are expected to increase through a significant growth in Arctic shipping (Corbett et al., 2010); intensification of resource extraction (Stohl et al., 2013) and population growth (Andrew, 2014). Due to their shorter lifetime relative to well-mixed pollutants such as CO<sub>2</sub>, targeting SLCPs through potential emission controls could have a substantial benefit in mitigating Arctic regional warming, particularly in the near-term (Shindell et al., 2012).

Tropospheric ozone is a secondary pollutant and is detrimental to human health (Lelieveld et al., 2015) and vegetation (Fuhrer, 2009) at the surface, whilst in the mid troposphere it acts as a greenhouse gas (Myhre et al., 2013). An increase in anthropogenic emissions of ozone precursors since pre-industrial times has led to an increase in tropospheric ozone in the northern hemisphere, and is a likely key contributor to the Arctic warming observed over this period (Shindell, 2007). Tropospheric ozone and its precursors can be transported from the mid-latitudes to the Arctic (Stohl, 2006). Therefore the Arctic ozone burden is sensitive to both long-range transport of pollutants and local sources. Yet at present, there is limited information on the key behaviour and controls of ozone at high latitudes, in part due to the limited in-situ observations.

### **1.3 Thesis Aims**

The overall aim of this thesis is to improve the understanding of processes controlling tropospheric ozone abundances and distributions in areas of limited in-situ observations at high latitudes. Using a chemistry transport model and satellite, aircraft and ground observations, this thesis will predominantly focus on tropospheric ozone and its precursors, an important SLCP in the context of

the Arctic. One of the main regions investigated is Western Siberia, a previously unresearched area which is key in terms of springtime pollutant import for the Arctic region. This thesis has three results chapters with the following research aims:

- 1. Evaluate emissions of NO<sub>2</sub> in Western Siberia using tropospheric column NO<sub>2</sub> observations from satellite in conjunction with modelled output from WRF-Chem.**
- 2. Quantify source contributions to tropospheric ozone in Western Siberia and estimate the contributions from different types and regions of vegetation to dry deposition loss of ozone.**
- 3. Quantify the key physical and chemical drivers behind daily and diurnal tropospheric ozone changes in Fairbanks at the surface and through the vertical column in Spring 2018.**

## **1.4 Thesis Layout**

This thesis contains 7 chapters. Chapter 1 introduces the research motivation, aim, objectives and layout. Chapter 2 provides a literature review of the key topics discussed through this thesis. Chapter 3 introduces the model used for this research. Chapter 4 presents WRF-Chem model evaluation against satellite measurements of tropospheric column NO<sub>2</sub>. Chapter 5 shows the contributions of the key source sectors in Western Siberia to tropospheric ozone, whilst also quantifying the impact of different vegetation types as ozone sinks through dry deposition, both north and south of 60°N. Chapter 6 presents WRF-Chem model evaluation against aircraft and surface observations of air temperature and tropospheric ozone in Fairbanks, Alaska. Chapter 7 summarises and discusses

the work undertaken in this thesis, presents the key findings in the context of the wider literature, and suggests potential future research opportunities.

## **2. Background**

### **2.1 Introduction**

This chapter presents background information on atmospheric chemistry, in particular the main species considered in this thesis: nitric oxide (NO), nitrogen dioxide (NO<sub>2</sub>) and tropospheric ozone (O<sub>3</sub>). Section 2.2 introduces the basic structure of Earth's atmosphere. Section 2.3 provides information on the tropospheric chemistry involved in this thesis. Section 2.4 discusses sources of air pollutants at high latitudes. Section 2.5 discusses climate impacts of pollutants at high latitudes. Section 2.6 discusses air quality impacts of pollutants at high latitudes. 2.7 summarises the main points from this Chapter, highlighting the key unknowns in the literature.

### **2.2 Earth's Atmosphere**

The atmosphere of the Earth is divided into four distinct layers, predominantly based on temperature variation with altitude (Figure 2.1). These are the troposphere, stratosphere, mesosphere and thermosphere. At first temperatures decrease with height (positive lapse rate) within the troposphere (~0-11 km). The troposphere height varies with latitude, being lower at high latitudes. Above the troposphere is the stratosphere, which extends to approximately 50km above the Earth's surface. An increase in temperature with height (negative lapse rate) in the stratosphere limits vertical mixing, leading to significant stratification. The temperature inversion within this layer occurs due the absorption of ultra-violet radiation by stratospheric ozone leading to a warming effect in this layer. Beyond the stratosphere are the mesosphere (~50 – 85 km) and the thermosphere (~85 – 110 km) (Holloway and Wayne, 2010).

The total mass of Earth's atmosphere is approximately  $5 \times 10^{18}$  kg, with half of this mass below 5.5 km and 99% below roughly 30 km (Holloway and Wayne, 2010). The atmosphere is predominantly made up of nitrogen (78%) and oxygen

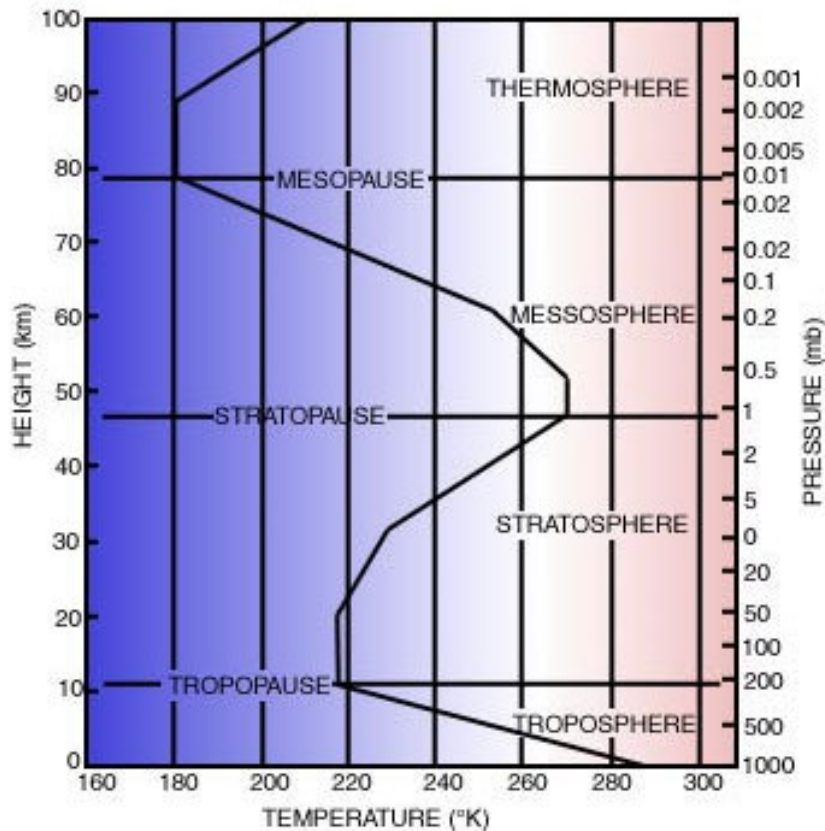


**Figure 2.11** – Generalised vertical distribution of temperature (solid line) throughout the atmosphere. Met Office (2017).

(21%). The remaining 1% is made up of argon (Ar), carbon dioxide (CO<sub>2</sub>), methane (CH<sub>4</sub>), neon (Ne), ozone (O<sub>3</sub>), water (H<sub>2</sub>O) and several biogenic and anthropogenic volatile organic compounds (VOCs). These gases are in the concentration ranges of parts per trillion (ppt) to parts per million (ppm), but despite these small concentrations they are important for both climate and air quality.

### 2.3 Tropospheric Chemistry

Approximately 90% of the atmospheric mass resides in the troposphere (Holloway and Wayne, 2010), with a large proportion of the minor trace-gas species and almost all aerosols and water vapour found there (Barry and Chorley, 2010). The troposphere is fairly self-contained due to the presence of a temperature inversion (the tropopause) acting as a “lid”, effectively limiting

convection. The height of the tropopause varies in both space and time, controlled by sea level temperature and pressure, which in turn is influenced by latitude, seasonality and short-term changes in surface pressure (Barry and Chorley, 2010). The height of the tropopause varies with latitude. Strong heating and vertical convective turbulence at the equator typically lead to a tropopause height of 16 km, whilst at the poles during winter it can be as low as 8 km (Barry and Chorley, 2010). Where strong temperature gradients occur in the troposphere, reflected in breaks in the tropopause near jet stream westerlies, tropospheric-stratospheric interchange can occur (Barry and Chorley, 2010). Though infrequent in occurrence, it can lead to dry, ozone-rich stratospheric air being brought down into the troposphere.

Atmospheric trace-gas species in the troposphere have a range of sources and sinks, both natural and anthropogenic, as well as varying lifetimes (Holloway and Wayne, 2010). They can have adverse impacts on the climate, air quality, human health and vegetation (Myhre, et al., 2013). Long-lived greenhouse gases (GHGs) such as carbon dioxide (CO<sub>2</sub>) (average atmospheric lifetime of 100 years), act to warm the atmosphere through absorbing outgoing longwave radiation, which causes an increase in temperature within the troposphere. Long-lived GHGs are well-mixed within the atmosphere and far from their source. CO<sub>2</sub> emissions are released during combustion of fossil fuels, and are currently increasing at an unprecedented rate, with this increase attributed to human activity (Holloway and Wayne, 2010; Myhre et al., 2013). Different trace-gas species have different lifetimes and influences on the atmosphere and subsequently, climate change. One way to quantify the impact of different species is to measure their radiative forcing effect (Myhre et al., 2013). Radiative forcing is defined as “the net change in the energy balance of the Earth system due to some imposed perturbation.” (Myhre et al., 2013). Radiative forcing is usually expressed as watts per square metre, which acts to quantify the energy imbalance that happens when the imposed change occurs and allows for comparisons across different forcing agents. Figure 2.2 shows the radiative forcing between 1750-2011 for different forcing agents (Myhre, et al., 2013).

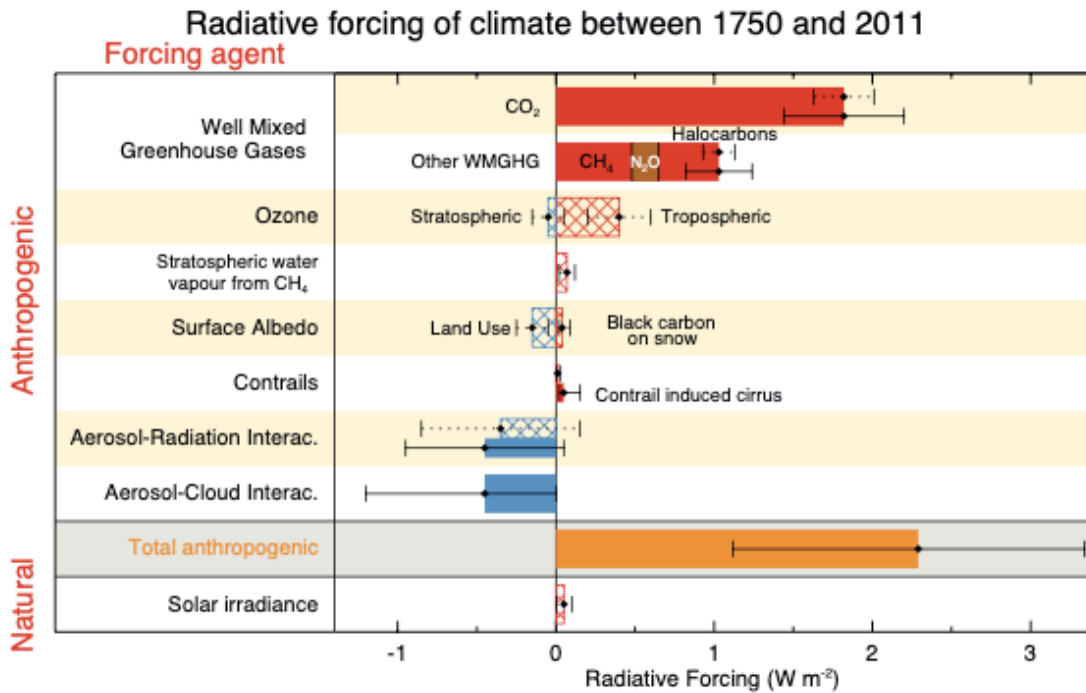


**Figure 2.12** – Bar chart showing radiative forcing (hatched) and effective radiative forcing (solid) between 1750 – 2011. Uncertainties are shown in dotted (radiative forcing) and solid lines (effective radiative forcing). IPCC AR5 estimates, taken from Myhre et al., (2013), Figure 8.15.

Tropospheric ozone is a GHG with a positive net radiative forcing effect (Skeie et al., 2020), which can be seen from Figure 2.2. Tropospheric ozone is the third strongest anthropogenic greenhouse gas forcer assessed in the fifth assessment report (AR5) by the Intergovernmental Panel on Climate Change (IPCC). This strong atmospheric warming from ozone is due to a strong band of absorption at 9.6  $\mu\text{m}$  in the infrared atmospheric window (8 – 14  $\mu\text{m}$ ). Ozone is not emitted at the surface, but is a secondary pollutant formed through photochemical oxidation of volatile organic compounds (VOCs), in the presence of nitrogen oxides ( $\text{NO}_x$ ) and sunlight (Crutzen et al., 1999). Ozone production is described in greater detail in Section 2.3.2. Tropospheric ozone is considered as a “short-lived climate pollutant” (SLCP) due to its relatively short lifetime (~23 days away from urban regions) (Stevenson et al., 2006). Due to this, tropospheric ozone is not well-mixed in the atmosphere, and is often enhanced

downwind of source regions of precursor emissions. As well as impacts on the climate, enhancements in near-surface tropospheric ozone degrade local air quality and are linked with premature mortality in humans (Jerrett et al., 2009; Lelieveld et al., 2015; Atkinson et al., 2016; Turner et al., 2016) and has detrimental impacts on vegetation (Fuhrer, 2009; Holloway et al., 2012; Rydsaa et al., 2016).

Tropospheric ozone is central to chemistry in the troposphere due to the role it plays in the initiation of photochemical oxidation processes via direct reaction, photolysis and subsequent reactions in the process of hydroxyl radical formation (Monks, 2005; Monks et al., 2015) (see Section 2.3.1.2).

### **2.3.1. Tropospheric Ozone**

The following Sections focus on the mechanisms most important when considering both tropospheric NO<sub>2</sub> and ozone in the context of Arctic air quality. This section is predominantly based on Holloway and Wayne (2010) and Seinfeld and Pandis (2006).

### 2.3.1.1 Ozone Formation

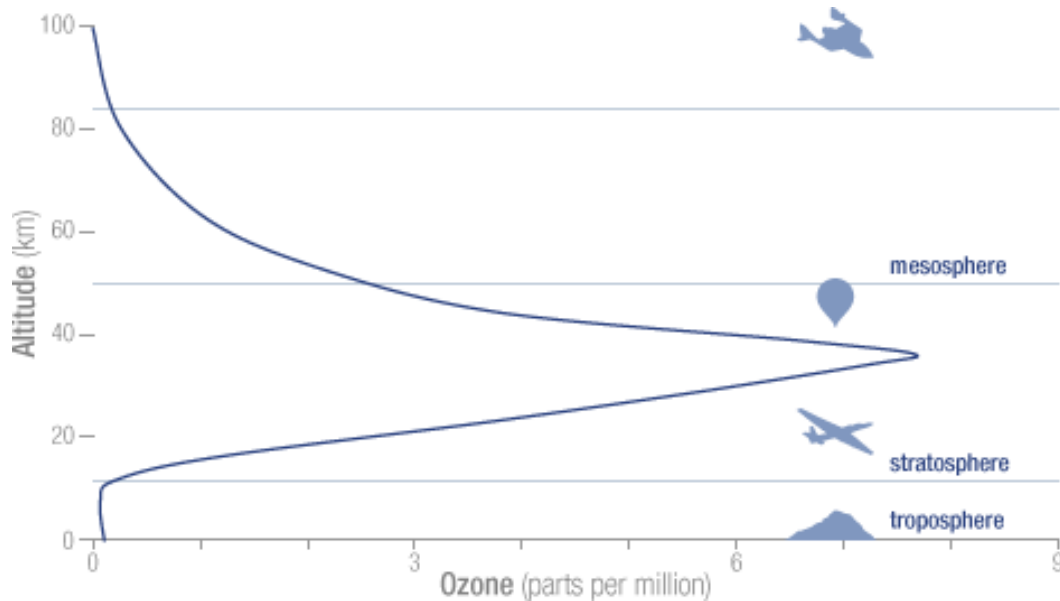


**Figure 2.13** – Average ozone profile in the atmosphere, peaking on average at 8 ppmv in the stratospheric ozone layer (NASA, 2018)

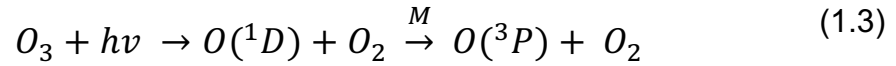
Ozone is found in trace amounts throughout the atmosphere, peaking in the stratosphere between 20 – 30 km altitude, in the region termed the ozone layer, as shown in Figure 2.3. In the stratosphere, ozone absorbs incoming shortwave solar radiation. Whilst in the troposphere, ozone is an air pollutant and greenhouse gas. Almost all ozone in both the stratosphere and the troposphere is formed through the addition of atomic oxygen to molecular oxygen:



$M$  represents a third body, usually either  $N_2$  or  $O_2$ . Atomic oxygen is formed by photolysis of  $O_2$  at  $\lambda < 242$  nm:



Reactions 1.1 and 1.2 lead to ozone production, but UV can also dissociate ozone to make atomic oxygen, which then can react with ozone to reform O<sub>2</sub>:



Where  $O(^1D)$  is the oxygen atom in its singlet state and  $O(^3P)$  is the oxygen in its triplet state. The cycle of reactions 1.2, 1.1, 1.3 and 1.4 is called the Chapman cycle (Chapman, 1930), which is responsible in explaining the location of the ozone layer in the stratosphere. A layered-like structure is expected for a species like ozone, whose concentrations are based on photochemical production rates in an atmosphere of varying optical density (Holloway and Wayne, 2010). For example, at high latitudes solar intensity is high, but there are limited amounts of O<sub>2</sub>, so there is little atomic oxygen production through photolysis, as seen in reaction 1.2. At low altitudes, there are high levels of O<sub>2</sub>, but limited levels of shortwave radiation at  $\lambda < 242$  nm (filtered by the above O<sub>2</sub> and O<sub>3</sub>) to make reaction 1.2 a source of atomic oxygen, and subsequently ozone. In between these two scenarios, a steady-state occurs which maximises the atomic oxygen production, and an abundance of O<sub>2</sub>, leading to increased ozone production (Figure 1.3). However, this source of ozone does not account for elevated levels of ozone observed in polluted regions at the surface, due to the required levels of shortwave radiation not penetrating down into the troposphere.

### 2.3.1.1 Ozone Production in the Troposphere

Ozone is a secondary pollutant and not emitted from the surface. The only known production pathway of ozone in the troposphere is through the photolysis of nitrogen dioxide (NO<sub>2</sub>) where  $\lambda < 424$  nm:



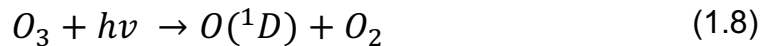
Ozone can also react with NO to reform NO<sub>2</sub>:



Reactions 1.5 – 1.7 are cyclical and are a sink and source of ozone in the troposphere. Nitrogen dioxide is photolysed at wavelengths less than 424 nm to create nitric oxide and molecular oxygen. This molecular oxygen reacts with atomic oxygen to reform ozone (source). The nitric oxide reacts with ozone to produce nitrogen dioxide (sink). Therefore, independent of any other reactions, this represents a null cycle with no net loss or production of ozone or NO<sub>x</sub> (NO + NO<sub>2</sub>). This indicates that for ozone to be readily produced in the troposphere, there must be another source of NO<sub>2</sub> other than reaction 1.7. Reaction 1.7 is important in highly polluted environments where it leads to extensive ozone loss and low ozone concentrations in high NO<sub>x</sub> areas.

### 2.3.1.2 Hydroxyl Radical

In the troposphere there are several species that are capable of absorbing solar radiation and then initiating radical-chain oxidation. For example, ozone photolysed at  $\lambda < 310$  nm, which is then a photochemical precursor of hydroxyl radicals (OH). Within the troposphere OH acts as a primary oxidant species with an extremely short lifetime and can react with many trace species. OH formation can occur through 2 main formation pathways. Firstly, when ozone is photolysed (as seen in reaction 1.3), it forms molecular oxygen and excited oxygen in its singlet state,  $O(^1D)$ , which can subsequently react with water ( $H_2O$ ) to yield OH:



Secondly, NO can be oxidised by the hydroperoxyl radical ( $HO_2$ ), which results in the formation of  $NO_2$  and OH:



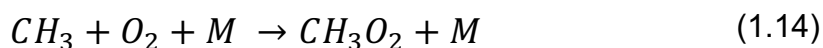
The production of  $NO_2$  in reaction 1.10 will lead to net production of ozone since NO has been converted to  $NO_2$  without consuming ozone. OH is often most abundant at the tropics, where there are high concentrations of water vapour, and significant photochemical loss of ozone, due to high amounts of solar radiation. The main sink of OH is through the oxidation of other trace gases in the troposphere, predominantly methane ( $CH_4$ ) and carbon monoxide (CO). Whilst in polluted regions, the loss to  $NO_2$  is also an important OH sink.

### 2.3.1.3 Oxidation of methane and carbon monoxide

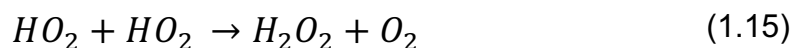
The major sink of the OH produced in Section 2.3.1.2 is through the oxidation of CH<sub>4</sub> and CO. In the unpolluted atmosphere, approximately 70% of OH reacts with CO and 30% with CH<sub>4</sub>. These oxidation processes can also lead to the production of peroxy radicals, facilitating oxidation of NO to produce NO<sub>2</sub>, therefore potentially acting as a precursor to further ozone production.



In both reactions 1.11 and 1.12 an active species is formed which is capable of adding molecular oxygen to produce different radical species:

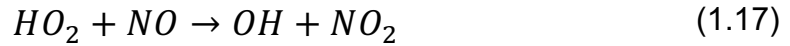


These radicals (HO<sub>2</sub> and CH<sub>3</sub>O<sub>2</sub>) are peroxy radicals, referred to as RO<sub>2</sub> (HO<sub>2</sub> is hydroperoxyl and CH<sub>3</sub>O<sub>2</sub> is methylperoxy). The atmospheric fates of these peroxy radicals depend on the abundance of NO<sub>x</sub>. In pristine environments, the HO<sub>2</sub> and CH<sub>3</sub>O<sub>2</sub> peroxy radicals are consumed through the reactions:



Hydrogen peroxide (H<sub>2</sub>O<sub>2</sub>) and methyl hydroperoxide (CH<sub>3</sub>OOH) can both dissolve in cloud droplets and be removed from the atmosphere in rain (wet

deposition), resulting in a net sink of HO<sub>x</sub> (OH + HO<sub>2</sub>). However, if NO<sub>x</sub> is present in the atmosphere, peroxy radicals can rapidly react with NO:



Reactions 1.17 and 1.18 lead to the generation of NO<sub>2</sub>, providing another source of NO<sub>2</sub> outside of the null-cycle described in reactions 1.5 – 1.7. Reaction 1.17 also leads to the regeneration of OH. Reaction 1.18 creates an alkoxy radical (RO), in this case methoxy, that can react with molecular oxygen:



Reaction 1.19 yields formaldehyde. The dominant loss mechanism for formaldehyde is through two photolysis pathways:



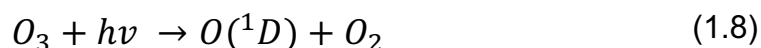
Reaction 1.20 is the main photolytic pathway ( $\lambda < 338$  nm), with both radicals re-entering the HO<sub>x</sub> chain. H re-joins via reaction 1.13, whilst HCO joins via the following reaction, also yielding CO in the process:



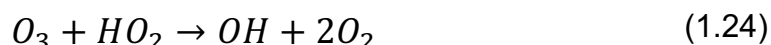
Formaldehyde can be formed from anthropogenic and naturally-sourced VOCs, which can in turn lead to the formation of ozone via reactions presented in this Section.

#### 2.3.1.4 Photochemical sinks of tropospheric ozone, $\text{NO}_x$ and $\text{HO}_x$

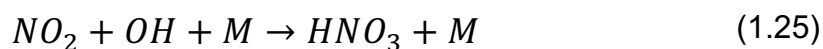
There is significant interplay between ozone,  $\text{NO}_x$  and  $\text{HO}_x$  in the troposphere. A loss of  $\text{HO}_x$  or  $\text{NO}_2$  can result in an overall net loss of ozone. Ozone itself has a number of chemical sinks in the troposphere:



To a lesser extent, ozone can also be removed from the atmosphere by reacting with  $\text{HO}_x$ :



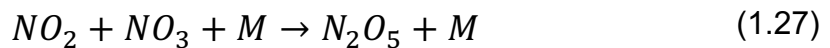
$\text{HO}_x$  is very reactive. OH readily acts to oxidise  $\text{CH}_4$  and CO as shown in reactions 1.11 and 1.12, whilst  $\text{HO}_2$  reacts with itself to form hydrogen peroxide (reaction 1.15), which can be removed through rain. OH can also react with  $\text{NO}_2$ , as part of an important cycle that results in a net loss of  $\text{NO}_x$ . During the daytime, when OH is readily available, this reaction leads to the formation of nitric acid ( $\text{HNO}_3$ ), which like hydrogen peroxide, can be removed by rain:



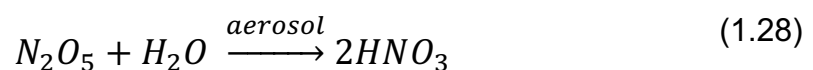
At the surface and in the lower troposphere this reaction is very efficient due to the high  $\text{NO}_2$  fraction of  $\text{NO}_x$ , leading to  $\text{NO}_x$  lifetimes of 1 – 2 days. However, in the upper troposphere where  $\text{NO}$  is more prominent, and less  $\text{NO}_2$  is available, the  $\text{NO}_x$  lifetime is 1 – 2 weeks. During the night, there is less  $\text{OH}$  due to no photolytic processes occurring. This then leaves  $\text{NO}_2$  and ozone available to react with one another to produce the nitrate radical ( $\text{NO}_3$ ):



During the day,  $\text{NO}_3$  can be rapidly photolysed to reform  $\text{NO}_x$ . However, during the night  $\text{NO}_3$  reacts with  $\text{NO}_2$  to form dinitrogen pentoxide ( $\text{N}_2\text{O}_5$ ):



$\text{N}_2\text{O}_5$  can then be lost on aerosol leading to the formation of nitric acid, which is subsequently removed through rain, resulting in a  $\text{NO}_x$  sink:



As mentioned when discussing reaction 1.25, the  $\text{NO}_x$  lifetime is relatively short, being 1-2 days in the lower troposphere. However, the influence of  $\text{NO}_x$  can be extended by a reservoir species which can then provide a  $\text{NO}_x$  source in regions where they are usually absent. One such reservoir species is peroxyacetyl nitrate, or PAN, which can be found in pristine, remote regions far from sources of  $\text{NO}_x$ . PAN is important because it is in thermal equilibrium with its precursors:



Above the boundary layer, where temperatures are low enough to allow for PAN to be stable, lifetime can be several months, resulting in significant transport from the source region. PAN will release  $NO_2$  as it reaches warmer surrounding air, often at lower altitudes. PAN has been shown to transport  $NO_2$  into the pristine Arctic and act as a significant source of lower troposphere ozone during the summer (Walker et al., 2012).

### 2.3.1.5 Ozone production dependencies

As shown in the previous Sections of this Chapter, ozone production is determined by concentrations of  $NO_x$  and the oxidation of CO and  $CH_4$ . VOCs can follow similar pathways to that of  $CH_4$ , and can react with OH to form the alkyl radical, R, which subsequently reacts with molecular oxygen to form  $RO_2$ :



This  $RO_2$  radical can then react with NO to form  $NO_2$ , and subsequently provide an ozone source:



Depending on the location of interest, a region can be dependent on either  $NO_x$  or VOC for ozone production. The relationship between ozone,  $NO_x$  and VOC concentrations is non-linear and often shown as an isopleth plot (Figure 1.4). In a  $NO_x$ -limited region,  $NO_x$  is in short supply, and this usually occurs where OH production is greater than that of  $NO_x$ . This is shown as the area to the left of

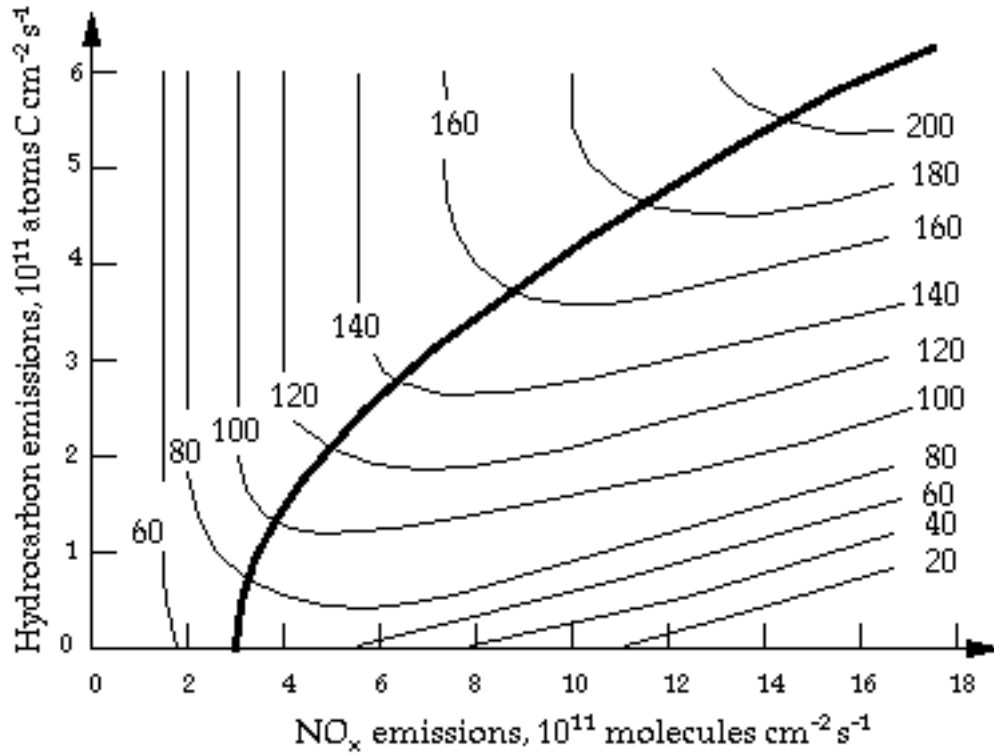


**Figure 2.14** – *Isopleth map showing ozone concentrations (ppbv) simulated by a regional photochemical model as a function of NO<sub>x</sub> and hydrocarbon emissions. Adapted from Sillman, et al., (1990).*

the thick line in Figure 1.4. In this situation, ozone concentrations are most sensitive to reductions/increases in NO<sub>x</sub> emissions. When the rate of OH production is less than that of NO<sub>x</sub> emissions, ozone production is VOC-limited (right-hand side of thick line in Figure 2.4), and ozone concentrations are most sensitive to changes in VOCs. In urban regions with high levels of NO<sub>x</sub> emissions, ozone is usually VOC-limited. In areas of significant NO emissions, usually associated with point source emissions (e.g. power plant), ozone concentrations can be suppressed due to reaction 1.7, termed titration.

## 2.4 Air Pollutants at High Latitudes

The following Sections 2.4 – 2.6 discuss high latitude air pollutants and their sources, as well as the air quality and radiative impacts of air pollutants in the high latitudes. In line with the overall aims of this thesis, the subsequent Sections predominantly focus on high latitude tropospheric ozone and its precursors.

### 2.4.1 Arctic Haze

Air pollution at high latitudes is not a new phenomenon, with aircraft pilots reporting a strange haze when flying in the Canadian and Alaskan Arctic during the 1950s (Greenaway, 1950; Mitchell, 1956). At the time the origin of the haze was unknown, and was attributed to ice crystals and blowing dust from riverbeds (Hole et al., 2006). Based on field experiments during the 1970s, this haze was found to reach a maximum during spring (Shaw and Wendler, 1972) and it was determined to be of anthropogenic origin (Rahn et al., 1977). Through both intensive field campaigns and long-term measurements it was discovered that the haze, termed Arctic haze, was anthropogenically-sourced due to large emissions from Europe and the former Soviet Union (Quinn et al., 2002; Quinn et al., 2007). These emissions were transported across large distances (hundreds of kilometres) and trapped in the Arctic air mass during winter leading to a springtime peak.

The Arctic haze is a mixture of sulfate and particulate organic matter, with smaller concentrations of ammonium, nitrate, dust and black carbon (Shao-Meng Li et al., 1993; Quinn et al., 2002). It also contains relatively high levels of ozone precursors such as  $\text{NO}_x$  and VOCs (Law and Stohl, 2007). Aircraft measurements have shown that the haze primarily resides in the lowest five kilometres of the atmosphere, whilst peaking in the lowest two kilometres (Quinn et al., 2007). Figure 2.5b shows the seasonal cycle of black carbon near-surface measurements from Alert, Canada, where concentrations peak in late springtime. At elevated altitudes, this peak can extend to late May time (Law

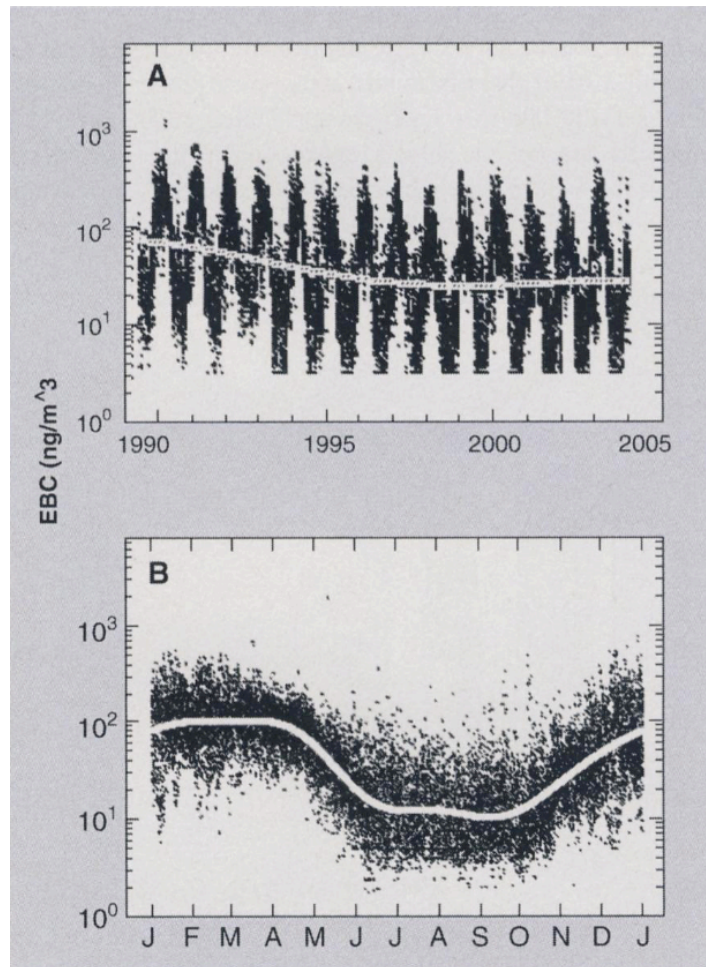


**Figure 2.15** – Long term trends (plot A) and seasonal variations (plot B) of 6-hourly equivalent BC concentrations at Alert. Adapted from Law and Stohl (2007).

and Stohl, 2007). Figure 2.5a highlights the long-term trend of elevated springtime levels of black carbon at Alert. Due to the presence of both sulfates and black carbon, the Arctic haze can lead to both scattering (Shaw, 1987) and to a lesser extent, absorption of short-wave radiation (Hansen and Rosen, 1984; Shaw, 1985). The result of this strong scattering and weaker absorption is a significant reduction in visibility (Quinn et al., 2007). This springtime peak is predominantly controlled by an interplay between complex, large-scale processes: strong surface-based temperature inversions, inhibited removal pathways of key haze components, and strong meridional transport of pollutants from the mid-latitudes, which intensifies during springtime (Shaw, 1995).

## 2.4.2 Long Range Transport

It is widely accepted that the Arctic haze is predominantly made up of pollution from sources outside of the Arctic, imported via long-range transport during the winter and spring months (Law and Stohl, 2007). This is due to efficient wintertime transport pathways at low levels from the mid-latitudes (Rahn, 1981), with slow removal processes due to the cold and dark environment (Shaw, 1995), and limited local sources of large-scale pollution (Barrie, 1986; Marelle et al., 2015). Large-scale import of air pollutants from Northern Eurasia during winter and spring is driven through mechanisms depicted in Figure 2.6 pathway 3, and described in this Section.

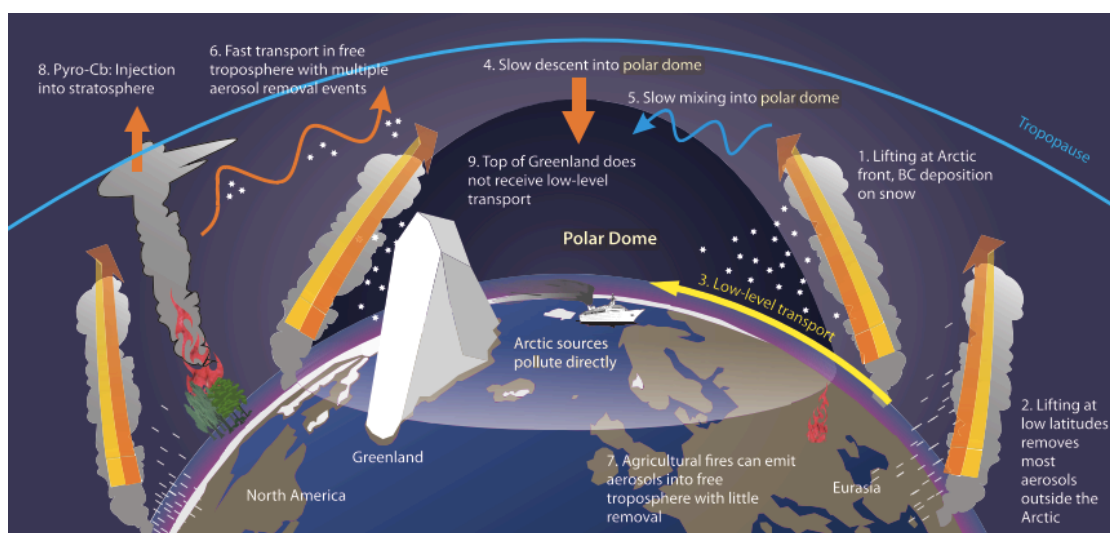


**Figure 2.16** – Schematic showing 3 key pathways for the transport of air pollution into the Arctic as described in Stohl et al., (2006): 1) wintertime low-level transport of already cold air into polar dome mainly from northern Eurasia; 2) lifting of pollutants at lower latitudes followed by upper tropospheric transport and slow descent or mixing into polar dome; 3) low-level transport from midlatitude emission regions followed by uplift at the Arctic front (AMAP, 2015).

During the winter and early spring, surface temperatures become extremely low, which results in frequent and persistent temperature inversions (Bradley et al., 1992), which in turn leads to very stable conditions and limited turbulent

exchange (Stohl, 2006). This causes an extremely dry Arctic troposphere, minimising dry deposition, resulting in enhanced aerosol lifetimes during the Arctic winter. Surfaces of constant potential temperature form closed domes over the Arctic (Fig 1.6) (Klonecki et al., 2003), isolating this extremely stable, dry air mass within the lower Arctic troposphere from the rest of the atmosphere. This barrier between the Arctic lower troposphere dome and above free troposphere is known as the Arctic front (Barrie, 1986).

Shown as transport pathway 3 in Figure 2.6, low-level transport is a key route for air pollution to enter the High Arctic, and contribute to the Arctic haze (Carlson, 1981; Iversen, 1984; Barrie, 1986; Stohl, 2006). This occurs because the polar dome is not symmetrical about the pole and can shift seasonally, for example in winter it can sit across Eurasia and extend as far south as 40°N (Barrie, 1986). As northern Eurasia has similarly low potential temperatures to that of the Arctic haze layers, and is located within the Arctic front, emitted pollutants (e.g. aerosols and ozone precursors) can move via isentropic transport, remaining at low-levels, limiting removal pathways through dry or wet deposition (Stohl, 2006).

Pollution from the densely populated regions of North America and southeast Asia can be transported to the Arctic mid and upper troposphere but cannot effectively penetrate the Arctic dome (Law and Stohl, 2007). This mechanism is shown as pathways 1 and 2 in Figure 2.6. Typically as pollution is emitted at source it is lifted at lower latitudes due to the warm and turbulent surface air, often leading to cloud formation (AMAP, 2015). This can lead to pollutant and aerosol removal through wet scavenging, typically occurring south of the Arctic. If the pollutant and aerosol is not scavenged out, it can penetrate the polar dome through slow descent from above, as shown in pathway 4 in Figure 2.6. However, descent from the upper troposphere to the surface can take several weeks (AMAP, 2015).

When high latitude pollutants are emitted at the surface but are not within the Arctic front (e.g. Europe, eastern Asia), they can travel at low levels towards the Arctic front (Stohl, 2006). This tends to lead to greater dry deposition of pollutants at the surface, due to the sources already being at high latitudes (Doherty et al., 2010). Upon arrival at the Arctic front boundary, lifting of the pollutants occur, due to being unable to penetrate the polar dome (pathway 1 in Figure 2.6).

Episodic biomass burning events, such as wildfires and agricultural fires, from outside of the Arctic can lead to an increase in pollution in the high latitudes (Stohl et al., 2006). Plumes originating from fires outside of the Arctic can be efficiently transported at high altitudes in the upper troposphere or even stratosphere, depending on their injection height (AMAP, 2015). This has led to distinct layers of aerosols (e.g black carbon) and pollutants ( $\text{NO}_x$  and CO) associated with fires being found in the Arctic stratosphere previously (Roiger et al., 2011).

The transport pathways shown in Figure 2.6 can be affected by seasonality and large-scale meteorological patterns, impacting long-range transport to the Arctic (AMAP, 2015). For example, the location of the Arctic front differs significantly during the summertime compared to winter, with a northward retreat, shifting to follow the coastal outline of Eurasia (Barrie, 1986). This northward retreat is one of the key reasons summertime pollution concentrations in the Arctic are lower (Stohl et al., 2006). Eckhardt et al., (2003) found that the North Atlantic Oscillation (NAO) exerts a strong control on pollution transport to the Arctic, especially during the spring and wintertime. In particular they found that during a positive NAO phase there was an increase in satellite-observed  $\text{NO}_2$  travelling polewards, when compared to a negative NAO phase. This difference was mainly attributed to a change in the pollution pathway of European-sourced pollution to the Arctic during a positive NAO phase. Further to this, Eckhardt et al., (2003) reported significant positive correlations between increased CO concentrations measured at 3 Arctic observation sites and positive NAO phases.

Previous studies based on satellite observations of CO, have also shown that a negative El Niño-Southern Oscillation (ENSO) can hinder efficient pollutant transport to the Arctic, (Fisher et al., 2010). Whilst Monks et al., (2012) used a global chemistry model to highlight the influence of ENSO on Arctic fire emissions, and the subsequent impact this had on Arctic CO interannual variability.

### **2.4.2 Local Emission Sources**

The Arctic lower troposphere is directly influenced by pollution from sources locally and from the Eurasian high-latitudes (Arnold et al., 2016). Local emission sources can be both anthropogenic or natural in origin, with varying influence seasonally. At present there is a severe lack of quantification of the key sources and subsequent impacts of high latitude emission sources (Schmale et al., 2018). There is a paucity of studies investigating local sources, and their wider impacts on both the inhabited areas in the Arctic, and their surrounding areas (Schmale et al., 2018). Furthermore, there are limited estimates as to the future of the Arctic in terms of population and economic growth, and how this will impact local emissions and air quality going forward. For example, Overland and Wang, (2013) predict that by 2050 the Arctic will be ice-free during the summer, which will likely lead to increased commercial shipping, fishing and tourism (Corbett et al., 2010; Browse et al., 2013; Meier et al., 2014; Allison and Bassett, 2015; Schmale et al., 2018). This is further compounded by the potential of future oil and gas exploration and extraction within the Arctic, with estimates suggesting that 30% of the world's undiscovered gas and 13% of undiscovered oil resources are located within the Arctic (Gautier et al., 2009). Population predictions suggest that the Arctic population is estimated to increase, especially in the North American Arctic close to resource extraction points, such as Canada, as the global demand for resources increases (Larsen and Fondahl, 2015). This further complicates predicting both current and future Arctic air quality.

### 2.4.2.1 Anthropogenic Sources

The main sources of anthropogenic emissions in the Arctic are in locations associated with industrial activities and/or large populations (AMAP, 2006). Yet a coherent evaluation of anthropogenic ozone precursor sources across the Arctic is lacking. The Arctic has a low population density, but there are a small number of large cities and towns, most notably Murmansk, Russia (300,000 population), Norilsk, Russia (180,000) and Tromsø, Norway (77,000). Anthropogenic sources of ozone precursors result from high temperature combustion of fossil fuels, associated with emissions from the transport sector, shipping and domestic heating (AMAP, 2015). Industrial activities in the Arctic linked to oil and gas extraction and exploration are another source of anthropogenic emissions, including gas flaring (Stohl et al., 2013; Schmale et al., 2018). Local emissions of ozone precursors are having an important influence on current Arctic atmospheric composition (Arnold et al., 2016).

Domestic combustion as a source for power generation and residential heating increases during the wintertime in the Arctic (Tran and Mölders, 2011). Yet it is often underestimated in emission inventories (Stohl et al., 2013) or missing entirely (Hienola et al., 2013). Combustion of wood, oil, coal and natural gas, and the use of diesel generators is often the primary source of heating in remote Arctic regions during the wintertime, and is primarily associated with emissions of NO<sub>x</sub>, CO and black carbon (Stohl et al., 2013). Cook stoves are frequently used in areas that have unreliable sources of power, such as remote regions of Alaska, and are often used in conjunction with diesel generators (Bluestein et al., 2008).

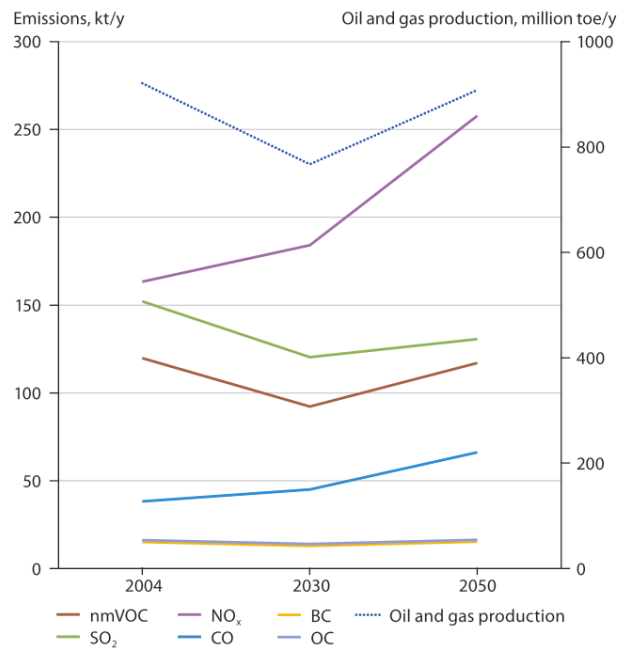


**Figure 2.17** – Projected oil and gas production in the Arctic region and associated emissions of selected air pollutants (Peters et al., 2011).

Oil and gas exploration and associated flaring are important sources of local Arctic emissions of ozone precursor species (Peters et al., 2011; Stohl et al., 2013). Current oil and gas production within the Arctic is at its highest level since the first commercial oil and gas activities began in the 1920s (Peters et al., 2011). The key areas of present active oil and gas activity include Canada, the USA, Norway and Russia, with the largest reserves located in the latter (Harsem et al., 2011). In the future it is suggested that with more access, and for longer periods of time due to sea ice melt, Arctic oil and gas development will become easier and more cost effective (Harsem et al., 2011; Peters et al., 2011). This is reflected in predicted NO<sub>x</sub> emissions associated with oil and gas production expected to continue to increase over the next 30 years (Fig. 2.7).

Gas flaring is a major source of black carbon and to a lesser extent, CO and NO<sub>2</sub> (Elvidge et al., 2009; Li et al., 2016). However, flaring activity is either missing or geographically misplaced in most emission inventories (Stohl et al., 2013). Emission efficiency of both trace gases and aerosols can vary depending on both combustion conditions and fuel composition, also leading to poor

quantification of air pollutants related to flaring (Li et al., 2016). This has led to significant uncertainties where flaring is included within emission inventories, with little available information on high latitude flaring volumes and emission factors (AMAP, 2015). In the Arctic there are significant flaring activities on gas fields in the Russian Arctic, with Russia the largest flaring nation in the world (Elvidge et al., 2009). Since 2004 Russian emissions of NO<sub>2</sub> from gas flaring have remained fairly constant (Li et al., 2016). Yet accurate quantification of both flaring volumes, and associated air pollutants, are needed, due to the large discrepancies between values reported in national statistics and satellite-observed values (AMAP, 2015).

As the Arctic continues to warm, sea ice thins and retreats, it is expected that Arctic shipping traffic is likely to increase (Corbett et al., 2010). Shipping is an important current source of black carbon, SO<sub>2</sub> and ozone precursors such as



**Figure 2.18** – Arctic shipping routes and maximum and minimum sea-ice extent for 2015 (AMAP, 2015).

NO<sub>x</sub> and VOCs in coastal Arctic regions (Corbett et al., 2010). It has been shown that shipping emissions can have a direct influence on air quality in coastal regions through enhanced ozone concentrations (Endresen et al., 2003; Aliabadi et al., 2015). Whilst future Arctic shipping activities will have important air quality impacts in the near-pristine region (Granier et al., 2006), also influencing both the future Arctic and global climate (Dalsøren et al., 2007; Tronstad Lund et al., 2012). The Arctic council's Arctic Marine Shipping Assessment (AMSA) report showed that in 2004, approximately 6000 ships operated within the Arctic (Arctic Council, 2009). This was predominantly made up of ships undertaking community re-supply, marine tourism and moving natural resources out of the Arctic. The regions where most of the shipping took place included coastal regions of northwest Russia, the ice-free waters off Norway, Greenland, Iceland and in the US Arctic (Arctic Council). However, the prospect of new shipping routes opening, such as the Northwest and Northeast Passages (Fig 2.8), as well as polar routes between Europe, North America and Asia, could lower travel distances by between 25 – 50% (Corbett et al., 2010). This could be further compounded by an increase in sightseeing cruises, which have significantly grown in popularity in the last decade (Eckhardt et al., 2013).

A limited number of future emission scenarios for the Arctic exist, but of those available there is significant uncertainty regarding future estimates of Arctic anthropogenic activity. Schmale et al., (2018) compared two different future scenario data sets, and found significant variation between projected policy and development scenarios (Fig. 2.9). This variation is linked to uncertainties in economic growth in the region (Amann et al., 2013) and the development and adoption of potential future air quality control policies. This spread in future Arctic emissions highlights the uncertainty in the current understanding of future Arctic emissions and the developments of any future emission control policies.

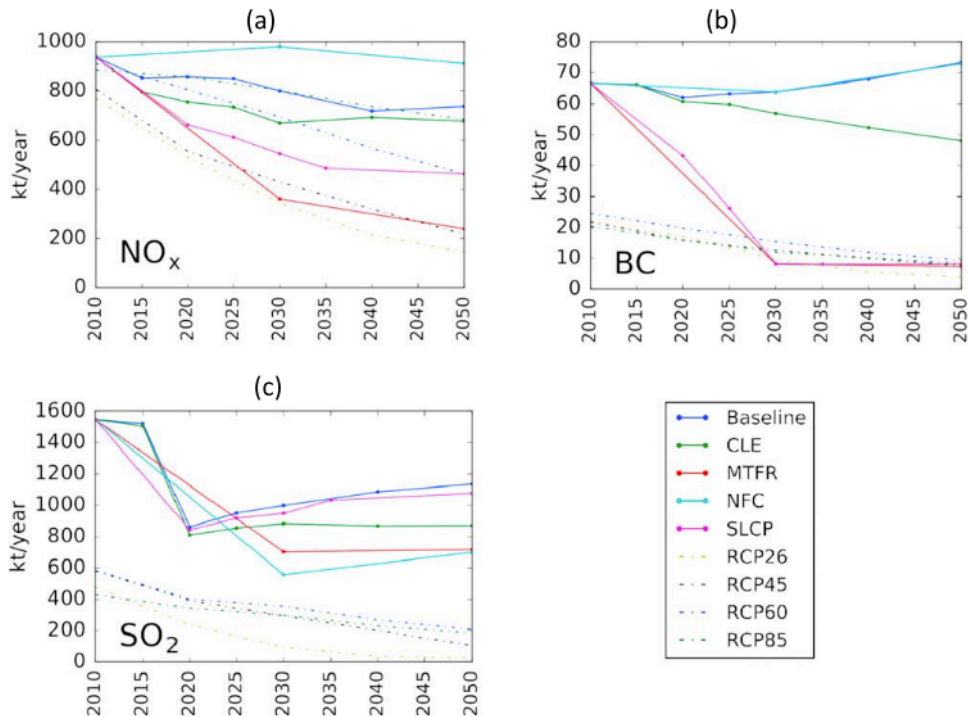


**Figure 2.19** – Future emission scenarios shown for  $\text{NO}_x$  (a), black carbon (b) and  $\text{SO}_2$  (c) based on ECLIPSE v5a and the Representative Concentration Pathway (RCP) emission data sets for regions north of  $60^\circ\text{N}$ . The coloured lines show different future scenarios from the ECLIPSE emissions: Baseline, current legislation (CLE), maximum technologically feasible reduction (MTFR), no further control (NFC) and short-lived climate-forcing pollutant mitigation (SLCP). The dotted lines show the different RCP scenarios. Adapted from Schmale et al., (2018).

#### 2.4.2.2 Natural Sources

Agricultural burning (often started by humans) and wildfires can be a significant source of aerosols and trace gases in the Arctic (Warneke et al., 2010). Emissions from forest fires are the greatest natural source of air pollutants in the Arctic (Giglio et al., 2013). These emissions tend to vary seasonally and spatially, with large interannual variability (Giglio et al., 2013). Yet information

on agricultural fires within the Arctic Circle is very limited (Schmale et al., 2018). This is complicated by an increase in recent high-impact fire events within the Arctic (Kukavskaya et al., 2016). McCarty et al., (2020) suggest that based on recent fire years (2019 and 2020), Arctic fire behaviour could be changing. An earlier onset of fires, more frequent below ground burning, and previously “fire-resistant” ecosystems are now burning (e.g. tundra bogs, fens and marshes). Arctic fire activity tends to have 2 annual peaks: one after snowmelt in March and April, and second in August, which is linked to long periods of dry, warm weather (Flannigan et al., 2009). However, these burning periods are likely to increase in length, and have an earlier onset as record warming continues in the Arctic (Warneke et al., 2010). Accurate fire detection and quantification is currently difficult for satellites, with large proportions of Arctic fires smouldering, and therefore undetectable (Waigl et al., 2017). For example, Waigl et al., (2017) found that satellite observations were unable to detect 45% of Alaskan wildfires for 2016, which led to significant biases in emissions associated to wildfires for this region. Arctic agricultural burning and wildfires are likely to increase in frequency, severity and extent in the future due to warmer and drier summers (Knorr et al., 2016), but currently predicting how these will influence future Arctic air quality is difficult, due to little knowledge surrounding key factors involved in calculating emission rates and emission factors.

## **2.5 Climate Impacts of Air Pollution at High Latitudes**

Tropospheric ozone has a positive net radiative forcing effect through the absorption of both longwave and shortwave solar radiation (Fig 2.2) (Myhre et al., 2013). Targeting ozone precursors through mitigation measures could provide improvements to local air quality, improve crop yields and lower annual premature deaths (Shindell et al., 2012). Mitigation measures could also influence climate on shorter time scales than that of carbon dioxide reduction methods (Shindell et al., 2012). However, ozone radiative forcing is strongly dependent on both altitude and latitude, and the so-called greenhouse effect is strongest where the temperature difference between the surface and cold tropopause is largest (AMAP, 2015). In the Arctic the tropopause is typically lower, and there are often strong surface-based inversions, resulting in smaller

temperature differences between the Earth's surface and the tropopause. This leads to a reduction in impact of ozone's radiative forcing in the Arctic (Berntsen et al., 1997).

Sand et al., (2016) showed that based on results from multiple chemical transport models, SLCPs have significantly contributed to recent Arctic warming. However, if stringent SLCP mitigation measures are put in place, Arctic warming could be cut by 0.2 K in 2050. Emissions from Asia were shown to be the largest source of SLCPs in the Arctic in terms of absolute amounts, but the Arctic was shown to be most sensitive, per unit mass emitted, to SLCP emissions from within the Arctic nations. The dominant source from within the Arctic was attributed to Russian flaring emissions, followed by forest fire and flaring emissions from the Nordic countries.

There are several uncertainties when considering the climate impact of SLCPs (e.g. tropospheric ozone), outlined in Stohl et al., (2015) and references within: First, at present there are large uncertainties associated with estimating the climate effects of SLCPs, which is also reflected in the effects of any potential emission reductions. Second, the climate impact for the non-methane SLCPs can depend strongly on both location and time (e.g. summer/winter). This can lead to complications when calculating a single value of Global Warming Potential (GWP) for such a large region as the Arctic. Third, due to their short-life times, non-methane SLCPs usually have a greater positive forcing influence closer to the source, but the extent to which these air pollutants can react with other species is an unresolved issue. For example, emissions of  $\text{NO}_x$  can lead to a shorter-lived positive radiative forcing effect due to increases in ozone, and a longer-lived negative radiative forcing effect due to the destruction of methane. Fourth, SLCPs can have influence on other global cycles, such as the hydrological cycle, and general atmospheric circulation. Finally, there are interdependencies between both SLCPs and long-term climate change. The impact that SLCPs can have on climate depend on the atmosphere in which they are emitted into to, whilst future changes to atmospheric composition,

temperature, relative humidity, surface albedo and circulation are likely to cause these impacts to change.

## **2.6 Air Quality Impacts at High Latitudes**

Enhanced tropospheric ozone is associated with multiple health problems, impacting the respiratory, cardiovascular and reproductive systems, whilst also being a cause of premature mortality (Lelieveld et al., 2015). Many of these epidemiological studies are undertaken around the world, in the USA, Europe and Asia. However, there are very few short-term and no long-term studies investigating air quality impacts at high latitudes (Schmale et al., 2018). Continuous measurements of key air quality indicator species are established in major cities at high latitudes, but these do not provide actual exposure for individuals (AMAP, 2006). A limited number of studies have investigated the impacts of indoor air pollution, focussing on indoor use of wood or coal stoves for heating (Guggisberg et al., 2003; Bulkow et al., 2012). The only study looking at Arctic air quality impacts on health from outdoor sources, investigated the effect of sulphur dioxide (SO<sub>2</sub>) from a Russian nickel smelter on lung function (Smith-Sivertsen et al., 2001). Despite regular exceedances of World Health Organisation (WHO) air quality limits for SO<sub>2</sub>, and evidence of vegetation damage (Gytarsky et al., 1995), there was no measurable reduction in lung function from the nickel smelter (Smith-Sivertsen et al., 2001). The limited number of studies investigating health impacts at high latitudes demonstrates potentially large knowledge gaps (Schmale et al., 2018).

Tropospheric ozone has negative effects on major staple crops across the globe, such as rice, wheat, corn and potato (Fuhrer, 2009). Ozone penetrates the leaf via the stomata, impairing photosynthesis through limiting stomatal functioning, degrades chlorophyll and negatively effects leaf area index (LAI). Ozone can also impact on reproduction through affecting pollen germination and tube growth (Black et al., 2000). As the Arctic warms it is expected that vegetation changes will lead to northward migration of the treeline and changes to the tundra biome (Bjorkman et al., 2018; Berner et al., 2020). At present the

Arctic boreal forest is a significant sink of ozone (Stjernberg et al., 2012). In particular the boreal forests in Siberia, Russia are so vast they are relevant for the global ozone budget. Yet, if changes are brought on by a warming climate, the ecology, biogenic emissions and surface deposition may change. Whilst increasing import of anthropogenically-sourced ozone from Europe could damage these Siberian forests, reducing the strength of the boreal forest ozone sink (Stjernberg et al., 2012).

## **2.7 Summary**

Tropospheric ozone is an air pollutant which degrades air quality, has a positive radiative forcing effect and is detrimental to human health. Tropospheric ozone is a secondary pollutant, with a lifetime of several weeks, formed through photochemical oxidation of VOCs, in the presence of NO<sub>x</sub> and sunlight.

Tropospheric ozone, its precursors and aerosols are transported to the Arctic from Eurasian source regions during winter, leading to the springtime peak termed Arctic Haze. The dominant source route is through low-level transport to the high latitudes. However, there is limited understanding on how these species, in particular tropospheric ozone, interact with the multiple local pollutant sources and sinks on the way to the Arctic. This is compounded by a paucity of in-situ observations over key regions. Limited efforts have been made to model this, but current anthropogenic emissions of ozone precursor species are likely poorly quantified for key Arctic regions.

### **3. Methodology**

This Chapter describes the air quality model and methods used within this thesis. Section 3.1 provides a brief background of air quality modelling. Section 3.2 introduces the WRF-Chem regional model. Section 3.3 presents the statistical tests used to evaluate model output throughout this thesis.

#### **3.1 Air Quality Modelling**

In-situ and remote sensing observations can provide an insight into chemical species present in the atmosphere at a given point in time. In-situ observations, such as ground, aircraft or balloon-based, can provide high spatial and temporal coverage, but these measurements are only available in close proximity of the instrument and can be limited in terms of altitude, latitude, longitude and time (Holloway and Wayne, 2010). Remote observations, such as ground, aircraft or satellite-based remote sensing, can provide measurements for regions that are distant from the instrument. However, these can often have relatively poor spatial resolution and can also be available for limited time periods (Holloway and Wayne, 2010). To resolve these issues, mathematical models have been used to simulate atmospheric conditions on a range of spatial scales for over a century (Bjerknes, 1904). A model provides the opportunity to test the current best understanding of particular processes, whilst also predict and test the impacts of changes within the current understanding.

The concept of using fundamental mathematical equations to forecast atmospheric conditions were first presented in Vilhelm Bjerknes's breakthrough 1904 paper (Bjerknes, 1904) (Gramelsberger, 2009), becoming known as Numerical Weather Prediction (NWP). Following the development of computational models in the 1950s advancements in atmospheric modelling led to highly sophisticated, three-dimensional models which can simulate the weather, climate and air quality both globally and regionally (sub 1 km horizontal resolution) using powerful super-computers. The subsequent mention of the term model in this Chapter refers to these three-dimensional, mathematical,

atmospheric models commonly used in air quality research, which focus on the troposphere (Grell et al., 2005).

Models can be applied to a range of scales, from local/regional to global. Regional models tend to focus on smaller regions of the globe (i.e. continental size or smaller) and run at both a higher temporal and spatial scale compared to a global model, usually using a more complex chemistry and aerosol scheme.

Models can be simulated “offline” to save computational cost, where the meteorological variables are simulated independent of chemistry, with meteorological variables usually provided from meteorological reanalysis data, or a general circulation model (GCM) (Zhang, 2008). These results are subsequently fed into a decoupled chemistry transport model (CTM), which advects the trace species and updates the chemistry (Holloway and Wayne, 2010). This process is commonly referred to as offline coupling. However, more frequently “online” models are now being used in the prediction of air quality (Grell et al., 2005). In the real world, chemical and physical processes in the atmosphere are coupled. Chemistry can impact on meteorology (e.g. changes to radiation budget), and meteorology can influence chemistry (e.g. wind speed/direction impacting on chemical transport) (Grell et al., 2005). “Online” CTMs have fully-integrated chemistry-aerosol and meteorology components, allowing feedbacks between the two at every model timestep, with no interpolation in space and time. These models can effectively be used as tools to investigate the regional effects of chemical and aerosol species in the atmosphere, but at a significant computational cost (Zhang, 2008). One such fully-coupled “online” regional CTM is the Weather Research and Forecasting with chemistry (WRF-Chem) model (Grell et al., 2005), which is used in this thesis.

### 3.2 Weather Research and Forecasting Model with Chemistry

In this thesis, regional chemical-transport simulations are undertaken using the fully coupled “online” WRF-Chem model version 3.7.1 (Grell et al., 2005; Fast et al., 2006). WRF-Chem consists of a core NWP model, the Weather Research and Forecasting (WRF) model (Skamarock et al., 2008). WRF was initially developed in partnership by the National Center for Atmospheric Research (NCAR), the National Oceanic and Atmospheric Administration (NOAA), the US Air Force, the Naval Research Laboratory, the University of Oklahoma, and the Federal Aviation Administration (Powers et al., 2017). To address an array of Earth system prediction beyond just weather, WRF has a range of extensions which are built to have two-way interaction with the atmospheric component such as: WRF-Chem (Air Chemistry), WRF-Hydro (Hydrology), WRF-Fire (Fire Weather), HWRF (Tropical Cyclones), WRF-Urban (Urban meteorology), WRF-Solar (Solar and wind energy), WRF-LES (Large-eddy-scale-modelling) and Polar WRF (Polar environments). Polar WRF does not contain chemical or aerosol species, and is focussed on Arctic atmosphere-land-ocean feedbacks only, therefore is not used in this thesis. WRF and the number of extended versions are strongly supported and developed through community feedback, whilst technical support is provided by NCAR, which includes user assistance, system oversight and integration of code contributions from worldwide users (Powers et al., 2017).

WRF-Chem has successfully been implemented into the WRF framework, creating two-way interactions between meteorology and chemistry (Grell et al., 2005). Transport of species uses the same vertical and horizontal coordinates (no interpolation), and the same physical parameterizations at the same model timesteps. WRF-Chem has multiple options for meteorological, aerosol and gas-phase processes, with varying levels of complexity, enabling a range of scientific investigations. In relation to the work presented in this thesis, WRF-Chem has been used numerous times to successfully investigate air quality at high latitudes in the past (Tran et al., 2011; Mölders et al., 2011; Sessions et al., 2011; Thomas et al., 2013; Louis Marelle et al., 2015; Marelle et al., 2017; Raut

et al., 2017; Antokhin et al., 2018), and has also been used in high latitude multi-model comparison projects (Eckhardt et al., 2015; Stohl et al., 2015).

### 3.2.1 Model Setup

All WRF-Chem model code (including all programs used in model workflow described below) is available to download from the NCAR website at the following location: <https://www2.acom.ucar.edu/wrf-chem>. This thesis used the WRFotron scripts provided by Christoph Knote and described at: <https://wrfchem-leeds.github.io/WRFotron/index.html>, which automate WRF-Chem simulations with reinitialised meteorology. A WRF-Chem simulation is split into 3 workflow stages, which WRFotron assists through automation: pre-processing, main simulation and postprocessing. WRFotron also allows for the creation of spin-up conditions prior to the main simulation to create the idealised model meteorological and chemical initial conditions.

Pre-processing is undertaken using the WRF Pre-processing System (WPS), which aims to prepare input to WRF for real-data simulations (Duda, 2012). Through the geogrid program, WPS initially creates the horizontal domain through defining values for static fields for all model grid points within the domain using horizontal interpolation (e.g. land use type, topography height, soil type etc). Then using external data input sources (e.g. Global Forecast System [GFS] data), WPS extracts the relevant input data using ungrrib (tool to extract information from General Regularly-distributed Information in Binary [GRIB] files). Using metgrid, WPS horizontally interpolates this extracted data to the simulation domain (defined by geogrid). Then finally, using the real program, these values are vertical interpolated to the WRF eta levels, creating both the initial and boundary meteorological conditions.

Following this, using latitude-longitude gridded input, gridded chemical and aerosol emissions are created for use in WRF-Chem (Barth et al., 2015). All pre-processors described in this paragraph are available to download from the

NCAR website (<https://www2.acom.ucar.edu/wrf-chem/wrf-chem-tools-community>). Anthropogenic emissions are created using the `anthro_emis` program, a mass conserving anthropogenic emissions pre-processor. This can use both regional and global input files and has been tested for multiple anthropogenic emission inventories. Biogenic emissions are created using the `bio_emiss` program, which in the case of this thesis uses the `megan_bio_emiss` version, an “online” version of the Model of Emissions of Gases and Aerosols from Nature (MEGAN) (Guenther et al., 2006). This provides estimate emissions of VOCs, NO<sub>x</sub> and CO from vegetation (Barth et al., 2015). Fire emissions are created using the `fire_emiss` program. The final step of pre-processing is to set the initial and boundary chemical conditions, which is done using the `mozbc` program. This program fills the chemical fields in the model domain with the global model output, which has been interpolated in both time and space (Pfister, 2012).

The base model is described in Table 3.1. The chemical and aerosol setup chosen is partly based on previous studies investigating regional air quality, whilst other setup parameters are chosen to reflect the interests in the high-latitudes. The general model setup is summarised here, with further detail provided in Sections 3.2.2, 3.2.3 and 3.2.4. Each Results Chapter within this thesis uses this base setup, with further model parameters described within each Chapter that are relevant to the scientific aims of that Chapter.

**Table 3.1** – WRF-Chem base setup used in this thesis.

<b>Model Parameter</b>	<b>WRF-Chem Option</b>
Vertical levels	33 vertical levels and 27 meteorological levels. Model top at 10 hPa.
Projection	Polar Stereographic Projection
Land surface model	Unified Noah land-surface model (Ek, 2003)
Planetary boundary layer scheme	Mellor-Yamada Nakanishi and Niino Level 2.5 PBL (Nakanishi and Niino, 2009)
Convective parametrisation	Grell 3D (Grell and Dévényi, 2002)

Cloud microphysics scheme	Thompson (Thompson et al., 2008)
Longwave radiation scheme	RRTM-G (Rapid Radiative Transfer Model for GCMs) longwave (Mlawer et al., 1997)
Shortwave radiation scheme	RRTM-G (Rapid Radiative Transfer Model for GCMs) shortwave (Pincus et al., 2003)
Initial and boundary meteorological conditions	NCEP GFS, supplemented with NCEP FNL (National Centers for Environmental Prediction [NCEP], 2021)
Photolysis scheme	Madronich Fast Tropospheric Ultraviolet-Visible (FTUV) (Tie, 2003)
Gas phase chemistry	Model of Ozone and Related Chemical Tracers (MOZART) V4 (Emmons et al., 2010)
Aerosol scheme	Model for Simulating Aerosol Interactions and Chemistry (MOSAIC) 4-Bin (Zaveri et al., 2008)
Mineral dust	GOCART dust emissions with AFWA modifications (Chin et al., 2002)
Initial and boundary chemical/aerosol conditions	MOZART V4 (National Center for Atmospheric Research [NCAR], 2021)

### 3.2.2 Physics

All model simulations within this thesis use a polar stereographic projection. This is the idealised map projection for high latitude studies as it limits the distortion seen closer to the poles in other projection options (e.g. Mercator). It is advised within the WRF user guides provided by NCAR if significant portions of the domain or regions of interest fall above 50 °N then the polar stereographic projection is the most suited projection. Static geography fields used within WPS are taken from the international geosphere-biosphere programme (IGBP) – modified moderate resolution imaging spectroradiometer (MODIS), used in conjunction with the Noah land surface model (Ek, 2003). This uses 20-category vegetation (land-use) data, which is provided by Boston University, with modifications made by NCEP.

In Chapters 4 and 5, the Mellor-Yamada Nakanishi and Niino Level 2.5 (MYNN2.5) planetary boundary layer (PBL) scheme is used (Nakanishi and Niino, 2009). Whilst in Chapter 6, the MYNN2.5 PBL is used and compared to the Yonsei University (YSU) PBL (Hong et al., 2006). The YSU PBL scheme is described in greater detail in Section 6.3.3. The MYNN 2.5 PBL is shown to be an improvement on previous iterations of the Mellor-Yamada (MY) PBL scheme, with improved performance at recreating PBL characteristics when compared with a large-eddy simulation (LES) of a convective boundary layer (Nakanishi and Niino, 2009). Recreating PBL characteristics is important for air quality at high latitudes that often suffer poor air quality under a strongly stratified PBL (Tran and Mölders, 2011). Atmospheric radiative transfer calculations are performed by the Rapid Radiative Transfer Model (RRTM) in both the shortwave (Pincus et al., 2003) and the longwave (Mlawer et al., 1997). The Thompson scheme was used as the cloud microphysics scheme (Thompson et al., 2008). The Thompson scheme is a double-moment bulk microphysics scheme commonly used in WRF, and plays a key role in the prediction of the occurrence, development and dissipation of weather systems (Lei et al., 2019). The Grell-3D cumulus physics scheme was used for convective parameterization (Grell and Dévényi, 2002). This acts to parameterise the effects of both deep and shallow convection by using the most up-to-date understanding of convective

clouds to help express the interactions between large scale flows and convective clouds.

Initial and boundary conditions for meteorology are from the NCEP Global Forecast System (GFS) 6-hourly analysis files. These files were used for grid analysis nudging every 6 hours, to avoid model meteorological fields drifting and limit errors in large scale transport. Nudging in WRF uses four-dimensional data assimilation (FDDA), which allows the model state to be relaxed continuously at each time step (6-hourly in this thesis) towards the observed state (Deng et al., 2007). Nudging adds an artificial forcing term to the governing equations that reflects the difference between the observed and modelled meteorology at a particular point in time (Otte, 2008). Previous work investigating the impact of nudging shows that the use of meteorological nudging in the Community Multiscale Air Quality Model (CMAQ) results in improved hourly surface ozone mixing rates (Otte, 2008). In Chapters 4 and 5 meteorological nudging takes place in all model layers above the PBL. Chapter 6 investigates the impacts of different nudging setups, with more detail provided in Table 6.1. Chemical nudging does not take place during any simulation to allow for a clearer understanding of model performance in capturing chemical loss, production and lifetime.

### **3.2.3. Chemistry**

Gas-phase chemistry is represented by the Model of Ozone and Related Chemical Tracers, version 4 (MOZART-4) (Emmons et al., 2010). MOZART-4 is an “offline” global chemical transport model for the troposphere. A detailed list documenting the 85 species and 196 reactions is described in Emmons et al., (2010). The MOZART-4 mechanism has been extensively used in previous regional WRF-Chem simulations investigating air quality. In this thesis I use updates to the photochemistry of aromatics, biogenic hydrocarbons, and other species relevant to air quality described in Knote et al., (2014). When using MOZART-4 it is advised that either the Tropospheric Ultraviolet-Visible (TUV) or

the fast-TUV (FTUV) (Tie, 2003) schemes are used for calculating photolysis rates (Emmons et al., 2010; Hodzic and Knote, 2014). In this thesis I use the FTUV photolysis scheme due to the computational costs compared to using the full TUV scheme. Detailed instructions are provided in Hodzic and Knote, (2014) on WRF-Chem namelist options when using the updated MOZART-4 and FTUV photolysis scheme, including a new species mapping list for all gases and aerosols.

Aerosol chemistry is represented by the Model for Simulating Aerosol Interactions and Chemistry (MOSAIC) 4-Bin scheme (Zaveri et al., 2008). MOSAIC was initially designed to work in conjunction with WRF-Chem and is designed to be highly modular so to allow for easy coupling with other chemical and microphysical processes (Zaveri et al., 2008). MOSAIC represents aerosol size distribution in either 4-bin or 8-bin sizes from between 39 nm and 10  $\mu\text{m}$  (Kazil, 2015), with a 4-bin setup advised when using the MOZART chemistry scheme. MOSAIC aerosol composition includes sulphate ( $\text{SO}_4$ ), sea salt (NaCl), methanesulfonate ( $\text{CH}_3\text{SO}_3$ ), carbonate ( $\text{CO}_3$ ), calcium (Ca), black carbon, (BC), primary organic mass (OC) and other inorganic mass (e.g. minerals, trace metals) (Zaveri et al., 2008). MOSAIC calculates aerosol number concentrations, as well as aerosol mass concentrations. In-cloud wet deposition occurs when cloud droplets that contain aerosols are converted to precipitation (Grell and Freitas, 2014). Dry deposition velocities are based on the resistance approach of Wesely (1989). In Chapter 4 and 5 of this thesis aqueous chemistry is switched off in the MOZART-MOSAIC 4-Bin setup (`chem_opt=201`), but is used in Chapter 6 (`chem_opt=202`). Aqueous chemistry is switched on in Chapter 6 due to the scientific aims of the Chapter. Further to this, the Chapter 6 study period is significantly shorter than that of Chapters 4 and 5, and running with aqueous chemistry has a greater computational cost.

### 3.2.4 Emissions

Due to the aims and subsequent model experiments of Chapters 4, 5 and 6, the anthropogenic emissions used within this thesis are described within the relevant Chapters.

Biomass burning emissions are from the Fire Inventory from NCAR (FINN) version 1.5 (Wiedinmyer et al., 2011). These are provided as daily, global estimates of trace gas and particle emissions from the open burning of biomass, which includes wildfire, agricultural fires and prescribed burning (Wiedinmyer et al., 2011). FINN uses satellite observations of active fires and land cover, with emission factors and estimated fuel loadings, which provide high spatial and temporal resolution open burning emission estimates (1km). For the location and timing of fires, FINN uses the MODIS Thermal Anomalies Product (Giglio et al., 2006). Biogenic emissions are calculated using the “online” Model of Emissions of Gases and Aerosols from Nature (MEGAN) (Guenther et al., 2006). MEGAN has 134 emitted chemical species, including VOCs, NO<sub>x</sub> and CO from vegetation at a high spatial resolution (1 km<sup>2</sup>) (Duhl et al., 2011). Dust emissions are from the Georgia Institute of Technology-Goddard Global Ozone Chemistry Aerosol Radiation and Transport (GOCART) model (Chin et al., 2002), with Air Force Weather Agency (AFWA) scheme (LeGrand et al., 2019). Results using the AFWA dust emission scheme with GOCART show marked improvements compared to the standard GOCART-WRF scheme, with key improvements to model algorithms permitting saltation flux to be modelled separately from dust emission.

Chapters 4 and 5 use MOZART-4 (Emmons et al., 2010) simulation output for both initial and boundary chemical and aerosol conditions. As described in Section 3.2.1, this is interpolated onto the WRF-Chem domain in the pre-processing stage using the mozbc program. MOZART-4 data is downloaded from the NCAR website at 6-hourly intervals at 1.9 x 2.5 degrees, with 56 vertical levels. Due to MOZART-4 simulation output being available for 01/2007 –

01/2018, Chapter 6 uses Whole Atmosphere Community Climate Model (WACCM) (Marsh et al., 2013) for initial and boundary chemical and aerosol conditions. The WACCM data is interpolated in the same way as MOZART-4 data, using the mozbc program.

### 3.3 Statistical Testing for Air Quality Modelling

It is essential to evaluate air quality model output against observations to assess model performances (Yu et al., 2006). The simplest statistical test is to calculate mean bias, an indicator of the difference between modelled output and observed values (Emery et al., 2017). Whilst it is also common to gain a measure of the relative or fractional difference between modelled output and observations, thus making the comparison unitless (Yu et al., 2006). Assessing the model error is often used to gauge model performance in meteorology, air quality and climate studies (Chai, 2014), with Thunis et al., (2012) proposing that root mean square error (RMSE) is the key measure of model skill. Correlation-based analysis is the measure of an association between two variables and allows the estimation of the strength of their relationship (Schober and Schwarte, 2018). One example of this is the Pearson product-moment correlation, often abbreviated to R, which is commonly used in air quality model and observation comparisons. To statistically compare modelled output with a range of observations throughout this thesis, I use the statistical tests described below.

$$R = \frac{\sum(M_i - \bar{M})(O_i - \bar{O})}{\{\sum(M_i - \bar{M})^2 \sum(O_i - \bar{O})^2\}^{\frac{1}{2}}} \quad (3.1)$$

$$\text{Mean Bias} = \sum(M_i - O_i) = \bar{M} - \bar{O} \quad (3.2)$$

$$\text{Fractional Mean Bias} = \frac{\sum(M_i - O_i)}{\sum O_i} \quad (3.3)$$

$$\text{RMSE} = \left[ \frac{1}{N} \sum (M_i - O_i)^2 \right]^{\frac{1}{2}} \quad (3.4)$$

Where  $M$  is model output,  $O$  is observed value and  $N$  is number of observations.

## **4. Evaluating regional NO<sub>2</sub> emissions in Western Siberia**

### **4.1 Introduction**

In this chapter, WRF-Chem and OMI satellite observations are used to evaluate tropospheric NO<sub>2</sub> concentrations in Western Siberia, a region of significant anthropogenic and natural NO<sub>2</sub> sources, which are poorly constrained. During spring the region acts as a “gateway” for poleward near-surface advection of Eurasian pollution into the Arctic (Stohl, 2007), which contributes to the well-characterised “Arctic haze” (Shaw, 1995; Quinn et al., 2008). However, a severe paucity of in-situ observations limits our understanding of sources, sinks and processing of pollution over Western Siberia. Current emission inventories have large uncertainties for high latitude emissions, including those from Western Siberia (Schmale et al., 2018).

The aim of this chapter is to evaluate tropospheric column NO<sub>2</sub> in Western Siberia through the use of NO<sub>2</sub> observations from satellite in conjunction with modelled output from WRF-Chem. In Section 4.2 two different anthropogenic emission inventories are introduced and compared. Section 4.3 discusses the Ozone Monitoring Instrument (OMI) used for model evaluation. Section 4.4 introduces the model setup and experiments used within this Chapter. Section 4.5 discusses the results of model simulations compared with satellite tropospheric column NO<sub>2</sub>.

### **4.2 Emission Inventories for Western Siberia**

Anthropogenic sources of NO<sub>x</sub> in Western Siberia include those associated with large urban regions such as transport, domestic heating and power generation (Stohl et al., 2013), as well as sources specific to industrial and commercial activities in the region, such as gas flaring (Huang et al., 2014; Huang et al., 2015; Marelle et al., 2018) and shipping (Corbett et al., 2010). In addition to fossil fuel combustion sources, during the summertime large wild and agricultural fires across Siberia emit substantial amounts of pollutants, including NO<sub>x</sub> (AMAP, 2015), and are the largest natural air pollutant source from within

the Arctic region (Schmale et al., 2018). The intensity and location of these fires vary annually, but the frequency of high impact Siberian fire events is increasing (Kukavskaya et al., 2016; Witze, 2020). At present, NO<sub>x</sub> emissions from these urban regions are uncertain, and poorly constrained by in-situ monitoring.

In this section, two emission datasets are compared and described, which are used in the WRF-Chem model in Section 4.5. Two different anthropogenic emission inventories are used: the EDGAR (Emissions Database for Global Atmospheric Research)-HTAP (Hemispheric Transport of Air Pollution) v2.2 inventory, and the ECLIPSE (Evaluating the Climate and Air Quality Impacts of Short-Lived Pollutants) V5a inventory. The ECLIPSE emissions used within this study are supplemented with anthropogenic soil NO<sub>x</sub> emissions from Global Emissions Initiative (GEIA) to account for missing agricultural NO<sub>x</sub> emissions associated with fertilized agricultural soils, see Sections 4.2.3 and 4.5.1.

#### **4.2.1 EDGAR HTAP v2**

The EDGAR-HTAP v2.2 (hereafter “EH2”) (Janssens-Maenhout et al., 2015) anthropogenic emissions used are for the year 2010 and acquired in a monthly 0.1° x 0.1° gridmap format and split into anthropogenic sectors (aircraft, shipping, energy, industry, transportation, residential and agriculture). 2010 EH2 emission species include: carbon monoxide (CO), sulphur dioxide (SO<sub>2</sub>), NO<sub>x</sub>, NMVOC, ammonia (NH<sub>3</sub>), particulate matter smaller than 10µm (PM<sub>10</sub>), particulate matter smaller than 2.5 µm (PM<sub>2.5</sub>), black carbon (BC), organic carbon (OC) and methane (CH<sub>4</sub>). The EH2 emissions are created through supplementing globally reported emissions with high spatial and temporal resolution regional inventories using information of the intensity and geospatial distribution of human activities, based on fuel-, technology- and process-dependant emission factors (Janssens-Maenhout et al., 2015). The overall aim of the Task Force Hemispheric Transport of Air Pollution (TF HTAP) is to produce an inventory capable of improving scientific understanding of long-range air pollution transport, impacts on human health, emission mitigation opportunities and to guide future policy decisions. These data are readily

available online in NetCDF format  
([http://edgar.jrc.ec.europa.eu/htap\\_v2/index.php?SECURE=123](http://edgar.jrc.ec.europa.eu/htap_v2/index.php?SECURE=123)).

#### **4.2.2 ECLIPSE v5a**

The ECLIPSE v5a (hereafter “ECL”) anthropogenic emissions used are for the year 2010 at a resolution of  $0.5^\circ \times 0.5^\circ$ . Shipping emission are downloadable separately at  $1^\circ \times 1^\circ$  resolution. ECL provides emissions for  $\text{SO}_2$ ,  $\text{NO}_x$ ,  $\text{NH}_3$ , NMVOC, BC, OC,  $\text{PM}_{2.5}$ ,  $\text{PM}_{10}$ , CO and  $\text{CH}_4$ . split into different anthropogenic sectors (agricultural waste burning, residential, energy, industry, transport, waste, and shipping). ECL is a project within the European Union’s Seventh Framework programme project in which the overarching aim is to design realistic and effective mitigation scenarios for SLCPs, whilst quantifying both their climate and air quality impacts. The first step of the ECL initiative was to create an anthropogenic emission inventory based on the current global legislation (CLE) to act as a reference baseline scenario for future emission scenarios to be compared to (Stohl et al., 2015). Data for this was created by the Greenhouse gas-Air pollution Interactions and Synergies (GAINS) model (Amann et al., 2011), an extended global version of the previous Regional Air Pollution Information and Simulation (RAINS) model, developed by the International Institute for Applied Systems Analysis (IIASA). The GAINS model contains information on the sources of emissions, environmental policies and mitigation efforts and opportunities for approximately 160 countries (Stohl, et al., 2015). The ECLIPSE emission data has been rigorously evaluated through comparisons with multiple ground-based and satellite observational data sets from Europe, Asia and the Arctic, with noted improvements for Arctic aerosols, when compared to previous studies (Stohl, et al., 2015).

#### **4.2.3 Anthropogenic Soil $\text{NO}_x$ Emissions**

Past studies have highlighted potential missing sources of anthropogenic soil  $\text{NO}_x$  emissions in current inventories, associated with fertilized agricultural soils and land management practises (Jaeglé et al., 2005; Ganzeveld et al., 2010;

Visser et al., 2019). Soil NO<sub>x</sub> emission fluxes can be influenced by land management practises such as the application of both natural and synthetic fertilisers, tillage, irrigation, compaction, planting and harvesting (Frolking et al., 1998). In particular it is suggested that during the summer in northern mid-latitude regions, soil NO<sub>x</sub> emissions can contribute up to half those from fossil fuel combustion (Jaeglé et al., 2005). Anthropogenic soil NO<sub>x</sub> emissions are not well represented in current global or regional models. Estimates of global soil NO<sub>x</sub> emissions have been undertaken through different methodologies, which include using top-down emission estimates (Vinken et al., 2014), scaling based upon multiple field measurement campaigns (Davidson and Kinglerlee, 1997), and using an empirical model (Yienger and Levy, 1995; Steinkamp and Lawrence, 2011). Despite this, global soil NO<sub>x</sub> estimates vary significantly (9-27 Tg per year) (Oikawa et al., 2015).

Agricultural NO<sub>x</sub> emissions are available within the EH2 inventory but missing in ECL, therefore ECL emissions used in this chapter are supplemented with additional anthropogenic soil NO<sub>x</sub> from the GEIA global soil NO<sub>x</sub> anthropogenic emissions, and distributed spatially according to the Yienger and Levy (1995) empirical model. These emissions include an explicit linear dependence of emission on nitrogen fertiliser rates for soils. These are available at 0.5° x 0.5° resolution from the GEIA website, and were added into the ECL emissions used for WRF-Chem simulations prior to the model pre-processing stage. Figure 4.3 shows spatial coverage of anthropogenic soil NO<sub>x</sub> added into ECL. The contributions per month from the anthropogenic Soil NO<sub>x</sub> emissions from this dataset to Western Siberia NO<sub>x</sub> emissions totals are presented in Table 4.2.

### **4.3 Ozone Monitoring Instrument Satellite Data**

To evaluate WRF-Chem I make use of satellite data from the Dutch OMI (Ozone Monitoring Instrument) for tropospheric NO<sub>2</sub> (DOMINO v2.0), on-board NASA's polar orbiting Aura satellite, launched in 2004 (Boersma et al., 2004; Boersma et al., 2011; Vinken et al., 2014). Due to the paucity of in-situ observations across Western Siberia, satellite observations can act as a reliable evaluation

tool both spatially and temporally. OMI is a nadir-viewing wide swath instrument which makes retrievals of trace gases through the Differential Optical Absorption Spectroscopy (DOAS) method. This involves using the on-board spectrometer to make UV-visible measurements. OMI provides estimates of tropospheric column NO<sub>2</sub> through first calculating the slant columns, which is the column density of NO<sub>2</sub> along the whole photon path through the atmosphere to the instrument (Vinken et al., 2014). Applying a tropospheric air mass factor (AMF), tropospheric vertical column density (VCD) of NO<sub>2</sub> can be retrieved. AMF values are calculated using a radiative transfer model and are a function of a number of variables, such as viewing geometry, surface reflectance, clouds and the radiative properties of the atmosphere. The calculation of the AMF also requires an a priori estimate of the trace gas vertical profile, which can be sensitive to the profile shape (Cooper et al., 2020). Satellite overpass time is approximately at 13:00 local time, with dimensions of the ground pixels ranging from 13-26km along track and 24-128km across track depending on the satellite viewing angle, as depicted in Figure 4.1 (Boersma et al., 2011). OMI tropospheric column NO<sub>2</sub> data is downloaded from the Tropospheric Emissions Monitoring Internet Service (TEMIS) website (<http://www.temis.nl/airpollution/no2.html>) for daily retrievals from 01/05/2011 – 31/08/2011 and then is gridded onto a 0.25° x 0.25° grid. All satellite retrievals have been quality controlled, with the removal of pixels where geometric cloud cover is greater than 20% or where there is a poor quality data flag.

A positive bias in the DOMINO v1.0 product has been identified in previous studies of up to 40% during the summertime (Zhou et al., 2009; Hains et al., 2010; Huijnen et al., 2010; Lamsal et al., 2010), which was attributed to errors in the a priori NO<sub>2</sub> profile, air mass factors and albedo. These errors were improved in the DOMINO v2.0 product (Boersma et al., 2011), which I use here. These improvements include updated calculations for the AMF that include better terrain height information and better surface albedo information. This improved product is shown to lower summertime satellite positive biases of tropospheric column NO<sub>2</sub> relative to retrievals using the previous version of the DOMINO product. These improvements are observed across the entire globe,

with particular improvements over heavily polluted regions (Boersma et al., 2011).

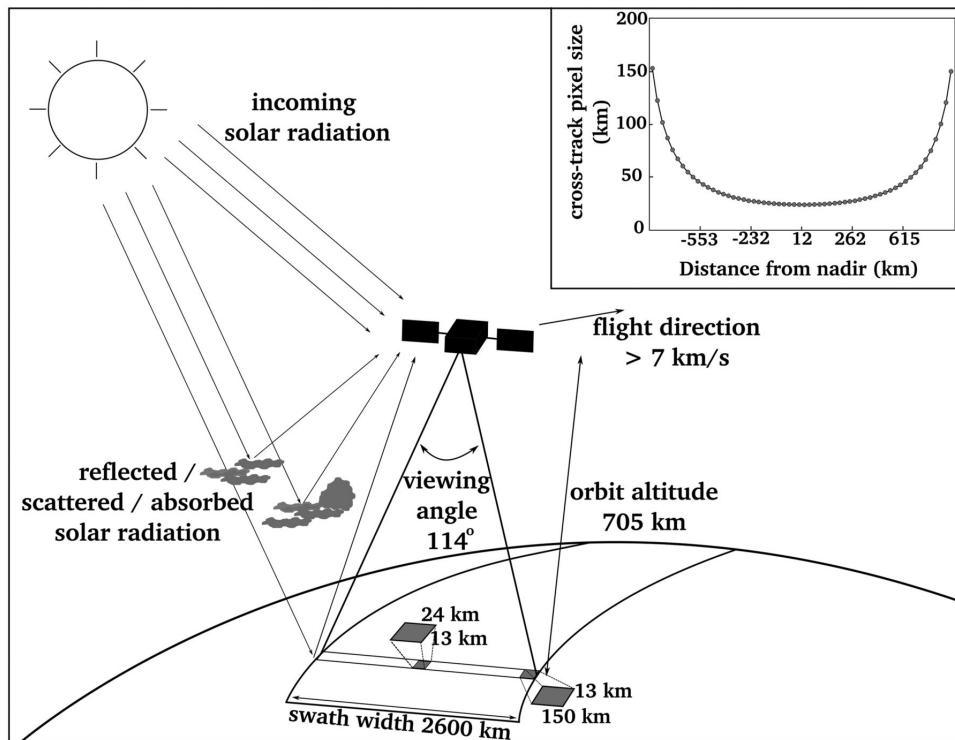


**Figure 4.1** - Schematic of OMI's measurement technique, highlighting key parameters. Adapted from McCormick et al. (2013).

To allow for a direct comparison of OMI with modelled column  $\text{NO}_2$ , averaging kernels (AK) are applied to model fields (Pope et al., 2015), to account for OMI vertical sensitivity varying through the tropospheric profile. AK provide a relative sensitivity of the satellite instrument to the abundance of species of interest at different vertical points within the column (Eskes and Boersma, 2003). Therefore the AK accounts for the fact that the OMI instrument has different sensitivities to the observed  $\text{NO}_2$  concentrations through the atmosphere, and these sensitivities can be applied to the model column values allowing for an accurate satellite/model comparison. Where tropospheric column  $\text{NO}_2$  retrievals use the DOAS method, AK are provided as a column vector.

To investigate statistically significant differences between satellite observed and modelled tropospheric columns, retrieval errors for the DOAS method are calculated to allow for a more robust statistical comparison. Following the method described in Pope et al. (2015), the random, systematic and smoothing errors associated with the DOAS retrievals are accounted for, producing a seasonal retrieval error for each grid square in the domain. This methodology determines the final satellite error term. Where the absolute mean bias of observation minus model output is greater than the derived final satellite error term, then the bias is significantly different (Pope et al., 2015).

All column comparisons presented in this work are undertaken at  $0.5^\circ \times 0.5^\circ$  resolution due to the computational cost of multiple months of comparisons for numerous model setups, and are limited to south of  $65^\circ\text{N}$  latitude. This latitude is chosen as a cut-off for the comparisons, since satellite retrieval uncertainty increases at higher latitudes, especially where solar zenith angle becomes greater than  $70^\circ$ . Furthermore,  $\pm 65^\circ$  is the latitudinal range used to map global  $\text{NO}_2$  VCD when using the DOAS retrieval method (Bucsela et al., 2006). Comparisons between model and satellite tropospheric columns only occur where there is a valid satellite observation.

#### **4.4 WRF-Chem Setups**

A detailed description of the WRF-Chem model setup used in this thesis is described in Chapter 3, whilst Table 4.1 describes the model experiments used within this chapter. Figure 4.2 shows the WRF-Chem domain over Western Siberia used in Chapters 4 and 5. This includes the Ob Valley region (approx.  $45\text{-}65^\circ\text{N}$ ,  $60\text{-}95^\circ\text{E}$ ) which is home to multiple populous cities, such as Novosibirsk (1.5 million people), Yekaterinburg (1.4 million), Novokuznetsk (550,000) and Tomsk (550,000). Model simulations are conducted between May and August 2011, with a spin-up period of 1 month preceding this. 2011 is chosen due to good availability of surface observations, whilst also being a year with limited wildfire activity. This simulation length is chosen as it represents the

optimum period of time for valid OMI satellite comparisons at the latitudes of interest.

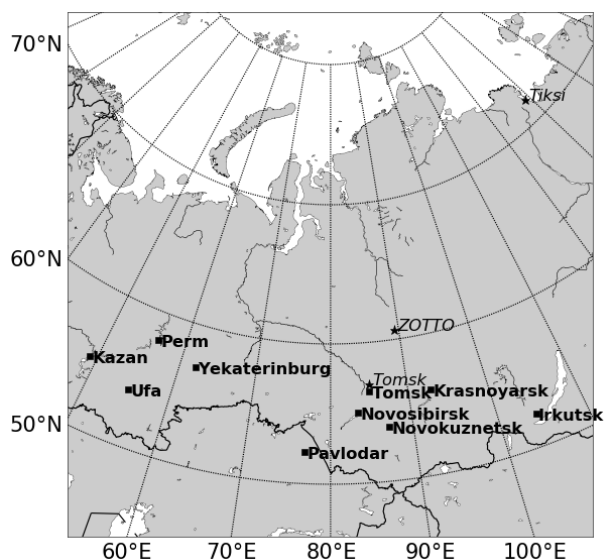


**Figure 4.2** - *Map of domain used for model simulations. Centred on Western Siberia region, major cities (squares) (population > 100,000) shown in bold. Observation sites (star symbols) are given in italics*

**Table 4.3** - *WRF-Chem model experimental descriptions*

<b>Model Simulation</b>	<b>Description</b>
ECL	Simulation using standard ECL emissions with GEIA anthropogenic soil NO <sub>x</sub> emissions
EH2	Simulation using standard EH2 emissions

ECL_SCALED	Simulation using ECL as described above, with transport and energy anthropogenic sectors scaled by factor of 2
fires_off	ECL_SCALED simulation with all biomass burning turned off within the model domain
trans_off	ECL_SCALED simulation with all transport sector emissions turned off within the model domain
ene_off	ECL_SCALED simulation with all energy sector emissions turned off within the model domain

## 4.5 Results

### 4.5.1 Anthropogenic Emission Inventory Comparisons

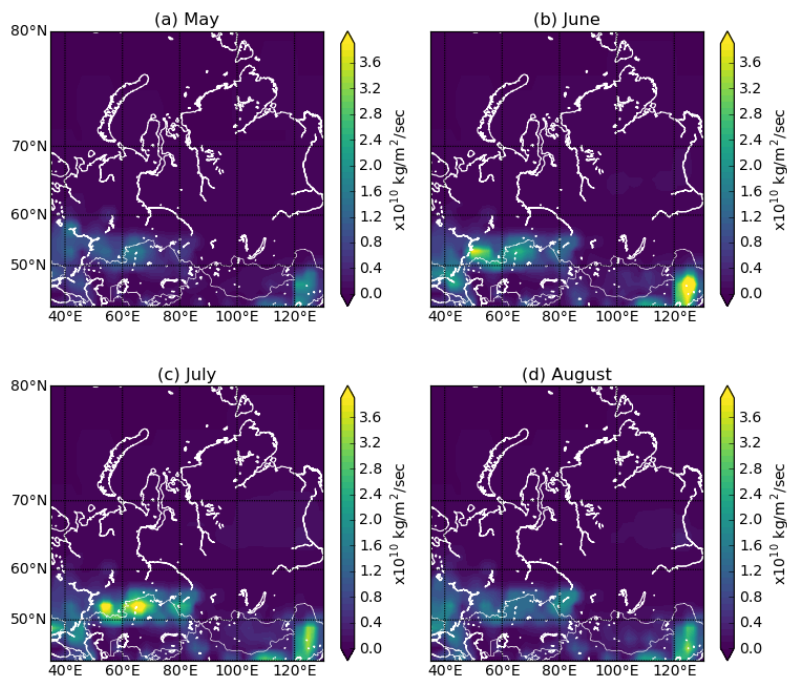


**Figure 4.3** - *Monthly mean plots of GEIA anthropogenic soil NO<sub>x</sub> emissions across Western Siberia.*

Anthropogenic soil NO<sub>x</sub> emissions within Western Siberia peak in July at 84.1 kilotons/month (Table 4.1). Figure 4.3 shows that the main source region is centred on the Central Chernozem and Volga Economic Regions (Approx. 50-60°N, 40-65°E), which occupy large areas of grassland, with more than 65% of this region used for agricultural purposes, and a key region in Russian farming (Curtis, 1996). During June and July there is also a large source located in the

south eastern corner of the domain, which is likely linked to farming fertilisation techniques associated with wheat farming in this region.

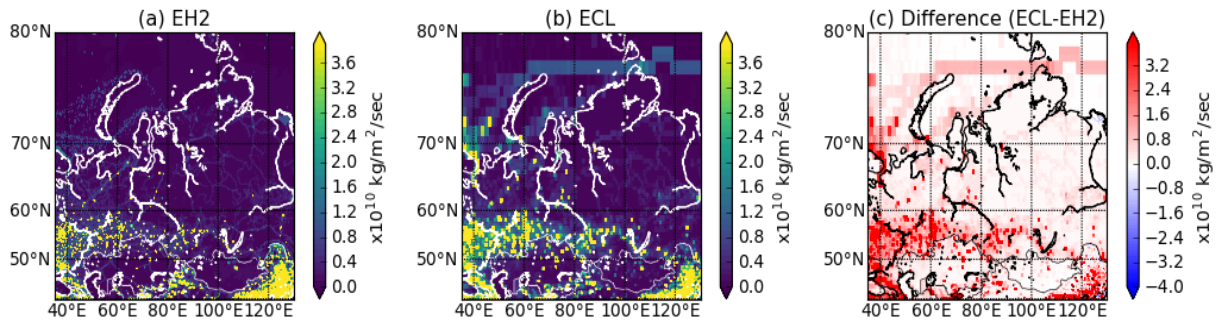


**Figure 4.4** –Spatial distribution of anthropogenic emissions according to EDGAR HTAP v2.2 (panel (a)) and ECLIPSE v5a (panel (b)) inventories. Difference between the 2 inventories is shown in panel (c) (ECLIPSE v5a – EDGAR HTAP v2.2).

Comparisons between the two anthropogenic emission inventories for NO<sub>x</sub> show larger emissions in the ECL inventory for Western Siberia (Fig. 4.4). NO<sub>x</sub> emissions within the domain are dominated by the Transport and Energy sectors, which together contribute 75% of emissions for EH2, and 82% for ECL respectively (Table 4.2). For both emission inventories the largest sector contribution is from transport, which accounts for 41% of total EH2 emissions and 48% of total ECL emissions. Figure 4.4 shows that despite larger magnitude of emissions in ECL, with the largest difference seen over the urban regions

**Table 4.2** - Total NO<sub>x</sub> emissions (kilotons per month) for the study domain from EH2 and ECL anthropogenic emission inventories, and soil NO<sub>x</sub> contribution from GEIA. Contributions from energy and transport sectors shown for each inventory.

	EH2 Total	EH2 Energy	EH2 Transport	ECL Total	ECL Energy	ECL Transport	GEIA Soil NO <sub>x</sub>
May	915.5	306.0	375.2	989.8	324.4	481.7	51.4
June	911.3	307.8	374.1	985.3	326.3	480.3	71.9
July	870.4	297.1	367.8	941.1	315.0	472.2	84.1
August	864.4	294.0	368.7	934.6	311.7	473.3	68.9
Total	<b>3561.6</b>	<b>1204.9</b>	<b>1485.8</b>	<b>3850.8</b>	<b>1277.4</b>	<b>1907.5</b>	<b>276.3</b>

within the domain, the spatial patterns of total emissions are similar in both inventories. Differences are also seen in the shipping emissions, with large emissions north of Murmansk in the ECL inventory, which is not seen to the same extent in EH2 emissions. ECL attempts to better account for point source emissions associated with gas flaring above 60°N, which can be seen between 60°E – 80°E (Stohl et al., 2015).

#### 4.5.1 Evaluation of WRF-Chem Tropospheric Column NO<sub>2</sub>

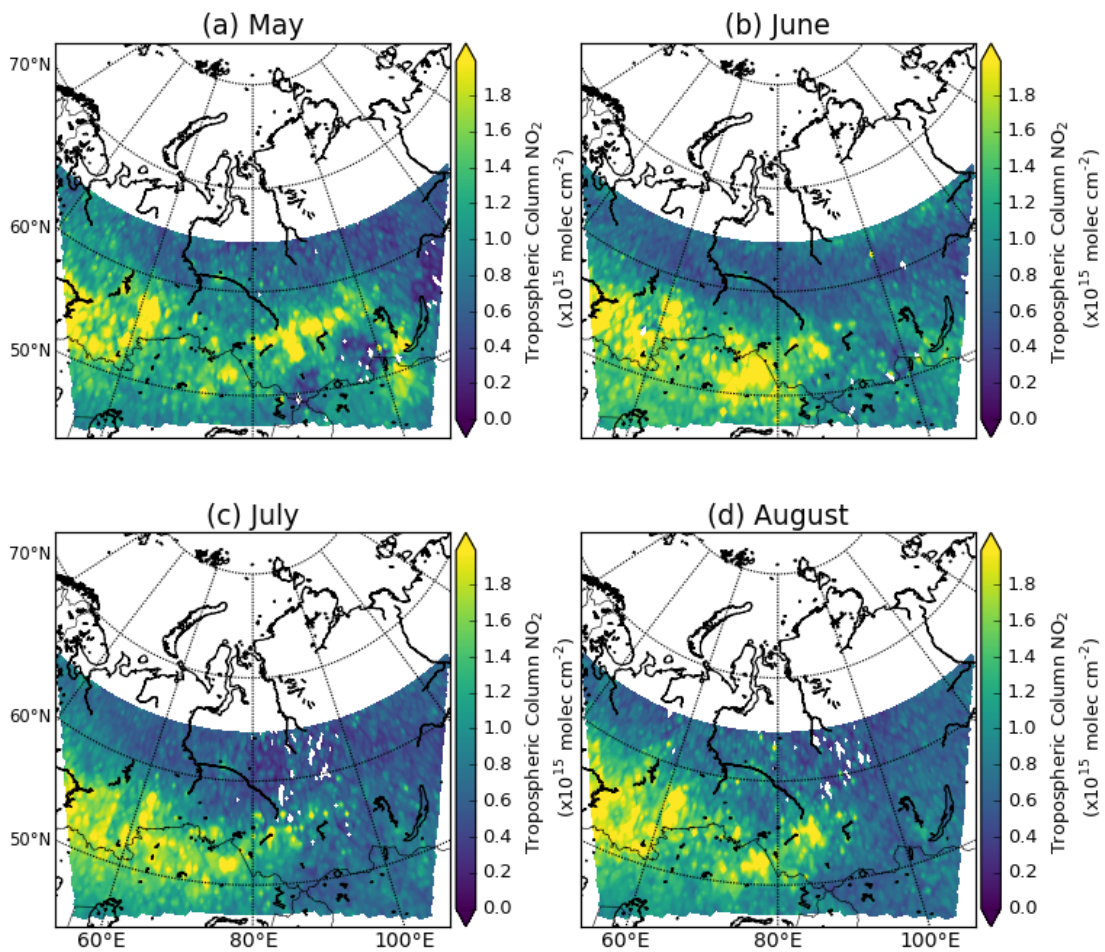


**Figure 4.5** - Observed tropospheric column NO<sub>2</sub>. Panels a-d show monthly mean OMI tropospheric column NO<sub>2</sub> for May – August.

The distribution of observed NO<sub>2</sub> from OMI show large areas of enhanced tropospheric column NO<sub>2</sub> in the west of the study domain associated with large anthropogenic emission regions. There are smaller observed values to the east of the domain, where population density is very low. Over urban regions with large emission sources south of 60°N, OMI tropospheric column NO<sub>2</sub> distributions show values exceeding  $2 \times 10^{15}$  molec cm<sup>-2</sup> (Fig. 4.5a-d), with some variability across the 4-month period. During May observations show high levels of tropospheric column NO<sub>2</sub> to the south of Lake Baikal at the city of Irkutsk (53°N, 108°E), which is not observed to the same extent during the summer months (JJA).

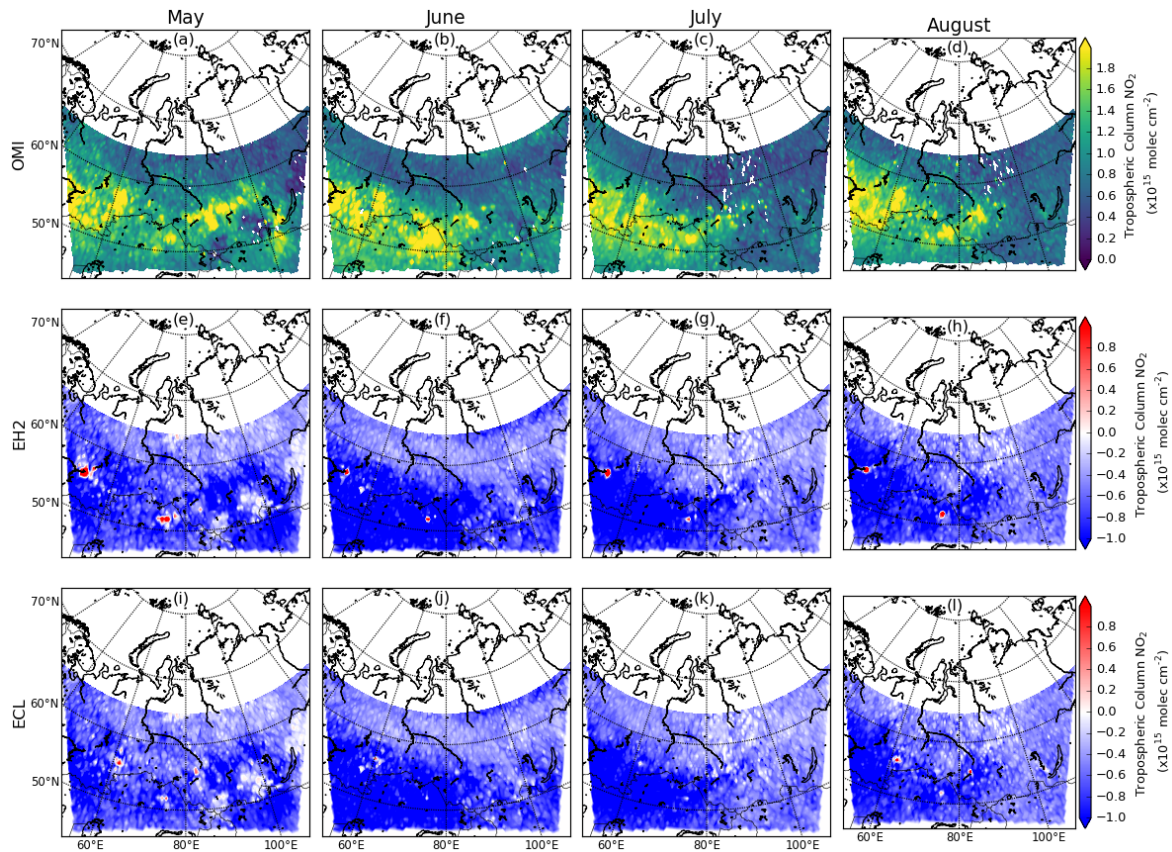


**Figure 4.6** - Observed and model-observed tropospheric column  $\text{NO}_2$ . Panels a-d show mean OMI tropospheric column  $\text{NO}_2$  for May-August. Panels e-h show WRF-Chem bias (model – satellite) using the EDGAR HTAP v2.2 anthropogenic emission inventory for May-August. Panels i-l show WRF-Chem bias using the ECLIPSE v5a anthropogenic emission inventory for May-August.

For both anthropogenic emission inventories (EH2 and ECL), an overall negative bias is seen in WRF-Chem tropospheric column  $\text{NO}_2$  when compared with OMI observations (Fig. 4.6). The greatest negative bias is during June for both anthropogenic emission inventories (Fig. 4.6f & 4.6j). For large parts of the domain that are located further from large anthropogenic sources, there is better agreement between the observed and modelled column  $\text{NO}_2$  values. In the EH2

simulation a positive tropospheric column  $\text{NO}_2$  bias is observed across the 4-month period at both Kazan ( $56^\circ\text{N}$ ,  $49^\circ\text{E}$ ) and Pavlodar ( $52^\circ\text{N}$ ,  $77^\circ\text{E}$ ), but despite this there is a continued overall negative bias for the domain. The prevalent negative bias regions ( $> 1 \times 10^{15}$  molec  $\text{cm}^{-2}$ ) are predominantly confined south of  $60^\circ\text{N}$ , and are mainly seen over the major city regions within the Ob Valley and the Western section of the domain.

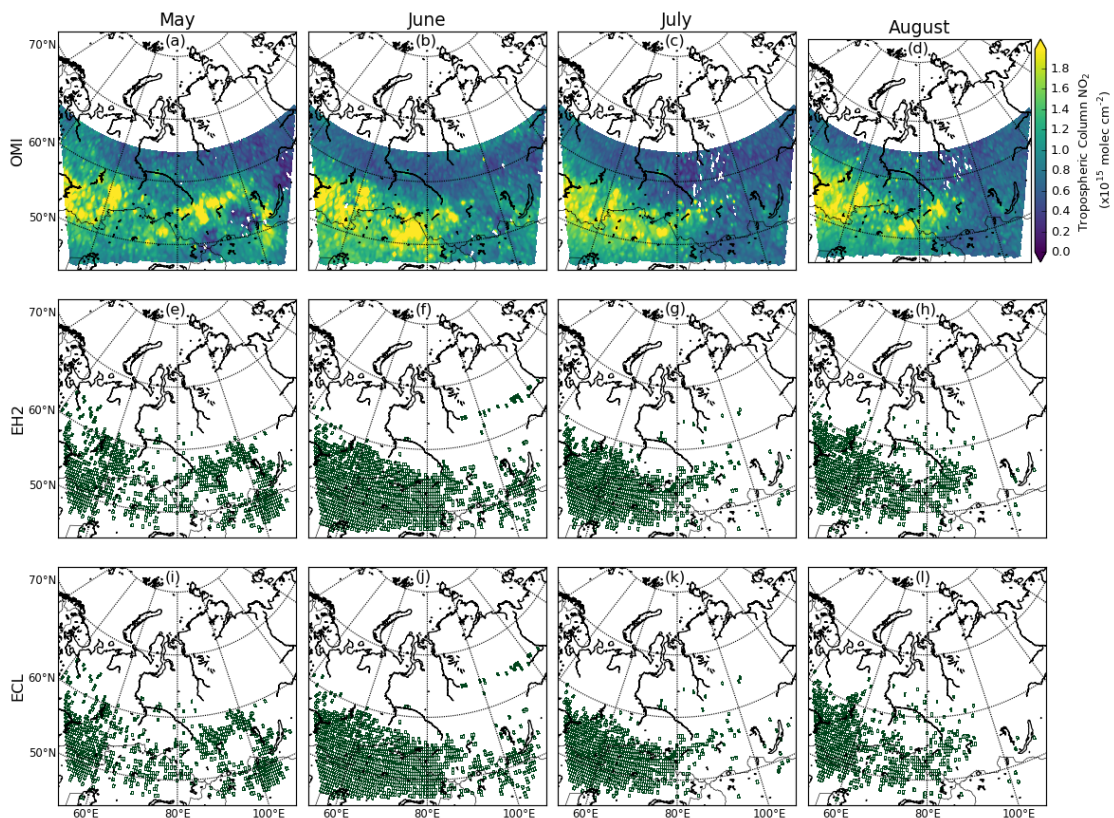


**Figure 4.7** - Observed tropospheric column  $\text{NO}_2$  and satellite/model significant differences. Panels a-d show mean OMI tropospheric column  $\text{NO}_2$  for April-August. Panels e-l show where modelled and satellite differences in tropospheric column  $\text{NO}_2$  are statistically different for May to August for EH2 (e-h) and ECL (i-l).

Figure 4.7 shows locations where model and satellite tropospheric column  $\text{NO}_2$  values have a statistically significant difference, i.e. where the magnitude of the mean bias is greater than the satellite error. The calculations for this are discussed in Section 4.3. During June, July and August there is a statistically

significant negative bias in the southwestern section of the domain using both anthropogenic emission inventories (Fig. 4.7). This significance is most prominent during June and July, particularly over urban regions. For large parts of the domain that are located further from large anthropogenic sources, there is better agreement between the observed and modelled column  $\text{NO}_2$  values.

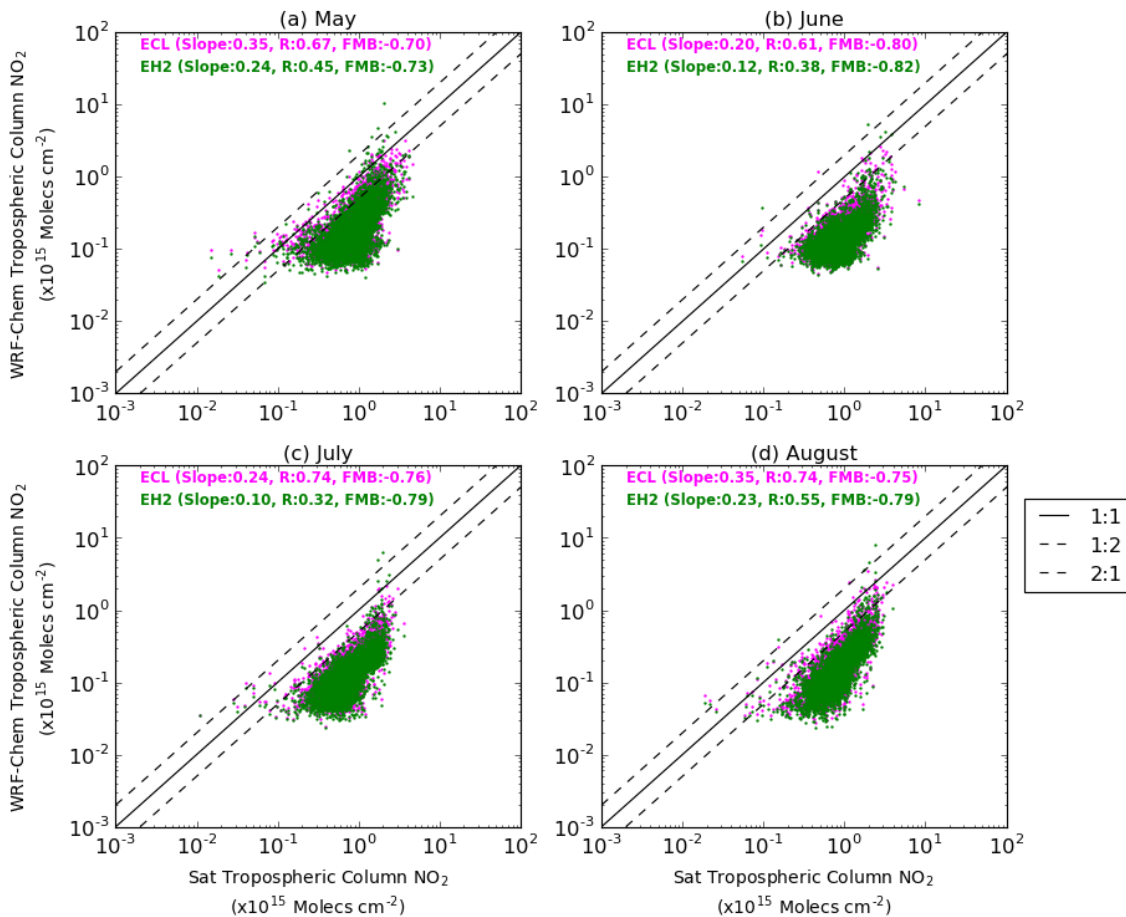


**Figure 4.8** - WRF-Chem simulated versus OMI tropospheric column  $\text{NO}_2$  using ECL (magenta) and EH2 (green), for May (a), June (b), July (c) and August (d). All plots show total domain south of  $65^\circ\text{N}$ . Slope, correlation coefficient (R) and fractional mean bias (FMB) are shown in each panel.

For all four months, the WRF-Chem simulations using ECL anthropogenic emissions provide better agreement with observations for tropospheric column

**Table 4.3** - Root mean squared error (RMSE) values for monthly simulated tropospheric column NO<sub>2</sub> in urban and background regions within Western Siberia when compared with OMI values, for each of the model simulations using EH2 and ECL emissions.

	EH2 (x10 <sup>15</sup> Molec cm <sup>-2</sup> )		ECL (x10 <sup>15</sup> Molec cm <sup>-2</sup> )	
	Urban	Background	Urban	Background
<b>May</b>	1.41	0.34	1.26	0.39
<b>June</b>	1.44	0.63	1.61	0.64
<b>July</b>	1.33	0.47	1.14	0.48
<b>August</b>	1.07	0.43	1.03	0.44

NO<sub>2</sub> over Western Siberia (Fig. 4.8). Despite this, negative biases persist across the entire simulated period with both anthropogenic emission inventories. In particular, negative biases are marked during June and July using either anthropogenic emission inventory, reflected in both the regression slope and FMB values for ECL during June (slope = 0.2; FMB = -0.80), and EH2 during July (slope = 0.1; FMB = -0.79). However, better correlation coefficients are produced using ECL anthropogenic emissions during July ( $r = 0.74$ ) and August ( $r = 0.74$ ), and with EH2 anthropogenic emissions during August ( $r = 0.55$ ), which suggests spatial patterns in NO<sub>2</sub> sources are well simulated, especially in ECL, but may be underestimated.

Background values for tropospheric column NO<sub>2</sub> across Western Siberia show little sensitivity to changing anthropogenic emission inventories across the entire 4-month period (Table 4.3). There is an improved RMSE value in urban regions within the domain when using the ECL anthropogenic emissions compared to EH2 in all months but June.

Major cities located within western Siberia generally show smaller fractional mean biases for tropospheric column NO<sub>2</sub> when using the ECL anthropogenic

emission inventory across the whole study period (Fig. 4.9). This is especially the case over Novosibirsk, Novokuznetsk and Tomsk in the centre of the domain, where the mean fractional bias is larger for almost all months when using the EH2 anthropogenic emissions, Novosibirsk in August being a notable exception. Examination of sector totals in the ECL and EH2 emissions datasets shows that the transport sector is the dominant source for  $\text{NO}_x$  in ECL and EH2 over Novosibirsk and Tomsk, whilst in Novokuznetsk it is the industrial sector (EH2) and energy sector (ECL). Despite the different dominant sector over Novokuznetsk, a mean negative bias is seen across all 4 months using both inventories.

The same overall pattern is replicated at the other major cities within the western section of the domain, with a predominantly lower fractional mean biases using the ECL anthropogenic emissions at nearly all cities (Kazan and Pavlodar being

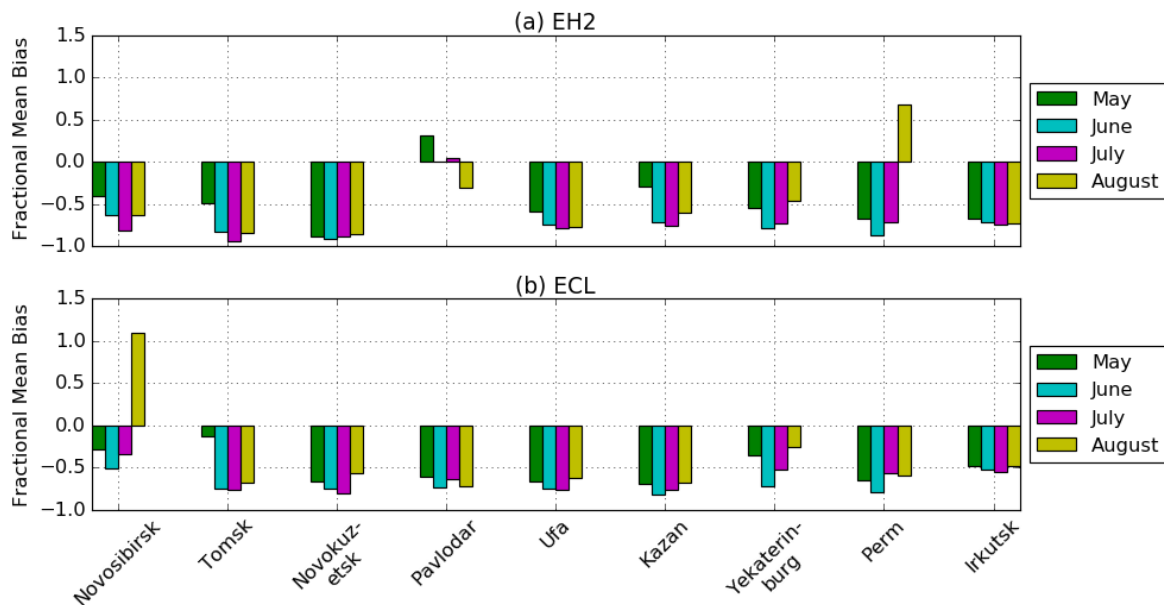


**Figure 4.9** - Fractional mean bias of monthly simulated tropospheric column  $\text{NO}_2$  for major cities (population >100,000) within Western Siberia when compared with OMI values. Panel (a) shows results using the EH2 anthropogenic emission inventory. Panel (b) shows results using the ECL anthropogenic emission inventory.

the only exceptions). In both of the anthropogenic emission inventories the cities in this western section of the domain are dominated by NO<sub>x</sub> emissions from the transport sector, with Yekaterinburg in the EH2 inventory the only city with a different anthropogenic sector as its main NO<sub>x</sub> source sector (Industry). The model bias could therefore suggest a potential underestimation of NO<sub>x</sub> emissions in the transport sectors of both anthropogenic inventories over urban areas.

#### **4.5.2 Model NO<sub>2</sub> Sensitivity tests**

Despite simulations using the ECL anthropogenic emissions providing better agreement with observations than those using EH2 emissions, large uncertainties remain, particularly in background regions. Therefore, to further investigate the sensitivity of the model NO<sub>2</sub> bias to anthropogenic emissions, I scale the dominant anthropogenic sectors (transport and energy) by a factor of 2 (hereafter called "ECL\_SCALED"). Based on analysis of the ECL emission inventory, these sectors combined account for 82% of total anthropogenic NO<sub>x</sub> emissions within the domain (Table 4.2).

### 4.5.3 Evaluation of WRF-Chem Tropospheric Column NO<sub>2</sub> Using Scaled Emissions

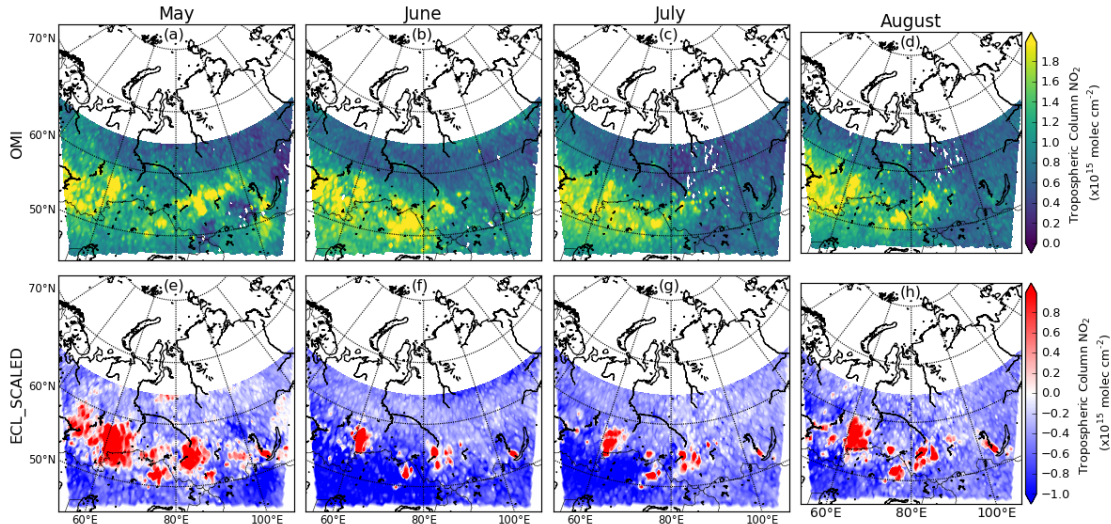


**Figure 4.10** - Observed and model-observed tropospheric column NO<sub>2</sub>. Panels a-d show mean OMI tropospheric column NO<sub>2</sub> for May-August. Panels e-h show WRF-Chem bias (model – satellite) using ECL\_SCALED anthropogenic emission inventory for May-August.

Across the total domain, using the ECL\_SCALED anthropogenic emissions leads to a positive bias in WRF-Chem tropospheric NO<sub>2</sub> in high emission regions, when evaluated against OMI tropospheric NO<sub>2</sub> observations (Fig. 4.10). This is especially the case during May, where large portions of the western section of the domain is demonstrating a positive bias. Despite this overestimation in source regions, there is little improvement in background

regions, especially during June, July and August, compared to the simulations using ECL (Fig. 4.6 & 4.10).

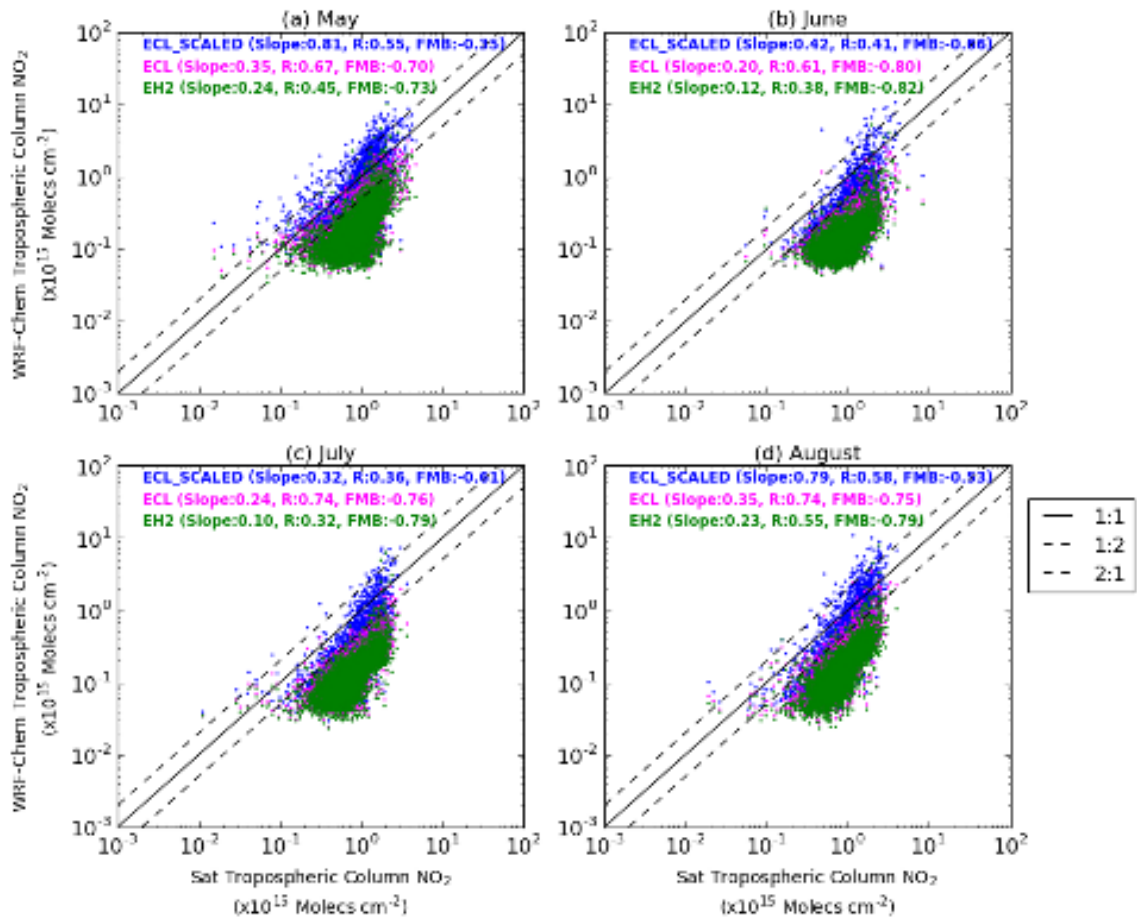


**Figure 4.11** - WRF-Chem simulated versus OMI tropospheric column NO<sub>2</sub> using ECL (magenta), EH2 (green), and ECL\_SCALED (blue) for May (a), June (b), July (c) and August (d). All plots show total domain south of 65°N. Slope, correlation coefficient (R) and fractional mean bias (FMB) are shown in each panel.

**Table 4.4** - Root mean squared error (RMSE) values for monthly simulated tropospheric column NO<sub>2</sub> in urban and background regions within Western Siberia when compared with OMI values, for each of the model simulations using ECL\_SCALED emissions.

	ECL_SCALED (x10 <sup>15</sup> molec cm <sup>-2</sup> )	
	Urban	Background
<b>May</b>	1.25	0.22
<b>June</b>	0.84	0.59
<b>July</b>	1.09	0.45
<b>August</b>	1.03	0.40

However, across Western Siberia as a whole, there is an overall improved model tropospheric column NO<sub>2</sub> when evaluated against OMI observations using the ECL\_SCALED emissions, compared to the standard ECL simulations, with a reduction in overall FMB for each month (Fig. 4.11). In particular there is an improvement over anthropogenic source regions where RMSE values for tropospheric column NO<sub>2</sub> improve for May, June and July, whilst remaining similar in August (Table 4.3 & 4.4). Despite this improvement over source regions, there is little change in the model error in background regions during June, July, August, although there is a marked reduction in background model error in May (Table 4.3 & 4.4), suggesting that the background tropospheric NO<sub>2</sub> is much less sensitive to anthropogenic emission increases.

FMB is reduced for most major cities within the domain, however the bias over both Novosibirsk and Yekaterinburg increases (Fig. 4.12). These cities showed relatively small biases when using the standard ECL simulation (Fig. 4.9), meaning that the emission scaling leads to an NO<sub>2</sub> overestimation.

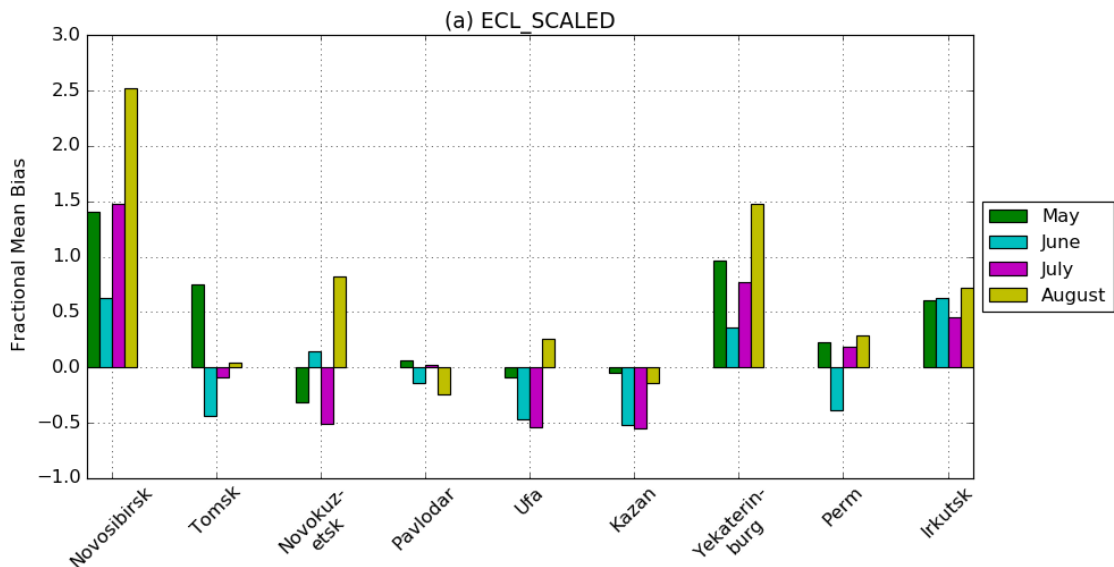


**Figure 4.12** - Fractional mean bias of monthly simulated tropospheric column  $\text{NO}_2$  for major cities (population >100,000) within Western Siberia when compared with OMI values. Panel (a) shows results using the ECL\_SCALED anthropogenic emission inventory.

#### 4.5.4 $\text{NO}_2$ Source Contributions

Based on the results in Sections 4.5.1 and 4.5.2, model simulations with the improved ECL\_SCALED anthropogenic emissions will be used to perform sensitivity simulations, since for tropospheric column  $\text{NO}_2$ , these emissions produced a smaller model bias against satellite observations. Three sensitivity simulations are used to gain a better understanding of the impacts of transport (trans\_off), energy (ene\_off) and fire (fires\_off) emissions. Transport and energy are chosen as the two dominant anthropogenic  $\text{NO}_x$  emission sectors. From here forward, the simulation titled “control” will use the ECL\_SCALED anthropogenic emissions and standard fire emissions.

Simulated surface  $\text{NO}_2$  concentrations show enhancements in regions close to major anthropogenic emission sources, mainly urban regions south of  $60^\circ\text{N}$ ,

throughout the 4-month study period (Fig. 4.13 a-d). Hotspots in OMI-observed NO<sub>2</sub> north of 60°N in the central and western portions of the domain are associated with the influence of high latitude gas flaring emissions and are evident as substantial reductions in the ene\_off simulation (Fig. 4.13 m-p). In the fires\_off sensitivity simulation (Fig. 4.13 e-h) there is a small reduction in NO<sub>2</sub> concentrations, including background regions not in close proximity to fire source regions, across all 4 monthly periods.

As expected, given their relative source sizes, NO<sub>2</sub> concentrations in Western Siberia are most sensitive to anthropogenic emissions relating to transport and energy activities (Fig. 4.13 i-p), rather than those associated with fires. Transport sector emissions are the largest source of surface NO<sub>2</sub> during the 4-month simulation (Fig. 4.13 i-l). A widespread reduction of surface NO<sub>2</sub> is simulated in the trans\_off simulation south of 60°N, both close to the urban source regions and in between cities, associated with on-road transport emissions on major highways. This is in line with previous research suggesting that motor transport is the largest source of emissions for Russian cities, with peak concentrations associated with large highways (Ginzburg et al., 2020).

Reductions in surface NO<sub>2</sub> in the ene\_off simulation are predominantly confined to the major urban regions (Fig. 4.13 p-t), which is likely due to emissions being point sources of high emissions associated with energy production facilities. However, emission reductions north of 60°N, associated with gas flaring can also be seen, but these reductions are not of the same magnitude as those south of 60°N. These locations correlate directly with areas highlighted by Huang et al., (2015) as the main regions of Russian flaring. At present there are significant uncertainties within global emission inventories for gas flaring, so it is likely that the values currently used may not be accurate and require improvements to their quantification (Schmale et al., 2018). This is highlighted by the discrepancies between observed and reported national values for Russian flaring activities (Li et al., 2016). These differences can be attributed to the fact that flaring is often seen as a disposal process and usually occurs in

remote locations, so there are limited records for volume of flared gas, leading to large amounts of uncertainty regarding the magnitude of gas flaring in Russia (Elvidge et al., 2009)

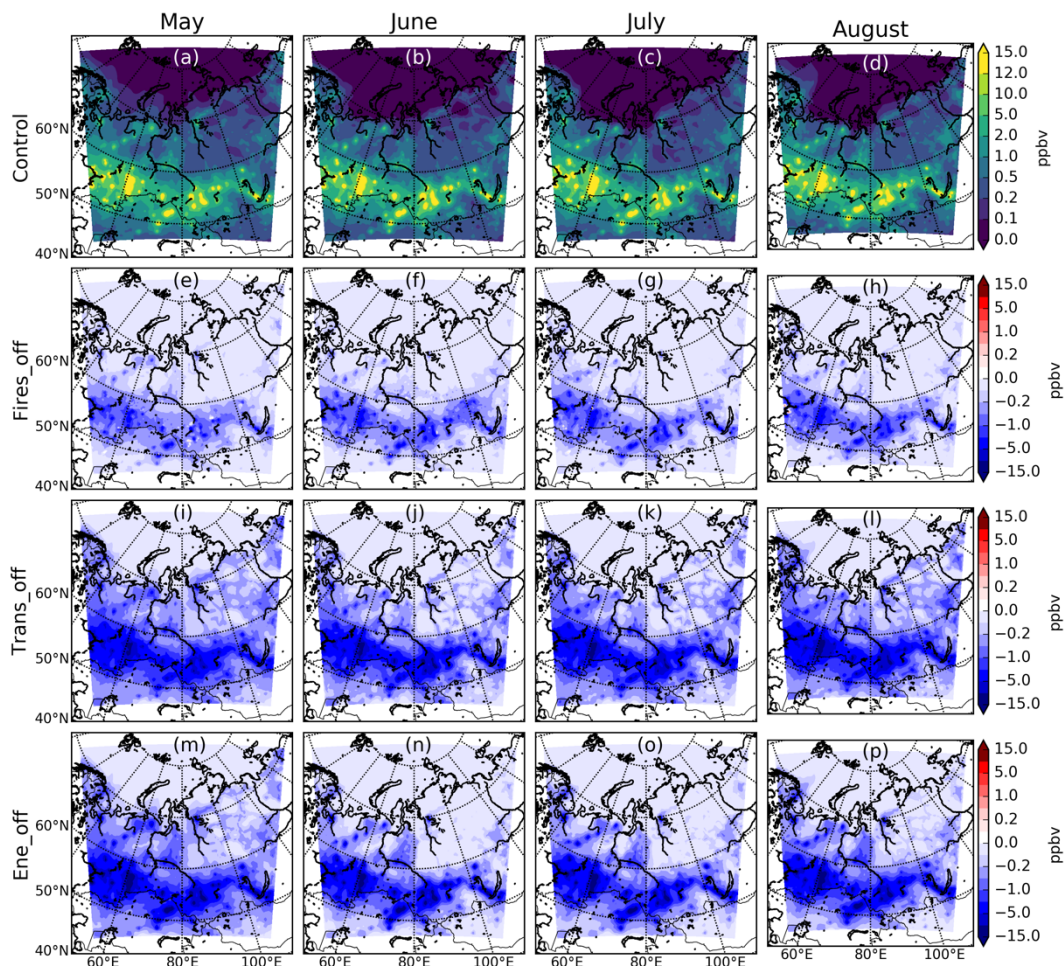


**Figure 4.13** - Simulated control and sensitivity run changes in surface  $\text{NO}_2$  concentrations. Panels (a)–(d) show monthly means of WRF-Chem surface  $\text{NO}_2$  for May–August using ECL\_SCALED emissions. Panels (e)–(h) show monthly means of WRF-Chem Surface  $\text{NO}_2$  with all fire emissions switched off in domain (fires\_off simulation) minus control simulation for May–August. Panels (i)–(l) show monthly means of WRF-Chem Surface  $\text{NO}_2$  with all transport emissions switched off in domain (trans\_off) minus control simulation for May–August. Panels (m)–(p) show monthly means of WRF-Chem Surface  $\text{NO}_2$  with all energy emissions switched off in domain (ene\_off) minus control simulation for May–August.

## 4.6 Summary

WRF-Chem shows an underestimation of tropospheric column  $\text{NO}_2$  when compared with OMI, despite the use of a more recent OMI retrieval product (DOMINO v2), which has reduced a previously characterised high bias in OMI  $\text{NO}_2$  columns in earlier product versions (Boersma et al., 2011). As well as bias from OMI observations, low model bias could also be a result of lacking or underestimated emissions within the region in current emissions datasets, or due to model errors in the  $\text{NO}_2$  atmospheric lifetime. The results from this Chapter suggest that from May – August the simulated spatial pattern in  $\text{NO}_2$  produced by the ECL anthropogenic emissions is consistent with observed  $\text{NO}_2$  from OMI ( $R=0.61-0.74$ ), but a persistent low bias continues throughout. Both EH2 (monthly FMB= -0.82 to -0.73) and ECL (monthly FMB= -0.80 to -0.70) produce simulated atmospheric distributions that underestimate the magnitude of satellite observed  $\text{NO}_2$  during this period. Scaling the 2 largest anthropogenic emission sectors in the model (transport and energy) by a factor of 2 results in an overall improvement in the underestimation of OMI column  $\text{NO}_2$  (monthly FMB=-0.66 to -0.35), but with overestimates in some urban regions, and little change to a persistent underestimate in background regions. Deficiencies in model tropospheric  $\text{NO}_y$  chemistry have been identified in previous studies as a contributor to bias in the simulated  $\text{NO}_x$  lifetime (Huijnen et al., 2010). These include removal through wet and dry deposition, and  $\text{NO}_x$  too readily converted to reservoir species such as nitric acid and peroxyacetyl nitrate (PAN). Model biases during summer could be an indication of errors in the conversion of  $\text{NO}_2$  to nitric acid, when OH concentrations are enhanced and the  $\text{NO}_2+\text{OH}$  reaction is more important. Future work is needed to better understand drivers of the model  $\text{NO}_2$  bias relative to OMI at high latitudes.

## **5. Key drivers of tropospheric ozone in Western Siberia: A quantification of high latitude sources and sinks.**

### **5.1 Introduction**

This chapter investigates tropospheric ozone in Western Siberia, with a focus on the key processes controlling surface ozone within the region. As discussed in Chapter 2, sources of tropospheric ozone are poorly characterised in the Arctic region, resulting in poor understanding of sensitivity of ozone and its impacts to potential changes in Arctic atmospheric processes, and remote and local emission sources (Law et al., 2017). Furthermore, interactions between tropospheric ozone and Siberian vegetation are not clearly understood, with previous studies demonstrating observations of suppressed high latitude ozone concentrations in air masses that have had extensive surface contact with Siberian forests (Hirdman et al., 2010; Engvall et al., 2012). Therefore a greater understanding of the extent to which this ozone sink mediates anthropogenic ozone influence in high latitude Siberia requires detailed quantification.

The aim of this Chapter is to better understand the key drivers in tropospheric ozone in Western Siberia, both north and south of 60°N. To answer this I use WRF-Chem to estimate the contributions from different types and regions of vegetation in Western Siberia to dry deposition loss of ozone produced from anthropogenic and fire emissions from the region. Section 5.2 introduces the surface observation sites used in this Chapter. Section 5.3 briefly describes the model setup used in this Chapter. Section 5.4 discuss the main findings within this Chapter, and Section 5.5 summarises the key findings.

### **5.2 Surface Observation Data**

Three separate ground observation sites are used in this Chapter to evaluate WRF-Chem output. These are located at Tomsk, Tiksi and the Zotino Tall Tower Observatory (ZOTTO). Due to the paucity of observations in this region, these observation sites do not provide wide scale evaluation, instead providing insight

into model performance at a small number of locations within the domain. The 3 observation sites are shown in Figure 5.1 (star symbols) in the context of the overall study domain.

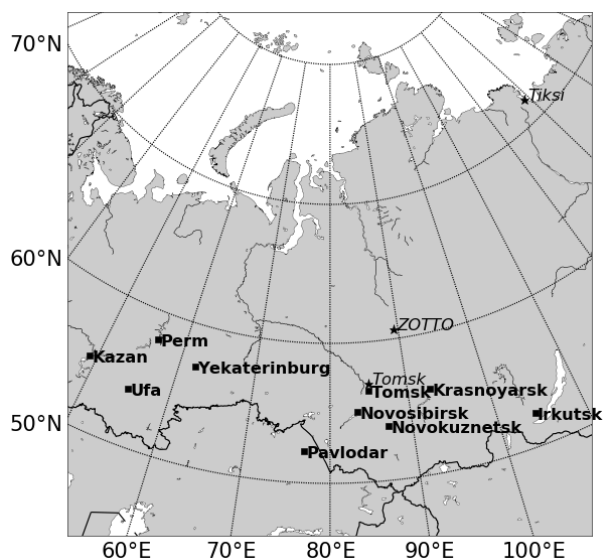


**Figure 5.1** - Map of domain used for model simulations. Centred on Western Siberia region, major cities (squares) (population > 100,000) shown in bold. Observation sites (star symbols) are given in italics

Tomsk observations are taken from the Fonovaya Observatory (56°N, 85°E), which is an Institute of Atmospheric Optics (IAO) observational site, part of the Russian Academy of Sciences (RAS) Siberian Branch (Antonovich et al., 2018). The station was created in 2009 to attempt to improve the Russian observation infrastructure across Western Siberia, where there is a significant lack of long-term observation sites. The site is located 60 km to the west of Tomsk (approx. 57°N, 85°E) in a rural, boreal location. Hourly ozone measurements are available at the surface from 2010 – 2011 (Davydov et al., 2018). These measurements are taken using an OPTEC 3.02-P chemiluminescence analyser at 10 m on an observational mast outside of the Observatory. Near real-time graphical representation of the data is available at <http://lop.iao.ru/EN/>.

The Zotino Tall Tower Observatory (ZOTTO) is situated in central Siberia (61°N, 89°E), close to the village of Zotino, located on the Yenisei river (Kozlova et al., 2008). The tower was constructed in September 2006, as part of a global project titled “Biogeochemical Responses to Rapid Climate Changes in Eurasia”. The tower is 304 m in height, with 6 measurement platforms at 4, 52, 92, 158, 227 and 301m for meteorological variables, and 2 air sampling inlets positioned at 30 and 301m for ozone measurements carried out by Dasibi 1008AH-type and Thermo Electron Model 42C-TL gas analysers, respectively (Moiseenko et al., 2019). At present, human impacts on the local air quality are minimal due to the low population density of the area. These observations are therefore useful in evaluating the background atmospheric composition in the central Siberian region. In this thesis I use hourly ozone measurements taken from 30 m.

The Tiksi Observatory (71.36°N, 128.53°E) is located at the mouth of the Lena River, on the remote northern Russia coast. It is situated in a region far from any major sources of anthropogenic pollution, other than the town of Tiksi (5000 population) which is 5 km northeast of the observatory. This location offers an opportunity to gain observations at high latitudes in a near pristine environment. At present, the observatory is run in collaboration with NOAA (National Oceanic and Atmospheric Administration), the Tiksi Data Centre at the Arctic and Antarctic Research Institute in St Petersburg, Russia, which is responsible for the collection and distribution of the data, the Yakutian Service for Hydrometeorology and Environmental Monitoring, and the FMI (Finnish Meteorological Institute) (Asmi et al., 2016; Uttal et al., 2016). For this thesis, I use hourly ozone concentrations measured with a Thermo Scientific Model 19i analyser, which are available for 2011 (<https://www.esrl.noaa.gov/gmd/dv/iadv/>).

### 5.3 WRF-Chem Setup

The WRF-Chem model is described in Chapter 3 in more detail. The model domain over Western Siberia and model experiments are the same as those described in the previous chapter (Sections 4.4, Fig. 4.4 and Table 4.1), with the ozone output used in this Chapter from those simulations.

In this Chapter I utilise modelled ozone dry deposition fluxes, output on an hourly temporal scale. WRF-Chem simulations use the Wesely dry deposition scheme (Wesely, 1989) to calculate dry deposition velocities, which provides the deposition velocity magnitude as:

$$|v_d| = (r_a + r_b + r_c)^{-1} \quad (5.1)$$

Where  $r_a$  is the aerodynamic resistance between a specified height and the surface,  $r_b$  is the boundary layer resistance, and  $r_c$  is the bulk surface resistance. The  $r_a$  and  $r_b$  components are reasonably well defined, and are largely dependent on large scale dynamics (Silva and Heald, 2018). Wesely (1989) provides bulk surface resistance estimates for 11 land use types across 5 different seasonal categories for ozone, which are used here.

To provide insight into the relative influences from different processes on regional ozone both at the surface and through the vertical column, WRF-Chem physical and chemical tendencies for ozone are output at every model timestep. These are calculated as the difference before and after each chemistry solver timestep (Barth et al., 2012). These tendencies include separate quantification of the change in ozone mixing ratio from convection, horizontal and vertical advection, vertical mixing (including dry deposition to the surface for the bottom layer) and chemical production. WRF-Chem diagnostic parameters that track net ozone production and advection tendency have been successfully used in the past to identify key controls on surface and vertical profiles of ozone (Barth et al., 2012; Sharma et al., 2017; Girach et al., 2017).

## 5.4 Results

### 5.4.1 Surface Ozone Evaluation

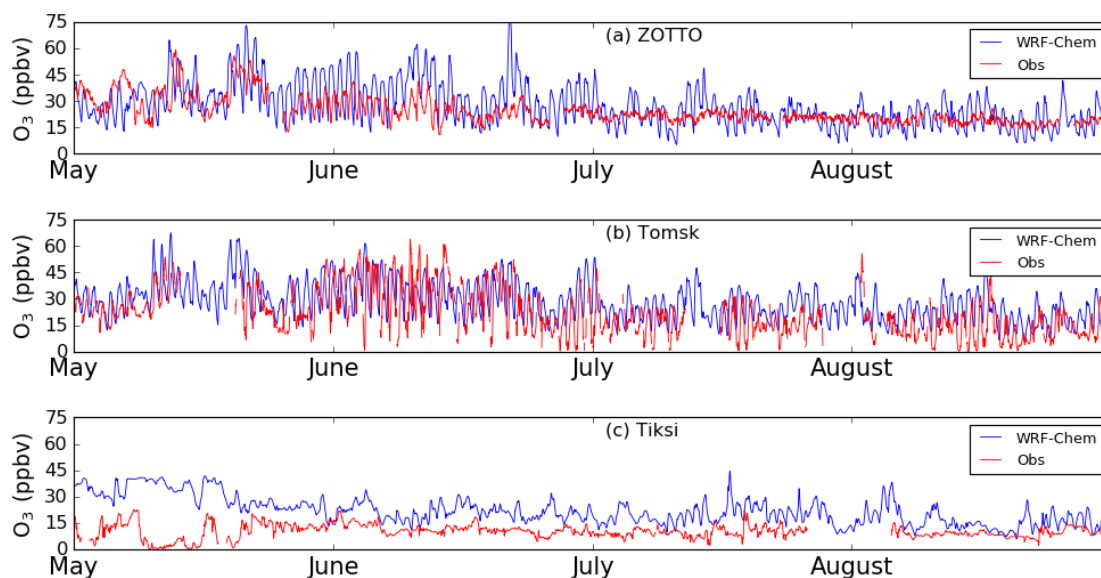


**Figure 5.2** – Hourly time series of surface ozone comparisons for WRF-Chem (blue) and ground observations (red) for three sites within the study domain: (a) ZOTTO, (b) Tomsk and (c) Tiksi. WRF-Chem output is taken from the ECL\_SCALED simulation.

Observed surface ozone at Tomsk, and to an extent ZOTTO, show clear diurnal patterns throughout the entire study period, but this is not as clear at the most remote observation site at Tiksi (Fig. 5.2). This diurnal cycle is strongest at Tomsk, which is likely driven by the close proximity to large anthropogenic urban sources of ozone precursor sources. WRF-Chem consistently overestimates the surface ozone diurnal cycle amplitude at ZOTTO throughout July and August, despite having a lower amplitude than May and June. This behaviour in the observations, and to an extent the model, is similar to that reported in previous studies investigating surface ozone in Siberia (Pochanart, 2003; Stjernberg et al., 2012). It was suggested that this observed summer surface minimum and limited diurnal cycle is attributed to enhanced ozone deposition to the boreal forest or chemical destruction with BVOCs near the forest canopy (Stjernberg

et al., 2012). During the middle of May at Tiksi observed ozone values are below 5 ppbv, which could be associated with an ozone depletion event (ODE), most common in the Arctic during Spring (Simpson et al., 2007). This supports previous findings that suggest observation sites in close proximity of the Arctic Ocean show low late-spring concentrations (AMAP, 2015).

The daily mean surface ozone observations at Tiksi for the 8<sup>th</sup>, 9<sup>th</sup> and 10<sup>th</sup> of May are 1.6, 2.0, and 4.2 ppbv respectively. Previous field campaigns using ship measurements have found ozone levels close to zero over the frozen Arctic Ocean during March – May (Jacobi et al., 2006). The majority of ODE occur at coastal observation sites, which Tiksi is, due to the release of reactive bromine species (Br and BrO) from sea salt in the frozen Arctic ocean (Thompson et al., 2017; Falk and Sinnhuber, 2018). During ice melt the release of bromine can lead to ozone depletion events, causing ozone concentrations to go from background concentrations (~30ppbv) to concentrations lower than 5ppbv within days (Cao et al., 2016; Zhao et al., 2016).

Mean surface ozone at ZOTTO during July (21.4 ppbv) and August (18.8 ppbv) and Tomsk in the same time period (July: 16.7 ppbv, August: 14.0 ppbv) are similar in magnitude to that seen during previous summer observation campaigns in Siberia (Stjernberg et al., 2012). These low surface values for ozone were attributed to a strong surface ozone sink, likely deposition to the large Siberian forests. Due to the significant coverage area of Siberian forests, it is relevant for the ozone budget on a global scale (Stjernberg et al., 2012).

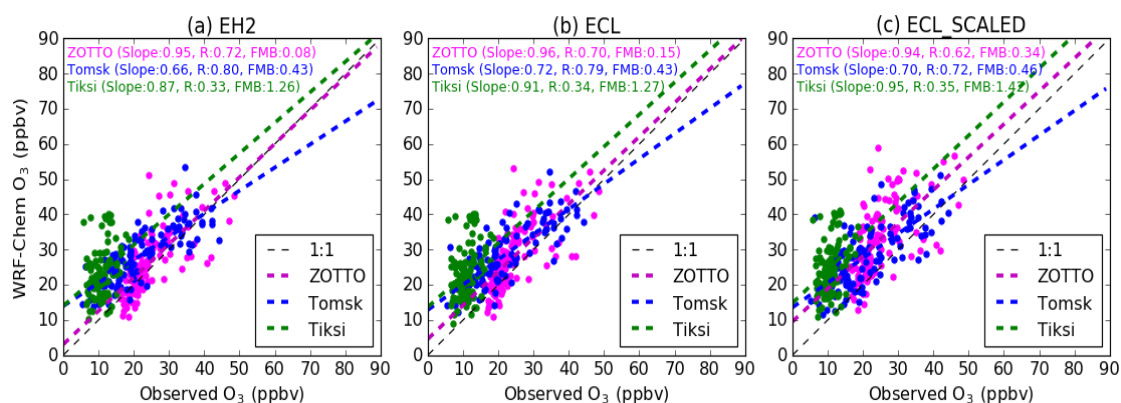


**Figure 5.3** - Daily mean surface ozone comparisons for three ground observation sites within the study domain: ZOTTO (magenta), Tomsk (blue) and Tiksi (green) for 01/05/11 – 31/08/11. Panel (a) shows WRF-Chem surface ozone using EH2 anthropogenic emissions; panel (b) shows WRF-Chem surface ozone using ECL anthropogenic emissions; panel (c) shows WRF-Chem surface ozone using ECL\_SCALED anthropogenic emissions.

WRF-Chem simulations suggest that tropospheric ozone at the 3 ground observation sites is relatively insensitive to the choice of anthropogenic emission inventory (Fig. 5.3). This is particularly the case at the 2 sites of Tomsk (EH2 FMB: 0.43; ECL FMB: 0.43) and Tiksi (EH2 FMB: 1.26; ECL FMB: 1.27). The greatest sensitivity to the differences between the anthropogenic emissions datasets is at ZOTTO, where the bias is improved using the EH2 emissions (EH2 FMB: 0.08; ECL FMB: 0.15). There is a consistent positive bias in modelled surface ozone values at all 3 observation sites, with the largest bias seen at Tiksi for both simulations (EH2 FMB: 1.26; ECL FMB: 1.27), which is also seen across the study period at all observation sites in Figure 5.2. Both model simulations also show substantially lower fractional mean bias values for ZOTTO when compared to the other observation sites, EH2 (FMB=0.08) and ECL (FMB=0.15). Due to the largely boreal forest land surface cover at the ZOTTO observation site, this could suggest improved model performance over boreal forest regions, when compared to the Arctic tundra at Tiksi. A summertime low ozone bias at Tiksi may also be indicative of an

underestimation in the ozone dry deposition sink, which has been shown to be a key ozone loss process for high latitude Siberia (Stjernberg et al., 2012).

The WRF-Chem simulation using the ECL\_SCALED anthropogenic emissions produce an increase in ozone FMB at all sites compared to both ECL and EH2 simulations (Fig 5.3c). However, given the limited spatial coverage of the ozone observations, the optimal model choice to use in the subsequent analysis is based on the more extensive NO<sub>2</sub> evaluation from Chapter 4. For the rest of this Chapter, the control simulation refers to the WRF-Chem simulation using ECL\_SCALED anthropogenic emissions.

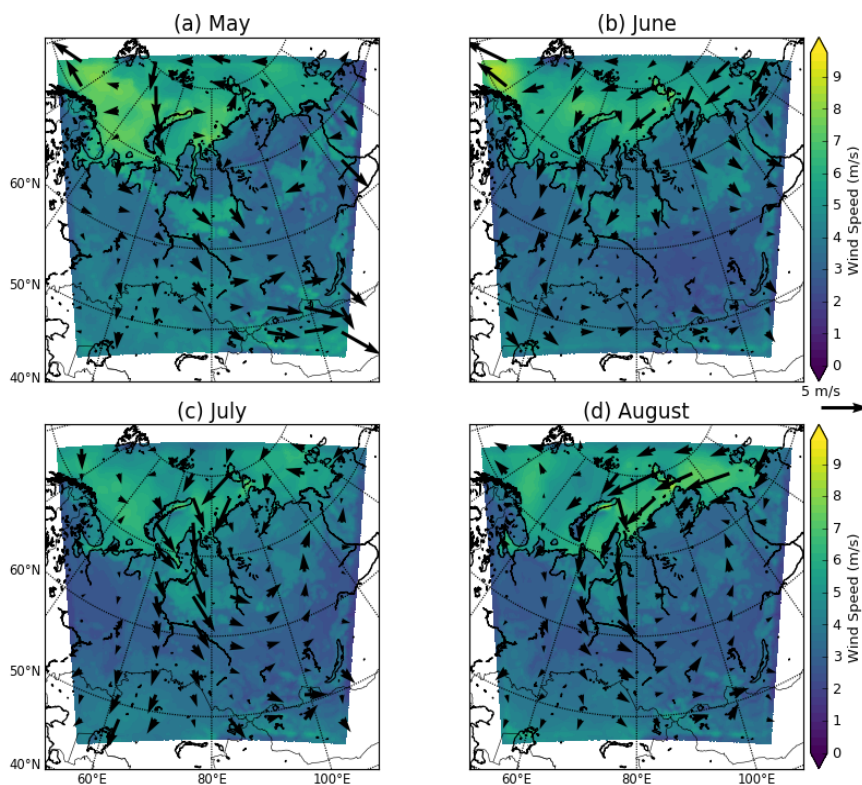


**Figure 5.4** - Panels (a) – (d) show monthly means of WRF-Chem surface wind direction plotted on top of wind speed.

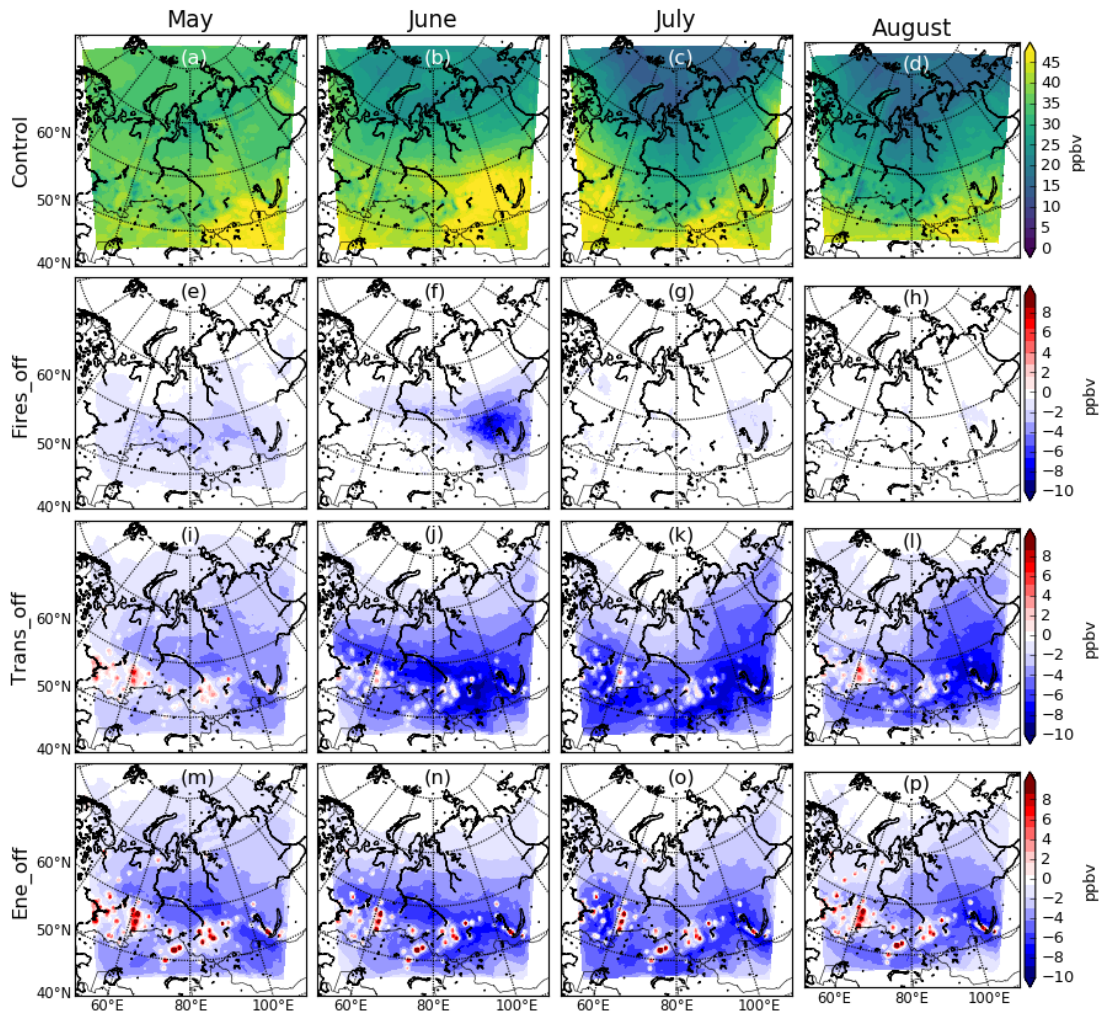


**Figure 5.5** - Simulated control and sensitivity run changes in surface ozone concentrations. Panels (a)–(d) show monthly means of WRF-Chem surface ozone for May–August using ECL\_SCALED emissions. Panels (e)–(h) show monthly means of WRF-Chem Surface ozone with all fire emissions switched off in domain (fires\_off simulation) minus control simulation for May–August. Panels (i)–(l) show monthly means of WRF-Chem Surface ozone with all transport emissions switched off in domain (trans\_off) minus control simulation for May–August. Panels (m)–(p) show monthly means of WRF-Chem Surface ozone with all energy emissions switched off in domain (ene\_off) minus control simulation for May–August.

Model-simulated surface ozone concentrations in Western Siberia are largest during May (mean=36.9 ppbv) (Fig. 5.5a), coinciding with the well-characterised springtime maximum in Arctic surface ozone (Quinn et al., 2008; Stohl et al., 2007). There is no clear dominant wind direction during May (Fig. 5.5a), with a weak westerly flow across the land north of 60°N, limiting the removal of ozone-rich air. This springtime maximum has been attributed to poleward import of ozone precursors and an increase in stratospheric downwelling, which is more frequent during late spring at high latitudes (Berchet et al., 2013). In July and August (Fig. 5.5c-d) a surface ozone gradient from north to south begins to emerge and is strongest during August (Fig. 5.5d). This results from smaller simulated ozone concentrations over the Arctic, where the mean surface ozone concentration north of 60°N is 21.9 ppbv, whilst south of 60°N it is 36.0 ppbv. These low concentrations of modelled surface ozone at high latitudes occur as wind directions change to a northerly direction during summer, limiting the import of ozone precursors from lower latitudes into the Arctic (Fig. 5.4c-d). During June-August (Fig. 5.5b-d), largest surface ozone concentrations occur over the areas of significant precursor emissions, where monthly surface ozone averages across the summer exceed 35 ppbv. During June (Fig. 5.5c) concentrations exceeding 45 ppbv are simulated in the region to the east of the Ob valley, which is associated with a major fire event during this month.

### 5.4.2 Ozone Source Contributions

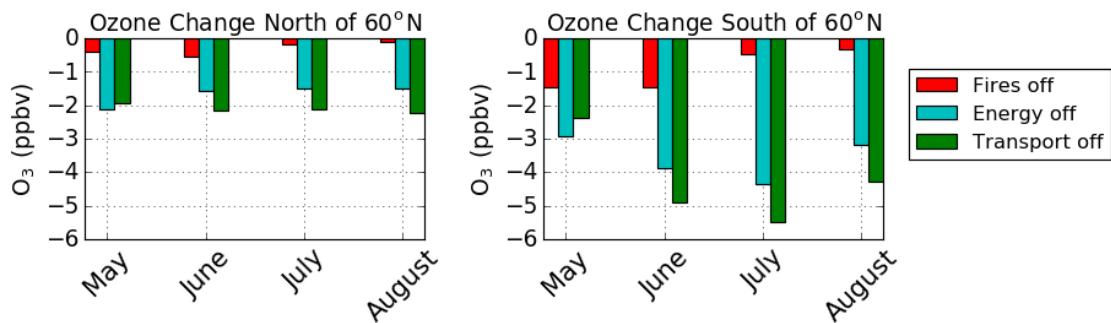


**Figure 5.6** - Surface ozone change relative to control simulation for the section of the domain north of 60°N (left panel) and south of 60°N (right panel) for the 3 sensitivity simulations, *fires\_off* (red), *ene\_off* (blue) and *trans\_off* (green).

Overall, surface ozone shows greatest sensitivity to anthropogenic emissions, compared with fire emissions (Fig. 5.5 & Fig. 5.6). In June, July and August, transport sector emissions produce the largest ozone sensitivity, while energy emissions dominate during May. This is the case for both north and south of 60°N, where the maximum differences relative to the control simulation for the transport off simulation occur in August north of 60°N (-2.2 ppbv) and in July (-5.5 ppbv) south of 60°N (Fig. 5.6). Across the 4-month period for the total domain, widespread reductions in surface ozone concentrations are seen in both the *trans\_off* (Fig. 5.5i-l) and *ene\_off* (Fig. 5.5m-p) simulations. However, within the *ene\_off* simulations an increase in ozone is simulated over urban regions with high anthropogenic emissions, due to a decrease in the loss of ozone via  $\text{NO} + \text{O}_3$  where  $\text{NO}_x$  emissions are reduced. In the *fires\_off* simulation there is a small reduction over a large area in surface ozone south of 60°N in May (Fig. 5.5e), whereas in June (Fig. 5.5f) there is a significant reduction of surface ozone to the east of the Ob valley, due to the large biomass burning event.

Anthropogenic emissions from the energy and transport sectors sourced from within the domain contribute more to surface ozone north of 60°N than fire

emissions for all months (Fig. 5.6), with surface ozone sourced from fires predominantly confined to south of 60°N. In the high fire month of June, the greatest influence of fires on surface ozone north of 60°N is seen for the entire study period, but the difference compared to the control simulation is less than 1 ppbv.

During May north of 60°N large contributions to surface ozone from energy emissions are seen, likely due to emissions associated with high latitude oil and gas extraction within the domain. This contribution is likely enhanced due to poleward movement of air which occurs during late springtime (Stohl, 2007) (Fig. 5.5). This period marks the beginning of the shift in wind direction north of 60°N during May/June to a more northerly flow bringing in cleaner Arctic air, which leads to efficient southward export of the energy sourced ozone at high latitudes, evident as an increase in surface ozone energy sector sensitivity south of 60°N from May to June (Fig. 5.6).

#### **5.4.4 Chemical and Dynamical Contributions to Simulated Ozone**

As described in Section 5.3 of this Chapter, WRF-Chem physical and chemical tendencies for ozone are used to provide insight into the relative influences from different processes on regional ozone both at the surface and through the vertical column. These are shown in 5.4.4.1 for: horizontal advection, vertical advection, convection, chemical processes and vertical mixing (including dry deposition).

##### **5.4.4.1 Total Domain**

To understand the impact of each tendency variable on the ozone within the boundary layer the results presented in this section show monthly mean values for ozone between surface – 900 hPa.

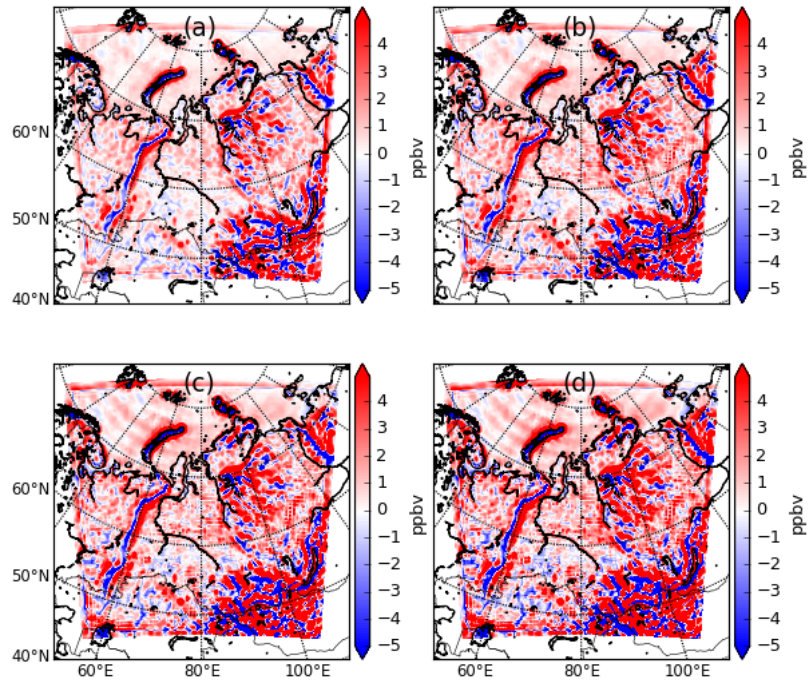


**Figure 5.7** – Change in ozone due to horizontal advection between the surface and 900 hPa for May (a), June (b), July (c) and August (d).

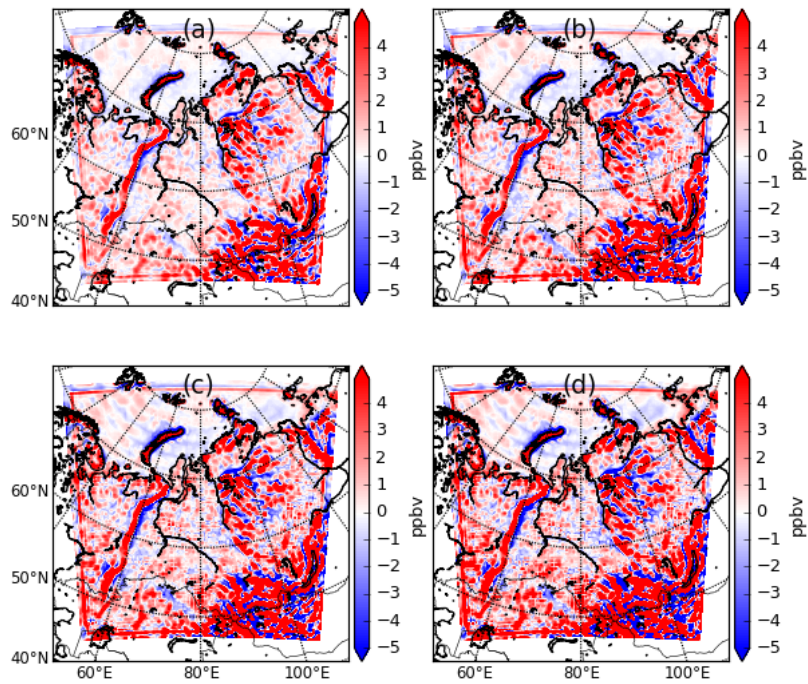


**Figure 5.8** – Change in ozone due to vertical advection between the surface and 900 hPa for May (a), June (b), July (c) and August (d).

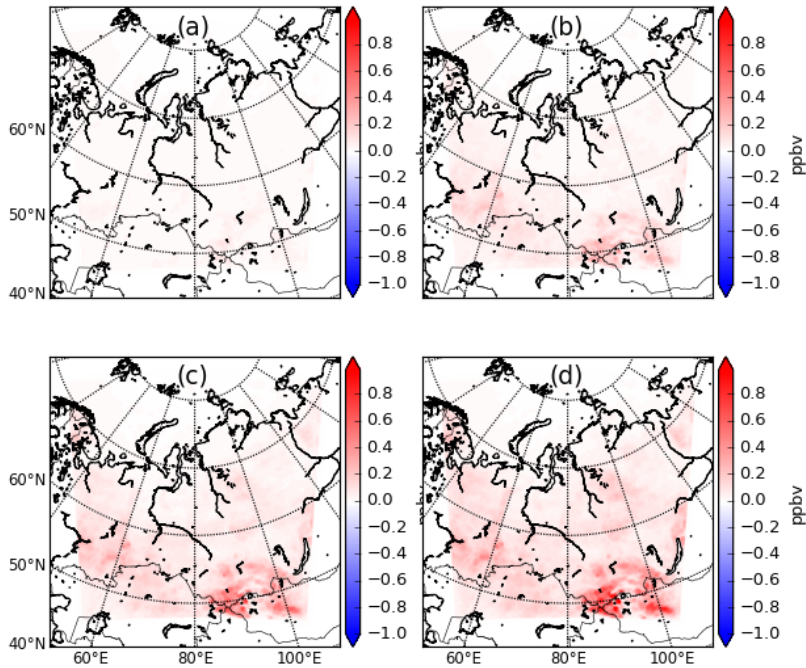


**Figure 5.9** – Change in ozone due to convection between the surface and 900 hPa for May (a), June (b), July (c) and August (d). Note axis -1 to 1 ppbv.

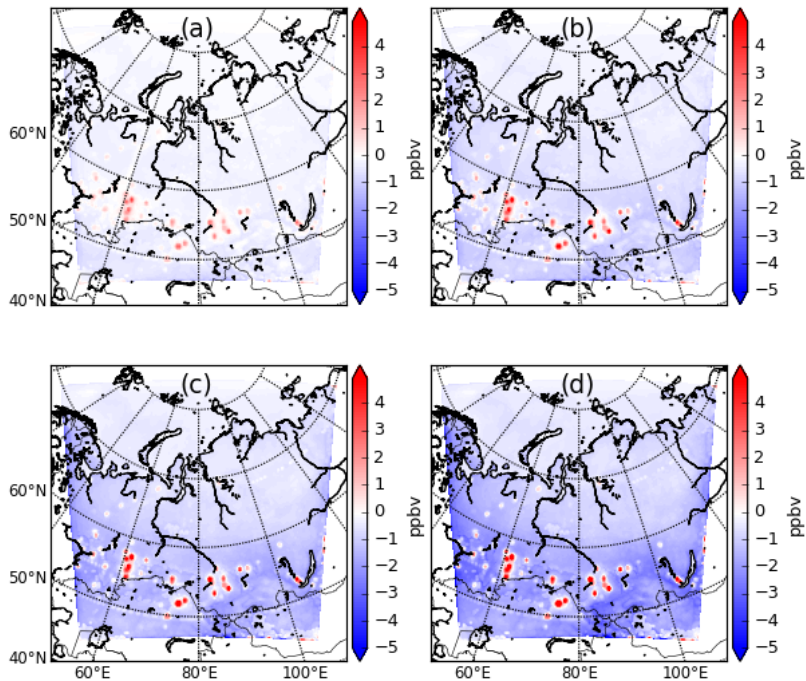


**Figure 5.10** – Change in ozone due to vertical mixing (and dry deposition) between the surface and 900 hPa for May (a), June (b), July (c) and August (d).

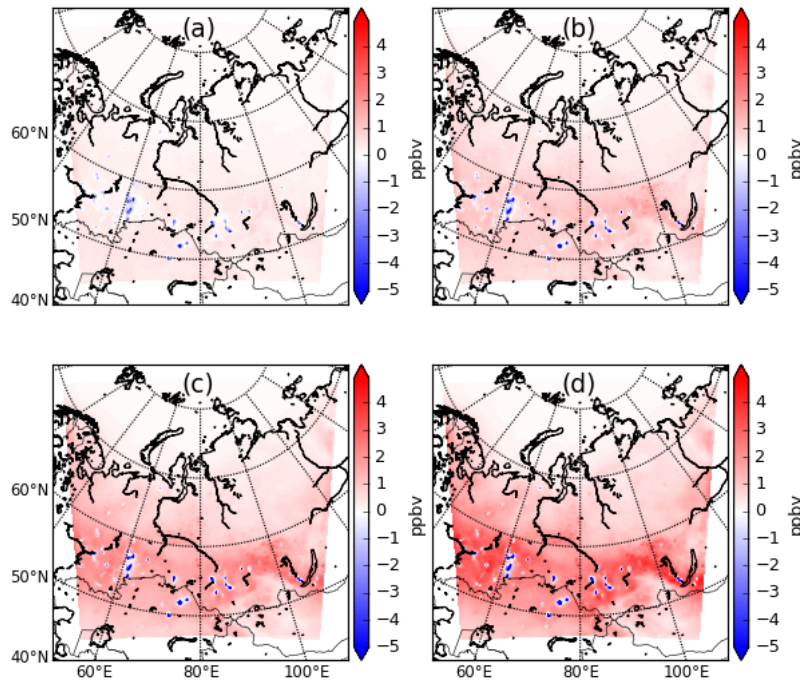


**Figure 5.11** – Change in ozone from chemistry between the surface and 900 hPa for May (a), June (b), July (c) and August (d).

Ozone in Western Siberia between the surface and 900 hPa is influenced by a range of different processes, with their influence varying across the domain. Over areas of complex topography, for example the Ural mountain range (approx. north to south along 60 °E) ozone is dominated by both vertical and horizontal advection (Fig. 5.7 & 5.8), likely associated with strong anabatic and katabatic wind flows. The South Ural region is also severely impacted by poor air quality associated with iron and steel companies, where the average annual concentration between 2006 – 2016 for NO<sub>2</sub> was 107 ug/m<sup>3</sup> in Karabash (55 °N 60 °E) (Ulrikh et al., 2017). The Sayan Mountain range in the south east corner of the domain (approx. 53 °N 95 °E), is also predominantly controlled by both vertical and horizontal advection. These variables show little change in their influence across the entire study period. The influence of these vertical and horizontal advection diminishes in lowland areas of the domain.

Convection has little impact on ozone in Western Siberia (Fig 5.9), and is associated with a limited surface ozone increase during the summer (Fig 5.9 b, c & d) in the south eastern section of the domain. This small increase of ozone could be due convection lifting lower tropospheric ozone to higher altitudes in the Sayan Mountains, where typically ozone lifetime is longer, which could be further impacted by the longer summer daylight in the summer time (Doherty et al., 2005).

Ozone vertical mixing causes significant losses across the majority of the domain (Fig. 5.10), likely due to the vertical mixing down of ozone and the subsequent dry deposition to the surface in the background regions. Ozone loss through export to higher latitudes could also lead to this modelled loss. Over the major emission source regions in the domain there is an increase in ozone, which peaks during August (Fig 5.10d). Multiple studies have shown vertical mixing to be the cause of localised surface ozone increases over polluted regions, due to the mixing down of higher concentrations of ozone from above, where ozone production efficiency is increased (Dickerson et al., 1987; Pickering et al., 1990; Lawrence et al., 2003). Figure 5.11 also shows ozone chemical loss over anthropogenic emission source regions, which could be associated with ozone being lost chemically through reacting with NO emitted at the surface. Through the use of a chemistry transport model, Lelieveld and Crutzen (1994) demonstrated both ozone production over polluted regions due to the vertical mixing of ozone to altitudes where ozone production efficiency is greater, as well ozone destruction due to greater surface mixing and the chemical removal of ozone through greater abundances of ozone depleting pathways.

#### **5.4.4.2 Vertical Profiles**

To further investigate the role of different chemical and physical tendencies on ozone over Western Siberia, the vertical profiles over 2 major cities are presented in this Section, to better understand how these processes effect the

ozone vertical profile and this changes across the study period. These profiles are for monthly means of ozone change per hour due to the relevant process.

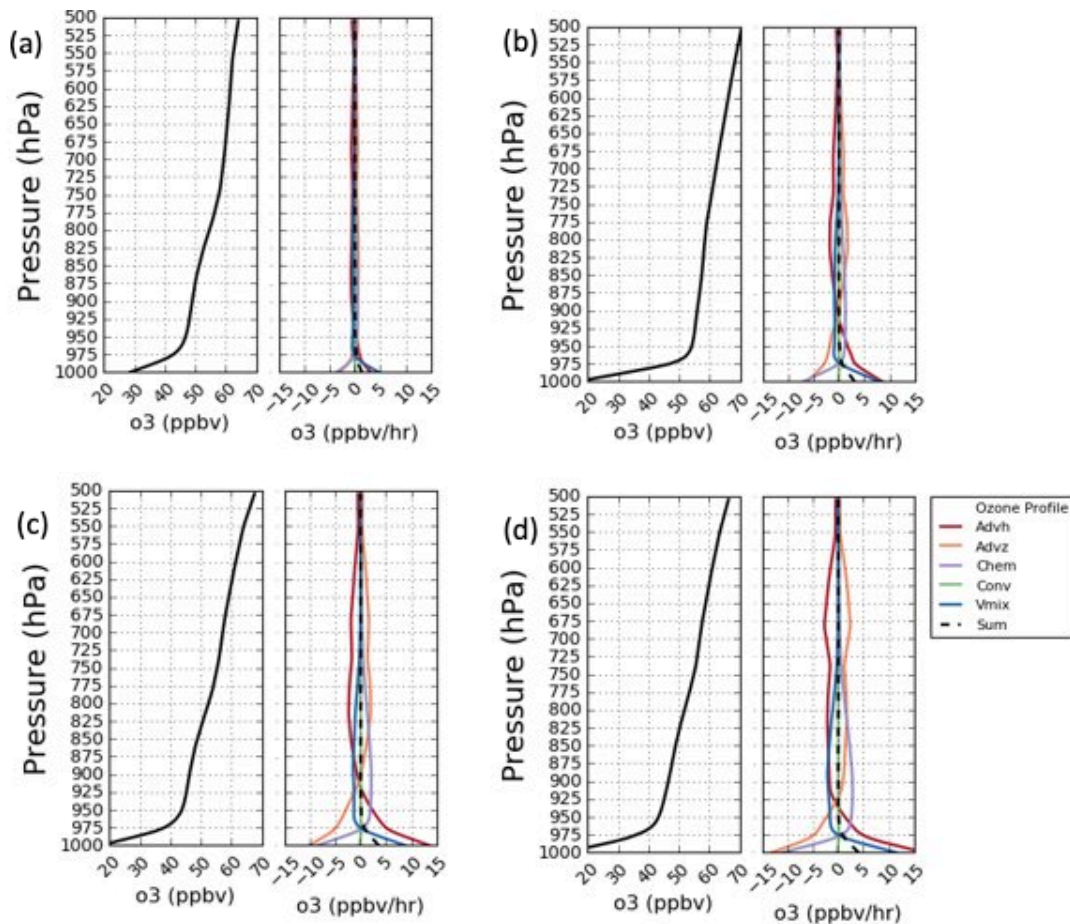


**Figure 5.12** – Monthly mean vertical profiles of hourly change in ozone due to chemical tendencies above Novosibirsk in May (a), June (b), July (c) and August (d). Horizontal advection (Advh) is shown in red, vertical advection (Advz) is shown in orange, chemistry (chem) is shown in purple, convection (conv) is shown in green, vertical mixing (vmix) is shown in blue and the sum of tendencies is shown in dashed line.

Over Novosibirsk (location shown in Fig. 5.1) during the summer (JJA) the different ozone tendencies are much smaller in magnitude for altitudes above 975 hPa, with the majority of their influence seen close to the surface (Fig 5.12). During May (Fig 5.12a) the local tendency variables have limited influence on ozone throughout the vertical column, with a small amount of loss associated with chemical processes, and small quantities of ozone production associated with vertical mixing. Due to small values during this month, their effect on overall ozone in the column is limited. Whilst convection has very limited influence on

ozone throughout the vertical column for the entirety of the study period, the other 4 tendency variables have greater influence through time across the study. In July and August (Fig. 5.12c & d) chemical production of ozone is the greatest source of ozone between 950 and 800 hPa, which is likely due to the ozone production efficiency increasing with altitude (Lelieveld and Crutzen, 1994). An increase in ozone production at these elevated altitudes could also be linked to the import of surface-emitted NO<sub>2</sub> emissions, producing larger quantities of ozone (Dickerson et al., 1987). This increase could also be attributed to an

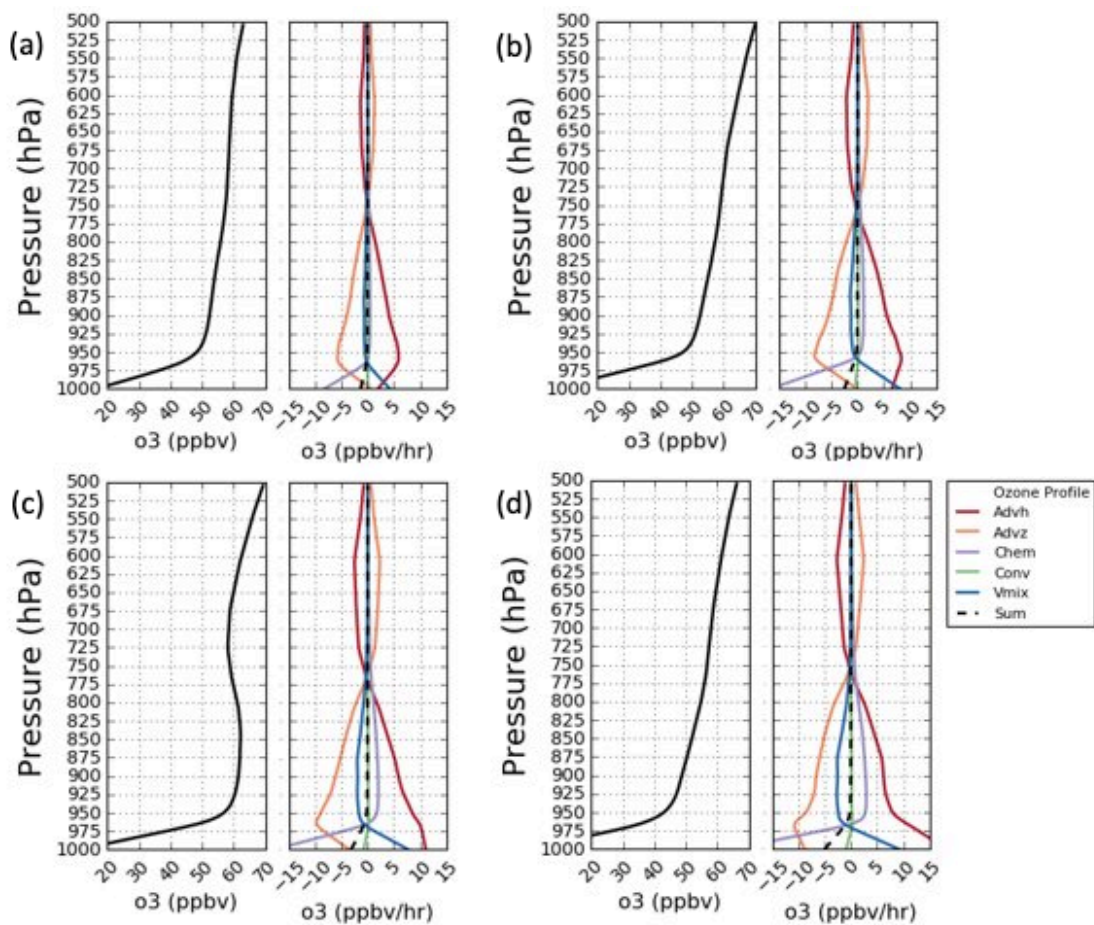


**Figure 5.13** - Monthly mean vertical profiles of hourly change in ozone due to chemical tendencies above Kazan in May (a), June (b), July (c) and August (d). Horizontal advection (Advh) is shown in red, vertical advection (Advz) is shown in orange, chemistry (chem) is shown in purple, convection (conv) is shown in green, vertical mixing (vmix) is shown in blue and the sum of tendencies is shown in dashed line.

increase in  $\text{NO}_x$  from lightning, which is more active during the summer months at high altitudes (Murray, 2016).

Over Kazan (location shown in Fig. 5.1) vertical and horizontal advection are the dominant processes controlling ozone in the lower troposphere during the study period, while chemical loss is significant close to the surface (Fig. 5.13). This significant loss at the surface leads to an overall loss of ozone for the entirety of the study period (dashed line, Fig. 5.13). During the summer months (JJA) advection has a significant effect on ozone, which is also shown in Figures 5.7 and 5.8, more so than that seen at Novosibirsk. This could be caused by the influence of the Urals, as previous studies have shown the mountain range to have far reaching impacts on both meteorology and air quality, termed “Ural-blocking” (Luo et al., 2016).

WRF-Chem chemical and physical tendencies highlight the key process controlling ozone above the boundary layer is large-scale advection, likely associated with the transport of air masses at the same altitude (Fig. 5.12 & 5.13). Previous research suggests there are still significant uncertainties regarding the main processes which directly control ozone abundancies within tropospheric air masses, which can differ based on the time of year (AMAP, 2015). Several springtime aircraft campaigns within the POLARCAT experiment (Jacob et al., 2010; Emmons et al., 2015) found that high latitude air masses were strongly influenced by boreal fires sourced from Siberia, and were found to be carrying anthropogenic ozone precursor emissions from Asia. Whilst model uncertainties are also highlighted in regards to PAN, an important reservoir species for  $\text{NO}_x$ , with modelled temperature biases enhancing PAN stability. This is important given the main loss of PAN is through thermal decomposition (Jacob et al., 2010). Model overestimations of PAN within tropospheric air masses when compared with springtime aircraft data could lead to uncertainties in simulating tropospheric ozone (Emmons et al., 2015). Summertime upper tropospheric ozone can also be directly influenced by the import of stratospheric ozone (Liang et al., 2011; Pankratova et al., 2011), which

may partly account for the increase in ozone at high altitudes during the summer months within the domain.

Near-surface chemical and physical tendencies show that whilst advection processes are of importance between the surface and 950 hPa, especially during July and August, the mixing down of ozone from aloft and subsequent strong surface-based chemical loss is also key (Fig. 5.12 & 5.13). This is in line with findings from the Transcontinental observation into the chemistry of the atmosphere (TROICA) fieldwork campaign, which found evidence of mixing down and subsequent surface-based chemical loss of ozone in Siberia (Pankratova et al., 2011). It was found that under the correct meteorological conditions the vertical mixing down of ozone-rich air from the free troposphere led to increased surface ozone concentrations. Consequently, in regions of more polluted air (i.e. cities) more active photochemical loss of ozone occurs through reacting with enhanced NO concentrations ( $O_3 + NO$ ) (Pankratova et al., 2011).

### 5.4.3 Ozone Dry Deposition

#### 5.4.3.1 Total Domain

To investigate the impact of vegetation as a surface sink of ozone in Western Siberia, I analysed ozone dry deposition fluxes from the WRF-Chem simulations shown in Figure 5.5. Maximum ozone dry deposition to the surface occurs during the summer months of June, July & August (Fig. 5.14b-d), which coincides with the summer peak in photosynthesis in vegetation (Karlsson et al., 2007; Stjernberg et al., 2012). Dry deposition fluxes are lower during May (Fig. 5.14a), which may contribute to the larger modelled ozone concentrations at high latitudes (Fig. 5.5a), as well as the potential increase in stratospheric downwelling during late springtime (Berchet et al., 2013).

Ozone dry deposition flux is most sensitive to anthropogenic ozone precursor emissions, especially during June, July and August (Fig 5.14). The reduction in dry deposition flux in the anthropogenic perturbation simulations is greater south of 60°N during this period but extends north of 60°N in July and August, for both the *trans\_off* and *ene\_off* simulations. This is despite relatively low concentrations of surface ozone at high latitudes during these months (Fig. 5.5c-d). This is likely due to enhanced photosynthesis activity and stomatal conductance during the summertime, leading to enhanced ozone deposition flux. In the *ene\_off* simulations there are localised increases of dry deposition close to the urban regions, likely caused by the increase in surface ozone seen in Figure 5.5m-p, due to a decrease in the loss of ozone via  $\text{NO} + \text{O}_3$  where  $\text{NO}_x$  emissions are reduced.

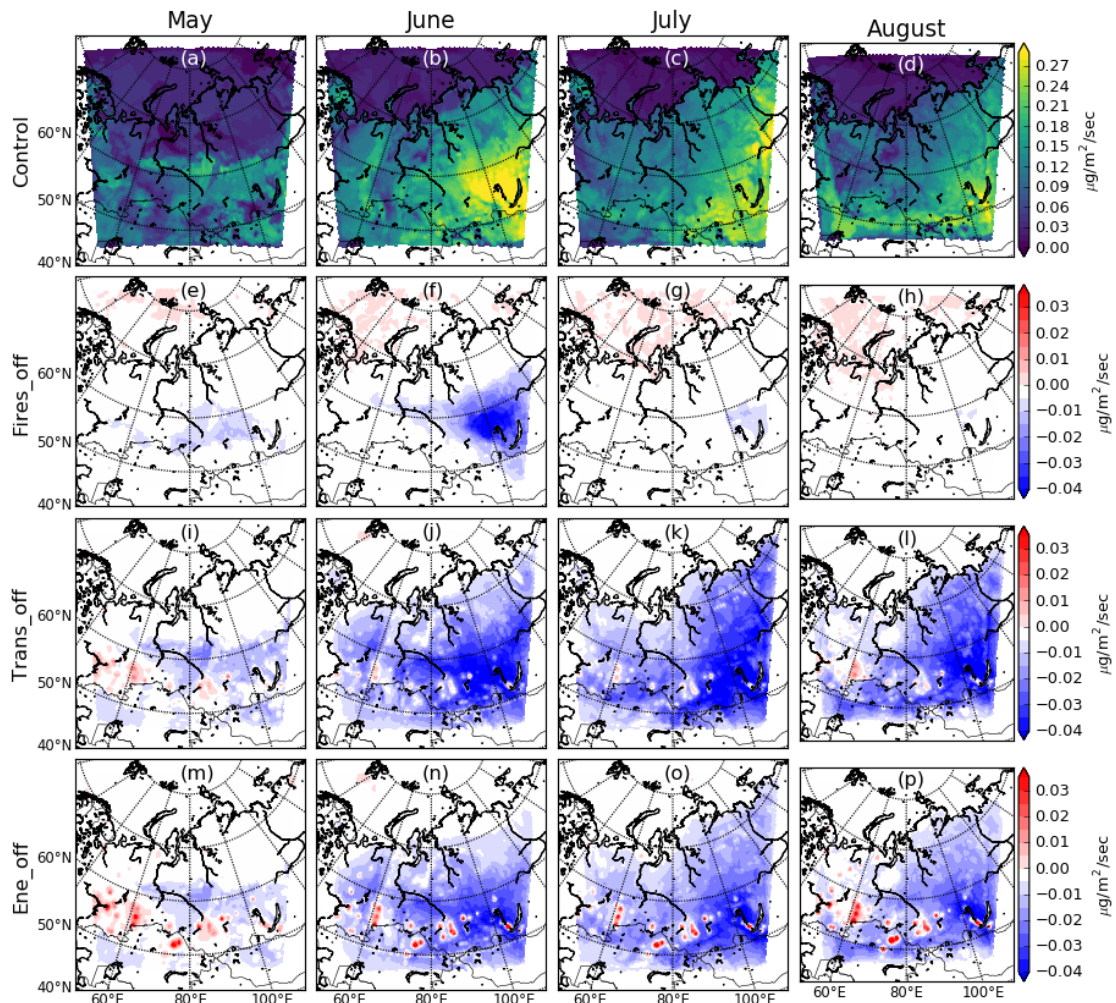


**Figure 5.14** - Simulated control and sensitivity run changes in surface ozone dry deposition flux. Panels (a)–(d) show monthly means of WRF-Chem surface ozone dry deposition flux for May–August using ECL\_SCALED emissions. Panels (e)–(h) show monthly means of WRF-Chem Surface ozone dry deposition flux with all fire emissions switched off in domain (fires\_off simulation) minus control simulation for May–August. Panels (i)–(l) show monthly means of WRF-Chem Surface ozone dry deposition flux with all transport emissions switched off in domain (trans\_off) minus control simulation for May–August. Panels (m)–(p) show monthly means of WRF-Chem Surface ozone dry deposition flux with all energy emissions switched off in domain (ene\_off) minus control simulation for May–August.

### 5.4.3.2 Land Surface Types

To further investigate the impact of vegetation as an ozone surface sink, I have calculated deposition velocities and quantified the total ozone deposited to each of the land surface types used in the land surface scheme for the model. This is the modified IGBP-MODIS Noah land surface scheme, as described in Chapter 3. For this analysis, similar land surface types have been grouped together to provide 8 distinct land cover categories (Fig. 5.15).

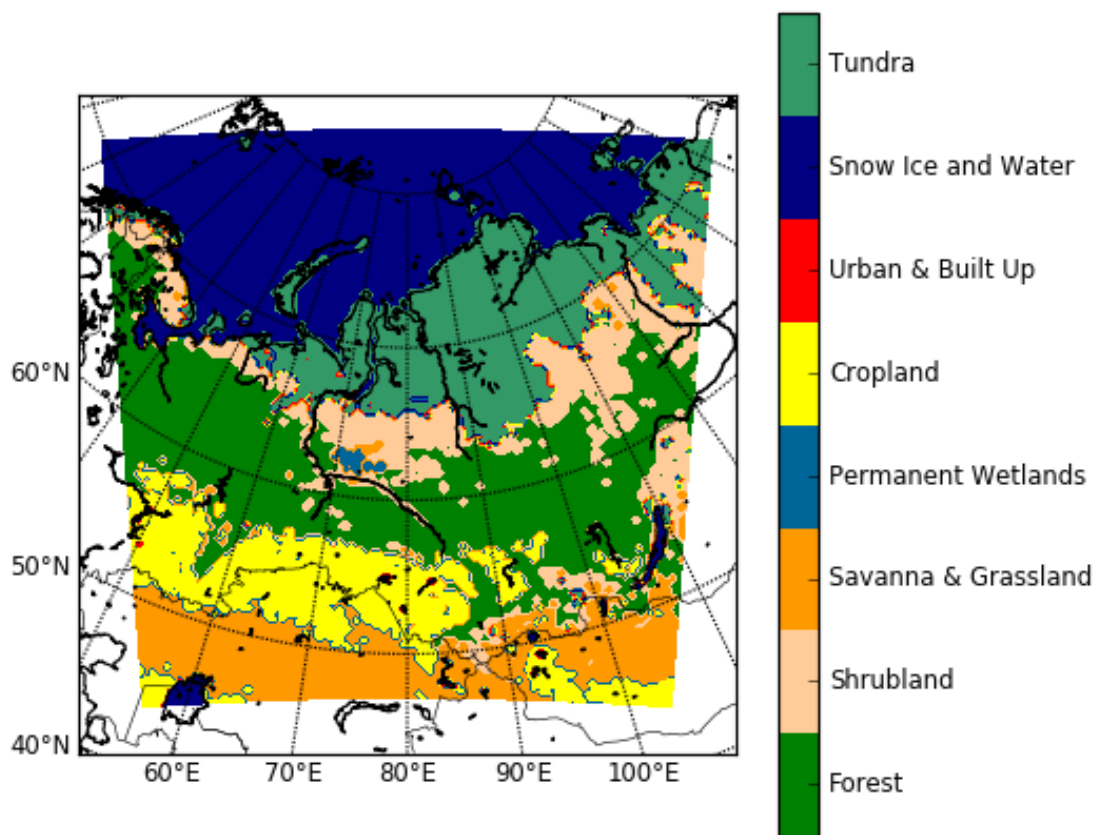


**Figure 5.15** – Grouped land surface types based on the modified IGBP MODIS Noah land surface scheme across Western Siberia for: Tundra (14.2% coverage of model domain), Snow, Ice and Water (22.3%), Urban & Built Up (0.1%), Cropland (10.8%), Permanent Wetlands (0.2%), Savanna & Grassland (13.1%), Shrubland (10.3%) and Forest (29.0%).

**Table 5.1** – WRF-Chem ozone deposition velocity to different model land surface types as shown in Figure 5.15.

Month	Ozone Deposition Velocity to Land Surface Type (cm s <sup>-1</sup> )							
	Forest	Shrubland	Savanna & Grassland	Permanent Wetlands	Croplands	Urban & Built Up	Snow, Ice & Water	Tundra
<b>May</b>	0.24	0.15	0.22	0.20	0.18	0.11	0.08	0.11
<b>June</b>	0.45	0.38	0.36	0.36	0.29	0.31	0.10	0.38
<b>July</b>	0.44	0.47	0.36	0.39	0.31	0.39	0.10	0.56
<b>August</b>	0.42	0.43	0.41	0.43	0.35	0.38	0.10	0.46
<b>Average</b>	0.39	0.36	0.33	0.35	0.28	0.30	0.10	0.38

Across the 4-month study period Siberian Forest acts as the most efficient land surface sink for ozone, especially during the summer months of June – August (Table 5.1). This highlights the importance of the Siberian forest as an important ozone surface sink, which due to its large expanse, can impact the global ozone budget (Stjernberg et al., 2012). The Siberian forest was also shown to be an intense surface ozone sink during the TROICA experiments (Pankratova et al., 2011). The summer modelled forest deposition velocities agree with 10 year-long observations (2002-2012) taken from forest observations at Hyytiälä, Finland (61.9°N, 24.3°E), with June – August mean ozone deposition velocities between 0.4 – 0.5 cm s<sup>-1</sup> (Clifton et al., 2020).

Tundra is the second largest on-land surface by area in the modelled domain, and all tundra is located north of 60°N (Fig 5.15). Behind Siberian forest, tundra is the second most efficient land surface ozone sink across the 4 month period,

but has the highest single month deposition velocity at  $0.56 \text{ cm s}^{-1}$  (Table 4.3). Van Dam et al. (2016) investigated ozone deposition to tundra at Toolik Lake, Alaska ( $68.6^\circ\text{N}$ ,  $149.6^\circ\text{W}$ ) during May – August 2011, the same study period as this Chapter. Their observations of ozone deposition velocities are lower than the modelled values here, at  $0.03 \text{ cm}^{-1}$  for May,  $0.12 \text{ cm}^{-1}$  for June,  $0.10 \text{ cm}^{-1}$  for July and  $0.08 \text{ cm}^{-1}$  for August. However, the likely influence from Toolik Lake, a 150 ha body of water, is highlighted as a reason for this. Ozone deposition velocities to water surfaces are significantly smaller than those to land (Wesely et al., 1981; Van Dam et al., 2016), as highlighted in Table 4.3. The July-August mean of  $0.51 \text{ cm s}^{-1}$  is also higher than historical observations of ozone deposition velocities taken over Arctic Tundra in Alaska ( $61.1^\circ\text{N}$ ,  $162.0^\circ\text{W}$ ) of  $0.30 \text{ cm s}^{-1}$  for July-August 1988 (Jacob, 1992).

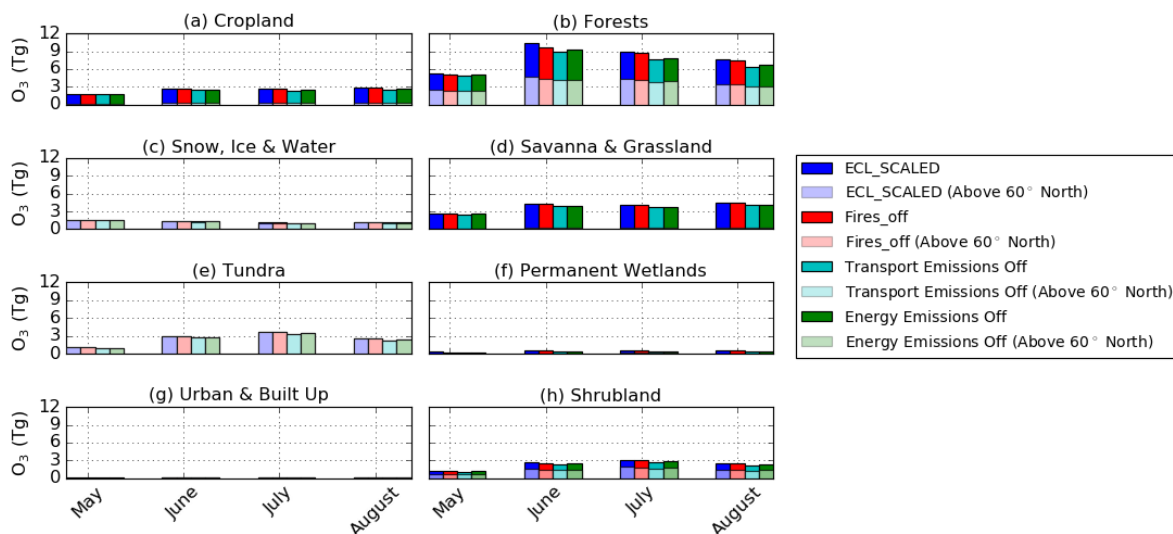


**Figure 5.16** - Quantity of ozone deposited to modified IGBP MODIS NOAH land surface cover categories per month for total domain (solid bars) and for the section of the domain north of  $60^\circ\text{N}$  (pale bars).

The largest deposition sink for ozone in the model domain is to forest vegetation, averaging 8.0 Tg of ozone deposition per month in the control simulation, peaking at 10.3 Tg of ozone deposition during June (Fig. 5.16b). Forest covers

29% of the domain, spanning large areas both north and south 60°N. For the total domain, “cropland” and “savanna & grassland” surface types account for an average of 2.5 and 3.9 Tg/month of ozone loss, respectively. North of 60°N, forest and tundra are the dominant sinks, which account for 65% of dry deposition flux, and 77% of the terrestrial surface cover at these latitudes.

Ozone deposition flux responds most in the trans\_off and ene\_off simulations, in particular during July and August. Deposited ozone reduces by 12% over forests when anthropogenic energy emissions are removed during August, and by 16% when anthropogenic transport emissions are removed during August. The impact of fires on ozone dry deposition within the domain is small compared to anthropogenic emissions, and is negligible north of 60°N. The greatest impact of the fires\_off simulation on ozone deposition occurs during May and June, with the largest percentage change for forest land cover (May: 4%, June: 6%).

Deposited ozone to croplands in the trans\_off simulation reduces by 10% in June and 13% in July (Fig. 5.16a). Ozone is known to have harmful effects on croplands, irreversibly damaging plant tissues resulting in a reduction of crop yields and forest growth (Fitzky et al., 2019). Enhanced levels of ozone can cause stomatal closure, hinder photosynthesis through chlorophyll degradation (Fuhrer, 2009), effect leaf area index and impact crop mass and number (Ainsworth, 2008). Croplands located at high latitudes are potentially at a greater risk due to significant lengths of sunlight during summer allowing for large periods of stomatal gas exchange, leading to a large cumulative ozone uptake (Karlsson et al., 2007). This is likely to be exacerbated by increasing future ozone concentrations at high latitudes, and an earlier start of the growing season (Karlsson et al., 2007).

## 5.5 Summary

The results presented in this Chapter suggest that Western Siberian ozone is influenced by an interplay between seasonality in atmospheric transport patterns, vegetation dry deposition uptake and photochemistry. WRF-Chem does not capture the low surface ozone concentrations and has a positive bias at all observation sites (Fig. 5.2 & 5.3). At the remotely located Tiksi, the model does not capture the likely ozone depletion event where daily mean surface ozone concentrations reach 1.6 ppbv. This model overestimation is likely due to poor representation of halogen chemistry within WRF-Chem, which is responsible for springtime ozone depletion events in the Arctic (Marelle et al., 2017). WRF-Chem also has a positive bias at ZOTTO, the observational site located within the Siberian forest, which suggests the model does not fully capture the magnitude of the Siberian forest, a significant surface ozone sink (Stjernberg et al., 2012).

WRF-Chem surface ozone is insensitive to differing anthropogenic emission inventories (Fig 5.3). Modelled surface ozone peaks in May (Fig 5.5a), which coincides with the well characterised Arctic haze (Stohl, 2006). This is associated with weak westerly flow north of 60°N in WRF-Chem during May (Fig5.4a), which limits the removal of ozone rich air. The transport and energy sector emissions have a more significant impact on surface ozone compared to fire emissions during the study period, with the relative importance of fire influence increasing south of 60°N (Fig. 5.6). During May, surface ozone is most sensitive to the energy sector, including north of 60°N, which is likely due to the inefficient removal of ozone sourced from oil and gas extraction and gas flaring activities. In the summer (June, July and August), surface ozone is most sensitive to transport emissions, which is supported by previous research highlighting the transport sector as the dominant sector for ozone precursor emissions (Ginzburg et al., 2020).

Vertical profiles of modelled physical and chemical tendencies for ozone show that above the boundary layer ozone is predominantly controlled by large scale

advection. Whilst near-surface ozone is influenced by an interplay between the vertical mixing down of ozone-rich air from above, and subsequent surface loss to NO ( $O_3 + NO$ ). This is in line with findings from the TROICA fieldwork campaign, which found evidence of mixing down and subsequent surface-based chemical loss of ozone in Siberia (Pankratova et al., 2011).

Siberian forests act as an important surface sink for ozone, especially during June, July and August when ozone surface fluxes are largest, and account for 37% of all ozone deposition in this period (Fig. 5.15 & 16). Throughout the study forest vegetation accounts for 8.0 Tg of ozone on average per month in the control simulation. Whilst north of 60°N tundra is an important sink alongside the Siberian forest.

With future northward migration of the treeline at high latitudes, gaining a greater understanding of how the Siberian forest could act as a sink for ozone in the future is important. However, with an increase in anthropogenic activity likely, and a continuing warming Arctic, coupled with continued long-range import of ozone precursor species, the ecology of the Siberian forest may change, impacting upon biogenic emissions and the Siberian forest as an efficient surface sink of ozone going forward. These changes could be of importance to the global ozone burden.

## **6. Physical and chemical controls of near-surface ozone in Fairbanks, Alaska.**

### **6.1 Introduction**

This chapter investigates tropospheric ozone in Fairbanks, Alaska, with a focus on better understanding the key drivers of change in near-surface ozone within the region. Fairbanks has had a long-term history of air quality research (Benson, 1965; Bowling, 1986). Frequent wintertime inversions have resulted in Fairbanks historically having serious and prolonged air quality problems, with the Environment Protection Agency (EPA) twice classifying the city as a serious nonattainment area due to continued exceedance of health standard limits (Alaska DEC, 2017; Alaska DEC, 2020). These persistent wintertime inversions act to trap pollutants near to the surface in the boundary layer, with no clear removal mechanism, causing stagnation and pollution build-up. This is exacerbated during the wintertime where there is a reliance on residential wood combustion and diesel generators for heating of homes (Ward et al., 2012). Wang and Hopke (2014) suggest that between 2005 - 2012 wintertime heating in Fairbanks was the key influence on air quality. At present, there are limited studies investigating air quality in Fairbanks, with most focusing on PM<sub>2.5</sub> source attribution due to the designation of Fairbanks and the nearby city of North Pole as a PM<sub>2.5</sub> nonattainment area in 2009 (Mölders and Kramm, 2010; Tran and Mölders, 2011; Ward et al., 2012; Ye and Wang, 2020). This has since been reclassified from “moderate” to “serious” nonattainment in 2017 (Ye and Wang, 2020).

At present, there is a lack of understanding regarding controls and behaviours of tropospheric ozone both at the surface and in the boundary layer in Fairbanks. Observations from a 2018 aircraft campaign across Alaska show that in Fairbanks ozone increases in the boundary layer during the day, whilst remaining at a near ~40 ppbv in the free troposphere. The aim of this Chapter is to first test multiple model setups to best simulate planetary boundary layer temperature as an indicator of boundary layer structure. Using this idealised

model setup I will then aim to gain a better understanding of the key physical and chemical drivers behind tropospheric ozone in Fairbanks at the surface and through the vertical column. Section 6.2 introduces the observational datasets used in this Chapter. Section 6.3 describes the model setup used in this Chapter. Section 6.4 discusses the main findings of this Chapter, whilst Section 6.5 summarises the key findings.

## 6.2 Observational Datasets

Fairbanks is situated in Interior Alaska, within a low-lying river valley, with incise topography typical of that associated with frequent and persistent temperature inversions (Ward et al., 2012). Due to Fairbanks being both far from the coast (~800km) and high in latitude (64.8°N), intense inversions can persist for long

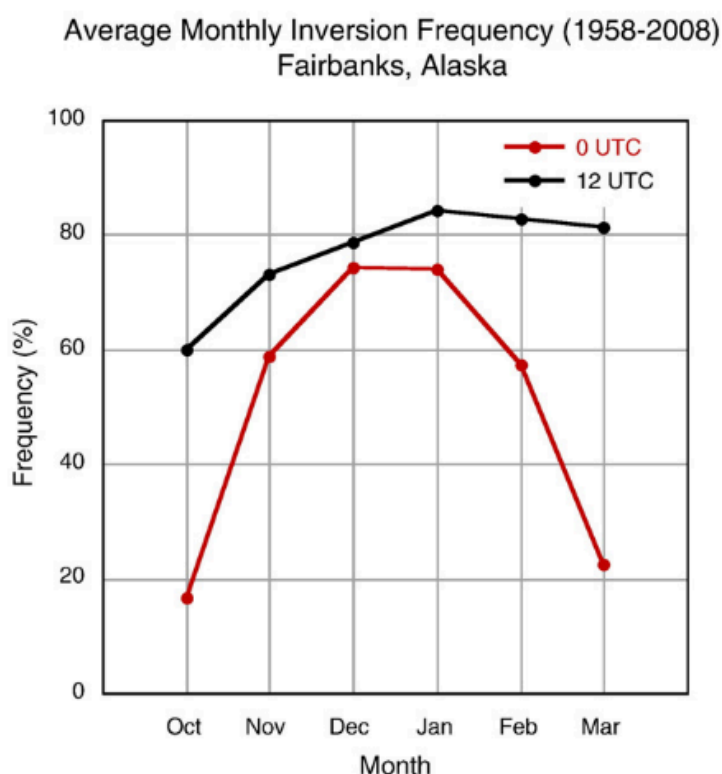


**Figure 6.1** - Surface-based temperature inversion frequency based on historic radiosonde data from Fairbanks, Alaska. The long-term mean frequency of temperature inversions shows the percentage of days with an inversion in a month. Radiosonde launches occur at 0000 UTC (1500 AST) and 1200 UTC (0300 AST). From Bourne et al., (2010).

periods of time (Tran and Mölders, 2011), due to stagnating weather systems. Based on historic radiosonde records from 1957-2008, Bourne et al., (2010) show that over Fairbanks during the coldest months (November – February), there is a semi-permanent surface based inversion, which on average is approximately 1000 – 1500m in height. Fig. 6.1 shows the frequency of temperature inversions by month for Fairbanks, demonstrating that typically during January – March, a temperature inversion is in-situ for more than 80% of the time at night (0300 Alaskan standard time (AST)). During December and January, daytime inversions (1500 AST) occur for more than 75% of the time, but there is a large drop off in daytime inversion frequency in February, and a further drop off in March. Bourne et al., (2010) attribute this daytime drop off in inversion frequency to a stronger diurnal cycle, promoting an increase in PBL mixing.

This Section introduces the different observation datasets used as model evaluation tools and the WRF-Chem setup.

### **6.2.1 Ground Observations**

Surface observations of both meteorological and pollutant variables are obtained from the National Core Network (NCore) station in Fairbanks, located at 64.8°N, -147.7°E. The monitoring station is situated in the grounds of the Fairbanks North Star Borough assessment building, located in the city centre. The NCore network is a United States Environmental Protection Agency (EPA) governed measurement system providing nationwide near real-time reporting of particulate matter, pollutant gases and meteorology which began in 2011 (EPA, 2011). These were downloaded at an hourly temporal scale for ozone (O<sub>3</sub>), nitric oxide (NO), nitrogen dioxide (NO<sub>2</sub>), and air temperature. Surface observational data is available upon request from <https://dec.alaska.gov/Applications/Air/airtoolsweb/Aq/Station/17>.

## 6.2.2 MACSSIMIZE Campaign

To attempt to address significant knowledge gaps in polar observational coverage and process understanding, the World Meteorological Organisation (WMO) initiated 2 major efforts to address the lagging forecasting capabilities at the poles (Goessling et al., 2016). These aimed to improve polar prediction for both the hourly-to-seasonal (Polar Prediction Project [PPP]) and seasonal-to-centennial (Polar Climate Predictability Initiative [PCPI]) time frames. To provide intensive observations, model simulations, predictions, verification, user engagement and educational activities, the Year of the Polar Prediction (YOPP) was established from mid-2017 to mid-2019 (Goessling et al., 2016). Within YOPP the 3-week measurement campaign titled Measurements of Arctic Clouds, Snow, and Sea Ice nearby the Marginal Ice Zone (MACSSIMIZE) was undertaken between 02/03/2018 – 28/03/2018 by the UK Met Office Facility for Airborne Atmospheric Measurements (FAAM) Bae146 aircraft. The aim of MACSSIMIZE was to (1) undertake snow emissivity measurements, (2) investigate boundary layer and energy balance measurements in both clear and cloudy skies, and (3) target orographic flows and their leeside impacts. These

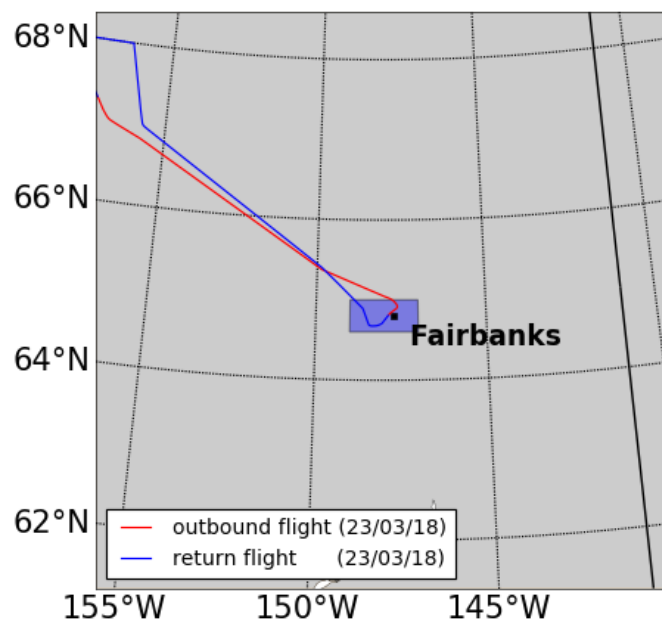


**Figure 6.2** - Example flight path for 23/03/18. Outbound flight shown in red, return flight shown in blue. Blue shaded area denotes nonattainment area.

flights were based out of Fairbanks, and would usually travel north spending varying amounts of time collecting measurements at different altitudes above different land surface types.

In this Chapter I use observations from flights where both air temperature and ozone (11<sup>th</sup>, 13<sup>th</sup>, 20<sup>th</sup>, 22<sup>nd</sup> and 23<sup>rd</sup>) were recorded. I use data from the aircraft when it is within the Fairbanks PM<sub>2.5</sub> nonattainment boundary, which is described in more detail in Section 6.3.2. The outbound and return flight paths are shown for an example day in Figure 6.2. All vertical profile information is stored at the CEDA archive: <https://catalogue.ceda.ac.uk/uuid/433c7351386c4a878fa05ca625126de3?jump=related-docs-anchor>.

### **6.2.3 Radiosonde Data**

Twice-daily radiosonde profiles were downloaded from the National Oceanic and Atmospheric Administration (NOAA) Integrated Global Radiosonde Archive (IGRA). These are available for 0300 and 1500 Alaskan Standard Time (GMT - 9) for air temperature. All radiosonde profiles are available to download from <https://ruc.noaa.gov/raobs/>.

## 6.3 WRF-Chem Setup

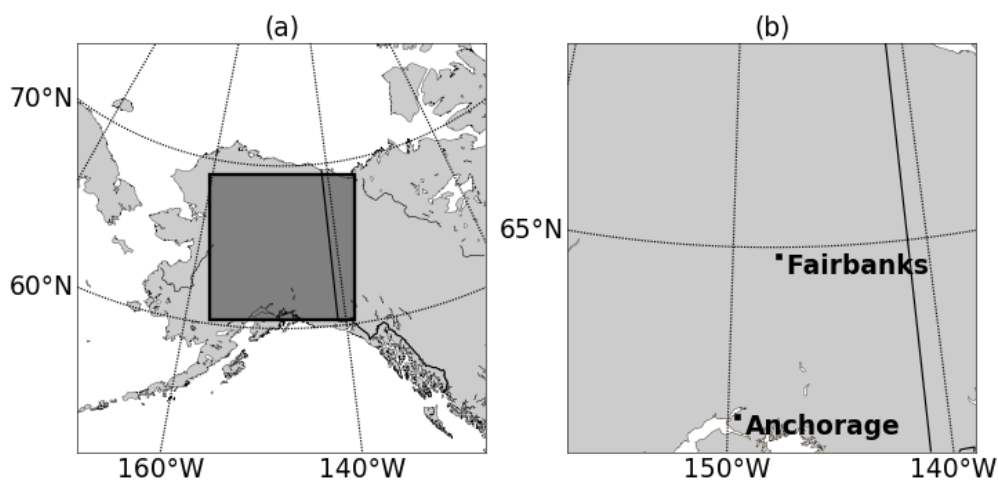


**Figure 6.3** – Panel (a) shows model domain in the context of Alaska and the surrounding area. Panel (b) shows the location of Fairbanks where the flight campaign is based, and the largest city in Alaska by population, Anchorage.

The WRF-Chem model setup is described in Chapter 3 in more detail. The model domain used in this Chapter is shown in Figure 6.3. The model setup in this Chapter differs to that used in Chapters 4 and 5, with the differences described here. In this chapter the model domain has a 10 km horizontal resolution, in a 100 x 100 cell grid encompassing Alaska. The model simulation period is from the 10/03/2018 – 31/03/2018, with a 2-week spin-up period. I use the same gas phase chemistry scheme (MOZART) and aerosol scheme (MOSAIC), but I also have aqueous chemistry included and extended treatment of organic aerosols (WRF-Chem Chem\_opt =202) (Hodzic and Knote, 2014). Chemical initial boundary conditions are taken from the Whole Atmosphere Climate Community Model (WACCM) (Marsh et al., 2013).

### 6.3.1 Anthropogenic Emissions

Historically, wintertime inversions have resulted in Fairbanks having serious and prolonged air quality problems, as anthropogenically-sourced pollution was

unable to leave the stable PBL. Due to an increase in automobile CO emissions during the 1990s, the Environmental Protection Agency (EPA) classified Fairbanks as a serious nonattainment area due to continued exceedance of the 8-hour CO health standard limit (Alaska DEC, 2017). This was successfully combatted through an improvement in automobile technology, which resulted in the removal of Fairbanks from the CO nonattainment list in the 2000s (Schmale et al., 2018). However, upon the change in EPA guidelines regarding fine particulate matter in 1997, Fairbanks has also more recently had severe issues with PM<sub>2.5</sub>, especially during the wintertime. PM<sub>2.5</sub> is detrimental to human health and associated with premature mortality (Lelieveld et al., 2015). Ward et al., (2012) attributed between 60-80% of all PM<sub>2.5</sub> during the 2008/09 – 2010/11 winters in Fairbanks to wood smoke, likely sourced from residential wood combustion. They also found contributions from other anthropogenic sources such as diesel exhausts (not detected – 10%), and automobiles (not detected – 7%). This is further supported by Wang and Hopke, (2014) who suggest that based upon compositional data from the EPA speciation network from 2005 – 2012, 40.5% of wintertime PM<sub>2.5</sub> is attributed to wood smoke. They suggest that wintertime heating in Fairbanks is the key influence on air quality. Subsequently this led to the designation of Fairbanks and the nearby city of North Pole as a PM<sub>2.5</sub> nonattainment area for exceeding the 24-hour PM<sub>2.5</sub> National Ambient Air Quality Standard (NAAQS) level (Alaska DEC, 2020).

Currently during the wintertime in Fairbanks there are significant emissions from traffic and other combustion sources (Tran and Mölders, 2011). In particular during the extended winter night time there is a reliance on fuel combustion (e.g. diesel generators and wood-burning stoves) for both residential heating and power supply. Further to this, people tend to use their car more frequently in colder temperatures.

Anthropogenic emissions used in this Chapter are from the Evaluating the Climate and Air Quality Impacts of Short-Lived Pollutants (ECLIPSE) version 6b anthropogenic emissions inventory (Klimont et al., in prep). These are the

newest iteration of emissions using the GAINS v4 model since the ECLIPSE v5a emission inventory, as described in Section 4.2.2. Improvements from ECLIPSE v5a include updated values for energy emissions from the International Energy Agency (IEA), additional data for mineral industries from the United States Geological Survey (USGS) and numerous updates for informal industries (e.g. brick making).

The ECLIPSE v6b anthropogenic emissions used are for the year 2015 at a resolution of  $0.5^\circ \times 0.5^\circ$ . This provides emissions for  $\text{SO}_2$ ,  $\text{NO}_x$ ,  $\text{NH}_3$ , NMVOC, BC, OC,  $\text{PM}_{2.5}$ ,  $\text{PM}_{10}$ , CO and  $\text{CH}_4$ , split into different anthropogenic sectors (agricultural waste burning, residential, energy, industry, transport, waste, solvent use, gas flaring and venting and shipping).

### **6.3.2 Socioeconomic Data and Application Center (SEDAC) Population**

#### **Data**

Due to the relative coarseness of the anthropogenic emission inventory ( $0.5^\circ \times 0.5^\circ$ ) and the scientific aims of this Chapter, I interpolate the ECLIPSE v6b emissions onto a population data grid from the Socioeconomic Data and Application Center (SEDAC) for the year 2015 at 10 km (CIESIN, 2018) to enable model simulations to be undertaken at a 10 km horizontal resolution. I use the Gridded Population of the World, Version 4 (GPW v4) population count which uses national census and population registration data to assign population data at 30 arc-second resolution ( $\sim 1$  km at equator), which is then aggregated to coarser resolutions. I interpolate all anthropogenic emissions within the Fairbanks  $\text{PM}_{2.5}$  nonattainment area (as described in Section 6.3.1) onto the GPW v4 grid at a 10 km horizontal resolution. Figure 6.4 shows the Fairbanks North Star Borough nonattainment area, and the approximate boundary used for the analysis in this Chapter.

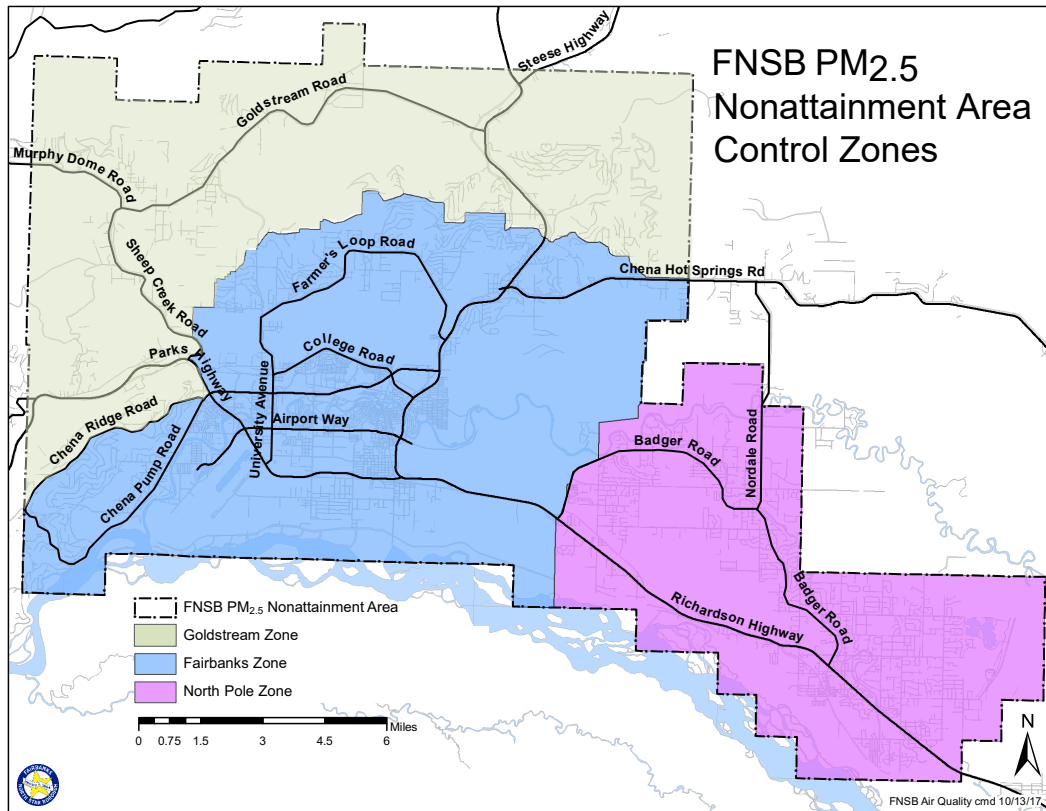


**Figure 6.4** – The Fairbanks North Star Borough region designated as a  $PM_{2.5}$  nonattainment zone in 2009 by the EPA, which includes the city of Fairbanks (Alaska DEC, 2020).

### 6.3.3 Planetary Boundary Layer Setups

To find the optimal planetary boundary layer (PBL) setup I compare 2 different PBL schemes commonly used in regional air quality model setups: the Mellor-Yamada-Nakanishi-Niino level 2.5 (MYNN2.5) (Nakanishi and Niino, 2004, 2009), and the Yonsei University (YSU) (Hong et al., 2006). The PBL layer is the turbulent layer that is in thermal contact with the surface. Having the best possible PBL setup is important, due to the relative importance the thermodynamic structure of the PBL can have on the vertical mixing of pollutants (Li et al., 2019). A stable boundary layer can lead to temperature inversions, minimal vertical mixing and potentially an accumulation of pollutants. Whereas an unstable boundary layer causes uniform mixing of pollutants in the PBL due

to convective turbulence and differing sizes of eddies (Barry and Chorley, 2010). Peckham et al., (2010) states that due to the potential large impact on model results a change in PBL scheme can cause, prior testing before research with WRF-Chem is advised.

The MYNN2.5 (hereafter “MYNN”) PBL is an improvement upon the Mellor-Yamada (MY) second-order turbulence closure model (Mellor and Yamada, 1974), which was commonly used to represent geophysical flows in numerical models (Nakanishi and Niino, 2004, 2009). The MY PBL was popular in part due to having a limited number of laboratory-measured constants and only one prognostic equation for the turbulent kinetic energy (TKE). Yet it provided reasonable second-order predictions and was not computationally expensive compared with other third-order turbulence closure models. (Mellor, 1973; Nakanishi and Niino, 2009; Yamada, 1977). Several improvements were made to the original model to address issues such as the slow growth of the convective boundary layer, and rapidly decaying turbulence in stable nocturnal boundary layers (Nakanishi and Niino, 2009). This improved model (renamed MYNN) has since been incorporated in multiple region-scale models, such as an operational weather prediction model at the Japan Meteorological Agency since 2007, and the WRF model.

On the other hand, the YSU is a non-local scheme, which explicitly calculates the TKE (Hong et al., 2006). This PBL scheme estimates the turbulent fluxes at particular points within the vertical column from the mean profiles of the entire domain of turbulent mixing. By accounting for both non-local mixing and the effect of significant eddies, the YSU scheme is often best used for simulations of convective and unstable PBLs (Misenis and Zhang, 2010).

I also implement different model meteorology nudging perturbations resulting in 6 unique PBL setups, as shown in table 6.1. More detail on nudging in WRF-Chem is given in Chapter 3. In this Chapter I investigate (1) the impacts of nudging throughout the entire vertical column, (2) nudging only above the PBL

and (3) no nudging (freerunning). In simulations that have nudging or partial nudging switched on, horizontal and vertical wind, potential temperature, and water vapour mixing ratio were nudged to GFS analysis on a 6 hourly basis using four-dimensional data assimilation (FDDA) (Deng et al., 2007). Nudging FDDA causes the model state to be relaxed towards the observed state at 6-hourly intervals.

**Table 6.4** - *WRF-Chem model setups describing 6 simulations using different PBL schemes and meteorological nudging options.*

<b>Model Simulation</b>	<b>Description</b>
MYNN	Simulation using the MYNN PBL scheme, with meteorological nudging throughout the entire vertical column.
MYNN FR	Simulation using the MYNN PBL scheme, with freerunning meteorology, and no nudging throughout the vertical column
MYNN FR-BL	Simulation using the MYNN PBL scheme, with freerunning meteorology within the PBL, and meteorological nudging above the PBL.
YSU	Simulation using the YSU PBL scheme, with meteorological nudging throughout the entire vertical column.
YSU FR	Simulation using the YSU PBL scheme, with freerunning meteorology, and no nudging throughout the vertical column

YSU FR-BL	Simulation using the YSU PBL scheme, with freerunning meteorology within the PBL, and meteorological nudging above the PBL.
-----------	---

## 6.4 Results

This section first introduces analysis on surface and vertical profiles of temperature based on the model setups described in Table 6.1 to determine the optimal setup for boundary layer temperature characteristics. Using this setup I then present results of analysis to better understand controls on ozone within the Fairbanks nonattainment area, as shown in Figure 6.4. Following this, I then test ozone sensitivity to (1) anthropogenic NO<sub>x</sub> emissions from within the domain, and (2) ozone values in the WACCM initial and chemical boundary conditions.

### 6.4.1 Model Air Temperature Evaluation

#### 6.4.1.1 Ground Observation Comparisons

Simulations where meteorological nudging takes place throughout the entire column show better agreement with observations and capture the diurnal pattern more effectively, when compared to simulations with partial or no meteorological nudging (Fig 6.5). The surface observations show a distinct change from 22/03/18 onwards, where a distinct diurnal cycle develops, which all model simulations replicate, but only the MYNN and YSU simulations capture the diurnal cycle well. During the period up to the 22/03/18 model simulations which have partial or no meteorological nudging tend to underestimate the night time temperature, this especially the case in the freerunning boundary layer simulations (MYNN FR-BL and YSU FR-BL). These findings match those of Mölders and Kramm, (2010) who showed that near surface air temperature simulations using WRF in Interior Alaska can differ significantly depending on physical packages chosen in the model setup. They found that WRF captured the temporal evolution of near surface air temperatures with sufficient accuracy, however during periods of intense temperature inversions, the model could not capture the full strength of the inversion. Mölders and Kramm, (2010) attribute this failure to capture intense inversions down to WRF's inability to simulate weather events in which extremely stable stratification occurs. Further to this, Mölders et al., (2011) found that when using WRF-Chem to simulate boundary layer characteristics in Interior Alaska the model did an acceptable job at

capturing moderate cold conditions, but could not recreate strongly stable stratifications events. Being able to capture these events is important, due to the degradation of localised air quality during such times, therefore of greatest interest to potential future emission-reduction strategies.

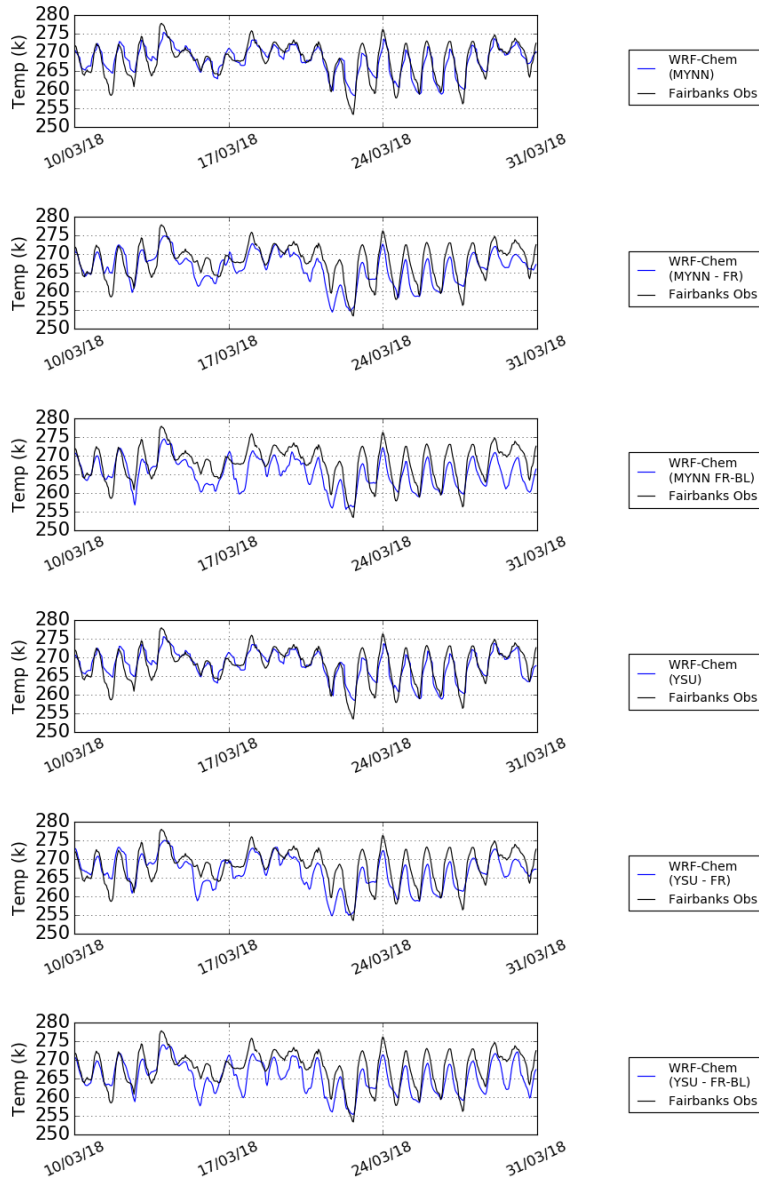


**Figure 6.5** – Time series plots showing model and observation air temperature comparisons at the NCore site in downtown Fairbanks for 10/03/18 – 31/03/18. Comparisons shown for model PBL setups described in Table 6.1.

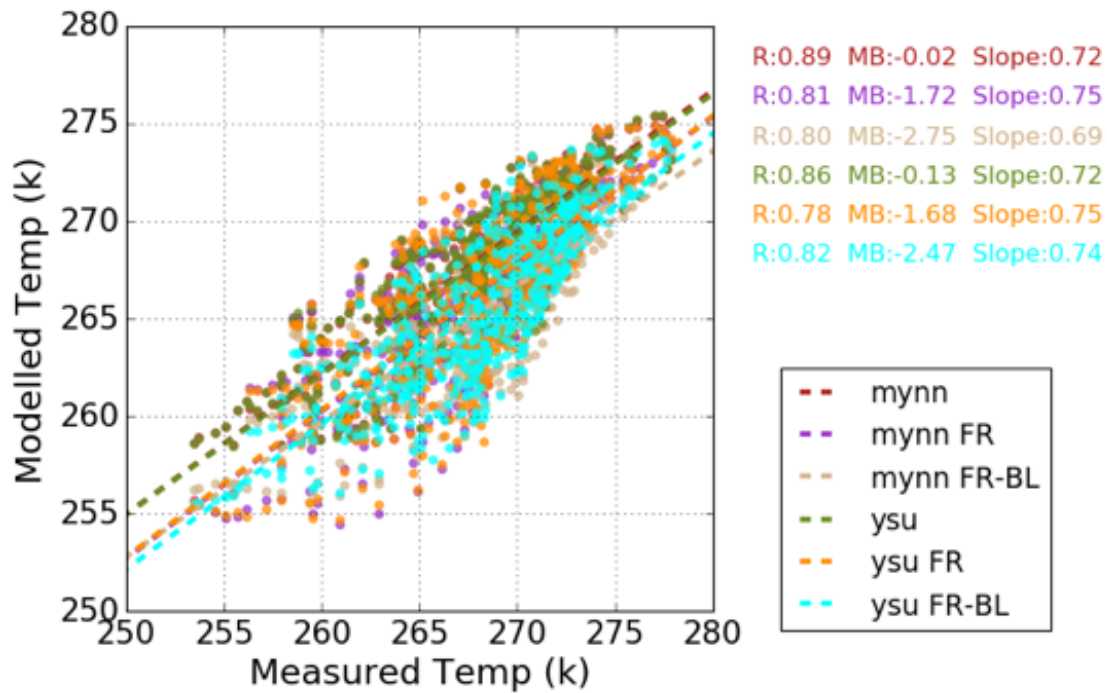


**Figure 6.6** – Scatter plot showing model and observation air temperature comparisons at the NCore site in downtown Fairbanks for 10/03/18 – 31/03/18. Comparisons shown for model PBL setups described in Table 6.1. Values shown for correlation coefficient ( $R$ ), mean bias ( $MB$ ) and slope.

Correlation coefficient values for each of the 6 model setups show that the MYNN and YSU simulations have a better agreement with observations of surface air temperature than those with partial or no meteorological nudging (Fig. 6.6). For the simulations using the MYNN PBL, the simulations with partial or no meteorological nudging have the poorest agreement with observations ( $R=0.8$ ), which is seen in the underestimation shown in Figure 6.5 for these 2 simulations. These simulations also have greatest mean bias values, showing model underestimation across the study period using these PBL setups. The model simulation using MYNN PBL with nudging through the column show the greatest correlation coefficient, and the smallest difference in mean bias out of all the model setups.

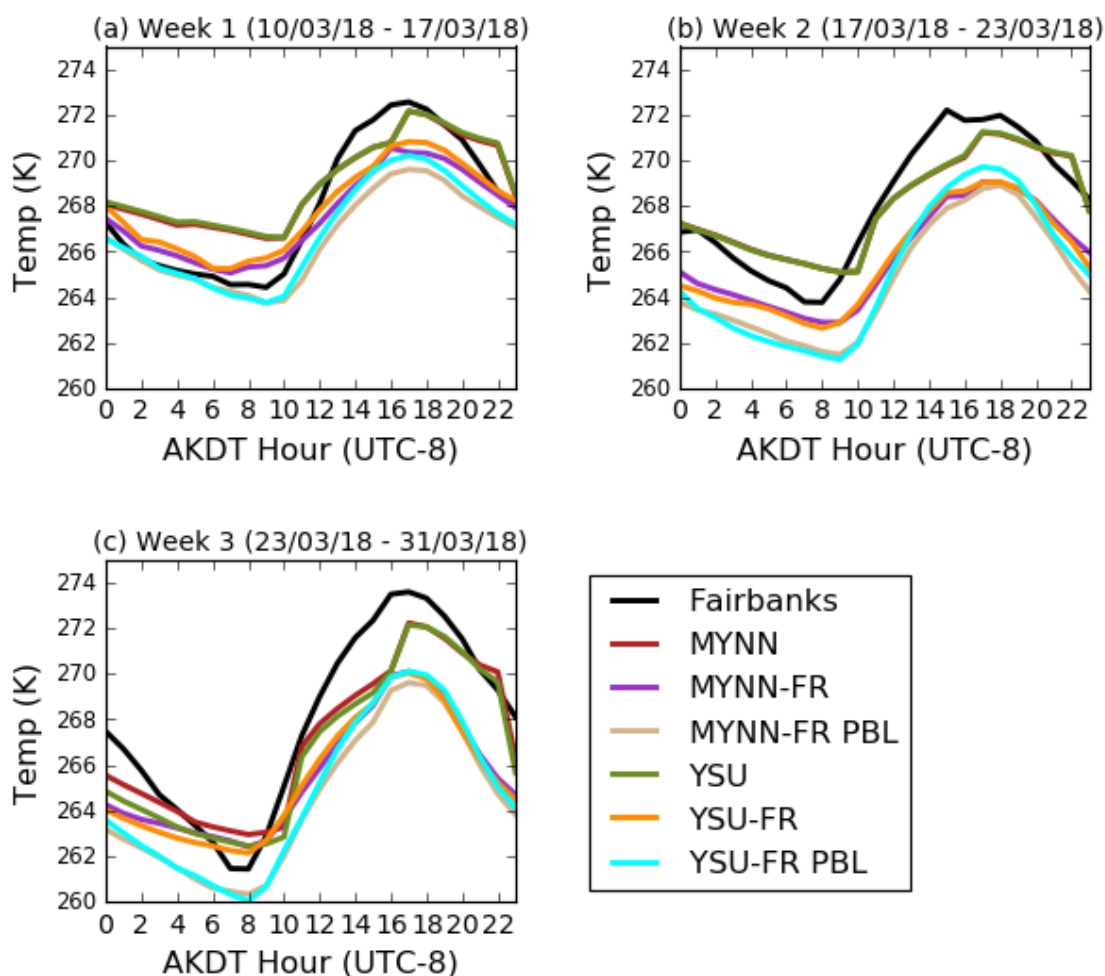


**Figure 6.7** – Weekly plots of simulated and observed surface air temperature diurnal cycles at the NCore site in downtown Fairbanks for: 10/03/18 – 16/03/18 (Week 1), 17/03/18 – 22/03/18 (Week 2) and 23/03/18 (Week 3).

To better understand the temporal evolution of surface air temperature, weekly mean diurnal plots are shown in Figure 6.7. Overall across the 3 weeks, all model simulations tend to underestimate the diurnal cycle of air temperature in Downtown Fairbanks. This is especially the case in both the YSU FR-BL and the MYNN FR-BL simulations. The simulations using meteorological nudging throughout the column (MYNN and YSU), performs best. However, both these model setups neither capture the night time low, or the day time high temperatures in any of the 3 weeks. This matches the findings of Mölders and

Kramm, (2010) who found that WRF captured the general temporal evolution of near-surface air temperature in Interior Alaska. They also found that changing the physics options in the model made little change to the temperature profile shape, but did cause the magnitude of the modelled temperatures to change. They stress the importance of capturing the total range of the diurnal cycle, due to the link between extreme cold temperatures, temperature inversions and the subsequent trapping of air pollutants (Mölders and Kramm, 2010).

### 4.1.2 Radiosonde Comparisons

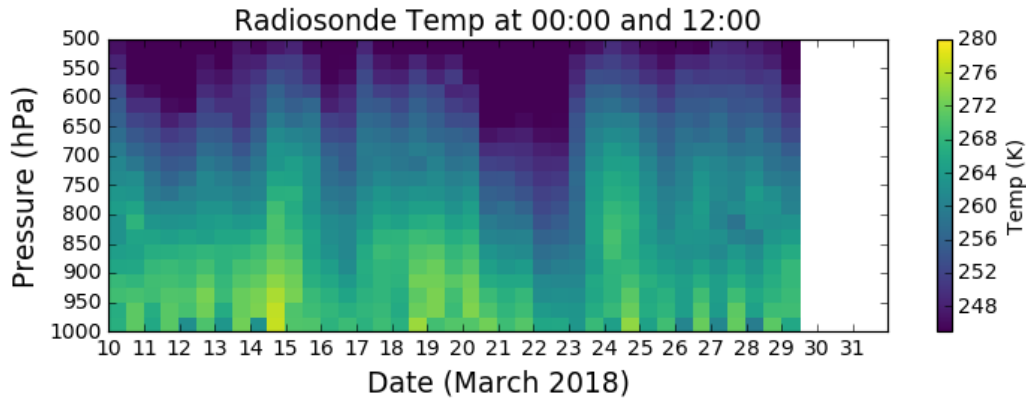


**Figure 6.8** – Vertical profile plot showing radiosonde vertical profiles from 10/03/18 – 29/03/18. Twice-daily sondes shown are at 0300 and 1500 local time. First sonde shown on plot for each respective day is at 0300.

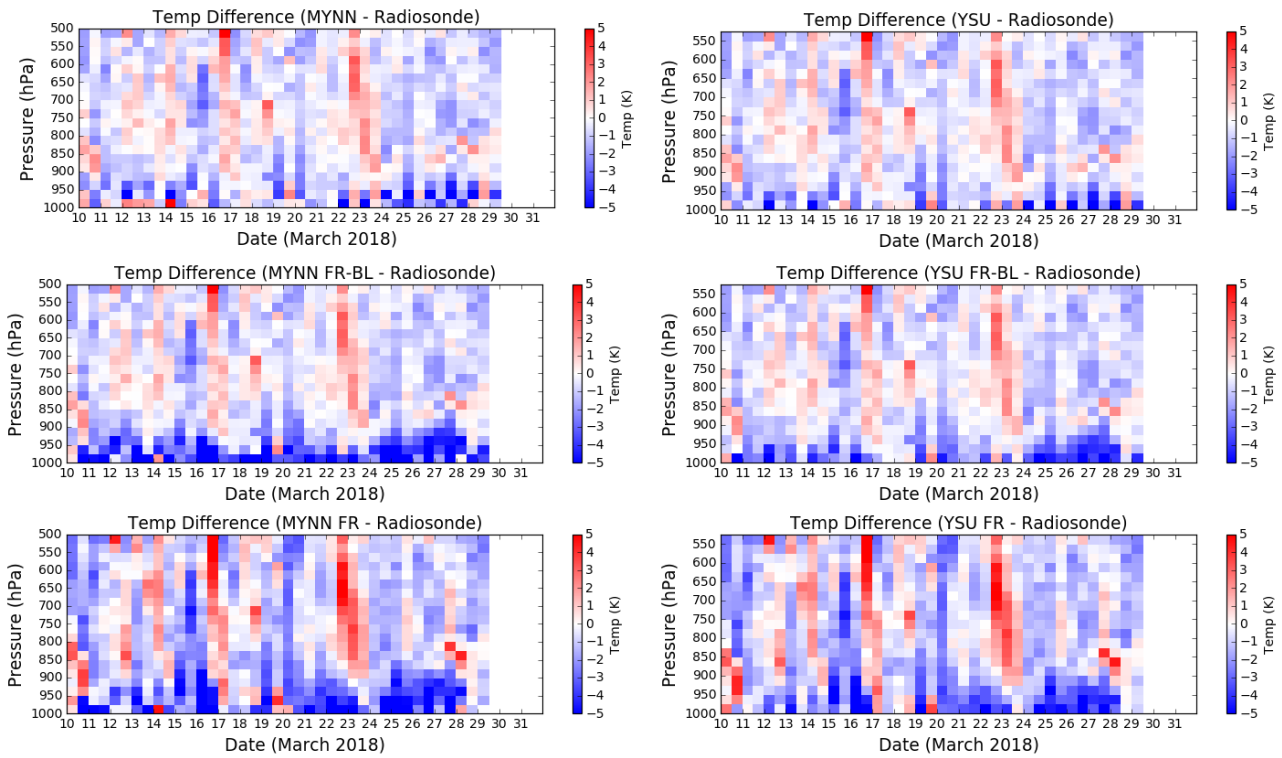


**Figure 6.9** – Mean bias plots showing vertical profiles from 10/03/18 – 29/03/18 for each model setup. Vertical plot shows model – observations at the same time as the radiosonde observations.

Vertical profiles of radiosonde observations released from Fairbanks show a distinct diurnal cycle from the 23/03/18 – 29/03/18 (Fig. 6.8), which matches that shown in the ground observations in Figure 6.5. Prior to this, an influx of colder air is observed between the 20/03/18 – 24/03/18 in the upper troposphere (750 – 500 hPa). Figure 6.9 shows the mean bias plots (model – observations) for the radiosonde observations, and the corresponding model output for that time. Depending on which model setup options are chosen, impacts the air temperature, especially close to the surface (surface – 900 hPa). Model simulations where meteorological nudging takes place throughout the vertical column, show the smallest air temperature bias close to the surface (Fig. 6.9). Greater model underestimations of air temperature occur when partial or no meteorological nudging takes place. The intrusion of cold air observed in Figure 6.8 is not captured by WRF-Chem, with a positive bias in all model simulations. This is likely due to WRF-Chem failing to capture fine spatial scale occurrences of cold air pooling, which could lead to the trapping and stagnation of cold air, which has been shown to be a feature in the incised topography of Fairbanks (Hartmann and Wendler, 2005). Localised cold air pools would be unlikely to be captured when using a 10 km horizontal modelled resolution. This bias is increased in both the MYNN and YSU simulations where there is no meteorological nudging present.

The diurnal cycle observed close to the surface is best recreated by WRF-Chem in the YSU standard simulation, with nudging throughout the vertical column. Despite this, all model setups underestimate air temperature, which matches findings from Mölders et al., (2011) who found WRF-Chem underestimated air temperature at Fairbanks. They suggest that this is likely due to evaporation from the Chena River which is unfrozen close to Fairbanks as a result of an influx of warm water from a nearby power plant. They also suggest that the coarseness of the meteorological data used in their study for initialisation could result in WRF-Chem failing to capture layers of moist air which in turn would influence air temperature.

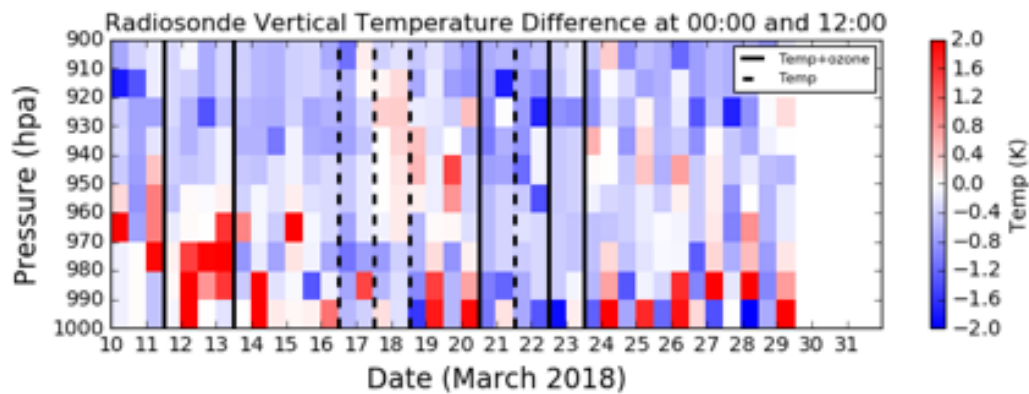


**Figure 6.10** – Contour plot showing radiosonde vertical temperature change from 10/03/18 – 29/03/18. Twice-daily sondes shown are at 0300 and 1500 local time. First sonde shown on plot for each respective day is at 0300. Red indicates an increase in temperature with elevation (temperature inversion occurring). Dashed lines are days where temperature observations are available and solid lines are where temperature and ozone observations are available.

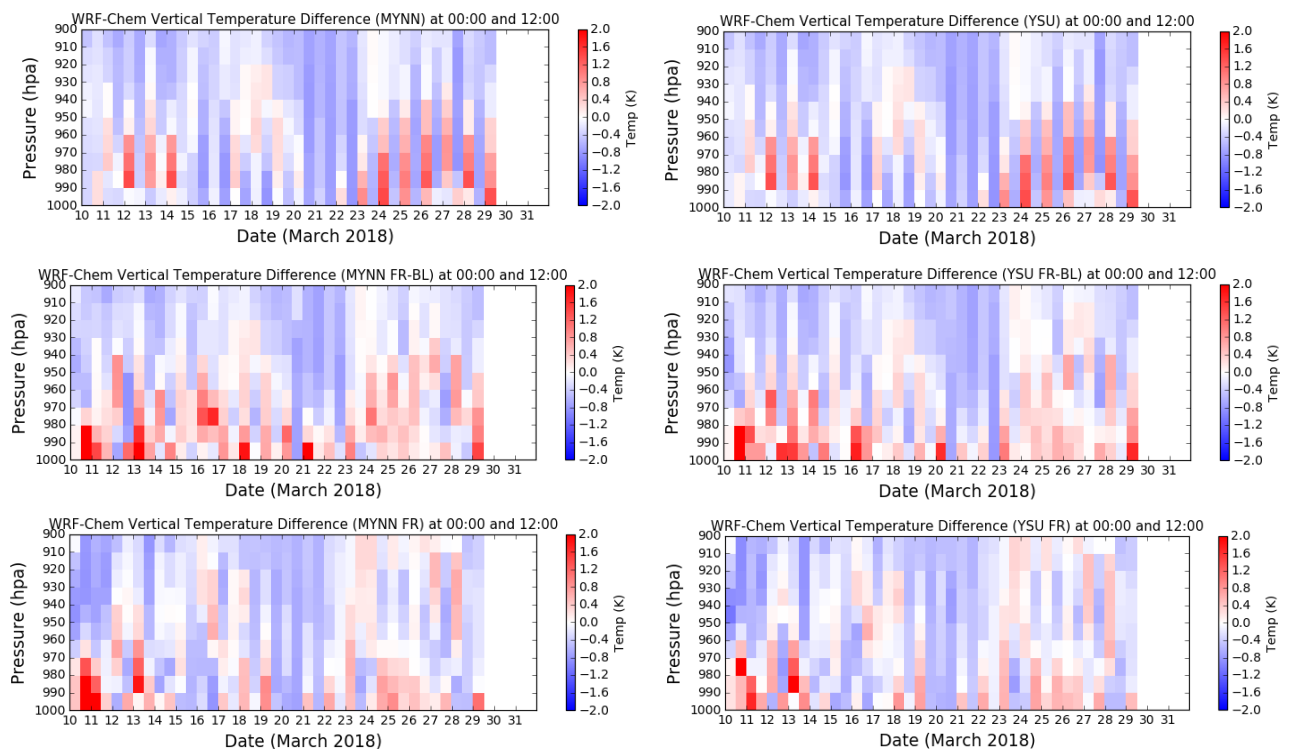


**Figure 6.11** – Mean bias plots showing vertical temperature change from 10/03/18 – 29/03/18 for each model setup. Contour plot shows model – observations at the same time as the radiosonde observations. Red indicates an increase in temperature with elevation.

In this Chapter a temperature inversion is defined as a temperature increase in altitude from the surface, with results from the surface to 900 hPa (~1000m) presented. A temperature inversion was observed on 12/20 (60%) of the nights between the 10/03/2018 – 30/03/2018 in the 3am (local time) radiosonde releases (Figure 6.10). On average, these extended to between 100-200m above the surface. Of the 12 inversions to occur during the study period, 10 are destroyed by the time the following afternoon radiosonde is released at 3pm. After the 24/03/2018 a clearer diurnal cycle appears where a temperature inversion occurs by 3am and is then destroyed by the afternoon, only for another inversion to occur the following night. This diurnal cycle is more typical for Fairbanks surface inversions at this time of year, with inversions occurring during 80% of the night (Bourne et al., 2010). During this period, when a surface-based inversion does not occur, elevated inversions slightly above the surface occur, which is very common during winter (Hartmann and Wendler, 2005). These persistent wintertime inversions usually occur under high pressure, which promotes slack winds and clear skies. In Fairbanks from mid-October to early May there is extensive snow-cover, which due a high surface albedo, acts to reflect shortwave radiation. This temperature-albedo feedback results in cooler temperatures close to the ground which promotes surface inversion growth (Tran and Mölders, 2011). In the winters of 2004-2009 there were 128 exceedances of the PM<sub>2.5</sub> 24 hr National Ambient Air Quality Standard (NAAQS), with all 128 exceedances associated with surface-based temperature inversions (Tran and Mölders, 2011).

All WRF-Chem simulations overestimate the occurrence of night time temperature inversions (MYNN: 14/20 (70%), MYNN FR-BL 16/20 (80%), MYNN FR 15/20 (75%), YSU 13/20 (65%), YSU FR-BL 18/20 (90%), YSU FR 13/20 (65%) (Figure 6.11). Despite this, the simulation using the YSU and YSU FR setups only simulates one more inversion, whilst the MYNN simulates 2 more inversions. These findings match those of Mölders et al., (2011) who found that overall, WRF-Chem captured the majority of the observed temperature inversions at Fairbanks. They suggest that some discrepancies between model and observed temperature inversions might be associated with model and

actual fine-scale topography. The simulations using partial nudging or no nudging cause surface inversions to persist longer and do not accurately recreate inversion daytime destruction. This is likely due to insufficient surface warming leading to near-surface mixing and subsequent dissipation of the any inversion. This is also seen in the modelled diurnal cycles (Fig. 6.7), where simulations using partial nudging or no nudging do not recreate daytime peak surface temperatures that are seen in the observations and the model simulations using nudging.

In both the MYNN and YSU simulations, the strong diurnal cycle seen in the observations is captured well, including the elevated inversions observed during the nights of the 27<sup>th</sup> and 28<sup>th</sup> (Fig. 6.11). The modelled inversion depth exceeds that in the observations, averaging 500m in both the MYNN and YSU simulations, compared to 225m in the observations for the period of 24/03/2018 – 30/03/2018. Mölders and Kramm, (2010) used the WRF model to investigate surface inversions in interior Alaska, and found that where the model sufficiently captured the diurnal cycle of surface temperature, in particular the total range of the cycle, the model would recreate the observed surface inversion. Figure 6.11c shows the week in which the more prominent diurnal cycle occurs, and the MYNN and YSU simulations almost capture the daytime peak, which likely allows for the destruction of the inversion, not captured by the other model setups.

6.4.1.3 Aircraft Vertical Profile Comparisons

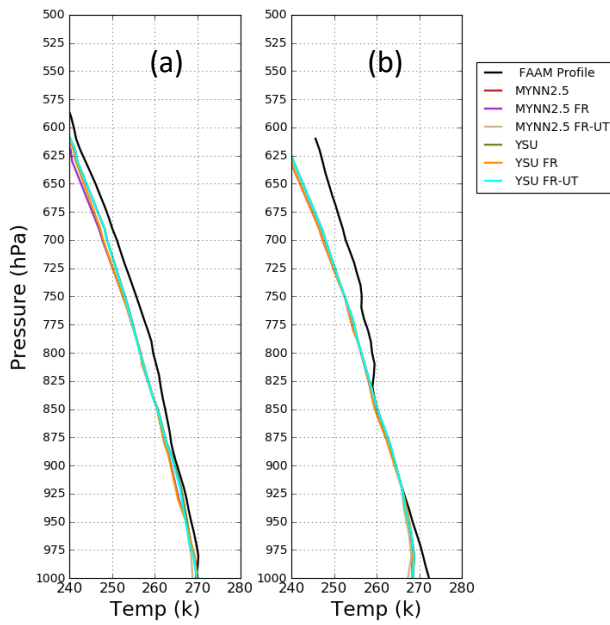


**Figure 6.12** – Comparison of simulated and observed vertical profiles from within the Fairbanks nonattainment area on the 11/03/18. Plot (a) shows the outbound flight, plot (b) shows return flight. Flight time is 1200 – 1645 local time.

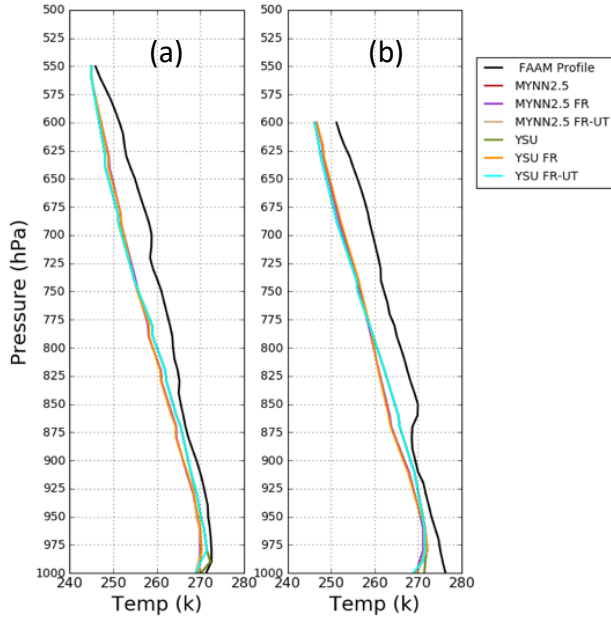


**Figure 6.13** – Comparison of simulated and observed vertical profiles from within the Fairbanks nonattainment area on the 13/03/18. Plot (a) shows the outbound flight, plot (b) shows return flight. Flight time is 1030 – 1530 local time.

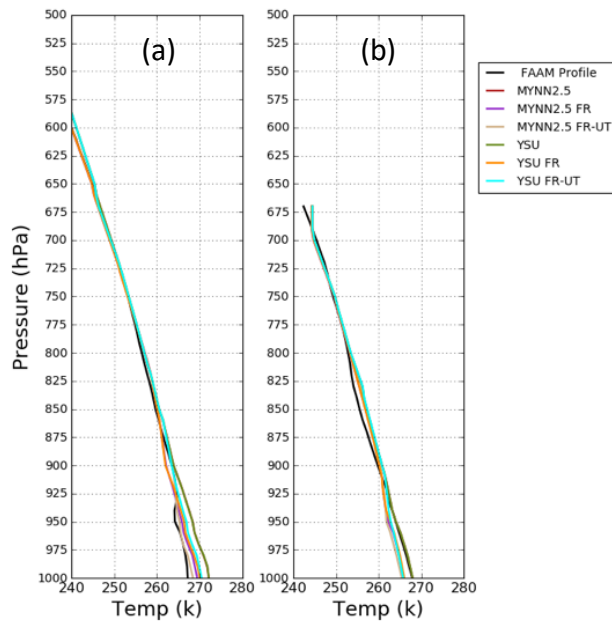


**Figure 6.14** – Comparison of simulated and observed vertical profiles from within the Fairbanks nonattainment area on the 20/03/18. Plot (a) shows the outbound flight, plot (b) shows return flight. Flight time is 1000 – 1535 local time.

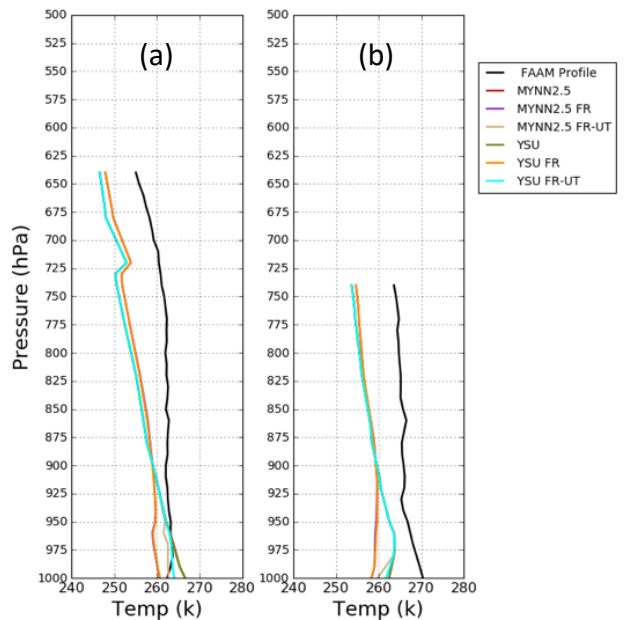


**Figure 6.15** – Comparison of simulated and observed vertical profiles from within the Fairbanks nonattainment area on the 22/03/18. Plot (a) shows the outbound flight, plot (b) shows return flight. Flight time is 1200 – 1730 local time.

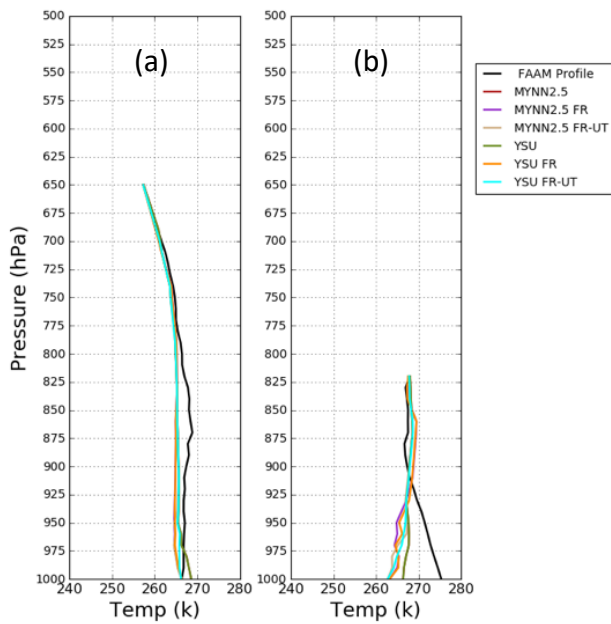


**Figure 6.16** – Comparison of simulated and observed vertical profiles from within the Fairbanks nonattainment area on the 23/03/18. Plot (a) shows the outbound flight, plot (b) shows return flight. Flight time is 1100 – 1630 local time.

Across the 5 flights from the MACSSIMIZE campaign where both ozone and temperature are recorded, WRF-Chem recreates the temperature profile on most days, but tends to underestimate air temperature on 3 out of the 5 flights (Fig. 6.12 – 6.16). This model underestimation using all model setups is greatest on the 22/03/2018, in particular on the return flight (Fig. 6.15). This could be to do with this being the latest return flight (1730 local time) and the model not capturing the daytime afternoon peak in temperature. All WRF-Chem simulations capture the outbound profile close to the surface, but do not capture the afternoon warming close to the surface in the aircraft observations.

#### 6.4.1.4 Overall Comparisons

**Table 6.2** – RMSE values shown for all model setup comparisons with observations presented in Section 6.4.1. Boxes coloured by RMSE value.

Ground Observations	2.00	3.91	3.20	2.29	3.61	3.39
Radiosonde	1.52	2.10	2.31	1.52	2.07	2.32
Flight - 11/03	3.90	3.88	4.21	3.90	3.98	4.12
Flight - 13/03	4.64	4.84	4.91	4.63	4.84	4.85
Flight - 16/03	3.74	4.16	4.50	3.74	3.86	4.46
Flight - 17/03	2.19	2.28	2.46	2.23	2.34	2.62
Flight - 18/03	1.85	1.58	2.31	1.86	1.67	2.29
Flight - 20/03	1.85	1.64	1.33	1.85	1.73	1.38
Flight - 21/03	4.18	3.91	3.55	3.83	3.66	3.11
Flight - 22/03	2.17	2.16	2.15	3.07	3.06	2.58
Flight - 23/03	1.90	2.52	2.60	1.96	2.39	2.51
Average	2.73	3.00	3.05	2.78	2.81	3.05
	MYNN	MYNN FR-PBL	MYNN FR	YSU	YSU FR-PBL	YSU FR

Based on the comparisons with all observations used in this Chapter and the 6 model setups, the WRF-Chem setup using the MYNN PBL and nudging throughout the entire column has the smallest error (MYNN RMSE: 2.73) (Table 6.2). The 2 simulations where entire column nudging takes place provide the smallest error when compared to partial or no meteorological nudging. RMSE values are calculated for all flights where temperature was recorded, not just the 5 days where temperature and ozone were recorded. The RMSE value incorporates both the outbound and return error in the overall value in Table 6.2. The model simulations and the flight on the 20/03/2018 provided the smallest average error between any observational dataset and model setups, where the

simulations with no meteorological nudging had the smallest error. The model simulations and the flight on the 13/03/2018 provided the greatest average error, which can be seen in Figure 6.13, where all model simulations underestimate the air temperature throughout the vertical column. Further to this, in the return flight the model does not accurately capture the increase in air temperature at the surface.

Based on the results presented in Table 6.2 the subsequent chemical analysis within this Chapter will be based on the MYNN setup with entire column nudging. This has shown to provide the smallest error when compared to an array of observational datasets for air temperature, which can act as a proxy for replicating the boundary layer. This simulation will be termed the control from this point forward in this Chapter. As this Chapter aims to better understand controls on ozone both at the surface and the vertical column, the following Sections include 2 sensitivity tests to understand the impacts that each has on the tropospheric ozone in WRF-Chem. Firstly the sensitivity to WACCM initial boundary conditions are investigated through a 20% reduction in WACCM ozone throughout the troposphere ( $IBC*0.8$ ). Secondly, the sensitivity to anthropogenically sourced  $NO_x$  is investigated, with a doubling of all anthropogenic  $NO_x$  from within the Fairbanks non-attainment area ( $NO_x*2$ ).

## 6.4.2 Model Surface NO Evaluation

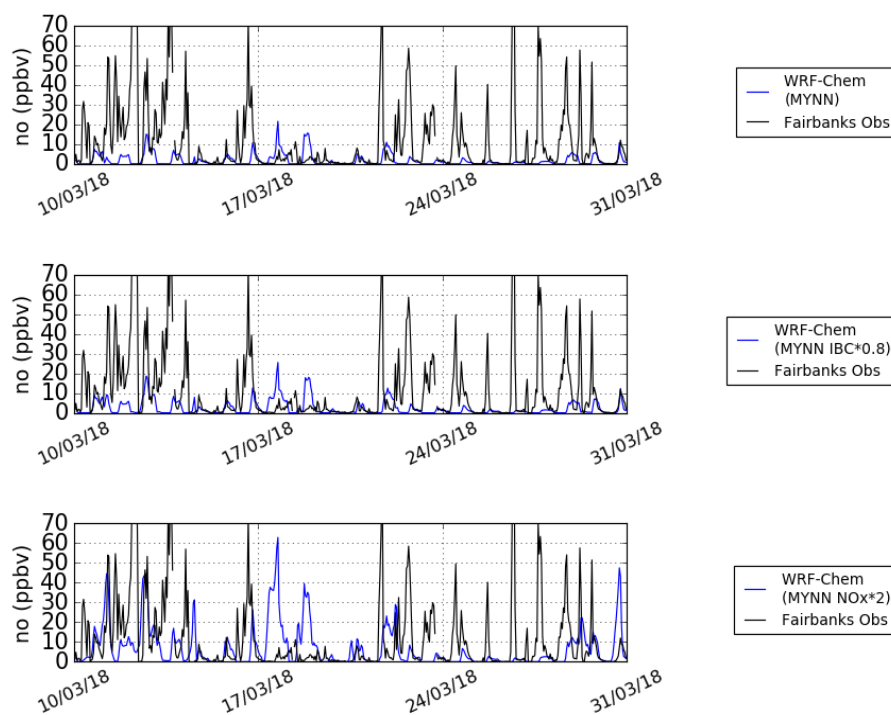


**Figure 6.17** - Time series plots showing model and observation NO comparisons at the NCore site in downtown Fairbanks for 10/03/18 – 31/03/18.

Modelled surface NO is underestimated throughout the study period in downtown Fairbanks for all model simulations (Fig. 6.17). In the control and IBC\*0.8 edit simulations, NO exceeds 20 ppbv once, whereas in the observations there are regular exceedances of 50 ppbv. In the model simulation with a doubling of anthropogenic NO<sub>x</sub> in the Fairbanks non-attainment area, there is an increase in surface NO, but there is still an underestimation when compared to the observed values. This is highlighted in the NO mean bias values in Figure 6.18 (control: -9.68; IBC\*0.8 edit: -9.08; NO<sub>x</sub>\*2: -4.45). Emmons et al., (2015) found that during the Polar Study using Aircraft, Remote Sensing, Surface Measurements and Models, of Climate, Chemistry, Aerosols and Transport (POLARCAT) Model Intercomparison Project (POLMIP) that

springtime NO is usually underestimated in models, which could be related to incorrect emission estimates. Ridley et al., (2000) attribute low NO<sub>x</sub> at the surface in the Arctic to chemical loss to reservoir species and subsequent dry deposition (e.g. HNO<sub>3</sub>), or transported out of the region in the gas phase (e.g. PAN). Enhanced surface ozone levels could also lead to ozone titration and removal of NO.

Liang et al., (2011) highlight the importance of correctly modelled values of NO<sub>y</sub> species (NO<sub>x</sub> + PAN + HNO<sub>3</sub>) in high-latitude air masses as well as stratospheric-tropospheric exchange rates, due to the influence that they can have on tropospheric Arctic ozone, NO<sub>x</sub> and PAN abundances at the surface.

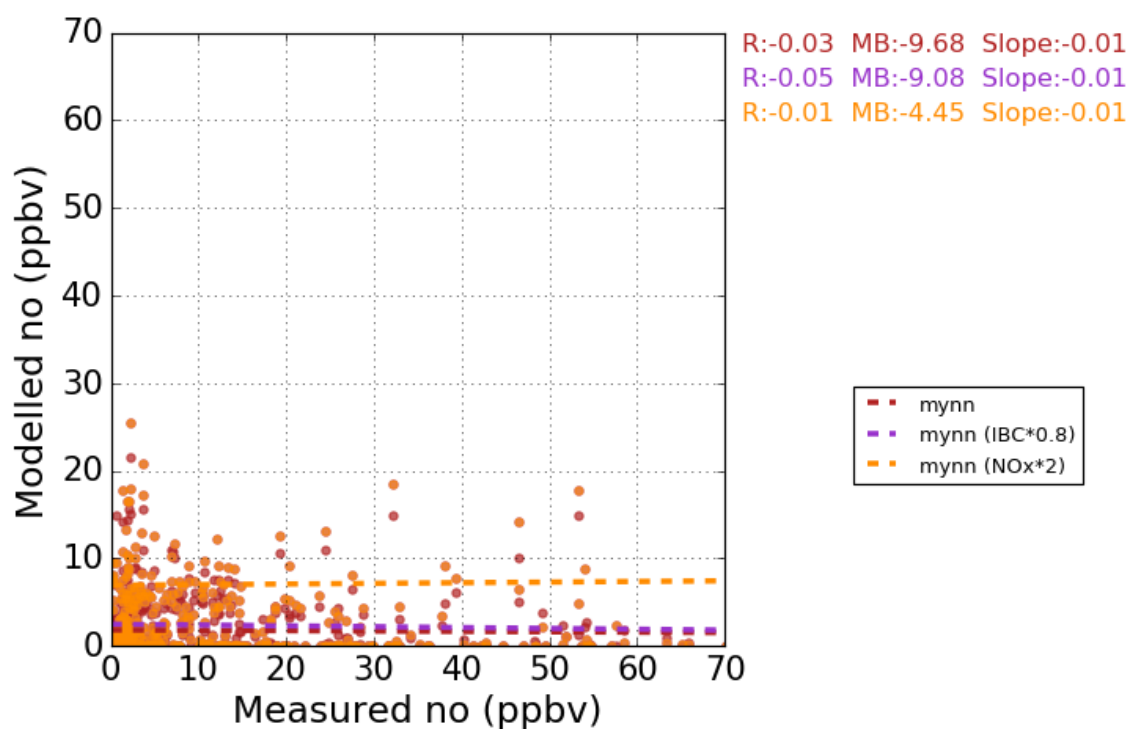


**Figure 6.18** - Scatter plot showing model and observation NO comparisons at the NCore site in downtown Fairbanks for 10/03/18 – 31/03/18. Values shown for correlation coefficient (*R*), mean bias (*MB*) and slope.

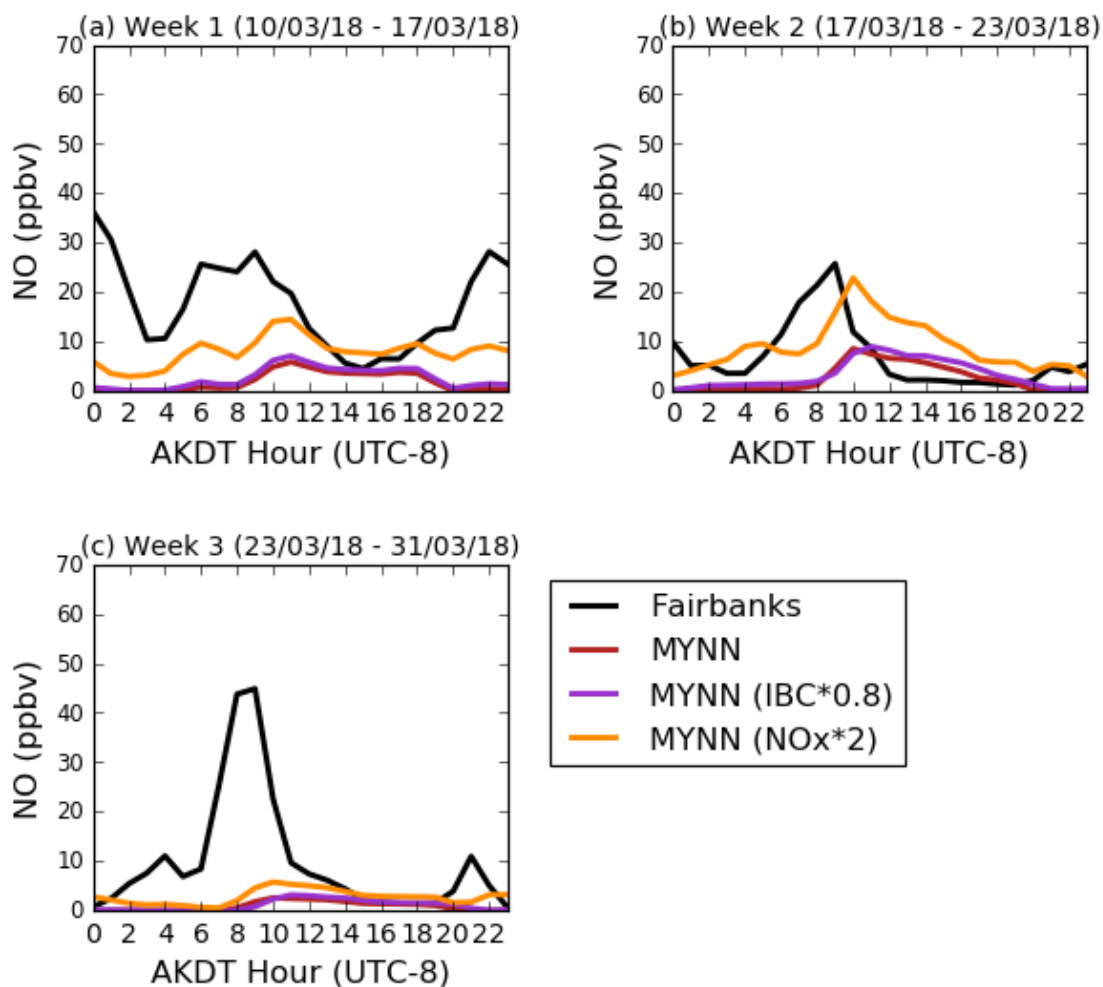


**Figure 6.19** - Weekly plots of simulated and observed surface NO diurnal cycles at the NCore site in downtown Fairbanks for: 10/03/18 – 16/03/18 (Week 1), 17/03/18 – 22/03/18 (Week 2) and 23/03/18 (Week 3).

Across the study period the WRF-Chem simulations partially capture the diurnal cycle of NO in downtown Fairbanks in the first two weeks, but do not capture the magnitude correctly. During the first 2 week period the models capture a morning peak in NO between 4am and 6am, likely associated with emissions from local transport. Week 3 shows a significant peak in NO values at approximately 8am. This coincides with the period of a more intense diurnal cycle of temperature inversions (Fig. 6.10), which could act to trap anthropogenically-sourced pollutants close to surface. This morning peak is not captured in any model setup.

### 6.4.3 Model Surface NO<sub>2</sub> Evaluation

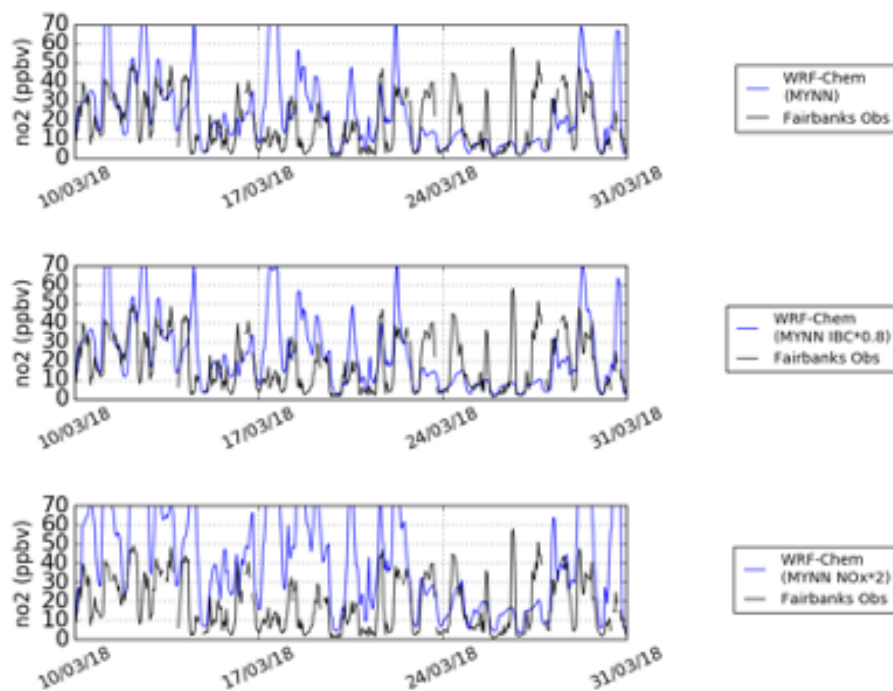


**Figure 6.20** - Time series plots showing model and observation NO<sub>2</sub> comparisons at the NCore site in downtown Fairbanks for 10/03/18 – 31/03/18.

All WRF-Chem simulations overestimates NO<sub>2</sub> in downtown Fairbanks, especially when anthropogenic NO<sub>x</sub> is doubled within the non-attainment area (Fig. 6.20 & 6.21). Overall in the control and IBC\*0.8 edit simulations, the model has a small overestimation (control MB: 4.96; IBC\*0.8 MB: 4.75), but a continued large spread of data when compared to the observations (control R: 0.39; IBC\*0.8 R: 0.37). The doubling of NO<sub>x</sub> lead to a large overestimation of surface NO<sub>2</sub> through the majority of the study period (NO<sub>x</sub>\*2.0 MB: 25.89) (Fig. 6.21). The final week of the study shows a diurnal pattern in terms of observed NO<sub>2</sub> in downtown Fairbanks, which corresponds to the period of temperature inversion-cycling seen in both the model and observations. Based on long-term analysis of controls on air quality in Fairbanks, it has been shown that NO<sub>2</sub> and air temperature at the surface are inversely correlated (Ye and Wang, 2020). This pattern of exceedances of 40 ppbv in surface NO<sub>2</sub> could, under the right

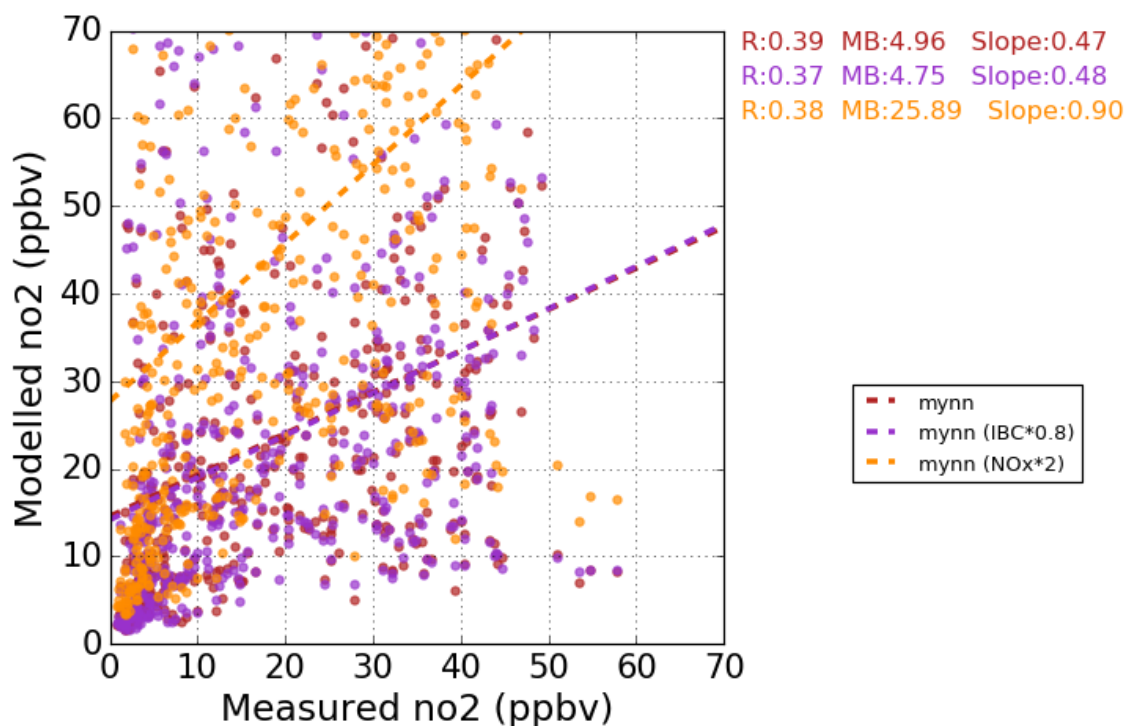


**Figure 6.21** - Scatter plot showing model and observation  $\text{NO}_2$  comparisons at the NCore site in downtown Fairbanks for 10/03/18 – 31/03/18. Values shown for correlation coefficient ( $R$ ), mean bias ( $MB$ ) and slope.

circumstances, lead to the formation of nitrate, and subsequently add to the  $\text{PM}_{2.5}$  concentrations near to the surface (Ye and Wang, 2020).

Across the entire study period the different model setups tend to capture the overall trend in the diurnal cycle of  $\text{NO}_2$  in downtown Fairbanks (Fig. 6.22). No model setup captures the morning correctly, with overestimations in weeks 1 and 2, and a morning underestimation in week 3. During weeks 1 and 3 the control and IBC\*0.8 simulations capture the afternoon low values seen in the observations, but overestimates this during week 2. There is a consistent over estimation during all weeks for the  $\text{NO}_x*2.0$  model simulation, but this overestimation is smaller during the final week. Joyce et al., (2014) used a 1-dimensional photochemical model to investigate  $\text{N}_2\text{O}_5$  reactions and sensitivities and found that in the Fairbanks area, appreciable amounts of the nitrate radical are formed due to the nocturnal oxidation of  $\text{NO}_2$  (Reaction 1.26, Chapter 3). This aligns with the findings of a previous study in Fairbanks, which measured  $\text{N}_2\text{O}_5$  in the nocturnal boundary layer (Ayers and Simpson, 2006).

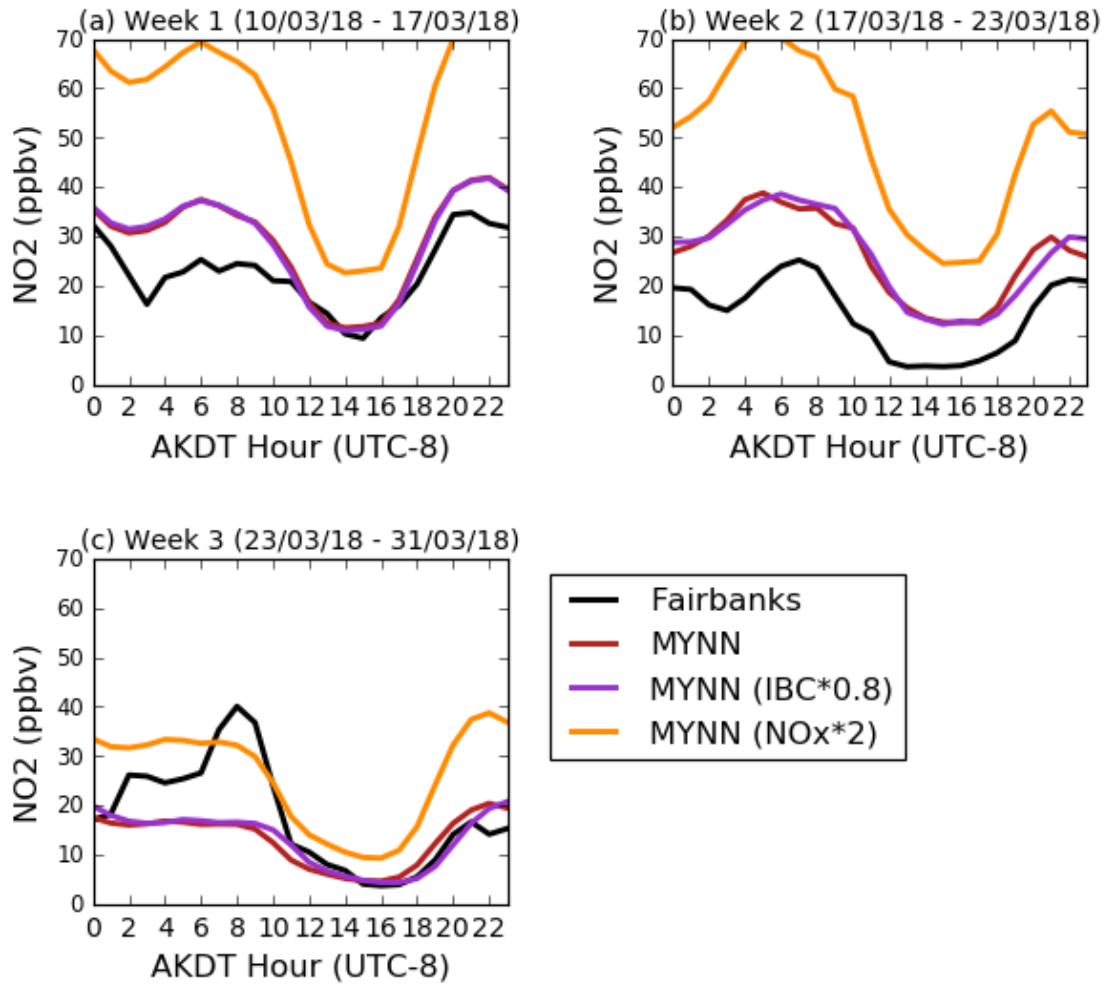


**Figure 6.22** - Weekly plots of simulated and observed surface NO<sub>2</sub> diurnal cycles at the NCore site in downtown Fairbanks for: 10/03/18 – 16/03/18 (Week 1), 17/03/18 – 22/03/18 (Week 2) and 23/03/18 (Week 3).

### 6.4.4 Model Surface NO<sub>x</sub> Evaluation

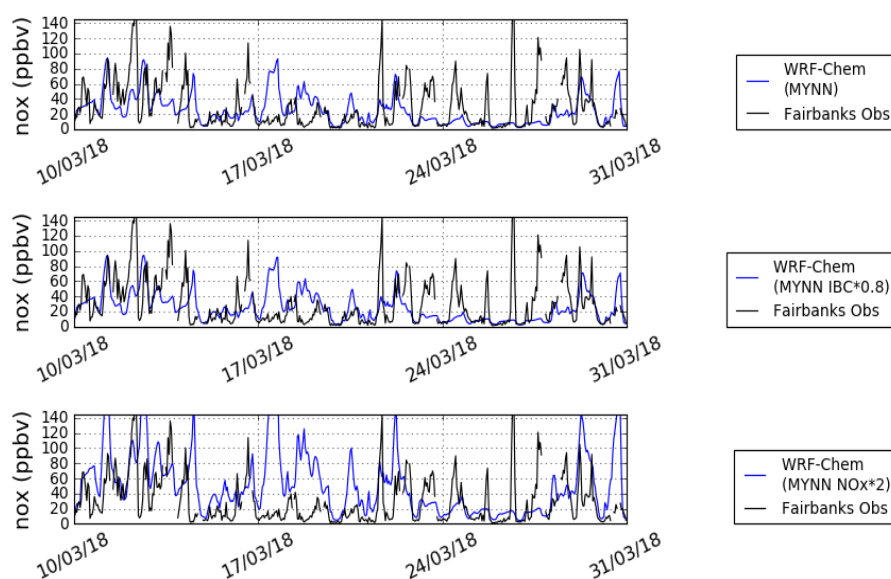


**Figure 6.23** - Time series plots showing model and observation NO<sub>x</sub> comparisons at the NCore site in downtown Fairbanks for 10/03/18 – 31/03/18.

WRF-Chem simulations using the control and IBC\*0.8 model setups underestimate surface NO<sub>x</sub> in downtown Fairbanks across the total study period (control MB: -4.72; IBC\*0.8 MB: -4.29) (Fig. 6.23 & 6.24). As seen in the previous result sections, this is likely due to significant underestimations in surface NO in the model. The WRF-Chem simulation using a doubling of anthropogenic NO<sub>x</sub> in the non-attainment area of Fairbanks leads to a large overestimation (NO<sub>x</sub>\*2 MB: 21.46). The low correlation coefficient for all 3 model simulations suggests that there is limited agreement between modelled and observed surface NO<sub>x</sub> values during the study period (control R: 0.25; IBC\*0.8 R: 0.25; NO<sub>x</sub>\*2 R: 0.25). Emmons et al., (2015) found discrepancies across the Arctic for different models suggesting that this is often caused by differences in chemistry and transport processes impacting on NO<sub>x</sub>.

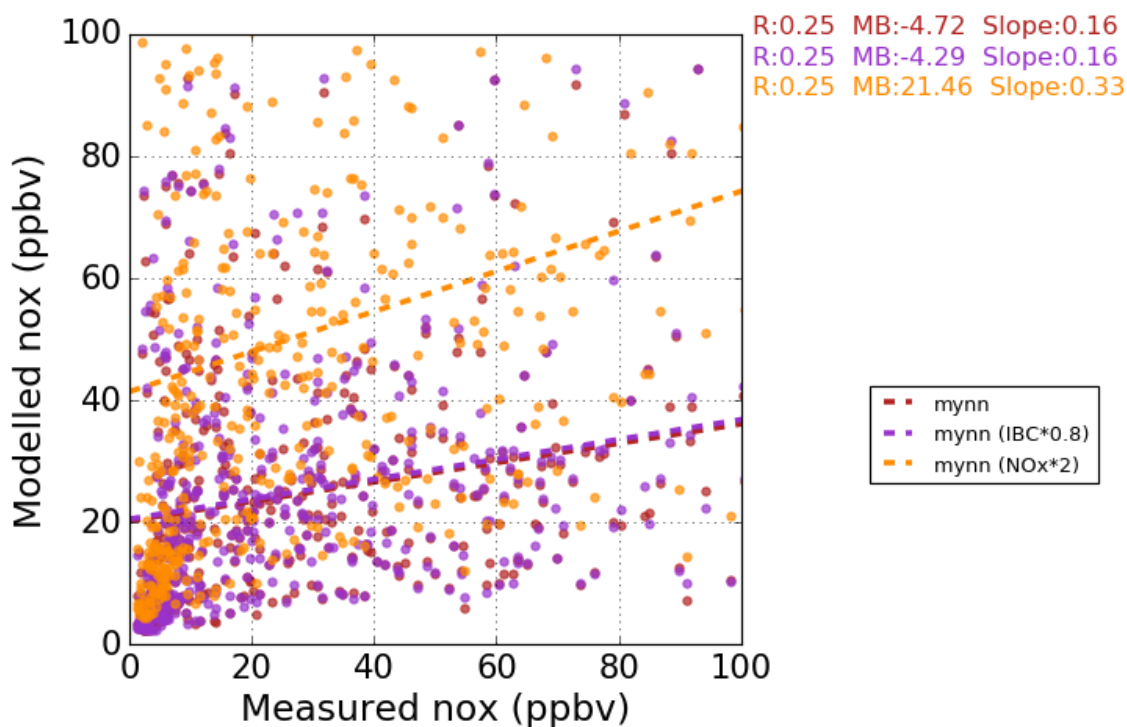


**Figure 6.24** - Scatter plot showing model and observation  $\text{NO}_x$  comparisons at the NCore site in downtown Fairbanks for 10/03/18 – 31/03/18. Values shown for correlation coefficient ( $R$ ), mean bias ( $MB$ ) and slope.

All WRF-Chem model simulations capture the diurnal cycle trend for surface  $\text{NO}_x$  in Fairbanks, with the control and IBC\*0.8 edit simulations capturing the magnitude for large portions of the day throughout the study period. As seen in the mean bias values in Figure 6.24, the  $\text{NO}_x*2$  edit overestimates the observed values at nearly all points of the day across the study period. The only point where observed values exceed the  $\text{NO}_x$  modelled estimate is between 8 and 9 am in week 3, which is associated with a peak in observed  $\text{NO}$ , which is not captured in any model setup.

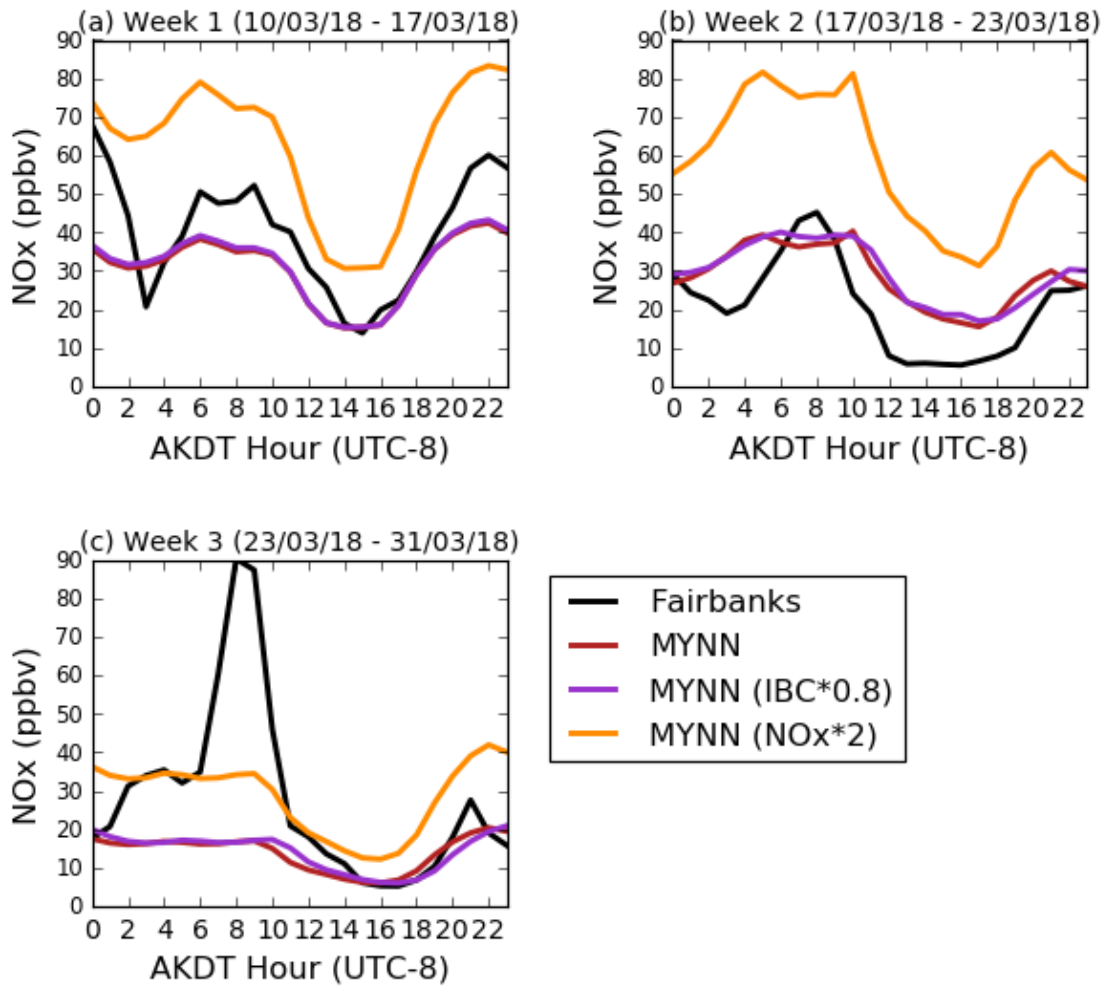


**Figure 6.25** - Weekly plots of simulated and observed surface NO<sub>x</sub> diurnal cycles at the NCore site in downtown Fairbanks for: 10/03/18 – 16/03/18 (Week 1), 17/03/18 – 22/03/18 (Week 2) and 23/03/18 (Week 3).

### 6.4.5 Model Surface Ozone Evaluation

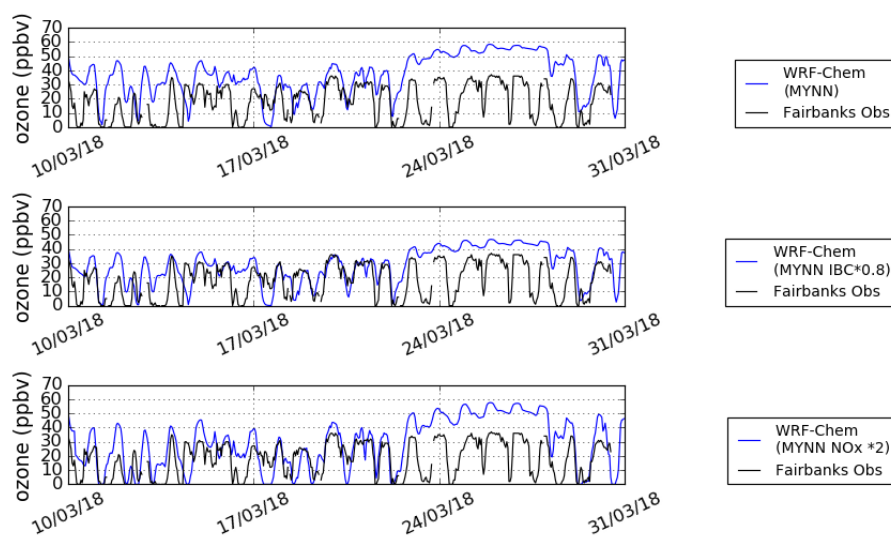


**Figure 6.26** - Time series plots showing model and observation ozone comparisons at the NCore site in downtown Fairbanks for 10/03/18 – 31/03/18.

WRF-Chem simulations overestimate modelled surface ozone in Fairbanks compared to observations (control MB: 18.93; IBC\*0.8 MB: 10.22; NO<sub>x</sub>\*0.8 MB: 11.34) (Fig. 6.26 & 6.27). The AMAP (2015) model intercomparison project found that a range of models show strong biases within the Arctic for both ozone and its precursors (Marelle et al., 2017). These are likely associated with a range of potential reasons, including uncertainties in emissions, transport of pollutants, inaccurate stratosphere-troposphere exchange rates and potential uncertainties relating to the OH radical.

During the first two weeks of the study period, all model setups follow a similar diurnal cycle to that of that observations (Fig. 6.26, Fig. 6.28a & b). However all model setups are unable to capture the majority of the diurnal cycle during the final week of the study period, where night time ozone fails to be removed (Fig.

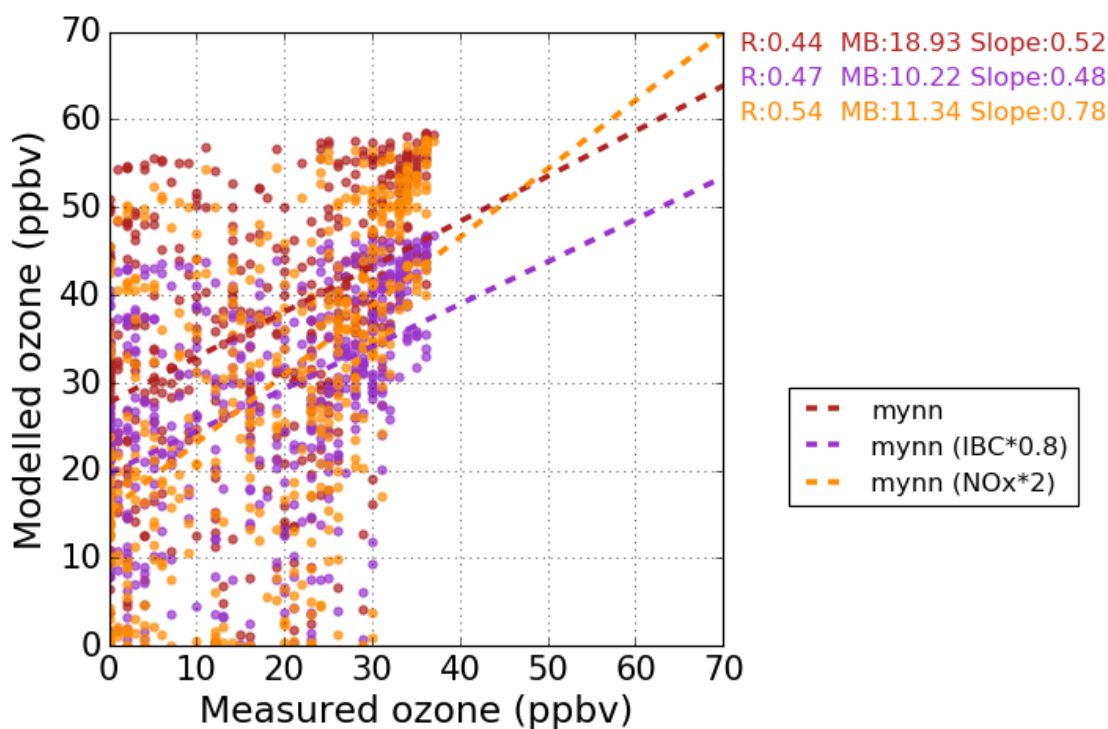


**Figure 6.27** - Scatter plot showing model and observation ozone comparisons at the NCore site in downtown Fairbanks for 10/03/18 – 31/03/18. Values shown for correlation coefficient ( $R$ ), mean bias ( $MB$ ) and slope.

6.28). This coincides with the period of more intense temperature inversions in the model (Fig. 6.11), suggesting modelled temperature inversions can lead to an increase in WRF-Chem surface ozone. These findings are supported by Hou and Wu (2016), who investigated the impacts of air pollution meteorology (temperature inversions and heatwaves) on ozone, and found temperature inversion-induced atmospheric stagnation to enhance the probability of a high ozone pollution event during spring. Similarly, previous studies have identified stagnation events, characterised by slack winds, no precipitation and boundary layer temperature inversions to lead to high ozone concentrations (Strode et al., 2015; Lu et al., 2019). Further to this, Schmale et al., (2018) stress the importance of accurately representing inversions within models in order to predict realistic ambient temperatures, which is important for certain high-latitude processes associated with air quality. Mölders et al., (2011) support this by demonstrating errors in WRF-Chem simulations over Fairbanks, due to an inability to accurately capture the full strength of multiple temperature inversions, resulting in model underestimations in nitrate and  $PM_{2.5}$ .

The simulation where anthropogenically-sourced  $\text{NO}_x$  is doubled ( $\text{NO}_x*2$ ) leads to an improved agreement with the observed values ( $\text{NO}_x*2$  R: 0.54), likely due to the increase of  $\text{NO} + \text{O}_3$  at the surface, which could partially account for the low values of  $\text{NO}$  (Fig. 6.17). However the  $\text{NO}_x*2$  edit does not capture the ozone diurnal cycle during the final week (Fig. 6.26 & 6.28), which coincides with  $\text{NO}$  values  $<5$  ppbv, even in the  $\text{NO}_x*2$  simulation. These high modelled ozone concentrations (24/03/18 – 28/03/18) could therefore be explained by less conversion of ozone by  $\text{NO}$  into  $\text{NO}_2$  in this period, which leads to high modelled surface ozone (Fig. 6.26) due to low levels of modelled  $\text{NO}$  (Fig. 6.17)

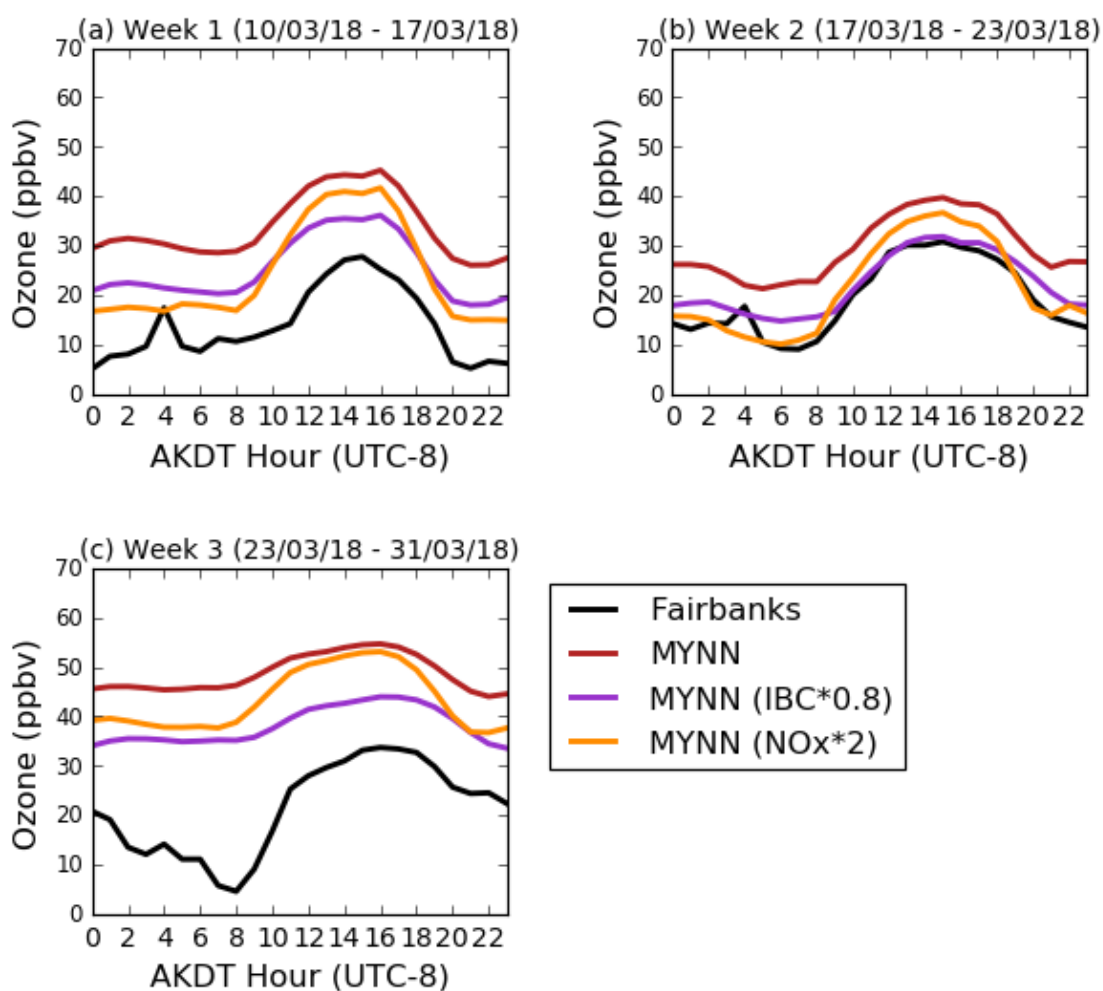


**Figure 6.28** - Weekly plots of simulated and observed surface ozone diurnal cycles at the NCore site in downtown Fairbanks for: 10/03/18 – 16/03/18 (Week 1), 17/03/18 – 22/03/18 (Week 2) and 23/03/18 (Week 3).

resulting in low levels of NO<sub>2</sub> (Fig. 6.20). This is described by Dumont (1996) as the “week-end effect”.

Previous studies looking at controls and distribution of surface-based ozone at high-latitudes are sparse, with most studies focussing on coastal observation sites such as Barrow and Tiksi, related to the impact of halogen chemistry (e.g. Simpson et al., 2007; Cao et al., 2016; Law et al., 2017; Marelle et al., 2017; Thompson et al., 2017).

### 6.4.6 Model Surface O<sub>x</sub> Evaluation

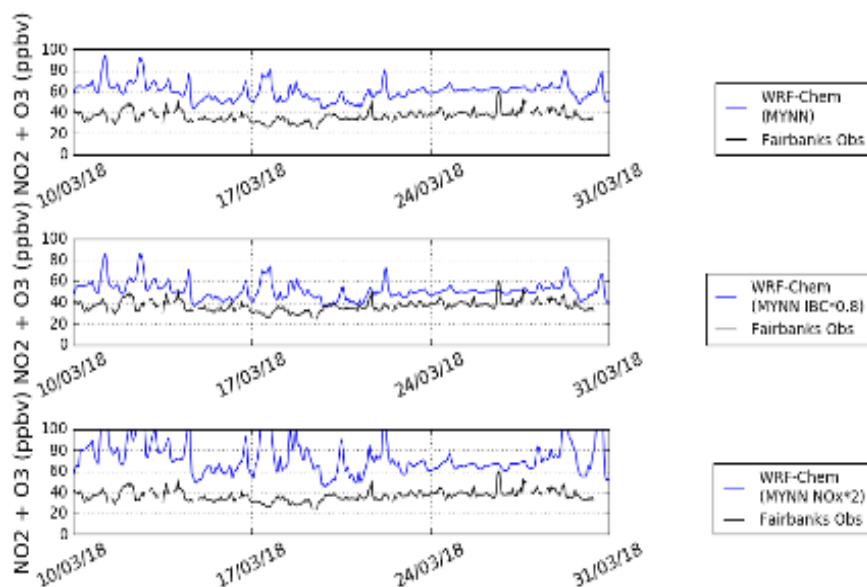


**Figure 6.29** - Time series plots showing model and observation O<sub>x</sub> comparisons at the NCore site in downtown Fairbanks for 10/03/18 – 31/03/18.

Due to the interplay between ozone, NO and NO<sub>2</sub> the term oxidant (O<sub>x</sub> = ozone + NO<sub>2</sub>) can be used to help gain insight into their chemical coupling (Kley et al., 1994; Notario et al., 2012). The concentration of O<sub>x</sub> is independent of the rapid photochemical reactions that convert ozone to NO<sub>2</sub> and vice-versa. This provides a better representation of ozone production, incorporating potential ozone production from NO<sub>2</sub> photolysis.

Modelled surface O<sub>x</sub> is consistently overestimated throughout the study period when compared to observations (control MB: 23.43; IBC\*0.8 MB: 14.61; NO<sub>x</sub>\*0.8 MB: 36.60) (Fig. 6.29 & 6.30). Scaling the initial boundary conditions (IBC\*0.8) lowers the mean bias, but there is still a 14.61 ppbv overestimation. As seen in Figure 6.26 and Figure 6.28, this scaling acts to improve the overall ozone model performance, but this does not impact the modelled surface NO<sub>2</sub> bias. This overall O<sub>x</sub> overestimation can be attributed to the modelled

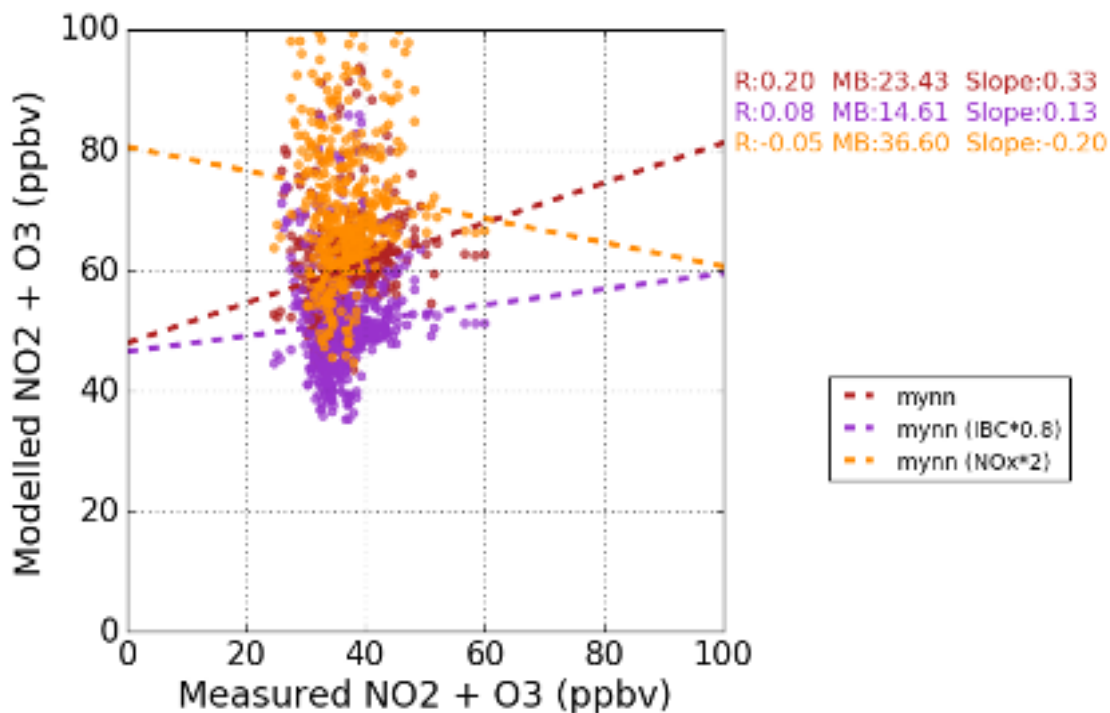


**Figure 6.30** - Scatter plot showing model and observation  $O_x$  comparisons at the NCore site in downtown Fairbanks for 10/03/18 – 31/03/18. Values shown for correlation coefficient ( $R$ ), mean bias ( $MB$ ) and slope.

simulations inability to accurately capture the diurnal cycle throughout the study period (Fig. 6.31). This is especially the case for the IBC\*0.8 and  $NO_x$ \*2 simulations during weeks 2 and 3, where they are unable to capture any diurnal cycle. For example, throughout the study period the observed surface  $O_x$  values tend to be between 20-30 ppbv at approximately 0300, and between 0-20 ppbv at approximately 1400 – 1600, but all model simulations are unable to accurately recreate this. This is supported by the low correlation coefficient values for all model setups (control  $R$ : 0.20; IBC\*0.8  $R$ : 0.08;  $NO_x$ \*0.8  $R$ : -0.05).

It is clear from the ozone,  $NO_2$  and  $O_x$  analysis that the  $NO_x$ \*2 leads to an overall improvement for surface ozone, but leads to a large overestimation in  $NO_2$ . This potentially indicates that there may be a missing model sink of  $NO_2$  that acts to lower both ozone formation and  $NO_2$  atmospheric abundances. Whilst the IBC\*0.8 simulation acts to provide a lower overall surface ozone concentration, but this alone does not account for the overestimation of surface ozone, as shown in Figures 6.26 and 6.27 respectively.

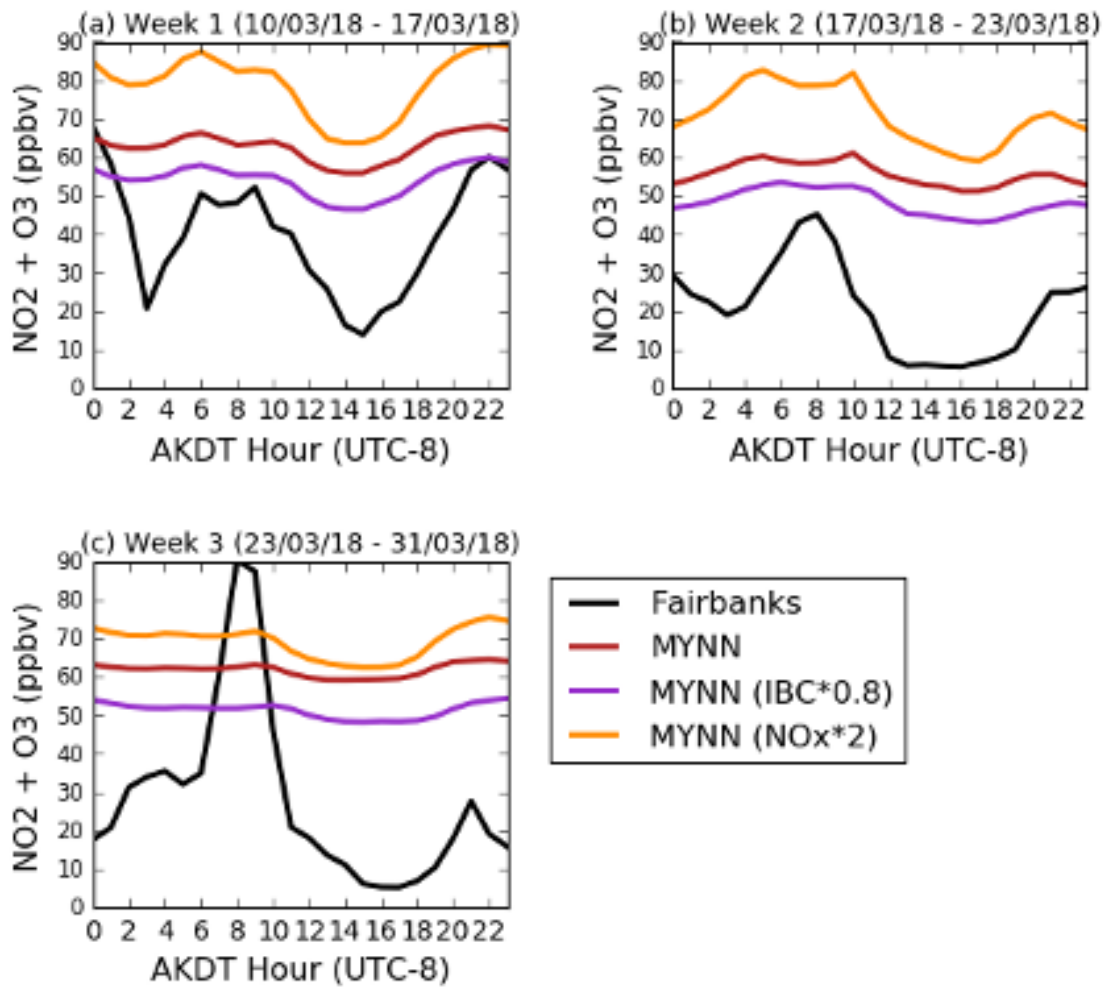


**Figure 6.31 - Weekly plots of simulated and observed surface  $O_x$  diurnal cycles at the NCore site in downtown Fairbanks for: 10/03/18 – 16/03/18 (Week 1), 17/03/18 – 22/03/18 (Week 2) and 23/03/18 (Week 3).**

### 6.4.7 MACSSIMIZE Flight Profiles

To gain further insight into the controls on the model vertical profiles of ozone during the MACSSIMIZE flight campaign, model chemical tendencies are output, as described in Section 5.3, in the previous Chapter. In this Section, vertical profiles of observed and modelled ozone are shown, as well as modelled ozone accumulated tendency rates for vertical mixing, chemistry and total advection (horizontal advection + vertical advection), which are shown as a rate of ozone change per hour. These are shown for when the FAAM aircraft is within the Fairbanks non-attainment area (Fig.6.4). These tendency rates are used to better understand the physical and chemical controls of the modelled ozone profiles. Of particular interest are the drivers of changes in near-surface ozone over the diurnal cycle, which the outgoing and return leg flight data from each flight day can help to illustrate.

**11/03/2018**

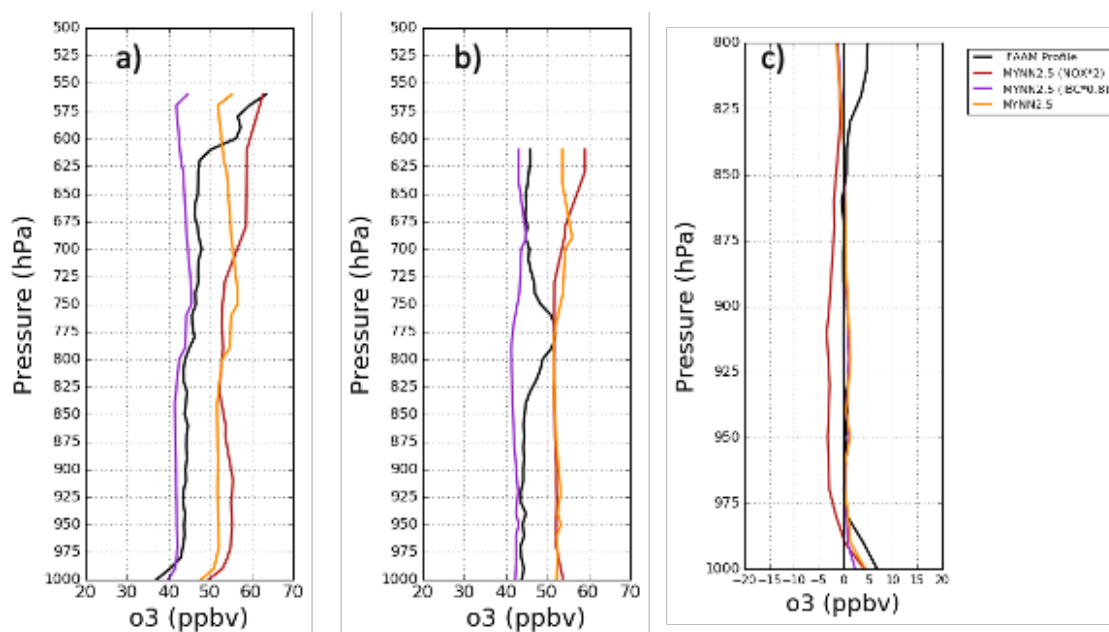


**Figure 6.32** – Vertical profiles on the 11/03/2018 of observed (black line) and model ozone for control (yellow line),  $\text{NO}_x \cdot 2$  (red line) and  $\text{IBC} \cdot 0.8$  (purple line) simulations. These are shown for the outbound flight at 1200 (panel a), return flight at 1645 (panel b), and the difference (return – outbound) between the two flights (panel c).

Observed ozone vertical profiles on the 11/03/2018 from Fairbanks show ozone production close to the surface between the take-off and landing flight times (1200 – 1645), whilst in the free troposphere there is very little change in ozone abundances (Fig. 6.32c). All WRF-Chem simulations reproduce the surface ozone increase, but are unable to capture the magnitude of the increase. The control and  $\text{NO}_x \times 2$  WRF-Chem simulations capture the ozone profile, but overestimate the ozone both at the surface and in the free troposphere. However, the  $\text{IBC} \times 0.8$  WRF-Chem simulation better replicates the ozone concentrations in the vertical column, both at the surface and the free troposphere. In the lower troposphere (surface – 800 hPa) the  $\text{NO}_x \times 2$  model simulates ozone loss above the surface between the outbound and return flights.

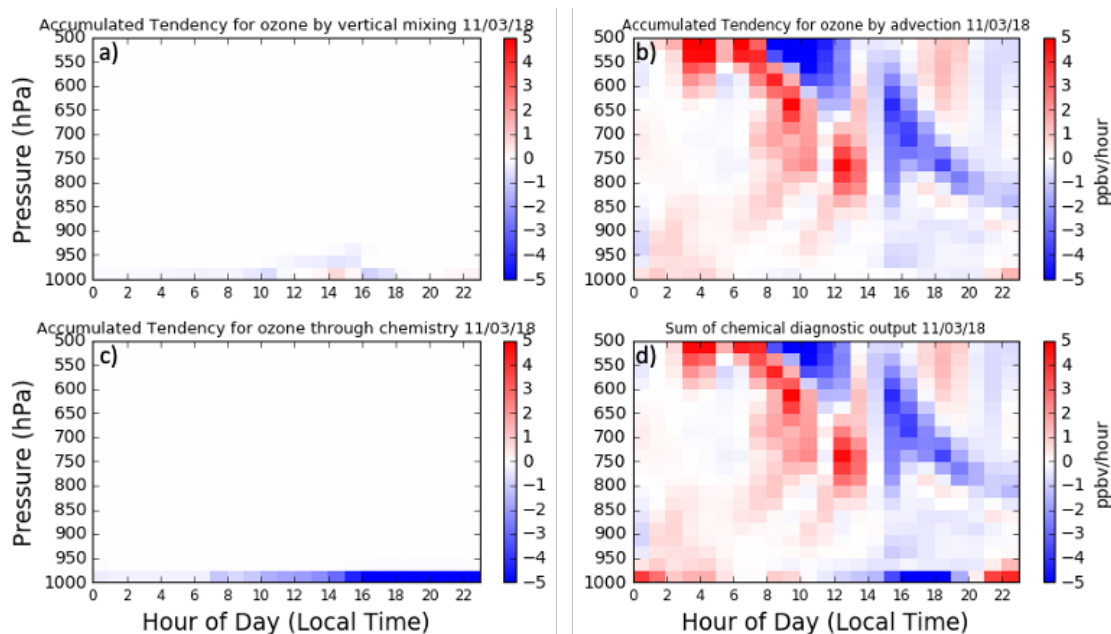


**Figure 6.33** – Accumulated tendencies on the 11/03/2018 for WRF-Chem (control) ozone for: vertical mixing (panel a), advection (panel b), chemistry (panel c) and the sum of all tendencies (panel d). Tendency rate is ppbv/hour.

WRF-Chem model tendencies suggest that in both the control (Fig. 6.33) and the  $\text{NO}_x \times 2$  (Fig. 6.34) simulation, the near-surface ozone is controlled by interplay between chemical loss and vertical mixing, whilst the free tropospheric

ozone is dictated by large scale advection in the model. During daylight hours (approximately 0800 – 1930), the vertical mixing and chemistry variables cause loss at the surface, especially during the late afternoon and at sunset. This is associated with the mixing down of ozone from the free troposphere due to an increase in the daytime boundary layer height, followed by chemical loss via  $\text{NO} + \text{O}_3$ . With the overestimation of modelled ozone in the control simulation (Fig. 6.32), if excess ozone is mixed down to the surface, this could account for the very low levels of surface NO in the model (Fig. 6.18) as it is lost through ozone titration, whilst also accounting for the loss of ozone through chemical processes. Subsequently, this could lead to too much  $\text{NO}_2$

A doubling of anthropogenic  $\text{NO}_x$  emissions in Fairbanks leads to an increase in surface ozone through vertical mixing in the afternoon (Fig. 6.34). This is likely linked to an increase in anthropogenically-sourced  $\text{NO}_2$  freely mixing in the elevated daytime boundary layer, leading to more ozone production aloft. This increase in modelled  $\text{NO}_x$  makes very little difference to the free troposphere

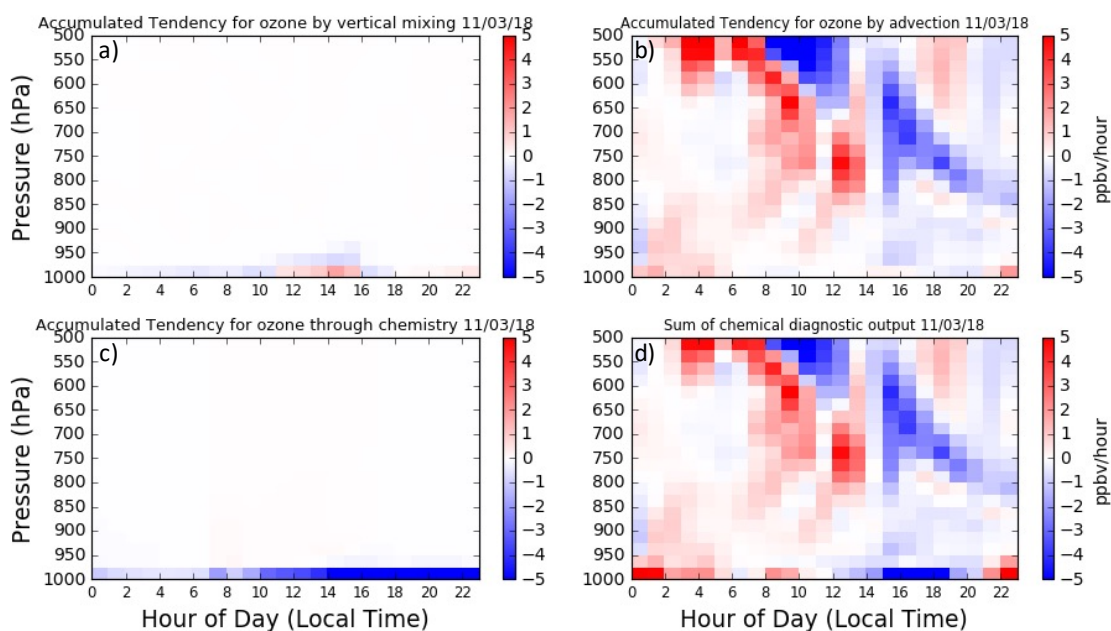


**Figure 6.34** – Accumulated tendencies on the 11/03/2018 for WRF-Chem ( $\text{NO}_x \times 2$  edit) ozone for: vertical mixing (panel a), advection (panel b), chemistry (panel c) and the sum of all tendencies (panel d). Tendency rate is ppbv/hour.

(Fig. 6.32 & 6.34), suggesting that this is predominantly controlled by the large scale advection and not influenced by surface emissions.

**20/03/2018**

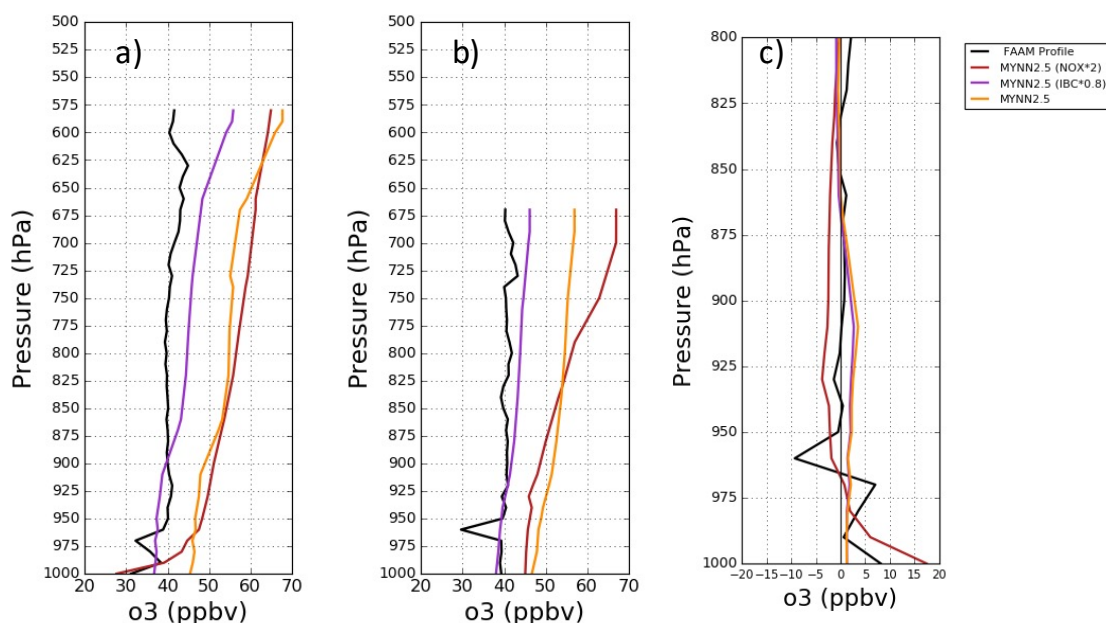


**Figure 6.35** – Vertical profiles on the 20/03/2018 of observed (black line) and model ozone for control (yellow line),  $\text{NO}_x^*2$  (red line) and  $\text{IBC}^*0.8$  (purple line) simulations. These are shown for the outbound flight at 1000 (panel a), return flight at 1535 (panel b), and the difference (return – outbound) between the two flights (panel c).

Observed ozone profiles on the 20/03/2018 show ozone increase at the surface between the flight take off time (1000) and return time (1535), and ozone increase at approximately 970 hPa (Fig. 6.35). The  $\text{NO}_x^*2$  WRF-Chem simulation captures the daytime surface ozone production, but no WRF-Chem simulation reproduces ozone production at 970 hPa. This could be associated with a strong surface inversion on the morning of the 20<sup>th</sup> (Fig. 6.10), which is seen in the radiosonde observations, but is not captured in any model setup. This inversion could act to trap elevated levels of ozone and precursors, which the model does not recreate. Similarly to the flight on the 11<sup>th</sup>, the control and  $\text{NO}_x^*2$  simulations do not capture the ozone concentrations in the free

troposphere, with a continual overestimation. Whilst the IBC\*0.8 simulation manages to capture the overall ozone profile in terms of magnitude, it does not capture the ozone production at the surface.

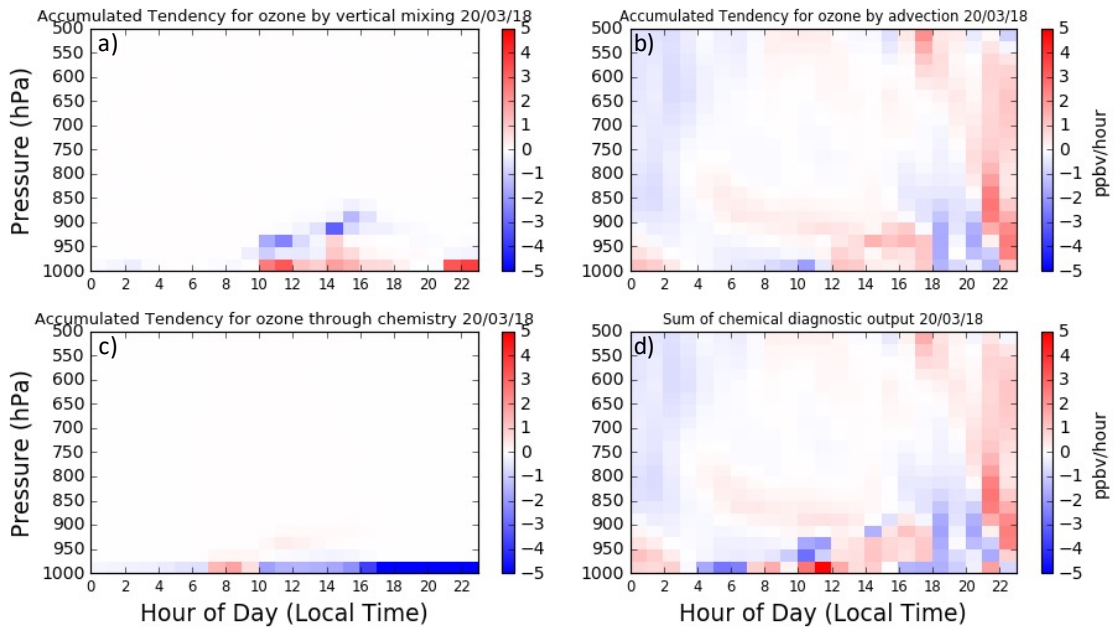


**Figure 6.36** - Accumulated tendencies on the 20/03/2018 for WRF-Chem (control) ozone for: vertical mixing (panel a), advection (panel b), chemistry (panel c) and the sum of all tendencies (panel d). Tendency rate is ppbv/hour.

WRF-Chem model tendencies indicate that during the daylight hours of the 20/03/2018 there is surface ozone increase, driven by near-surface vertical mixing (Fig. 6.36 & 6.37). Ozone production attributed to vertical mixing occurs in the model from the surface up to 925 hPa, which acts to offset the ozone lost at the surface through reacting with NO, which is enhanced in the NO<sub>x</sub>\*2 simulation. Modelled concentrations of surface NO<sub>2</sub> on the 20<sup>th</sup> are 30 ppbv (control) and 55 ppbv (NO<sub>x</sub>\*2) higher than the observed value at 0800, which is readily photolysed at sunrise leading to ozone chemical production at the surface. This suggests that there is either a missing or underestimated sink of NO<sub>2</sub> during the night, or that due to a positive bias in night-time ozone (e.g. Fig 6.28b), too much NO<sub>2</sub> is formed overnight. This early morning ozone production turns to ozone loss at 1000, likely associated with the increase of modelled NO seen in the diurnal cycle of week 2 (Fig. 6.19) at this time.

Modelled ozone in the free troposphere shows very little change throughout the day (Fig. 6.36 and 6.37), with limited advection contribution during the diurnal cycle. Observations from the aircraft between 1000 and 1535 support this, showing very little difference in ozone above 900 hPa (Fig. 6.35).

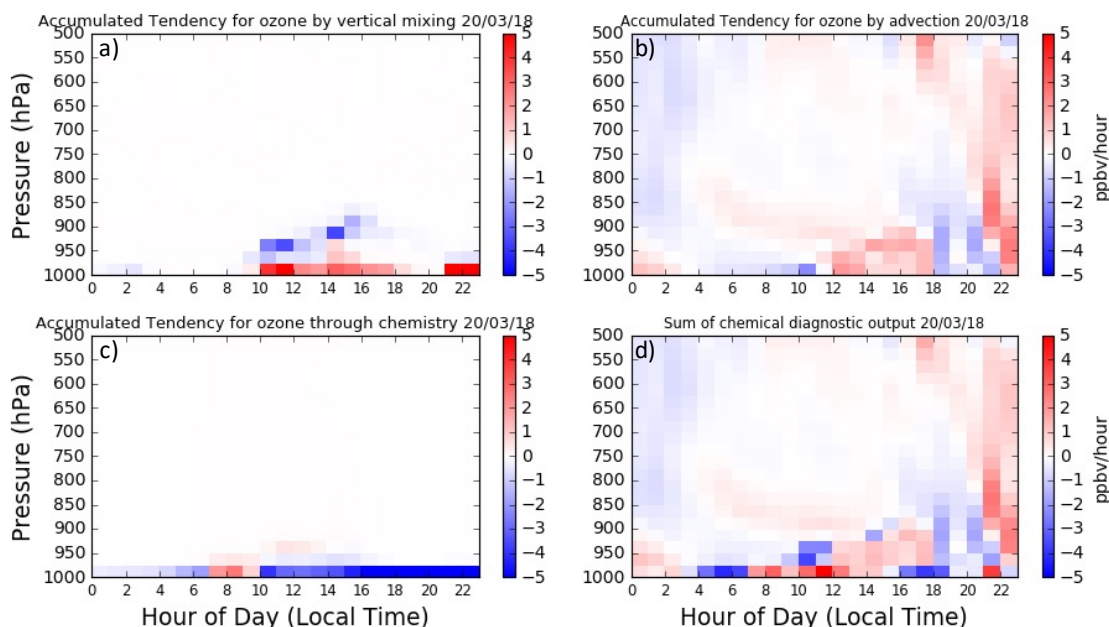


**Figure 6.37** – Accumulated tendencies on the 20/03/2018 for WRF-Chem ( $\text{NO}_x \cdot 2$  edit) ozone for: vertical mixing (panel a), advection (panel b), chemistry (panel c) and the sum of all tendencies (panel d). Tendency rate is ppbv/hour.

### **23/03/2018**

Observed ozone profiles on the 23/03/2018 show a 10 ppbv increase in surface ozone concentrations between 1100 and 1630 (Fig. 6.38). WRF-Chem simulations are unable to capture this, with the  $\text{NO}_x \cdot 2$  simulation showing a 13 ppbv loss in ozone at the surface during this period. Modelled free tropospheric ozone shows little change between the two flights, whilst the observations fluctuate between both ozone loss and gain throughout the vertical column.

A temperature inversion occurs during both the observations (Fig. 6.10) and the modelled simulations (Fig. 6.11) at 0300 on the 23<sup>rd</sup>. This could explain the

observed overall decrease in surface ozone via chemical loss, as the strong inversion leads to a built up of trapped near-surface NO, resulting in surface ozone loss. Vertical mixing leads to an increase in surface ozone onwards from 1000. This could be due to the daytime destruction of the temperature inversion,

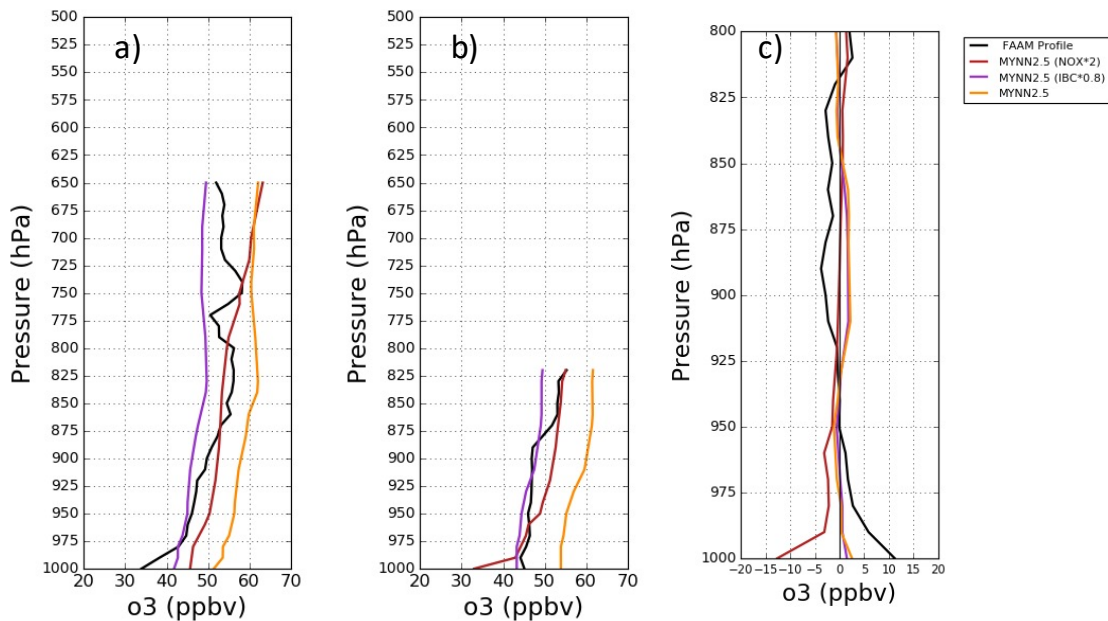


**Figure 6.38** – Vertical profiles on the 23/03/2018 of observed (black line) and model ozone for control (yellow line),  $\text{NO}_x \cdot 2$  (red line) and  $\text{IBC} \cdot 0.8$  (purple line) simulations. These are shown for the outbound flight at 1100 (panel a), return flight at 1630 (panel b), and the difference (return – outbound) between the two flights (panel c).

allowing ozone-rich air above the inversion layer to mix down to the surface. Whilst in the  $\text{NO}_x \cdot 2$  model simulation the associated increase in anthropogenically-sourced NO leads to a decrease in surface ozone concentrations.

WRF-Chem model tendencies show ozone increase occurs between 1200 and 1500 at the surface, primarily controlled by the vertical mixing down of ozone, likely from the free troposphere, where WRF-Chem overestimates ozone concentrations (Fig. 6.39 & 6.40). This would account for the continued low levels of NO, as we see continued chemical loss of surface ozone throughout

the day. Following this, there is surface ozone loss at 1600, which coincides with very low NO<sub>2</sub> (Fig. 6.20 & 6.22) and NO (Fig. 6.17 & 6.19) surface levels. The modelled free tropospheric ozone is controlled by large-scale advection terms.

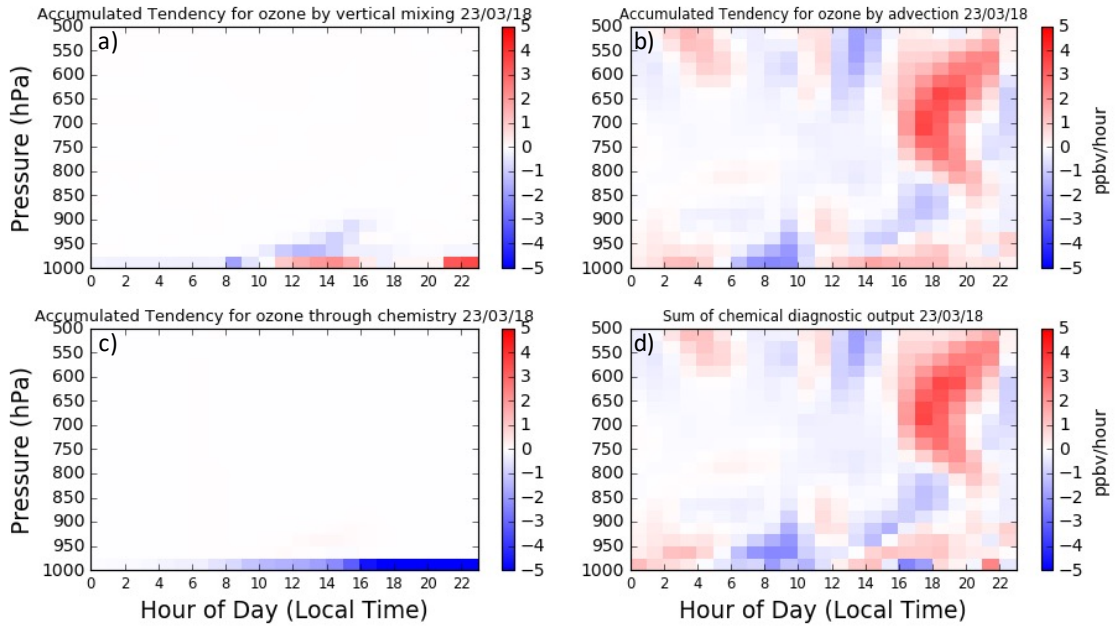


**Figure 6.39** - Accumulated tendencies on the 23/03/2018 for WRF-Chem (control) ozone for: vertical mixing (panel a), advection (panel b), chemistry (panel c) and the sum of all tendencies (panel d). Tendency rate is ppbv/hour.

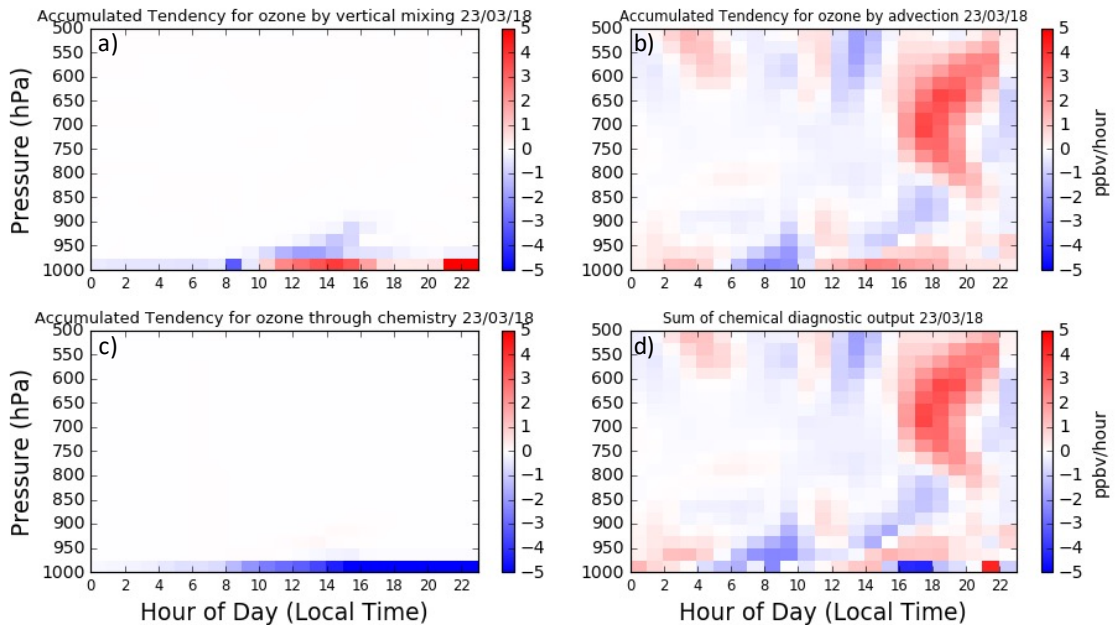


**Figure 6.40** – Accumulated tendencies on the 23/03/2018 for WRF-Chem (NO<sub>x</sub>\*2 edit) ozone for: vertical mixing (panel a), advection (panel b), chemistry (panel c) and the sum of all tendencies (panel d). Tendency rate is ppbv/hour.

## 6.5 Summary

The surface air temperature at Fairbanks, Alaska is sensitive to different WRF-Chem planetary boundary layer schemes and meteorological nudging setups. Simulations where meteorological nudging takes place throughout the entire vertical column best match surface observations (Fig 6.6) with high correlation coefficients (MYNN R = 0.89; YSU R = 0.86) and small mean bias (MYNN = -0.02k; YSU = -0.13k).

Model setups using meteorological nudging best match the temperature profiles recorded from radiosonde observations, but all models show a persistent negative bias, especially close to the surface (Fig 6.9). This matches results from previous work investigating modelling air temperature in Fairbanks (Mölders et al., 2011), where WRF-Chem was found to underestimate air temperature. All WRF-Chem model setups did a good job of capturing surface-based temperature inversions throughout the study, with the simulations where meteorological nudging throughout the column occurs, performing best (MYNN overestimated by 2 inversions, YSU overestimated by 1 inversion) (Fig. 6.11). This slight overestimation is likely due to insufficient warming leading to near-surface mixing and subsequent dissipation of any inversion. Based on extensive model evaluation of air temperature against an array of observations, the MYNN PBL with meteorological nudging throughout the column was shown to have the smallest error compared to observations (Table 6.2).

Modelled surface ozone is overestimated in the control simulation and the two sensitivity simulations (control MB: 18.93; IBC\*0.8 MB: 10.22; NO<sub>x</sub>\*0.8 MB: 11.34) (Fig 6.26 & 6.27), which matches the findings from a model intercomparison project as a part of AMAP (2015). These overestimations could be associated with uncertainties in emissions, transport of pollutants, inaccurate stratosphere-troposphere exchange rates and potential uncertainties relating to the OH radical.

Based on evaluation against observations from the MACSSIMIZE aircraft campaign, modelled ozone in the control simulation is overestimated. The IBC\*0.8 simulation improves modelled upper-tropospheric ozone and matches observations, but does not capture surface ozone concentrations. Whilst the  $\text{NO}_x \times 2$  simulation improves surface ozone concentrations, but leads to significant overestimations in surface  $\text{NO}_2$ . This suggests that there could be a missing model sink of  $\text{NO}_2$ , coupled with too high ozone concentrations within the model initial boundary conditions.

Based on WRF-Chem model tendencies, large scale advection is the key driver of modelled ozone in the upper troposphere throughout the study period. Whilst at the near-surface an interplay between ozone being vertically mixed down from ozone-rich air above and subsequent ozone loss to NO ( $\text{O}_3 + \text{NO} = \text{NO}_2$ ), dominates ozone abundancies. This could account for the positive model bias in surface  $\text{NO}_2$ , as we see an influx of ozone from above, this is lost through reacting with NO, leading to increased model surface  $\text{NO}_2$  concentrations.

## 7. Conclusion

The overall objective of this thesis was to improve the understanding of processes controlling tropospheric ozone abundances and distributions in areas of limited in-situ observations at high latitudes, using the regional chemistry transport model WRF-Chem in conjunction with satellite, aircraft and ground observations. Tropospheric ozone is detrimental to air quality, human health and vegetation, and also acts as a greenhouse gas in the troposphere. High latitude tropospheric ozone has contributed to increased warming of the Arctic relative to the global average, leading to accelerated sea ice retreat and loss, whilst degrading the air quality in Arctic cities. Therefore identifying the key processes controlling ozone in the high latitudes, especially in regions of limited in-situ observations, is of great importance for any future mitigation strategies. The results in this thesis provide a new understanding of key sources of ozone precursor emissions in Western Siberia, whilst also quantifying the impact of different vegetation types as dry deposition sinks of ozone within the region. Finally, the key chemical and physical processes controlling near-surface ozone at two high latitude locations are also presented. The remainder of this Chapter discusses the completion of the research aims that were detailed in Chapter 1, as well as potential future research.

### 7.1 Completion of Aims

**Research Aim 1: Evaluate emissions of NO<sub>2</sub> in Western Siberia through the use of tropospheric column NO<sub>2</sub> observations from satellite in conjunction with modelled output from WRF-Chem.**

Chapter 4 uses satellite observations of tropospheric column NO<sub>2</sub> from OMI to provide insight into key NO<sub>2</sub> source regions across Western Siberia. Major anthropogenic sources of NO<sub>2</sub> are identified through WRF-Chem evaluation using two different anthropogenic global emission inventories, whilst this

Chapter also investigates the contribution of western Siberian fires to overall NO<sub>2</sub> abundances.

WRF-Chem simulations using both ECLIPSE and EDGAR-HTAP2 anthropogenic emission inventories were found to show an underestimation in tropospheric column NO<sub>2</sub>, when compared to OMI observations, especially over urban regions within the model domain. A high correlation coefficient value suggests that the spatial pattern of the emissions are correct, but that the magnitude of emissions are poorly quantified. This is the first time NO<sub>2</sub> emissions have been investigated in western Siberia, but the underestimation is in line with other high latitude emission inventory analysis (AMAP, 2015; Schmale et al., 2018).

NO<sub>2</sub> in western Siberia was shown to be most sensitive to emissions from the transport and energy sectors. The transport sector in particular had the largest influence on western Siberian NO<sub>2</sub>, which agrees with previous studies showing high transport emissions in Russia (Ginzburg et al., 2020). Natural NO<sub>2</sub> emissions originating from fires within the western Siberian domain were limited during the study period, with 2011 not being as high a fire year compared to previous years.

To attempt to improve the model underestimation of observed tropospheric column NO<sub>2</sub>, the largest two anthropogenic sectors in the ECLIPSE anthropogenic emission inventory were scaled. This led to an overall improvement in model underestimation of OMI column NO<sub>2</sub>, but this is mainly due to overestimations in urban regions, with little change to the persistent underestimations in background regions. These background biases could be linked to deficiencies in model tropospheric NO<sub>y</sub> chemistry (Huijnen et al., 2010), or potential model errors in the conversion of NO<sub>2</sub> to nitric acid, when OH concentrations are enhanced and the NO<sub>2</sub>+OH reaction is more important.

**Research Aim 2: Quantify source contributions to tropospheric ozone in Western Siberia, and estimate the contributions from different types and regions of vegetation to dry deposition loss of ozone.**

In Chapter 5 this thesis addresses the contribution of atmospheric transport, vegetation dry deposition and photochemistry to surface tropospheric ozone in western Siberia. During late springtime modelled ozone north of 60°N was shown to be mainly influenced by high latitude emissions associated with the energy sector, most likely gas flaring. This was shown to be predominantly controlled by westerly wind patterns, previously identified by Stohl (2006), which contribute to the late spring pollutant build up, the Arctic Haze. These westerly flows lead to pollutants remaining at the high latitudes, limiting export. This result provides further evidence to the importance of improving the quantification of high latitude emissions going forward. For the remainder of the study period, both north and south of 60°N, ozone within the domain is most sensitive to emissions from the transport sector.

Fire emissions are shown to have a limited contribution to surface ozone concentrations within the domain, with the greatest influence seen in June. Relative to the June control simulation, the Fires\_off simulation leads to a small change in surface ozone concentrations south of 60°N (-1.3 ppbv), whilst making limited change north of 60°N (-0.3 ppbv). Minimal fire activity in July and August results in very little change in these months.

Using model physical and chemical tendency output, key processes controlling near-surface ozone vertical profiles were investigated. Based on vertical profiles above major cities within Western Siberia, ozone above the boundary layer is controlled by the advection of large-scale air masses. Whilst the results in this thesis show that surface ozone is influenced by advection, but is also impacted by an interplay between the vertical mixing down of ozone-rich air from aloft, and the subsequent loss through reacting with NO close to the surface. These findings support previous work looking at a near-surface ozone in Siberia, which

through train-based observations evidenced the mixing down and subsequent surface-based chemical loss of ozone in Siberia (Pankratova et al., 2011).

Chapter 5 highlights the importance of the Siberian forest as a surface sink for ozone through dry deposition, especially during the summer (June, July & August). The Siberian forest vegetation accounts for 8.0 Tg of ozone deposition per month during the control simulation across the total domain, whilst “savanna & grassland” accounts for 3.9 Tg/month of ozone loss. This result supports the findings by Stjernberg et al. (2012), who also highlighted the importance of Siberian forests as a sink, potentially influencing the global ozone budget. I also show that north of 60°N, forest and tundra are the dominant sinks, which account for 65% of dry deposition flux, and 77% of the terrestrial surface cover at these latitudes.

**Research Aim 3: Quantify the key physical and chemical drivers behind daily and diurnal tropospheric ozone changes in Fairbanks at the surface and through the vertical column in Spring 2018.**

In Chapter 6 I use WRF-Chem in conjunction with aircraft campaign data to investigate the key physical and chemical drivers behind variability in surface ozone in Fairbanks, an Arctic city prone to poor air quality. Through comparisons of different model PBL schemes and meteorological nudging setups, I show that air temperature is best captured using the MYNN PBL and where nudging throughout the whole column occurs, but WRF-Chem cannot capture the observed low temperatures, especially during temperature inversions.

WRF-Chem simulations show a positive ozone bias above the boundary layer and a positive NO<sub>2</sub> bias at the surface. However, there is a significant underestimation of surface NO, resulting in underestimated total surface NO<sub>x</sub>. Two sensitivity studies tested modelled ozone sensitivity to Fairbanks NO<sub>x</sub> emissions and model upper boundary conditions. Results suggest that upper

troposphere ozone is sensitive to a 20% reduction in initial boundary condition ozone, which brings the values in-line with observations. Whilst a doubling of  $\text{NO}_x$  emissions from within Fairbanks improves the model ozone bias at the surface, but still leads to model overestimation above the boundary layer.

I found that the key physical and chemical drivers behind tropospheric ozone changes matched those reported in Chapter 5. Tropospheric ozone above the boundary layer was controlled by large-scale advection. Whilst at the near-surface an interplay between ozone being vertically mixed down from ozone-rich air above and subsequent ozone loss to NO ( $\text{O}_3 + \text{NO} = \text{NO}_2$ ), dominates ozone abundances, suppressing surface ozone.

Further results from this chapter suggest that due to a positive bias in ozone above the boundary layer, increased quantities of ozone are vertically mixed down, further increasing  $\text{NO}_2$  formation at the surface leading to the high  $\text{NO}_2$  bias. This suggests that surface  $\text{NO}_2$  production is controlled by the ozone loss.

## 7.2 Synthesis

Through the use of WRF-Chem and satellite, aircraft and ground-based observations, this thesis has highlighted the sensitivity of high latitude tropospheric ozone and its precursors to local anthropogenic emissions, in particular from the energy and transport sectors. An evaluation of existing global anthropogenic emissions suggest that high latitude  $\text{NO}_x$  emission sources are spatially well represented, but the magnitude of emissions likely underestimated. Through the use of WRF-Chem ozone tendencies, key physical and chemical drivers in high latitude tropospheric ozone are identified (Fig. 7.1). Model experiments show that high latitude ozone above the boundary layer is controlled by large scale advection processes within air masses. Whilst surface ozone is controlled by an interplay between the vertical mixing down of ozone-rich air from aloft, and the subsequent loss of ozone at the surface through reacting with  $\text{NO}$ , resulting in suppressed surface ozone. This leads to

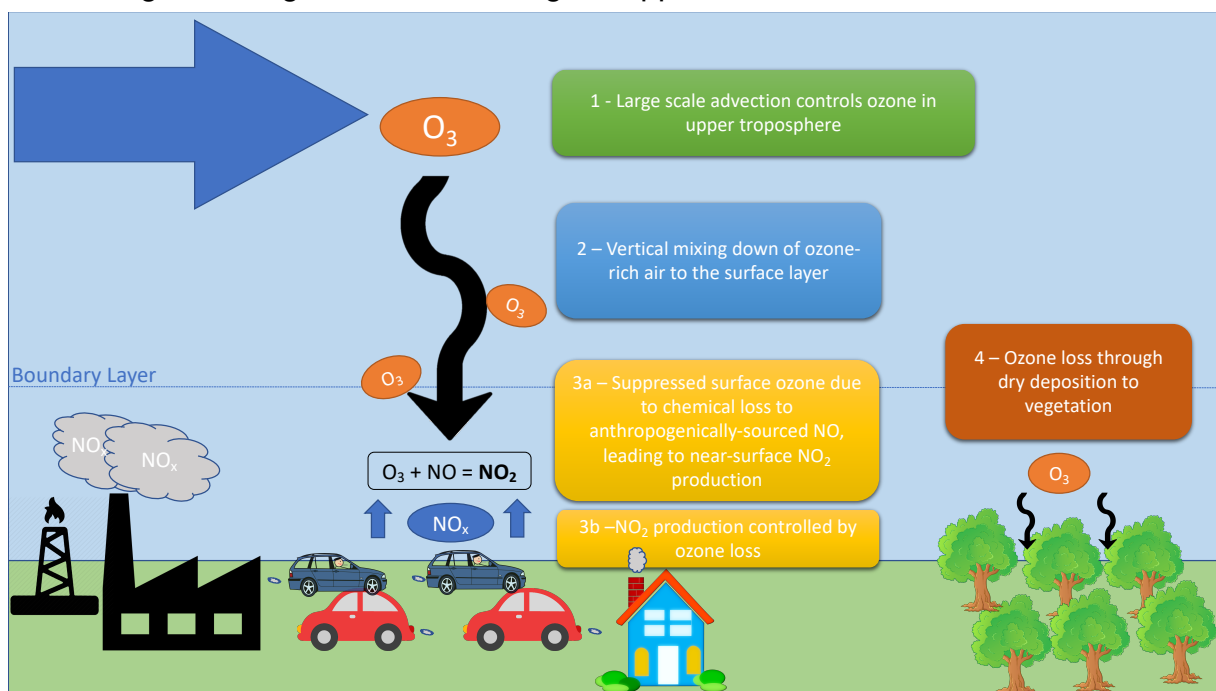


**Figure 7.1** – Schematic illustration of key processes controlling tropospheric ozone over high-latitude regions. 1 - Upper tropospheric ozone is controlled by large scale advection. 2 - Mixing down of ozone-rich air to surface layer. 3 - Suppressed surface ozone through reaction with  $\text{NO}$  leads to  $\text{NO}_2$  production. 4 - Major loss mechanism of ozone is via dry deposition to vegetation, in particular the Siberian forest.

NO<sub>2</sub> production at the surface, which is important when considering local air quality. Siberian forest was also shown to be an important ozone loss mechanism through dry deposition, which is important for global ozone concentrations. However, it is unclear how this will be affected by increasing Arctic temperatures, potential shifts in vegetation, and increases in high latitude ozone concentrations in the future.

### 7.3 Future Work

The results in this thesis highlight a number of areas of uncertainty and potential challenges which future research could help to address.

In an attempt to address model NO<sub>2</sub> biases over Western Siberia, NO<sub>2</sub> sensitivity to NO + O<sub>3</sub> kinetic rate uncertainties could be investigated in WRF-Chem. It has been shown that this reaction rate in particular (NO + O<sub>3</sub>) has large uncertainties at low temperatures (Ridley et al., 2017), something which is relevant for ozone studies based at high latitudes, for example under conditions of strong temperature inversions. Previous aircraft campaigns have shown potential errors in the Jet Propulsion Laboratory (JPL) rate constants for the NO + O<sub>3</sub> reaction at low temperatures, which is important for interpreting observations of tropospheric NO<sub>2</sub> columns (Silvern. et al., 2018).

Chapter 5 highlights the importance of vegetation, especially the Siberian forest, as a dry deposition sink for near-surface ozone. However, future warming of the Arctic will lead to significant changes in the composition, density and distribution of Arctic vegetation, which would likely have impacts for ozone dry deposition (Pearson et al., 2013). Coupled with widespread greening at high latitudes (Myers-Smith et al., 2020), future large-scale ecological responses to climate change have large associated uncertainties, and need to be better understood. Through the use of future climate scenario emission inventories, further work could investigate the impact of proposed changes to the Arctic vegetation, and how this would impact future Arctic ozone concentrations.

To further build upon the results in Chapter 6 focussed on Fairbanks, Alaska, an improved emission inventory could be used, to better represent localised emissions from Fairbanks. This could help to potentially address the overestimation of surface NO<sub>2</sub>. This could be in the form of a higher resolution inventory, or an Alaskan specific inventory which is available through the National Emission Inventory (NEI), created by the United States Environmental Protection Agency (EPA). Further to this, to provide a better representation of temperature inversions and cold air pooling in Fairbanks a higher horizontal resolution simulation could be undertaken (e.g. 1 km), which could aim to better capture the formation, stagnation and destruction of inversions in Fairbanks. For a better computational cost, this could involve simulating a nested domain over Fairbanks, whilst continuing to simulate the rest of Alaska at 10 km.

This thesis provides a better understanding of controls on high latitude ozone, with potential benefits to people local to the areas of interest (e.g. Western Siberia and Fairbanks, Alaska). For example, results from Results Chapters 1 and 2 could feed into future mitigation strategies tackling air quality in the region, highlighting the importance of anthropogenic emissions, especially those from the energy and transport sectors. Results Chapter 3 is the first time a modelling study has investigated ozone in Fairbanks, therefore the model setup and initial results could provide a reference for future modelling efforts in the region going forward.

## List of References

- Arctic Council, Arctic Marine Shipping Assessment 2009 Report, Technical report, Arctic Council, Tromsø, Norway,, 2009.
- Ainsworth, E.A. 2008. Rice production in a changing climate: A meta-analysis of responses to elevated carbon dioxide and elevated ozone concentration. *Global Change Biology*. **14**(7), pp.1642–1650.
- Aliabadi, A.A., Staebler, R.M. and Sharma, S. 2015. Air quality monitoring in communities of the Canadian Arctic during the high shipping season with a focus on local and marine pollution. *Atmospheric Chemistry and Physics*. **15**(5), pp.2651–2673.
- Allison, E.H. and Bassett, H.R. 2015. Climate change in the oceans: Human impacts and responses. *Science*. **350**(6262), pp.778–782.
- Amann, M., Bertok, I., Borken-Kleefeld, J., Cofala, J., Heyes, C., Höglund-Isaksson, L., Klimont, Z., Nguyen, B., Posch, M., Rafaj, P., Sandler, R., Schöpp, W., Wagner, F. and Winiwarter, W. 2011. Cost-effective control of air quality and greenhouse gases in Europe: Modeling and policy applications. *Environmental Modelling and Software*. [Online]. **26**(12), pp.1489–1501. Available from: <http://dx.doi.org/10.1016/j.envsoft.2011.07.012>.
- Amann, M., Klimont, Z. and Wagner, F. 2013. Regional and global emissions of air pollutants: Recent trends and future scenarios. *Annual Review of Environment and Resources*. **38**, pp.31–55.
- AMAP 2015. *AMAP assessment 2015: Black carbon and ozone as Arctic climate forcers*.
- Andrew, R. 2014. *Socio-Economic Drivers of Change in the Arctic. Amap Technical Report No. 9*.
- Antokhin, P.N., Gochakov, A. V., Kolker, A.B. and Penenko, A. V. 2018. Comparison of WRF-CHEM Chemical Transport Model Calculations with Aircraft Measurements in Norilsk. *Atmospheric and Oceanic Optics*. **31**(4),

pp.372–380.

Arctic Monitoring and Assessment Programme (AMAP) 2017. *Snow, Water, Ice and Permafrost in the Arctic (SWIPA) 2017*.

Arnold, S., Law, K.S., Brock, C.A., Thomas, J.L., Starkweather, S.M., Salzen, K. vonB, Stohl, A., Sharma, S., Lund, M.T., Flanner, M.G., Petaja, T., Tanimoto, H., Gamble, J., Dibb, J.E., Melamed, M., Johnson, N., Fidel, M., Tynkkynen, V.-P., Baklanov, A., Eckhardt, S., Monks, S. a., Browse, J. and Bozem, H. 2016. Arctic air pollution: Challenges and opportunities for the next decade. *Elementa.*, pp.1–17.

Asmi, E., Kondratyev, V., Brus, D., Laurila, T., Lihavainen, H., Backman, J., Vakkari, V., Aurela, M., Hatakka, J., Viisanen, Y., Uttal, T., Ivakhov, V. and Makshtas, A. 2016. Aerosol size distribution seasonal characteristics measured in Tiksi, Russian Arctic. *Atmospheric Chemistry and Physics*. **16**(3), pp.1271–1287.

Atkinson, R.W., Butland, B.K., Dimitroulopoulou, C., Heal, M.R., Stedman, J.R., Carslaw, N., Jarvis, D., Heaviside, C., Vardoulakis, S., Walton, H. and Anderson, H.R. 2016. Long-term exposure to ambient ozone and mortality: A quantitative systematic review and meta-analysis of evidence from cohort studies. *BMJ Open*. **6**(2), pp.1–10.

Ayers, J.D. and Simpson, W.R. 2006. Measurements of N<sub>2</sub>O<sub>5</sub> near Fairbanks, Alaska. *Journal of Geophysical Research Atmospheres*. **111**(14).

Baker, L.H., Collins, W.J., Olivié, D.J.L., Cherian, R., Hodnebrog, Ø., Myhre, G., Quaas, J. and Samset, B.H. 2015. Climate responses to anthropogenic emissions of short-lived climate pollutants. *Atmospheric Chemistry and Physics Discussions*. **15**(3), pp.3823–3862.

Barrie, L.A. 1986. Arctic air pollution: An overview of current knowledge. *Atmospheric Environment (1967)*. **20**(4), pp.643–663.

Barth, M.C., Lee, J., Hodzic, A., Pfister, G., Skamarock, W.C., Worden, J., Wong, J. and Noone, D. 2012. Thunderstorms and upper troposphere chemistry during the early stages of the 2006 North American Monsoon. *Atmospheric Chemistry and Physics*. **12**(22), pp.11003–11026.

Benson, C. 1965. : OF ALASKA ICE FOG : LOW TEMPERATURE AIR POLLUTION by.

Berchet, A., Paris, J.D., Ancellet, G., Law, K.S., Stohl, A., Nédélec, P., Arshinov, M.Y., Belan, B.D. and Ciais, P. 2013. Tropospheric ozone over Siberia in spring 2010: Remote influences and stratospheric intrusion. *Tellus, Series B: Chemical and Physical Meteorology*. **65**(1), pp.0–14.

Berner, L.T., Massey, R., Jantz, P., Forbes, B.C., Macias-Fauria, M., Myers-Smith, I., Kumpula, T., Gauthier, G., Andreu-Hayles, L., Gaglioti, B. V., Burns, P., Zetterberg, P., D'Arrigo, R. and Goetz, S.J. 2020. Summer warming explains widespread but not uniform greening in the Arctic tundra biome. *Nature Communications*. [Online]. **11**(1), pp.1–12. Available from: <http://dx.doi.org/10.1038/s41467-020-18479-5>.

Berntsen, T.K., Isaksen, I.S.A., Myhre, G., Fuglestvedt, J.S., Stordal, F., Alsvik Larsen, T., Freckleton, R.S. and Shine, K.P. 1997. Effects of anthropogenic emissions on tropospheric ozone and its radiative forcing. *Journal of Geophysical Research Atmospheres*. **102**(23), pp.28101–28126.

Bjorkman, A.D., Myers-Smith, I.H., Elmendorf, S.C., Normand, S., Rüger, N., Beck, P.S.A., Blach-Overgaard, A., Blok, D., Cornelissen, J.H.C., Forbes, B.C., Georges, D., Goetz, S.J., Guay, K.C., Henry, G.H.R., HilleRisLambers, J., Hollister, R.D., Karger, D.N., Kattge, J., Manning, P., Prevéy, J.S., Rixen, C., Schaepman-Strub, G., Thomas, H.J.D., Vellend, M., Wilmking, M., Wipf, S., Carbognani, M., Hermanutz, L., Lévesque, E., Molau, U., Petraglia, A., Soudzilovskaia, N.A., Spasojevic, M.J., Tomaselli, M., Vowles, T., Alatalo, J.M., Alexander, H.D., Anadon-Rosell, A., Angers-Blondin, S., Beest, M. te, Berner, L., Björk, R.G., Buchwal, A., Buras, A., Christie, K., Cooper, E.J., Dullinger, S., Elberling, B., Eskelinen, A., Frei, E.R., Grau, O., Grogan, P., Hallinger, M., Harper, K.A., Heijmans, M.M.P.D., Hudson, J., Hülber, K., Iturrate-Garcia, M., Iversen, C.M., Jaroszynska, F., Johnstone, J.F., Jørgensen, R.H., Kaarlejärvi, E., Klady, R., Kuleza, S., Kulonen, A., Lamarque, L.J., Lantz, T., Little, C.J., Speed, J.D.M., Michelsen, A., Milbau, A., Nabe-Nielsen, J., Nielsen, S.S., Ninot, J.M., Oberbauer, S.F., Olofsson, J., Onipchenko, V.G., Rumpf, S.B.,

- Semenchuk, P., Shetti, R., Collier, L.S., Street, L.E., Suding, K.N., Tape, K.D., Trant, A., Treier, U.A., Tremblay, J.P., Tremblay, M., Venn, S., Weijers, S., Zamin, T., Boulanger-Lapointe, N., Gould, W.A., Hik, D.S., Hofgaard, A., Jónsdóttir, I.S., Jorgenson, J., Klein, J., Magnusson, B., Tweedie, C., Wookey, P.A., Bahn, M., Blonder, B., van Bodegom, P.M., Bond-Lamberty, B., Campetella, G., Cerabolini, B.E.L., Chapin, F.S., Cornwell, W.K., Craine, J., Dainese, M., de Vries, F.T., Díaz, S., Enquist, B.J., Green, W., Milla, R., Niinemets, Ü., Onoda, Y., Ordoñez, J.C., Ozinga, W.A., Penuelas, J., Poorter, H., Poschlod, P., Reich, P.B., Sandel, B., Schamp, B., Sheremetev, S. and Weiher, E. 2018. Plant functional trait change across a warming tundra biome. *Nature*. **562**(7725), pp.57–62.
- Black, V.J., Black, C.R., Roberts, J.A. and Stewart, C.A. 2000. Impact of ozone on the reproductive development of plants. *New Phytologist*. **147**(3), pp.421–447.
- Bluestein, J., Rackley, J. and Baum, E. 2008. *Sources and Mitigation Opportunities to Reduce Emissions of Short-term Arctic Climate Forcers*.
- Boersma, K.F., Eskes, H.J. and Brinksma, E.J. 2004. Error analysis for tropospheric NO<sub>2</sub> retrieval from space. *Journal of Geophysical Research: Atmospheres*. **109**(4).
- Boersma, K.F., Eskes, H.J., Dirksen, R.J., Van Der A, R.J., Veefkind, J.P., Stammes, P., Huijnen, V., Kleipool, Q.L., Sneep, M., Claas, J., Leitão, J., Richter, A., Zhou, Y. and Brunner, D. 2011. An improved tropospheric NO<sub>2</sub> column retrieval algorithm for the Ozone Monitoring Instrument. *Atmospheric Measurement Techniques*. **4**(9), pp.1905–1928.
- Bourne, S.M., Bhatt, U.S., Zhang, J. and Thoman, R. 2010. Surface-based temperature inversions in Alaska from a climate perspective. *Atmospheric Research*. [Online]. **95**(2–3), pp.353–366. Available from: <http://dx.doi.org/10.1016/j.atmosres.2009.09.013>.
- Bowling, S.A. 1986. Climatology of high-latitude air pollution as illustrated by Fairbanks and Anchorage, Alaska. *J. Clim. Appl. Meteorol.* **25**(1), pp.22–34.
- Bradley, R.S., Keimig, F.T. and Diaz, H.F. 1992. Climatology of surface-based

- inversions in the North American Arctic. *Journal of Geophysical Research*. **97**(D14).
- Browse, J., Carslaw, K.S., Schmidt, A. and Corbett, J.J. 2013. Impact of future Arctic shipping on high-latitude black carbon deposition. *Geophysical Research Letters*. **40**(16), pp.4459–4463.
- Bucsela, E.J., Celarier, E.A., Wenig, M.O., Gleason, J.F., Veefkind, J.P., Boersma, K.F. and Brinksma, E.J. 2006. Algorithm for NO<sub>2</sub> vertical column retrieval from the ozone monitoring instrument. *IEEE Transactions on Geoscience and Remote Sensing*. **44**(5), pp.1245–1257.
- Bulkow, L.R., Singleton, R.J., DeByle, C., Miernyk, K., Redding, G., Hummel, K.B., Chikoyak, L. and Hennessy, T.W. 2012. Risk factors for hospitalization with lower respiratory tract infections in children in rural Alaska. *Pediatrics*. **129**(5).
- Cao, L., He, M., Jiang, H., Grosshans, H. and Cao, N. 2016. Sensitivity of the reaction mechanism of the ozone depletion events during the arctic spring on the initial atmospheric composition of the troposphere. *Atmosphere*. **7**(10).
- Carlson, T.N. 1981. Speculations on the movement of polluted air to the Arctic. *Atmospheric Environment (1967)*. **15**(8), pp.1473–1477.
- Chai, T. 2014. Root mean square error (RMSE) or mean absolute error (MAE)? *Geoscientific Model Development Discussions*. **7**(1), pp.1525–1534.
- Chin, M., Ginoux, P., Kinne, S., Torres, O., Holben, B.N., Duncan, B.N., Martin, R. V., Logan, J.A., Higurashi, A. and Nakajima, T. 2002. Tropospheric aerosol optical thickness from the GOCART model and comparisons with satellite and sun photometer measurements. *Journal of the Atmospheric Sciences*. **59**(3 PT 1), pp.461–483.
- Clifton, O.E., Paulot, F., Fiore, A.M., Horowitz, L.W., Correa, G., Baublitz, C.B., Fares, S., Goded, I., Goldstein, A.H., Gruening, C., Hogg, A.J., Loubet, B., Mammarella, I., Munger, J.W., Neil, L., Stella, P., Uddling, J., Vesala, T. and Weng, E. 2020. Influence of Dynamic Ozone Dry Deposition on Ozone Pollution. *Journal of Geophysical Research: Atmospheres*. **125**(8), pp.1–

21.

- Cohen, J., Zhang, X., Francis, J., Jung, T., Kwok, R., Overland, J., Ballinger, T.J., Bhatt, U.S., Chen, H.W., Coumou, D., Feldstein, S., Gu, H., Handorf, D., Henderson, G., Ionita, M., Kretschmer, M., Laliberte, F., Lee, S., Linderholm, H.W., Maslowski, W., Peings, Y., Pfeiffer, K., Rigor, I., Semmler, T., Stroeve, J., Taylor, P.C., Vavrus, S., Vihma, T., Wang, S., Wendisch, M., Wu, Y. and Yoon, J. 2020. Divergent consensus on Arctic amplification influence on midlatitude severe winter weather. *Nature Climate Change*. **10**(1), pp.20–29.
- Cooper, M.J., Martin, R. V., Henze, D.K. and Jones, D.B.A. 2020. Effects of a priori profile shape assumptions on comparisons between satellite NO<sub>2</sub> columns and model simulations. *Atmospheric Chemistry and Physics*. **20**(12), pp.7231–7241.
- Corbett, J.J., Lack, D.A., Winebrake, J.J., Harder, S. and Silberman, J.A. 2010. Arctic shipping emissions inventories and future scenarios. *Atmospheric Chemistry and Physics*. **10**(19), pp.9689–9704.
- Crutzen, P.J., Lawrence, M.G. and Pöschl, U. 1999. On the background photochemistry of tropospheric ozone. *Tellus, Series A: Dynamic Meteorology and Oceanography*. **51**(1 SPEC. ISS.), pp.123–146.
- Dalsøren, S.B., Endresen, Ø., Isaksen, I.S.A., Gravir, G. and Sörgård, E. 2007. Environmental impacts of the expected increase in sea transportation, with a particular focus on oil and gas scenarios for Norway and northwest Russia. *Journal of Geophysical Research Atmospheres*. **112**(2).
- Van Dam, B., Helmig, D., Doskey, P. V. and Oltmans, S.J. 2016. Summertime surface O<sub>3</sub> behavior and deposition to tundra in the Alaskan Arctic. *Journal of Geophysical Research*. **121**(13), pp.8055–8066.
- Davidson, E.A. and Kinglerlee, W. 1997. A global inventory of nitric oxide emissions from soils. *Nutrient Cycling in Agroecosystems*. **48**(1–2), pp.37–50.
- Dickerson, R.R., Huffman, G.J., Luke, W.T., Nunnermacker, L.J., Pickering, K.E., Leslie, A.C.D., Lindsey, C.G., Slinn, W.G.N., Kelly, T.J., Daum, P.H.,

- Delany, A.C., Greenberg, J.P., Zimmerman, P.R., Boatman, J.F., Ray, J.D. and Stedman, D.H. 1987. Thunderstorms: An important mechanism in the transport of air pollutants. *Science*. **235**(4787), pp.460–465.
- Doherty, R.M., Stevenson, D.S., Collins, W.J. and Sanderson, M.G. 2005. Influence of convective transport on tropospheric ozone and its precursors in a chemistry-climate model. *Atmospheric Chemistry and Physics*. **5**(12), pp.3205–3218.
- Doherty, S.J., Warren, S.G., Grenfell, T.C., Clarke, A.D. and Brandt, R.E. 2010. Light-absorbing impurities in Arctic snow. *Atmospheric Chemistry and Physics*. **10**(23), pp.11647–11680.
- Eckhardt, S., Hermansen, O., Grythe, H., Fiebig, M., Stebel, K., Cassiani, M., Baecklund, A. and Stohl, A. 2013. The influence of cruise ship emissions on air pollution in Svalbard &ndash; A harbinger of a more polluted Arctic? *Atmospheric Chemistry and Physics*. **13**(16), pp.8401–8409.
- Eckhardt, S., Quennehen, B., Olivie, D.J.L., Berntsen, T.K., Cherian, R., Christensen, J.H., Collins, W., Crepinsek, S., Daskalakis, N., Flanner, M., Herber, A., Heyes, C., Hodnebrog, Huang, L., Kanakidou, M., Klimont, Z., Langner, J., Law, K.S., Lund, M.T., Mahmood, R., Massling, A., Myriokefalitakis, S., Nielsen, I.E., Nøjgaard, J.K., Quaas, J., Quinn, P.K., Raut, J.C., Rumbold, S.T., Schulz, M., Sharma, S., Skeie, R.B., Skov, H., Uttal, T., Von Salzen, K. and Stohl, A. 2015. Current model capabilities for simulating black carbon and sulfate concentrations in the Arctic atmosphere: A multi-model evaluation using a comprehensive measurement data set. *Atmospheric Chemistry and Physics*. **15**(16), pp.9413–9433.
- Eckhardt, S., Stohl, A., Beirle, S., Spichtinger, N., James, P., Forster, C., Junker, C., Wagner, T., Platt, U. and Jennings, S.G. 2003. The North Atlantic Oscillation controls air pollution transport to the Arctic. *Atmospheric Chemistry and Physics*. **3**(5), pp.1769–1778.
- Ek, M.B. 2003. Implementation of Noah land surface model advances in the National Centers for Environmental Prediction operational mesoscale Eta model. *Journal of Geophysical Research*. **108**(D22), pp.1–16.

- Elvidge, C.D., Ziskin, D., Baugh, K.E., Tuttle, B.T., Ghosh, T., Pack, D.W., Erwin, E.H. and Zhizhin, M. 2009. A fifteen year record of global natural gas flaring derived from satellite data. *Energies*. **2**(3), pp.595–622.
- Emery, C., Liu, Z., Russell, A.G., Odman, M.T., Yarwood, G. and Kumar, N. 2017. Recommendations on statistics and benchmarks to assess photochemical model performance. *Journal of the Air and Waste Management Association*. [Online]. **67**(5), pp.582–598. Available from: <http://dx.doi.org/10.1080/10962247.2016.1265027>.
- Emmons, L.K., Arnold, S.R., Monks, S.A., Huijnen, V., Tilmes, S., Law, K.S., Thomas, J.L., Raut, J.C., Bouarar, I., Turquety, S., Long, Y., Duncan, B., Steenrod, S., Strode, S., Flemming, J., Mao, J., Langner, J., Thompson, A.M., Tarasick, D., Apel, E.C., Blake, D.R., Cohen, R.C., Dibb, J., Diskin, G.S., Fried, A., Hall, S.R., Huey, L.G., Weinheimer, A.J., Wisthaler, A., Mikoviny, T., Nowak, J., Peischl, J., Roberts, J.M., Ryerson, T., Warneke, C. and Helmig, D. 2015. The POLARCAT Model Intercomparison Project (POLMIP): Overview and evaluation with observations. *Atmospheric Chemistry and Physics*. **15**(12), pp.6721–6744.
- Emmons, L.K., Walters, S., Hess, P.G., Lamarque, J.F., Pfister, G.G., Fillmore, D., Granier, C., Guenther, A., Kinnison, D., Laepfle, T., Orlando, J., Tie, X., Tyndall, G., Wiedinmyer, C., Baughcum, S.L. and Kloster, S. 2010. Description and evaluation of the Model for Ozone and Related chemical Tracers, version 4 (MOZART-4). *Geoscientific Model Development*. **3**(1), pp.43–67.
- Endresen, Ø., Sørsgård, E., Sundet, J.K., Dalsøren, S.B., Isaksen, I.S.A., Berglen, T.F. and Gravir, G. 2003. Emission from international sea transportation and environmental impact. *Journal of Geophysical Research: Atmospheres*. **108**(17).
- Eskes, H.J. and Boersma, K.F. 2003. Averaging kernels for DOAS total-column satellite retrievals. *Atmospheric Chemistry and Physics*. [Online]. **3**(5), pp.1285–1291. Available from: <http://www.atmos-chem-phys.net/3/1285/2003/>.
- F., S.R., J., J.D., R., T.K., T., S., J., E.M., C., C.R., L., L.J., R., H.S., K., U., D.,

- C.J., O., W.P., J., P. and B., P.I. 2018. Observed NO/NO<sub>2</sub> ratios in the upper troposphere imply errors in NO-NO<sub>2</sub>-O<sub>3</sub> cycling kinetics or an unaccounted NO<sub>x</sub> reservoir. *Geophysical Research Letters*. [Online]. **0**(ja). Available from: <https://agupubs.onlinelibrary.wiley.com/doi/abs/10.1029/2018GL077728>.
- Falk, S. and Sinnhuber, B.M. 2018. Polar boundary layer bromine explosion and ozone depletion events in the chemistry-climate model EMAC v2.52: Implementation and evaluation of AirSnow algorithm. *Geoscientific Model Development*. **11**(3), pp.1115–1131.
- Fast, J.D., Gustafson, W.I., Easter, R.C., Zaveri, R.A., Barnard, J.C., Chapman, E.G., Grell, G.A. and Peckham, S.E. 2006. Evolution of ozone, particulates, and aerosol direct radiative forcing in the vicinity of Houston using a fully coupled meteorology-chemistry-aerosol model. *Journal of Geophysical Research Atmospheres*. **111**(21), pp.1–29.
- Fisher, J.A., Jacob, D.J., Purdy, M.T., Kopacz, M., Le Sager, P., Carouge, C., Holmes, C.D., Yantosca, R.M., Batchelor, R.L., Strong, K., Diskin, G.S., Fuelberg, H.E., Holloway, J.S., Hyer, E.J., McMillan, W.W., Warner, J., Streets, D.G., Zhang, Q., Wang, Y. and Wu, S. 2010. Source attribution and interannual variability of Arctic pollution in spring constrained by aircraft (ARCTAS, ARCPAC) and satellite (AIRS) observations of carbon monoxide. *Atmospheric Chemistry and Physics*. **10**(3), pp.977–996.
- Fitzky, A.C., Sandén, H., Karl, T., Fares, S., Calfapietra, C., Grote, R., Saunier, A. and Rewald, B. 2019. The Interplay Between Ozone and Urban Vegetation—BVOC Emissions, Ozone Deposition, and Tree Ecophysiology. *Frontiers in Forests and Global Change*. **2**(September), pp.1–17.
- Flannigan, M.D., Krawchuk, M.A., De Groot, W.J., Wotton, B.M. and Gowman, L.M. 2009. Implications of changing climate for global wildland fire. *International Journal of Wildland Fire*. **18**(5), pp.483–507.
- Fuhrer, J. 2009. Ozone risk for crops and pastures in present and future climates. *Naturwissenschaften*. **96**(2), pp.173–194.

- Ganzeveld, L., Bouwman, L., Stehfest, E., Van Vuuren, D.P., Eickhout, B. and Lelieveld, J. 2010. Impact of future land use and land cover changes on atmospheric chemistry-climate interactions. *Journal of Geophysical Research Atmospheres*. **115**(23), pp.1–18.
- Gautier, D.L., Bird, K.J., Charpentier, R.R., Grantz, A., Houseknecht, D.W., Klett, T.R., Moore, T.E., Pitman, J.K., Schenk, C.J., Schuenemeyer, J.H., Sørensen, K., Tennyson, M.E., Valin, Z.C. and Wandrey, C.J. 2009. Assessment of undiscovered oil and gas in the arctic. *Science*. **324**(5931), pp.1175–1179.
- Giglio, L., Csiszar, I. and Justice, C.O. 2006. Global distribution and seasonality of active fires as observed with the Terra and Aqua Moderate Resolution Imaging Spectroradiometer (MODIS) sensors. *Journal of Geophysical Research: Biogeosciences*. **111**(2), pp.1–12.
- Giglio, L., Randerson, J.T. and Van Der Werf, G.R. 2013. Analysis of daily, monthly, and annual burned area using the fourth-generation global fire emissions database (GFED4). *Journal of Geophysical Research: Biogeosciences*. **118**(1), pp.317–328.
- Ginzburg, A.S., Semenov, V.A., Semutnikova, E.G., Aleshina, M.A., Zakharova, P. V. and Lezina, E.A. 2020. Impact of COVID-19 Lockdown on Air Quality in Moscow. *Doklady Earth Sciences*. **495**(1), pp.862–866.
- Girach, I.A., Ojha, N., Nair, P.R., Pozzer, A., Tiwari, Y.K., Ravi Kumar, K. and Lelieveld, J. 2017. Variations in O<sub>3</sub>, CO, and CH<sub>4</sub> over the Bay of Bengal during the summer monsoon season: Shipborne measurements and model simulations. *Atmospheric Chemistry and Physics*. **17**(1), pp.257–275.
- Gramelsberger, G. 2009. Conceiving Meteorology as the exact science of the atmosphere: Vilhelm Bjerknes's paper of 1904 as a milestone. *Meteorologische Zeitschrift*. **18**(6), pp.669–673.
- Granier, C., Niemeier, U., Jungclaus, J.H., Emmons, L., Hess, P., Lamarque, J.F., Walters, S. and Brasseur, G.P. 2006. Ozone pollution from future ship traffic in the Arctic northern passages. *Geophysical Research Letters*. **33**(13), pp.1–5.

- Grell, G.A. and Dévényi, D. 2002. A generalized approach to parameterizing convection combining ensemble and data assimilation techniques. *Geophysical Research Letters*. **29**(14), pp.10–13.
- Grell, G.A. and Freitas, S.R. 2014. A scale and aerosol aware stochastic convective parameterization for weather and air quality modeling. *Atmospheric Chemistry and Physics*. **14**(10), pp.5233–5250.
- Grell, G.A., Peckham, S.E., Schmitz, R., McKeen, S.A., Frost, G., Skamarock, W.C. and Eder, B. 2005. Fully coupled chemistry within the WRF model. *Atmospheric Environment*. [Online]. **39**(37), pp.6957–6975. Available from: <http://www.sciencedirect.com/science/article/B6VH3-4HC6M4X-1/2/9afcb084535a6d67f238ee5e22f9037f>.
- Guenther, A., Karl, T., Harley, P., Wiedinmyer, C., Palmer, P.I. and C., G. 2006. Estimates of global terrestrial isoprene emissions using MEGAN. *Atmospheric Chemistry and Physics Discussions*. [Online]. **6**(1), pp.107–173. Available from: <https://hal.archives-ouvertes.fr/hal-00295995/%0Ahttp://www.atmos-chem-phys.net/6/3181/2006/acp-6-3181-2006.pdf>.
- Guggisberg, M., Hessel, P.A., Michaelchuk, D. and Atiemo, M. 2003. Particulate matter and gaseous contaminants in indoor environments in an isolated northern community. *International journal of circumpolar health*. **62**(2), pp.120–129.
- Gytarsky, M.L., Karaban, R.T., Nazarov, I.M., Sysygina, T.I. and Chemeris, M. V. 1995. Monitoring of forest ecosystems in the Russian Subarctic: effects of industrial pollution. *Science of the Total Environment*. **164**(1), pp.57–68.
- Hains, J.C., Boersma, K.F., Mark, K., Dirksen, R.J., Cohen, R.C., Perring, A.E., Bucsela, E., Volten, H., Swart, D.P.J., Richter, A., Wittrock, F., Schoenhardt, A., Wagner, T., Ibrahim, O.W., Roozendael, M. Van, Pinardi, G., Gleason, J.F., Veefkind, J.P. and Levelt, P. 2010. Testing and improving OMI DOMINO tropospheric NO<sub>2</sub> using observations from the DANDELIONS and INTEX-B validation campaigns. *Journal of Geophysical Research Atmospheres*. **115**(5).
- Hansen, A.D.A. and Rosen, H. 1984. Vertical distributions of particulate carbon,

- sulfur, and bromine in the arctic haze and comparison with ground-level measurements at Barrow, Alaska. *Geophysical Research Letters*. **11**(5), pp.381–384.
- Harsem, Ø., Eide, A. and Heen, K. 2011. Factors influencing future oil and gas prospects in the Arctic. *Energy Policy*. [Online]. **39**(12), pp.8037–8045. Available from: <http://dx.doi.org/10.1016/j.enpol.2011.09.058>.
- Hartmann, B. and Wendler, G. 2005. Climatology of the winter surface temperature inversion in Fairbanks, Alaska. *85th AMS Annual Meeting, American Meteorological Society - Combined Preprints*. (April), pp.2767–2773.
- Hienola, A.I., Pietikäinen, J.P., Jacob, D., Pozdun, R., Petäjä, T., Hyvärinen, A.P., Sogacheva, L., Kerminen, V.M., Kulmala, M. and Laaksonen, A. 2013. Black carbon concentration and deposition estimations in Finland by the regional aerosol-climate model REMO-HAM. *Atmospheric Chemistry and Physics*. **13**(8), pp.4033–4055.
- Hodzic, A. and Knote, C. 2014. MOZART gas-phase chemistry with MOSAIC aerosols. , p.7.
- Hole, L.R., Christensen, J., Ginzburg, V.A., Makarov, V., Pershina, N.A., Polischuk, A.I., Ruoho-Airola, T., Svistov, P.P. and Vasilenko, V.N. 2006. *AMAP Assessment 2006: Acidifying Pollutants , Arctic Haze , and Acidification in the Arctic*.
- Hollaway, M.J., Arnold, S.R., Challinor, A.J. and Emberson, L.D. 2012. Intercontinental trans-boundary contributions to ozone-induced crop yield losses in the Northern Hemisphere. *Biogeosciences*. **9**(1), pp.271–292.
- Hong, S.Y., Noh, Y. and Dudhia, J. 2006. A new vertical diffusion package with an explicit treatment of entrainment processes. *Monthly Weather Review*. **134**(9), pp.2318–2341.
- Hou, P. and Wu, S. 2016. Long-term Changes in Extreme Air Pollution Meteorology and the Implications for Air Quality. *Scientific Reports*. [Online]. **6**(October 2015), pp.1–9. Available from: <http://dx.doi.org/10.1038/srep23792>.

- Huang, K., Fu, J.S., Hodson, E.L., Dong, X., Cresko, J., Prikhodko, V.Y., Storey, J.M. and Cheng, M.D. 2014. Identification of missing anthropogenic emission sources in Russia: Implication for modeling arctic haze. *Aerosol and Air Quality Research*. **14**(7), pp.1799–1811.
- Huang, K., Fu, J.S., Prikhodko, V.Y., Storey, J.M., Romanov, A., Hodson, E.L., Cresko, J., Morozova, I., Ignatieva, Y. and Cabaniss, J. 2015. Russian anthropogenic black carbon: Emission reconstruction and arctic black carbon simulation. *Journal of Geophysical Research*. **120**(21), 11,306–11,333.
- Huijnen, V., Eskes, H.J., Poupkou, A., Elbern, H., Boersma, K.F., Foret, G., Sofiev, M., Valdebenito, A., Flemming, J., Stein, O., Gross, A., Robertson, L., D'Isidoro, M., Kioutsioukis, I., Friese, E., Amstrup, B., Bergstrom, R., Strunk, A., Vira, J., Zyryanov, D., Maurizi, A., Melas, D., Peuch, V.H. and Zerefos, C. 2010. Comparison of OMI NO<sub>2</sub> tropospheric columns with an ensemble of global and European regional air quality models. *Atmospheric Chemistry and Physics*. **10**(7), pp.3273–3296.
- Iversen, T. 1984. On the atmospheric transport of pollution to the Arctic. *Geophysical Research Letters*. **11**(5), pp.457–460.
- Jacob, D.J. 1992. Deposition of ozone to tundra. *Journal of Geophysical Research*. **97**(D15).
- Jacob, D.J., Crawford, J.H., Maring, H., Clarke, A.D., Dibb, J.E., Emmons, L.K., Ferrare, R.A., Hostetler, C.A., Russell, P.B., Singh, H.B., Thompson, A.M., Shaw, G.E., McCauley, E., Pederson, J.R. and Fisher, J.A. 2010. The arctic research of the composition of the troposphere from aircraft and satellites (ARCTAS) mission: Design, execution, and first results. *Atmospheric Chemistry and Physics*. **10**(11), pp.5191–5212.
- Jacobi, H.W., Kaleschke, L., Richter, A., Rozanov, A. and Burrows, J.P. 2006. Observation of a fast ozone loss in the marginal ice zone of the Arctic Ocean. *Journal of Geophysical Research Atmospheres*. **111**(15).
- Jaeglé, L., Steinberger, L., Martin, R. V. and Chance, K. 2005. Global partitioning of NO<sub>x</sub> sources using satellite observations: Relative roles of fossil fuel combustion, biomass burning and soil emissions. *Faraday*

*Discussions*. **130**(x), pp.407–423.

Janssens-Maenhout, G., Crippa, M., Guizzardi, D., Dentener, F., Muntean, M., Pouliot, G., Keating, T., Zhang, Q., Kurokawa, J., Wankmüller, R., Denier Van Der Gon, H., Kuenen, J.J.P., Klimont, Z., Frost, G., Darras, S., Koffi, B. and Li, M. 2015. HTAP-v2.2: A mosaic of regional and global emission grid maps for 2008 and 2010 to study hemispheric transport of air pollution. *Atmospheric Chemistry and Physics*. **15**(19), pp.11411–11432.

Jerrett, M., Burnett, R.T., Arden Pope, C., Ito, K., Thurston, G., Krewski, D., Shi, Y., Calle, E. and Thun, M. 2009. Long-term ozone exposure and mortality. *New England Journal of Medicine*. **360**(11), pp.1085–1095.

Joyce, P.L., Von Glasow, R. and Simpson, W.R. 2014. The fate of NO<sub>x</sub> emissions due to nocturnal oxidation at high latitudes: 1-D simulations and sensitivity experiments. *Atmospheric Chemistry and Physics*. **14**(14), pp.7601–7616.

Karlsson, P.E., Tang, L., Sundberg, J., Chen, D., Lindskog, A. and Pleijel, H. 2007. Increasing risk for negative ozone impacts on vegetation in northern Sweden. *Environmental Pollution*. **150**(1), pp.96–106.

Kley, D., Geiss, H. and Mohnen, V.A. 1994. Tropospheric ozone at elevated sites and precursor emissions in the United States and Europe. *Atmospheric Environment*. **28**(1), pp.149–158.

Klonecki, A., Hess, P., Emmons, L., Smith, L., Orlando, J. and Blake, D. 2003. Seasonal changes in the transport of pollutants into the Arctic troposphere-model study. *Journal of Geophysical Research: Atmospheres*. **108**(4).

Knorr, W., Dentener, F., Hantson, S., Jiang, L., Klimont, Z. and Arneth, A. 2016. Air quality impacts of European wildfire emissions in a changing climate. *Atmospheric Chemistry and Physics*. **16**(9), pp.5685–5703.

Knote, C., Hodzic, A., Jimenez, J.L., Volkamer, R., Orlando, J.J., Baidar, S., Brioude, J., Fast, J., Gentner, D.R., Goldstein, A.H., Hayes, P.L., Knighton, W.B., Oetjen, H., Setyan, A., Stark, H., Thalman, R., Tyndall, G., Washenfelder, R., Waxman, E. and Zhang, Q. 2014. Simulation of semi-explicit mechanisms of SOA formation from glyoxal in aerosol in a 3-D

- model. *Atmospheric Chemistry and Physics*. **14**(12), pp.6213–6239.
- Kozlova, E.A., Manning, A.C., Kisilyakhov, Y., Seifert, T. and Heimann, M. 2008. Seasonal, synoptic, and diurnal-scale variability of biogeochemical trace gases and O<sub>2</sub> from a 300-m tall tower in central Siberia. *Global Biogeochemical Cycles*. **22**(4), pp.1–16.
- Kukavskaya, E.A., Buryak, L. V., Shvetsov, E.G., Conard, S.G. and Kalenskaya, O.P. 2016. The impact of increasing fire frequency on forest transformations in southern Siberia. *Forest Ecology and Management*. [Online]. **382**, pp.225–235. Available from: <http://dx.doi.org/10.1016/j.foreco.2016.10.015>.
- Lamsal, L.N., Martin, R. V., Van Donkelaar, A., Celarier, E.A., Bucsela, E.J., Boersma, K.F., Dirksen, R., Luo, C. and Wang, Y. 2010. Indirect validation of tropospheric nitrogen dioxide retrieved from the OMI satellite instrument: Insight into the seasonal variation of nitrogen oxides at northern midlatitudes. *Journal of Geophysical Research Atmospheres*. **115**(5), pp.1–15.
- Law, K.S., Roiger, A., Thomas, J.L., Marelle, L., Raut, J.C., Dalsøren, S., Fuglestedt, J., Tuccella, P., Weinzierl, B. and Schlager, H. 2017. Local Arctic air pollution: Sources and impacts. *Ambio*. **46**(s3), pp.453–463.
- Law, K.S. and Stohl, A. 2007. Arctic Air Pollution: Origins and Impacts. *Science*. [Online]. **315**(5818), pp.1537–1540. Available from: <http://www.sciencemag.org/cgi/doi/10.1126/science.1137695>.
- Lawrence, M.G., von Kuhlmann, R., Salzmann, M. and Rasch, P.J. 2003. The balance of effects of deep convective mixing on tropospheric ozone. *Geophysical Research Letters*. **30**(18), pp.3–6.
- LeGrand, S.L., Polashenski, C., Letcher, T.W., Creighton, G.A., Peckham, S.E. and Cetola, J.D. 2019. The AFWA dust emission scheme for the GOCART aerosol model in WRF-Chem v3.8.1. *Geoscientific Model Development*. **12**(1), pp.131–166.
- LEI, H., GUO, J., CHEN, D. and YANG, J. 2019. Comparison of two double-moment microphysics schemes in aspects of warm-rain droplet spectra and

- raindrop budget. *Atmospheric and Oceanic Science Letters*. [Online]. **12**(6), pp.424–433. Available from: <https://doi.org/10.1080/16742834.2019.1664882>.
- Lelieveld, J. and Crutzen, P.J. 1994. Role of deep cloud convection in the ozone budget of the troposphere. *Science*. **264**(5166), pp.1759–1761.
- Lelieveld, J., Evans, J.S., Fnais, M., Giannadaki, D. and Pozzer, A. 2015. The contribution of outdoor air pollution sources to premature mortality on a global scale. *Nature*. [Online]. **525**(7569), pp.367–371. Available from: <http://www.nature.com/doi/10.1038/nature15371>.
- Li, C., Hsu, N.C., Sayer, A.M., Krotkov, N.A., Fu, J.S., Lamsal, L.N., Lee, J. and Tsay, S.C. 2016. Satellite observation of pollutant emissions from gas flaring activities near the Arctic. *Atmospheric Environment*. [Online]. **133**, pp.1–11. Available from: <http://dx.doi.org/10.1016/j.atmosenv.2016.03.019>.
- Li, X., Hu, X.-M., Ma, Y., Wang, Y., Li, L. and Zhao, Z. 2019. Impact of planetary boundary layer structure on the formation and evolution of air-pollution episodes in Shenyang, Northeast China. *Atmospheric Environment*. [Online]. **214**(May), p.116850. Available from: <https://doi.org/10.1016/j.atmosenv.2019.116850>.
- Liang, Q., Rodriguez, J.M., Douglass, A.R., Crawford, J.H., Olson, J.R., Apel, E., Bian, H., Blake, D.R., Brune, W., Chin, M., Colarco, P.R., Da Silva, A., Diskin, G.S., Duncan, B.N., Huey, L.G., Knapp, D.J., Montzka, D.D., Nielsen, J.E., Pawson, S., Riemer, D.D., Weinheimer, A.J. and Wisthaler, A. 2011. Reactive nitrogen, ozone and ozone production in the Arctic troposphere and the impact of stratosphere-troposphere exchange. *Atmospheric Chemistry and Physics*. **11**(24), pp.13181–13199.
- Lu, X., Zhang, L. and Shen, L. 2019. Meteorology and Climate Influences on Tropospheric Ozone: a Review of Natural Sources, Chemistry, and Transport Patterns. *Current Pollution Reports*. **5**(4), pp.238–260.
- Luo, D., Xiao, Y., Diao, Y., Dai, A., Franzke, C.L.E. and Simmonds, I. 2016. Impact of Ural blocking on winter warm Arctic-cold Eurasian anomalies. Part II: The link to the North Atlantic Oscillation. *Journal of Climate*. **29**(11), pp.3949–3971.

- Marelle, L., Raut, J.C., Law, K.S., Berg, L.K., Fast, J.D., Easter, R.C., Shrivastava, M. and Thomas, J.L. 2017. Improvements to the WRF-Chem 3.5.1 model for quasi-hemispheric simulations of aerosols and ozone in the Arctic. *Geoscientific Model Development*. **10**(10), pp.3661–3677.
- Marelle, L., Raut, J.C., Law, K.S. and Duclaux, O. 2018. Current and Future Arctic Aerosols and Ozone From Remote Emissions and Emerging Local Sources—Modeled Source Contributions and Radiative Effects. *Journal of Geophysical Research: Atmospheres*, pp.1–22.
- Marelle, L., Raut, J.C., Thomas, J.L., Law, K.S., Quennehen, B., Ancellet, G., Pelon, J., Schwarzenboeck, A. and Fast, J.D. 2015. Transport of anthropogenic and biomass burning aerosols from Europe to the Arctic during spring 2008. *Atmospheric Chemistry and Physics*. **15**(7), pp.3831–3850.
- Marelle, Louis, Thomas, J.L., Raut, J.C., Law, K.S., Jalkanen, J.P., Johansson, L., Roiger, A., Schlager, H., Kim, J., Reiter, A. and Weinzierl, B. 2015. Air quality and radiative impacts of Arctic shipping emissions in the summertime in northern Norway: From the local to the regional scale. *Atmospheric Chemistry and Physics Discussions*. **15**(13), pp.18407–18457.
- Marsh, D.R., Mills, M.J., Kinnison, D.E., Lamarque, J.F., Calvo, N. and Polvani, L.M. 2013. Climate change from 1850 to 2005 simulated in CESM1(WACCM). *Journal of Climate*. **26**(19), pp.7372–7391.
- McCarty, J.L., Smith, T.E.L. and Turetsky, M.R. 2020. Arctic fires re-emerging. *Nature Geoscience*. [Online]. **13**(10), pp.658–660. Available from: <http://dx.doi.org/10.1038/s41561-020-0641-y>.
- Meier, W., Hovelsrud, G., van Oort, B., Key, J., Kovacs, K., Michel, C., Haas, C., Granskog, M., Gerland, S., Perovich, D., Makshtas, A. and Reist, J. 2014. Arctic sea ice in transformation: A review of recent observed changes and impacts on biology and human activity. *Reviews of Geophysics*. **51**, pp.185–217.
- Mellor, G. 1973. Analytic Prediction of the Properties of Stratified Planetary Surface Layers. *Journal of the Atmospheric Sciences*. **30**, pp.1061–1069.

- Mellor, G. and Yamada, T. 1974. A Hierarchy of Turbulence Closure Models for Planetary Boundary Layers. *Journal of the atmospheric Sciences*. [Online]. **31**, pp.1791–1806. Available from: <http://dx.doi.org/10.1016/j.jsames.2011.03.003><https://doi.org/10.1016/j.gr.2017.08.001><http://dx.doi.org/10.1016/j.precamres.2014.12.018><http://dx.doi.org/10.1016/j.precamres.2011.08.005><http://dx.doi.org/10.1080/00206814.2014.902757><http://dx.doi.org/10.1016/j.atmosres.2010.04.005>.
- Misenis, C. and Zhang, Y. 2010. An examination of sensitivity of WRF/Chem predictions to physical parameterizations, horizontal grid spacing, and nesting options. *Atmospheric Research*. [Online]. **97**(3), pp.315–334. Available from: <http://dx.doi.org/10.1016/j.atmosres.2010.04.005>.
- Mlawer, E.J., Taubman, S.J., Brown, P.D., Iacono, M.J. and Clough, S.A. 1997. Radiative transfer for inhomogeneous atmospheres: RRTM, a validated correlated-k model for the longwave. *Journal of Geophysical Research Atmospheres*. **102**(14), pp.16663–16682.
- Mölders, N. and Kramm, G. 2010. A case study on wintertime inversions in Interior Alaska with WRF. *Atmospheric Research*. [Online]. **95**(2–3), pp.314–332. Available from: <http://dx.doi.org/10.1016/j.atmosres.2009.06.002>.
- Mölders, N., Tran, H.N.Q., Quinn, P., Sassen, K., Shaw, G.E. and Kramm, G. 2011. Assessment of WRF/Chem to simulate sub-Arctic boundary layer characteristics during low solar irradiation using radiosonde, SODAR, and surface data. *Atmospheric Pollution Research*. [Online]. **2**(3), pp.283–299. Available from: <http://www.atmospolres.com/articles/Volume2/issue3/APR-11-035.pdf>.
- Monks, P.S. 2005. Gas-phase radical chemistry in the troposphere. *Chemical Society Reviews*. **34**(5), pp.376–395.
- Monks, P.S., Archibald, A.T., Colette, A., Cooper, O., Coyle, M., Derwent, R., Fowler, D., Granier, C., Law, K.S., Mills, G.E., Stevenson, D.S., Tarasova, O., Thouret, V., Von Schneidmesser, E., Sommariva, R., Wild, O. and Williams, M.L. 2015. Tropospheric ozone and its precursors from the urban to the global scale from air quality to short-lived climate forcer. *Atmospheric*

*Chemistry and Physics*. **15**(15), pp.8889–8973.

Monks, S.A., Arnold, S.R. and Chipperfield, M.P. 2012. Evidence for El Niño-Southern Oscillation (ENSO) influence on Arctic CO interannual variability through biomass burning emissions. *Geophysical Research Letters*. **39**(14), pp.1–6.

Murray, L.T. 2016. Lightning NO<sub>x</sub> and Impacts on Air Quality. *Current Pollution Reports*. [Online]. **2**(2), pp.115–133. Available from: <http://dx.doi.org/10.1007/s40726-016-0031-7>.

Myers-Smith, I.H., Kerby, J.T., Phoenix, G.K., Bjerke, J.W., Epstein, H.E., Assmann, J.J., John, C., Andreu-Hayles, L., Angers-Blondin, S., Beck, P.S.A., Berner, L.T., Bhatt, U.S., Bjorkman, A.D., Blok, D., Bryn, A., Christiansen, C.T., Cornelissen, J.H.C., Cunliffe, A.M., Elmendorf, S.C., Forbes, B.C., Goetz, S.J., Hollister, R.D., de Jong, R., Lorant, M.M., Macias-Fauria, M., Maseyk, K., Normand, S., Olofsson, J., Parker, T.C., Parmentier, F.J.W., Post, E., Schaepman-Strub, G., Stordal, F., Sullivan, P.F., Thomas, H.J.D., Tømmervik, H., Treharne, R., Tweedie, C.E., Walker, D.A., Wilkening, M. and Wipf, S. 2020. Complexity revealed in the greening of the Arctic. *Nature Climate Change*. [Online]. **10**(2), pp.106–117. Available from: <http://dx.doi.org/10.1038/s41558-019-0688-1>.

Nakanishi, M. and Niino, H. 2004. An improved Mellor-Yamada Level-3 model with condensation physics: Its design and verification. *Boundary-Layer Meteorology*. **112**(1), pp.1–31.

Nakanishi, M. and Niino, H. 2009. Development of an Improved Turbulence Closure Model for the Atmospheric Boundary Layer. *Journal of the Meteorological Society of Japan*. **87**(5), pp.895–912.

Notario, A., Bravo, I., Adame, J.A., Díaz-de-Mera, Y., Aranda, A., Rodríguez, A. and Rodríguez, D. 2012. Analysis of NO, NO<sub>2</sub>, NO<sub>x</sub>, O<sub>3</sub> and oxidant (OX=O<sub>3</sub>+NO<sub>2</sub>) levels measured in a metropolitan area in the southwest of Iberian Peninsula. *Atmospheric Research*. [Online]. **104–105**(2), pp.217–226. Available from: <http://dx.doi.org/10.1016/j.atmosres.2011.10.008>.

Oikawa, P.Y., Ge, C., Wang, J., Eberwein, J.R., Liang, L.L., Allsman, L.A., Grantz, D.A. and Jenerette, G.D. 2015. Unusually high soil nitrogen oxide

- emissions influence air quality in a high-temperature agricultural region. *Nature Communications*. **6**.
- Otte, T.L. 2008. The impact of nudging in the meteorological model for retrospective air quality simulations. Part I: Evaluation against national observation networks. *Journal of Applied Meteorology and Climatology*. **47**(7), pp.1853–1867.
- Overland, J.E. and Wang, M. 2013. When will the summer Arctic be nearly sea ice free? *Geophysical Research Letters*. **40**(10), pp.2097–2101.
- Pankratova, N. V., Elansky, N.F., Belikov, I.B., Lavrova, O. V., Skorokhod, A.I. and Shumsky, R.A. 2011. Ozone and nitric oxides in the surface air over northern Eurasia according to observational data obtained in TROICA experiments. *Izvestiya - Atmospheric and Ocean Physics*. **47**(3), pp.313–328.
- Pearson, R.G., Phillips, S.J., Lorant, M.M., Beck, P.S.A., Damoulas, T., Knight, S.J. and Goetz, S.J. 2013. Shifts in Arctic vegetation and associated feedbacks under climate change. *Nature Climate Change*. **3**(7), pp.673–677.
- Peters, G.P., Nilssen, T.B., Lindholt, L., Eide, M.S., Glomsrød, S., Eide, L.I. and Fuglestad, J.S. 2011. Future emissions from shipping and petroleum activities in the Arctic. *Atmospheric Chemistry and Physics*. **11**(11), pp.5305–5320.
- Pickering, K.E., Thompson, A.M., Dickerson, R.R., Luke, W.T., McNamara, D.P., Greenberg, J.P. and Zimmerma, P.R. 1990. Model calculations of tropospheric ozone production potential following observed convective events. *Journal of Geophysical Research*. **95**(D9).
- Pincus, R., Barker, H.W. and Morcrette, J.J. 2003. A fast, flexible, approximate technique for computing radiative transfer in inhomogeneous cloud fields. *Journal of Geophysical Research: Atmospheres*. **108**(13), pp.1–5.
- Pithan, F. and Mauritsen, T. 2014. Arctic amplification dominated by temperature feedbacks in contemporary climate models. *Nature Geoscience*. **7**(3), pp.181–184.

- Pochanart, P. 2003. Regional background ozone and carbon monoxide variations in remote Siberia/East Asia. *Journal of Geophysical Research*. [Online]. **108**(D1), p.4028. Available from: <http://doi.wiley.com/10.1029/2001JD001412>.
- Powers, J.G., Klemp, J.B., Skamarock, W.C., Davis, C.A., Dudhia, J., Gill, D.O., Coen, J.L., Gochis, D.J., Ahmadov, R., Peckham, S.E., Grell, G.A., Michalakes, J., Trahan, S., Benjamin, S.G., Alexander, C.R., Dimego, G.J., Wang, W., Schwartz, C.S., Romine, G.S., Liu, Z., Snyder, C., Chen, F., Barlage, M.J., Yu, W. and Duda, M.G. 2017. The weather research and forecasting model: Overview, system efforts, and future directions. *Bulletin of the American Meteorological Society*. **98**(8), pp.1717–1737.
- Quinn, P. K., Bates, T.S., Baum, E., Doubleday, N., Fiore, A.M., Flanner, M., Fridlind, A., Garrett, T.J., Koch, D., Menon, S., Shindell, D., Stohl, A. and Warren, S.G. 2007. Short-lived pollutants in the Arctic: their climate impact and possible mitigation strategies. *Atmospheric Chemistry and Physics Discussions*. **7**, pp.15669–15692.
- Quinn, P.K., Miller, T.L., Bates, T.S., Ogren, J.A., Andrews, E. and Shaw, G.E. 2002. A 3-year record of simultaneously measured aerosol chemical and optical properties at Barrow, Alaska. *Journal of Geophysical Research: Atmospheres*. **107**(11).
- Quinn, Patricia K, Shaw, G.E., Andrews, E., Dutton, E.G., Ruoho-Airola, T. and Gong, S.L. 2007. Arctic haze: current trends and knowledge gaps. *Tellus, Series B: Chemical and Physical Meteorology*. **59**(1), pp.99–114.
- Rahn, K.A. 1981. Relative importances of North America and Eurasia as sources of arctic aerosol. *Atmospheric Environment (1967)*. **15**(8), pp.1447–1455.
- Rahn, K.A., Borys, R.D. and Shaw, G.E. 1977. The Asian source of Arctic haze bands. *Nature*. **268**(5622), pp.713–715.
- Raut, J.C., Marelle, L., Fast, J.D., Thomas, J.L., Weinzierl, B., Law, K.S., Berg, L.K., Roiger, A., Easter, R.C., Heimerl, K., Onishi, T., Delanoë, J. and Schlager, H. 2017. Cross-polar transport and scavenging of Siberian aerosols containing black carbon during the 2012 ACCESS summer

- campaign. *Atmospheric Chemistry and Physics*. **17**(18), pp.10969–10995.
- Ridley, B., Walega, J., Montzka, D., Grahek, F., Atlas, E., Flocke, F., Stroud, V., Deary, J., Gallant, A., Boudries, H., Bottenheim, J., Anlauf, K., Worthy, D., Sumner, A.L., Splawn, B. and Shepson, P. 2000. Is the arctic surface layer a source and sink of NO(x) in winter/spring? *Journal of Atmospheric Chemistry*. **36**(1), pp.1–22.
- Ridley, D.A., Cain, M., Methven, J. and Arnold, S.R. 2017. Sensitivity of tropospheric ozone to chemical kinetic uncertainties in air masses influenced by anthropogenic and biomass burning emissions. *Geophysical Research Letters*. **44**(14), pp.7472–7481.
- Roiger, A., Schlager, H., Schäfler, A., Huntrieser, H., Scheibe, M., Aufmhoff, H., Cooper, O.R., Sodemann, H., Stohl, A., Burkhardt, J., Lazzara, M., Schiller, C., Law, K.S. and Arnold, F. 2011. In-situ observation of Asian pollution transported into the Arctic lowermost stratosphere. *Atmospheric Chemistry and Physics*. **11**(21), pp.10975–10994.
- Rydsaa, J.H., Stordal, F., Gerosa, G., Finco, A. and Hodnebrog 2016. Evaluating stomatal ozone fluxes in WRF-Chem: Comparing ozone uptake in Mediterranean ecosystems. *Atmospheric Environment*. [Online]. **143**, pp.237–248. Available from: <http://dx.doi.org/10.1016/j.atmosenv.2016.08.057>.
- Sand, M., Berntsen, T.K., Von Salzen, K., Flanner, M.G., Langner, J. and Victor, D.G. 2016. Response of Arctic temperature to changes in emissions of short-lived climate forcers. *Nature Climate Change*. **6**(3), pp.286–289.
- Schmale, J., Arnold, S.R., Law, K.S., Thorp, T., Anenberg, S., Simpson, W.R., Mao, J. and Pratt, K.A. 2018. Local Arctic air pollution: A neglected but serious problem. *Earth's Future*. [Online], pp.1–28. Available from: <http://doi.wiley.com/10.1029/2018EF000952>.
- Schober, P. and Schwarte, L.A. 2018. Correlation coefficients: Appropriate use and interpretation. *Anesthesia and Analgesia*. **126**(5), pp.1763–1768.
- Screen, J.A. and Simmonds, I. 2010. The central role of diminishing sea ice in recent Arctic temperature amplification. *Nature*. [Online]. **464**(7293),

pp.1334–1337. Available from: <http://dx.doi.org/10.1038/nature09051>.

- Sessions, W.R., Fuelberg, H.E., Kahn, R.A. and Winker, D.M. 2011. An investigation of methods for injecting emissions from boreal wildfires using WRF-Chem during ARCTAS. *Atmospheric Chemistry and Physics*. **11**(12), pp.5719–5744.
- Shao-Meng Li, Barrie, L.A. and Sirois, A. 1993. Biogenic sulfur aerosol in the Arctic troposphere: 2. Trends and seasonal variations. *Journal of Geophysical Research*. **98**(D11).
- Sharma, A., Ojha, N., Pozzer, A., Mar, K.A., Beig, G., Lelieveld, J. and Gunthe, S.S. 2017. WRF-Chem simulated surface ozone over south Asia during the pre-monsoon: Effects of emission inventories and chemical mechanisms. *Atmospheric Chemistry and Physics*. **17**(23), pp.14393–14413.
- Shaw, G.E. 1987. Aerosols as climate regulators: A climate-biosphere linkage? *Atmospheric Environment (1967)*. **21**(4), pp.985–986.
- Shaw, G.E. 1985. On the climatic relevancy of Arctic Haze: static energy balance considerations. *Tellus, Series B*. **37**(B1), pp.50–52.
- Shaw, G.E. 1995. The Arctic haze phenomenon. *Bulletin - American Meteorological Society*. **76**(12), pp.2403–2413.
- Shindell, D. 2007. Local and remote contributions to Arctic warming. *Geophysical Research Letters*. **34**(14), pp.1–5.
- Shindell, D., Kuylensstierna, J.C.I., Vignati, E., van Dingenen, R., Amann, M., Klimont, Z., Anenberg, S.C., Müller, N., Janssens-Maenhout, G., Raes, F., Schwartz, J., Faluvegi, G., Pozzoli, L., Kupiainen, K., Hoglund-Isaksson, L., Emberson, L., Streets, D., Ramanathan, V., Hicks, K., Oanh, N.T.K., Milly, G., Williams, M., Demkine, V. and Fowler, D. 2012. Simultaneously Mitigating Near-Term Climate Change and Improving Human Health and Food Security. *Science*. [Online]. **335**(6065), pp.183–189. Available from: <http://www.sciencemag.org/cgi/doi/10.1126/science.1210026>.
- Silva, S.J. and Heald, C.L. 2018. Investigating Dry Deposition of Ozone to Vegetation. *Journal of Geophysical Research: Atmospheres*. **123**(1), pp.559–573.

- Simpson, W.R., Von Glasow, R., Riedel, K., Anderson, P., Ariya, P., Bottenheim, J., Burrows, J., Carpenter, L.J., Frieß, U., Goodsite, M.E., Heard, D., Hutterli, M., Jacobi, H.W., Kaleschke, L., Neff, B., Plane, J., Platt, U., Richter, A., Roscoe, H., Sander, R., Shepson, P., Sodeau, J., Steffen, A., Wagner, T. and Wolff, E. 2007. Halogens and their role in polar boundary-layer ozone depletion. *Atmospheric Chemistry and Physics*. **7**(16), pp.4375–4418.
- Skamarock, W.C., Klemp, J.B., Dudhia, J.B., Gill, D.O., Barker, D.M., Duda, M.G., Huang, X.-Y., Wang, W. and Powers, J.G. 2008. A description of the Advanced Research WRF Version 3, NCAR Technical Note TN-475+STR. *Technical Report*. (June), p.113.
- Skeie, R.B., Myhre, G., Hodnebrog, Ø., Cameron-Smith, P.J., Deushi, M., Hegglin, M.I., Horowitz, L.W., Kramer, R.J., Michou, M., Mills, M.J., Olivieri, D.J.L., Connor, F.M.O., Paynter, D., Samset, B.H., Sellar, A., Shindell, D., Takemura, T., Tilmes, S. and Wu, T. 2020. Historical total ozone radiative forcing derived from CMIP6 simulations. *npj Climate and Atmospheric Science*. [Online]. **3**(1). Available from: <http://dx.doi.org/10.1038/s41612-020-00131-0>.
- Smith-Sivertsen, T., Bykov, V., Melbye, H., Tchachtchine, V., Selnes, A. and Lund, E. 2001. Sulphur dioxide exposure and lung function in a Norwegian and Russian population living close to a nickel smelter. *International journal of circumpolar health*. **60**(3), pp.342–359.
- Steinkamp, J. and Lawrence, M.G. 2011. Improvement and evaluation of simulated global biogenic soil NO emissions in an AC-GCM. *Atmospheric Chemistry and Physics*. **11**(12), pp.6063–6082.
- Stevenson, D.S., Dentener, F.J., Schultz, M.G., Ellingsen, K., van Noije, T.P.C., Wild, O., Zeng, G., Amann, M., Atherton, C.S., Bell, N., Bergmann, D.J., Bey, I., Butler, T., Cofala, J., Collins, W.J., Derwent, R.G., Doherty, R.M., Drevet, J., Eskes, H.J., Fiore, A.M., Gauss, M., Hauglustaine, D.A., Horowitz, L.W., Isaksen, I.S.A., Krol, M.C., Lamarque, J.F., Lawrence, M.G., Montanaro, V., Müller, J.F., Pitari, G., Prather, M.J., Pyle, J.A., Rast, S., Rodriguez, J.M., Sanderson, M.G., Savage, N.H., Shindell, D.T.,

- Strahan, S.E., Sudo, K. and Szopa, S. 2006. Multimodel ensemble simulations of present-day and near-future tropospheric ozone. *Journal of Geophysical Research Atmospheres*. **111**(8).
- Stjernberg, A.C.E., Skorokhod, A., Paris, J.D., Elansky, N., Nédélec, P. and Stohl, A. 2012. Low concentrations of near-surface ozone in Siberia. *Tellus, Series B: Chemical and Physical Meteorology*. **64**(1).
- Stohl, a., Berg, T., Burkhardt, J.F., Fjæraa, a. M., Forster, C., Herber, a., Hov, Ø., Lunder, C., McMillan, W.W., Oltmans, S., Shiobara, M., Simpson, D., Solberg, S., Stebel, K., Ström, J., Tørseth, K., Treffeisen, R., Virkkunen, K. and Yttri, K.E. 2006. Arctic smoke – record high air pollution levels in the European Arctic due to agricultural fires in Eastern Europe. *Atmospheric Chemistry and Physics Discussions*. **6**(5), pp.9655–9722.
- Stohl, A. 2006. Characteristics of atmospheric transport into the Arctic troposphere. *Journal of Geophysical Research Atmospheres*. **111**(11), pp.1–17.
- Stohl, A., Aamaas, B., Amann, M., Baker, L.H., Bellouin, N., Berntsen, T.K., Boucher, O., Cherian, R., Collins, W., Daskalakis, N., Dusinska, M., Eckhardt, S., Fuglestvedt, J.S., Harju, M., Heyes, C., Hodnebrog, Hao, J., Im, U., Kanakidou, M., Klimont, Z., Kupiainen, K., Law, K.S., Lund, M.T., Maas, R., MacIntosh, C.R., Myhre, G., Myriokefalitakis, S., Olivi??, D., Quaas, J., Quennehen, B., Raut, J.C., Rumbold, S.T., Samset, B.H., Schulz, M., Seland, Shine, K.P., Skeie, R.B., Wang, S., Yttri, K.E. and Zhu, T. 2015. Evaluating the climate and air quality impacts of short-lived pollutants. *Atmospheric Chemistry and Physics*. **15**(18), pp.10529–10566.
- Stohl, A., Aamaas, B., Amann, M., Baker, L.H., Bellouin, N., Berntsen, T.K., Boucher, O., Cherian, R., Collins, W., Daskalakis, N., Dusinska, M., Eckhardt, S., Fuglestvedt, J.S., Harju, M., Heyes, C., Hodnebrog, Hao, J., Im, U., Kanakidou, M., Klimont, Z., Kupiainen, K., Law, K.S., Lund, M.T., Maas, R., MacIntosh, C.R., Myhre, G., Myriokefalitakis, S., Olivié, D., Quaas, J., Quennehen, B., Raut, J.C., Rumbold, S.T., Samset, B.H., Schulz, M., Seland, Shine, K.P., Skeie, R.B., Wang, S., Yttri, K.E. and Zhu, T. 2015. Evaluating the climate and air quality impacts of short-lived

- pollutants. *Atmospheric Chemistry and Physics*. **15**(18), pp.10529–10566.
- Stohl, A., Klimont, Z., Eckhardt, S., Kupiainen, K., Shevchenko, V.P., Kopeikin, V.M. and Novigatsky, A.N. 2013. Black carbon in the Arctic: The underestimated role of gas flaring and residential combustion emissions. *Atmospheric Chemistry and Physics*. **13**(17), pp.8833–8855.
- Strode, S.A., Rodriguez, J.M., Logan, J.A., Cooper, O.R., Witte, J.C., Lamsal, L.N., Damon, M., Van Aartsen, B., Steenrod, S.D. and Strahan, S.E. 2015. Trends and variability in surface ozone over the United States. *Journal of Geophysical Research*. **120**(17), pp.9020–9042.
- Thomas, J.L., Raut, J.C., Law, K.S., Marelle, L., Ancellet, G., Ravetta, F., Fast, J.D., Pfister, G., Emmons, L.K., Diskin, G.S., Weinheimer, A., Roiger, A. and Schlager, H. 2013. Pollution transport from North America to Greenland during summer 2008. *Atmospheric Chemistry and Physics*. **13**(7), pp.3825–3848.
- Thompson, C.R., Shepson, P.B., Liao, J., Huey, L.G., Cantrell, C., Flocke, F. and Orlando, J. 2017. Bromine atom production and chain propagation during springtime Arctic ozone depletion events in Barrow, Alaska. *Atmospheric Chemistry and Physics*. **17**(5), pp.3401–3421.
- Thompson, G., Field, P.R., Rasmussen, R.M. and Hall, W.D. 2008. Explicit forecasts of winter precipitation using an improved bulk microphysics scheme. Part II: Implementation of a new snow parameterization. *Monthly Weather Review*. **136**(12), pp.5095–5115.
- Thunis, P., Pederzoli, A. and Pernigotti, D. 2012. Performance criteria to evaluate air quality modeling applications. *Atmospheric Environment*. **59**, pp.476–482.
- Tie, X. 2003. Effect of clouds on photolysis and oxidants in the troposphere. *Journal of Geophysical Research*. **108**(D20).
- Tran, H.N.Q. and Mölders, N. 2011. Investigations on meteorological conditions for elevated PM<sub>2.5</sub> in Fairbanks, Alaska. *Atmospheric Research*. [Online]. **99**(1), pp.39–49. Available from: <http://dx.doi.org/10.1016/j.atmosres.2010.08.028>.

- Tran, T.T., Tran, H.N.Q., Cahill, C.F., Mölders, N. and Leelasakultum, K. 2011. Assessment of WRF/Chem PM<sub>2.5</sub> forecasts using mobile and fixed location data from the Fairbanks, Alaska winter 2008/09 field campaign. *Atmospheric Pollution Research*. [Online]. **3**(2), pp.180–191. Available from: <http://dx.doi.org/10.5094/APR.2012.018>.
- Tronstad Lund, M., Eyring, V., Fuglestedt, J., Hendricks, J., Lauer, A., Lee, D. and Righi, M. 2012. Global-mean temperature change from shipping toward 2050: Improved representation of the indirect aerosol effect in simple climate models. *Environmental Science and Technology*. **46**(16), pp.8868–8877.
- Turner, M.C., Jerrett, M., Pope, C.A., Krewski, D., Gapstur, S.M., Diver, W.R., Beckerman, B.S., Marshall, J.D., Su, J., Crouse, D.L. and Burnett, R.T. 2016. Long-Term Ozone Exposure and Mortality in a Large Prospective Study. *American journal of respiratory and critical care medicine*. **193**(10), pp.1134–1142.
- Ulrikh, D. V., Ivanova, S. V. and Riabchikova, I.A. 2017. Assessment of Inhalation Risk to Public Health in the Southern Ural. *IOP Conference Series: Materials Science and Engineering*. **262**(1).
- Uttal, T., Starkweather, S., Drummond, J.R., Vihma, T., Makshtas, A.P., Darby, L.S., Burkhart, J.F., Cox, C.J., Schmeisser, L.N., Haiden, T., Maturilli, M., Shupe, M.D., De Boer, G., Saha, A., Grachev, A.A., Crepinsek, S.M., Bruhwiler, L., Goodison, B., McArthur, B., Walden, V.P., Dlugokencky, E.J., Persson, P.O.G., Lesins, G., Laurila, T., Ogren, J.A., Stone, R., Long, C.N., Sharma, S., Massling, A., Turner, D.D., Stanitski, D.M., Asmi, E., Aurela, M., Skov, H., Eleftheriadis, K., Virkkula, A., Platt, A., Førlund, E.J., Iijima, Y., Nielsen, I.E., Bergin, M.H., Candlish, L., Zimov, N.S., Zimov, S.A., O'Neill, N.T., Fogal, P.F., Kivi, R., Konopleva-Akish, E.A., Verlinde, J., Kustov, V.Y., Vassel, B., Ivakhov, V.M., Viisanen, Y. and Intrieri, J.M. 2016. International arctic systems for observing the atmosphere: An International Polar Year Legacy Consortium. *Bulletin of the American Meteorological Society*. **97**(6), pp.1033–1056.
- Vinken, G.C.M., Boersma, K.F., Maasakkers, J.D., Adon, M. and Martin, R. V.

2014. Worldwide biogenic soil NO<sub>x</sub> emissions inferred from OMI NO<sub>2</sub> observations. *Atmospheric Chemistry and Physics*. **14**(18), pp.10363–10381.
- Visser, A.J., Boersma, K.F., Ganzeveld, L.N. and Krol, M.C. 2019. European NO<sub>x</sub> emissions in WRF-Chem derived from OMI: impacts on summertime surface ozone. *Atmospheric Chemistry and Physics Discussions*. (2), pp.1–36.
- Waigl, C.F., Stuefer, M., Prakash, A. and Ichoku, C. 2017. Detecting high and low-intensity fires in Alaska using VIIRS I-band data: An improved operational approach for high latitudes. *Remote Sensing of Environment*. [Online]. **199**, pp.389–400. Available from: <http://dx.doi.org/10.1016/j.rse.2017.07.003>.
- Walker, T.W., Jones, D.B.A., Parrington, M., Henze, D.K., Murray, L.T., Bottenheim, J.W., Anlauf, K., Worden, J.R., Bowman, K.W., Shim, C., Singh, K., Kopacz, M., Tarasick, D.W., Davies, J., Von Der Gathen, P., Thompson, A.M. and Carouge, C.C. 2012. Impacts of midlatitude precursor emissions and local photochemistry on ozone abundances in the Arctic. *Journal of Geophysical Research Atmospheres*. **117**(1), pp.1–17.
- Wang, Y. and Hopke, P.K. 2014. Is Alaska truly the great escape from air pollution? – Long term source apportionment of fine particulate matter in Fairbanks, Alaska. *Aerosol and Air Quality Research*. **14**(7), pp.1875–1882.
- Ward, T., Trost, B., Conner, J., Flanagan, J. and Jayanty, R.K.M. 2012. Source Apportionment of PM<sub>2.5</sub> in a Subarctic Airshed - Fairbanks, Alaska. *Aerosol and Air Quality Research*. **12**(4), pp.536–543.
- Warneke, C., Froyd, K.D., Brioude, J., Bahreini, R., Brock, C.A., Cozic, J., De Gouw, J.A., Fahey, D.W., Ferrare, R., Holloway, J.S., Middlebrook, A.M., Miller, L., Montzka, S., Schwarz, J.P., Sodemann, H., Spackman, J.R. and Stohl, A. 2010. An important contribution to springtime Arctic aerosol from biomass burning in Russia. *Geophysical Research Letters*. **37**(1).
- Wesely, M.L. 1989. Parameterization of surface resistances to gaseous dry deposition in regional-scale numerical models. *Atmospheric Environment*. **41**(SUPPL.), pp.52–63.

- Wesely, M.L., Cook, D.R. and Williams, R.M. 1981. 1973; Wesely. . **20**, pp.459–471.
- Wiedinmyer, C., Akagi, S.K., Yokelson, R.J., Emmons, L.K., Al-Saadi, J.A., Orlando, J.J. and Soja, A.J. 2010. The Fire INventory from NCAR (FINN) – a high resolution global model to estimate the emissions from open burning. *Geoscientific Model Development Discussions*. [Online]. **3**(4), pp.2439–2476. Available from: <http://www.geosci-model-dev-discuss.net/3/2439/2010/>.
- Witze, A. 2020. Why Arctic fires are bad news for climate change. *Nature*. **585**, pp.336–337.
- Yamada, T. 1977. A numerical experiment on pollutant dispersion in a horizontally-homogeneous atmospheric boundary layer. *Atmospheric Environment (1967)*. **11**(11), pp.1015–1024.
- Ye, L. and Wang, Y. 2020. Long-term air quality study in fairbanks, alaska: Air pollutant temporal variations, correlations, and pm2.5 source apportionment. *Atmosphere*. **11**(11), pp.2010–2011.
- Yienger, J.J. and Levy, H. 1995. Empirical model of global soil-biogenic NO<sub>x</sub>emissions. *Journal of Geophysical Research*. **100**(D6).
- Yu, S., Eder, B., Dennis, R., Chu, S.-H. and Schwartz, S.E. 2006. New unbiased symmetric metrics for evaluation of air quality models. *Atmospheric Science Letters*. [Online]. **7**(1), pp.26–34. Available from: <http://doi.wiley.com/10.1002/asl.125>.
- Zaveri, R.A., Easter, R.C., Fast, J.D. and Peters, L.K. 2008. Model for Simulating Aerosol Interactions and Chemistry (MOSAIC). *Journal of Geophysical Research Atmospheres*. **113**(13), pp.1–29.
- Zhang, Y. 2008. Online-coupled meteorology and chemistry models: History, current status, and outlook. *Atmospheric Chemistry and Physics*. **8**(11), pp.2895–2932.
- Zhao, X., Strong, K., Adams, C., Schofield, R., Yang, X., Richter, A., Friess, U., Blechschmidt, A.M. and Koo, J.H. 2016. A case study of a transported bromine explosion event in the Canadian high arctic. *Journal of*

*Geophysical Research*. **121**(1), pp.457–477.

Zhou, Y., Brunner, D., Boersma, K.F., Dirksen, R. and Wang, P. 2009. An improved tropospheric NO<sub>2</sub> retrieval for OMI observations in the vicinity of mountainous terrain. *Atmospheric Measurement Techniques*. **2**(2), pp.401–416.